Proceedings

International Conference on Nuclear Science and Technology

Nuclear Society Of Iran | Atomic Energy Organization of Iran | Nuclear Sciences and Technologies Research Institute

Papers on:

Fusion Energy & Plasma

*In this booklet, you will find the selected papers presented at the **First International Conference on Nuclear Science and Technology**, held from May 6-8, 2024, in Isfahan, Iran.*
We hope you find it informative and enjoyable!

ICNST 2024

Contact and Accessibility

icnst2024.com
registration@icnst2024.com


بسم الله الرحمن الرحیم

The Conference President's Message
ICNST 2024

Attendees, guests, and colleagues

I would like to warmly welcome you to the first International Conference on Nuclear Science and Technology (ICNST 2024). It has been a real honor and privilege to serve as the president of this conference. The conference this year has brought together an incredible diversity of authors and speakers from universities, government, and industry to share ideas and new perspectives on a wide range of radiation applications, nuclear reactors, particle accelerators, radiation measurements, fusion and plasma, stable and radioactive isotopes, radiation safety and security, nuclear agriculture, fuel cycle, lasers, education and training and nuclear governance.

Climate change, a new topic which has been added to this year's agenda as an important worldwide issue. a matter that has been brought up as a critical concern at the majority of IAEA conferences and nuclear scientific assemblies in recent years.

Panel discussions and exhibitions are being introduced as side activities in an attempt to keep this scientific meeting from becoming one-dimensional and increase its effectiveness.

More than 520 complete papers have been approved for this conference; when combined with the additional panels, get-togethers, and side activities, it is anticipated that over 1000 people will attend in person in the historical and touristic city of Isfahan. We look forward to welcoming participants to share their practical ideas and to enjoy an academical and cultural three days in Isfahan.

I'll close by wishing you everyone an incredible, instructive, and transformative experience during ICNST2024 and I hope that this conference can pave the route for academic materials to be used in industry and everyday life.

Prof. Javad Karimi-Sabet
President of ICNST2024
Javad Karimi-Sabet

welcome statment of scientific secretary
ICNST 2024

"In the name of God, the Merciful,

Prior to giving the stage to address this distinguished forum, let me take this opportunity to express our deep gratitude, on behalf of all attendees, for His Excellency Mr. Islami's scientific, educational, and motivational remarks, as well as for his excellent organization of this conference.

I would also like to express our appreciation to His Excellency Dr. Mortazavi, Governor-General of Isfahan Province, for his constructive and useful support in enabling this meeting to take place.

This is a great pleasure and honor to extend a warm greeting to each and every one of you for the International Conference on Nuclear Science and Technology, scheduled from May 6th to May 8th, 2024, in the historic city of Isfahan, Iran.

With the aim of advancing our knowledge of nuclear science and technology, this conference is a major global convergence of experts, researchers, and practitioners. It is a platform for the sharing of creative concepts, the presentation of state-of-the-art research, and the formation of cooperative alliances.

As the scientific secretary of this prestigious event, I am particularly excited about the diverse array of participants expected to grace us with their presence. From the esteemed scientists and engineers of Russian universities and research centers to representatives from Islamic countries, friendly nations, and beyond, this conference promises to be a melting pot of perspectives, experiences, and expertise.

The extensive coverage of this conference is another aspect of its uniqueness. We have nearly 900 participants representing 22 countries around the world. Of the 900 participants, 620 are authors covering 13 major topics. There are 421 papers for oral and poster presentations, with additional documents for publication in ISC journals. There will be 3 plenary sessions, 16 panel discussions, 20 parallel oral presentation sessions, and 3 poster sessions.

Prof. Hosein Afarideh
Scientific Secretariat of ICNST2024

Organizers

Nuclear Society Of Iran (NSI)

Atomic Energy Organization of Iran (AEOI)

Nuclear Science and Technology Research Institute (NSTRI)

Scientific Partnership

International Atomic Energy Agency (IAEA)

Isfahan University

Sharif University

Kurchatov Institute

Amirkabir University of Technology (Tehran Polytechnique)

Shahid Beheshti University

Isfahan University of Technology

Shiraz University

Islamic Azad University

K. N. Toosi University of Technology

Ferdowsi University of Mashhad

Kerman Graduate University of Technology

Sahand University of Technology

University of Tabriz

Islamic World Scieence Citation Center

Journal of Nuclear Science and Technology (JonSat)

Radiation Physics and Engineering journal

Nuclear Watch

Cooperative Organization

Isfahan Governorate

Isfahan Municipality

Abbasi Hotel

Iran Atomic Energy Production & Development Co.

Iran's Nuclear Raw Materials & Fuel Production Co.

Radiation Application Development Co.

Ofogh Consulting Engineers Co.

Nuclear Power Plant Safety Development & Promotion Co.

Nuclear Power Plant Engineering & Construction Co.

Engineering & Design of Industrial Simulator Co.

Energy Industry Development Engineering Co

Atomic Power Plant Pepair & support

Nuclear Reactors Fuel Co.

Iran Radioactive Waste Management Co.

Mesbah Energy Co.

Iran Gharb Industrial, Mining and Energy Co.

Pars Isotope Co.

Center for Laser Science & Technology of Iran

Centrifuge Production of Iran Co.

Plasma Technology Development Co.

Rasa Technology and Innovation Center

Behyaar Sanaat Sepahan Co.

Nuclear Data Base of Iran (NDB)

Parto think tank (strategic studies of nuclear industry development)

International Conference Alerts

Local Scientific Board

RAW	NAME	ROLE	AFFILIATION
1	**Prof. Hossein Afarideh**	**Chairman of Local Scientific Board**	**Amirkabir University of Technology (Tehran Polytechnique)(AUT)**
2	**Prof. Mohammad Ghanadi Maragheh**	**Member of The Local Scientific Board**	**Nuclear Science and Technology Research Institute of Iran (NSTRI)**
3	**Prof. Mohammad Lamei Rashti**	**Member of The Local Scientific Board**	**Nuclear Science and Technology Research Institute of Iran (NSTRI)**
4	**Prof. Mohammad Bagher Ghofrani**	**Member of The Local Scientific Board**	**Sharif University of Technology (SUT)**
5	**Prof. Hosein Faghihian**	**Member of The Local Scientific Board**	**University of Isfahan (UI)**
6	**Prof. Javad Rahighi**	**Member of The Local Scientific Board**	**Institute for Research in Fundamental Sciences (IPM)**
7	**Prof. Seyed Amirhossein Feghhi**	**Member of The Local Scientific Board**	**Shahid Beheshti University (SBU)**

Scientific Committee

RAW	NAME	ROLE	AFFILIATION
1	**Prof. Ali Akbar Salehi**	**Member of The Scientific Committe**	**Sharif University of Technology (SUT)**
2	**Prof. Seyyed Javad Ahmadi**	**Member of The Scientific Committe**	**Nuclear Science and Technology Research Institute of Iran (NSTRI)**
3	**Prof. Farhoud Ziaee**	**Member of The Scientific Committe**	**Nuclear Science and Technology Research Institute of Iran (NSTRI)**
4	**Prof. Saeed Hamidi**	**Member of The Scientific Committe**	**University of Arak**
5	**Prof. Seyedzafarollah Kalantari**	**Member of The Scientific Committe**	**Isfahan University of Technology (IUT)**
6	**Prof. Naser Bagheri Moghaddam**	**Member of The Scientific Committe**	**National Research Institute for Science Policy (NRISP)**
7	**Prof. Naser Vosoghi**	**Member of The Scientific Committe**	**Sharif University of Technology (SUT)**
8	**Prof. Seied Rabi Mahdavi**	**Member of The Scientific Committe**	**Iran University of Medical Sciences**
9	**Prof. Meisam Torab Mostaedi**	**Member of The Scientific Committe**	**Nuclear Science and Technology Research Institute of Iran (NSTRI)**
10	**Prof. Fereydoun Abbasi Davani**	**Member of The Scientific Committe**	**Shahid Beheshti University (SBU)**
11	**Prof. Seyed Farhad Masoudi**	**Member of The Scientific Committe**	**K.N.Toosi University of Technology**
12	**Prof. Rasool Ruknizadeh**	**Member of The Scientific Committe**	**University of Isfahan (UI)**
13	**Prof. Gholamreza Raeesali**	**Member of The Scientific Committe**	**Nuclear Science and Technology Research Institute of Iran (NSTRI)**
14	**Prof. Asghar Sedighzadeh**	**Member of The Scientific Committe**	

15	**Prof. Hossein Kazeminejad**	**Member of The Scientific Committe**	**Nuclear Science and Technology Research Institute of Iran (NSTRI)**
16	**Prof. Seyyed Jaber Safdari**	**Member of The Scientific Committe**	**Nuclear Science and Technology Research Institute of Iran (NSTRI)**
17	**Prof. Omid Reza Kakuee**	**Member of The Scientific Committe**	**Nuclear Science and Technology Research Institute of Iran (NSTRI)**
18	**Prof. Alireza Keshtkar**	**Member of The Scientific Committe**	**Nuclear Science and Technology Research Institute of Iran (NSTRI)**
19	**Prof. Fereshte Haj esmail Beigi**	**Member of The Scientific Committe**	**Nuclear Science and Technology Research Institute of Iran (NSTRI)**
20	**Prof. Masoud Mahjour-shafiei**	**Member of The Scientific Committe**	**Nuclear Science and Technology Research Institute of Iran (NSTRI)**
21	**Prof. Mahmoud Payami Shabestar**	**Member of The Scientific Committe**	**Nuclear Science and Technology Research Institute of Iran (NSTRI)**
22	**Prof. Ali Bahrami Samani**	**Member of The Scientific Committe**	**Nuclear Science and Technology Research Institute of Iran (NSTRI)**
23	**Dr. Farhanaz Motamedi**	**Member of The Scientific Committe**	**Nuclear Science and Technology Research Institute of Iran (NSTRI)**
24	**Dr. Faezeh Rahmani**	**Member of The Scientific Committe**	**K.N.Toosi University of Technology**
25	**Dr. Ebrahim Moghiseh**	**Member of The Scientific Committe**	**Nuclear Science and Technology Research Institute of Iran (NSTRI)**
26	**Dr. Iraj Jabari**	**Member of The Scientific Committe**	**University of Isfahan (UI)**
27	**Dr. Nima Ghal-Eh**	**Member of The Scientific Committe**	**Ferdowsi University of Mashhad**
28	**Dr. Mitra Athari Alaf**	**Member of The Scientific Committe**	**Islamic Azad University Science and Research Branch**
29	**Dr. Gholamreza Etaati**	**Member of The Scientific Committe**	
30	**Dr. Amir Movafeghi**	**Member of The Scientific Committe**	**Nuclear Science and Technology Research Institute of Iran (NSTRI)**

Executive Committee

RAW	NAME	ROLE
1	Dr. Farshad Ghasemi	Chairman of the Executive Committee
2	Dr. Ehsan Molazadeh	Member of The Executive Committee
3	Dr. Seyyed Ghasem Biniaz	Member of The Executive Committee
4	Mr. Aliakbar Aminidoust	Member of The Executive Committee
5	Ms. Fatemeh Zamani	Member of The Executive Committee
6	Ms. Mahya Pazoki	Member of The Executive Committee
7	Mr. Hosein Maleki	Member of The Executive Committee
8	Mr. Maziar Dalili	Member of The Executive Committee
9	Mr. Shojaei	Member of The Executive Committee
10	Ms. Fatemeh Rezaei	Member of The Executive Committee
11	Mr. Reza Rafiei	Member of The Executive Committee
12	Ms. Seyyedeh Elham Ebrahimi	Member of The Executive Committee

Fusion Energy & Plasma

Fusion Energy & Plasma

ICNST 2024
International Conference on Nuclear Science and Technology
6- 8 MAY 2024 | Isfahan, Iran

Accurate power measurement in dielectric barrier discharge in argon and a radio frequency power supply of 13.56 MHz (Paper ID: 1030)

Bashiry.S*[*1], Zahednia.N[1], Bakhshzad Mahmoudi.M[1]
[1]*Plasma and Fusion Research School*
Nuclear Science and Technology Research Institute, AEOI
Tehran, Iran

Abstract

Dielectric Barrier Discharge at atmospheric pressure is a major source of cold plasma generation. This system has various uses in business, and it has lately attracted a great deal of research interest. Accurate power consumption measurement in a dielectric barrier discharge plasma actuator is crucial for comparing devices. Power measurement in plasma is difficult owing to the presence of transient current peaks with high amplitude and frequency. This article analyzes the benefits and drawbacks of several ways for determining power consumption in plasma and introduces the most appropriate method, the electric charge method, as an accurate method of power measurement. One of the most difficult aspects of power computation is determining the appropriate monitor capacitor, as detailed in this article. The essential considerations for a more precise power measurement are discussed below, as well as the power consumption in the discharge plasma of the dielectric barrier with argon and a 13.56 MHz radio frequency power source, which is measured and estimated with the Q-V diagram.

Keywords: Power consumption, Electric charge method, The monitor capacitor, Lissajous curve

Introduction

The calculation of electricity consumption for dielectric barrier discharge (DBD) plasma actuators has become a popular research issue in the last decade. A DBD is an actuator that has two electrodes separated by a dielectric. One electrode is exposed to current, while the other is surrounded by dielectric. An alternating current voltage (AC) in the kilovolt range is applied to the electrodes, resulting in a discharge plasma. There are typically two ways of functioning. A standard DBD operation uses voltage waveforms in the kHz frequency band, whereas the second mode uses pulse waveforms [1]. Fig.1 depicts the schematic of the DBD plasma device with argon and radiofrequency power supply.

Manley [2] was the first person to develop the loading technique for calculating power in discharge between parallel plates. Wagner et al. [3] and Borcia et al. [4] explain this approach in their work on

plasma-based material processing. Thomas et al. [5] attempted to measure both the power and impedance of the actuator. In 2017, Ashpis and colleagues [1] utilized the shunt resistance procedure and the capacitor monitor method to assess the actuator's power usage. The measurements were taken simultaneously and compared immediately.

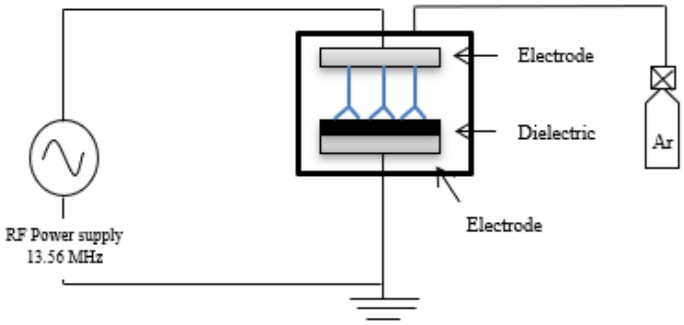

Fig. 1. schematic of a DBD with an electrode covered by dielectric.

Power is typically determined using measurements of voltage and current waveforms. The current waveform in DBD actuators is not smooth, even though the signal voltage is. Fast and dynamic sparks characterize the current chart, making them more challenging to collect and solve accurately. As a result, power measurement is not nearly as easy as it appears and necessitates extra attention to the measuring method and data-gathering equipment [1]. This article discusses challenges relating to reliable power measurement and, eventually, power measurement in DBD with argon and 13.56 MHz radio frequency power source, with an emphasis on the charge-voltage (Q-V) measuring technique.

In general, there are two ways to measure the consumption of power. There are two methods: electric current and electric charge. Current-based approaches record voltage and current data in the time domain. Instantaneous power is calculated by multiplying two signals. A current can be measured using a shunt resistor or a Rogowski coil [1].

The electric charge technique measures the load using a capacitor with a specific capacity, known as a monitor capacitor, that is connected in series between the covered actuator electrode and the ground. In general, the so-called "capacitor method" is the most accurate way to measure plasma power and allows for more precise electrical identification of reactor characteristics. For example, by combining electrical

characteristics with an appropriate equivalent circuit model, the average voltage of the gas gap where the DBD plasma ignites may be estimated with high precision. This is a constant voltage known as the "ignition voltage" or U_b. The ignition voltage U_b operates as a scale for measuring the electric field in the DBD plasma and is ideal for analyzing plasma chemistry within the reactor [6,7].

Power Measurement in Dbd Actuator

When the monitor capacitor's instantaneous charge Q_m and the actuator's instantaneous voltage V_{in} are drawn about each other, a Lissajous curve is formed on the Q_m-V_{in} plane. The Q_m-V_{in} diagram is most used to calculate power loss during discharge using the area covered by the hysteresis loop [1]. In several current papers, the resulting equations for estimating the power are based on the geometric properties of the Q_m-V_{in} diagram, assuming a perfect parallelogram [2, 8], which seldom occurs. The following relationship between area and average power applies to any form of the Q_m-V_{in} diagram [9].

$$I_m(t) = C_m \frac{dV_m(t)}{dt} \tag{1}$$

The instantaneous power P(t) in DBD may be calculated using the equation below:

$$P(t) = V_{in}(t).I_{in}(t) = V_{in}(t).C_m \frac{dV_m(t)}{dt} \tag{2}$$

To compute average power P, integrate equation (2) concerning time and replace the load relation in the equation:

$$\begin{aligned} \overline{\mathrm{P}} &= \frac{1}{\mathrm{T}} \int_0^{\mathrm{T}} \mathrm{V_{in}(t)} \,.\, \mathrm{C_m} \frac{\mathrm{dV_m(t)}}{\mathrm{dt}} \,\mathrm{dt} \\ &= \frac{1}{\mathrm{T}} \oint_{\substack{\text{one} \\ \text{cycle}}}^{1} \mathrm{V_{in}} \,\mathrm{dQ_m} \end{aligned} \tag{3}$$

$\boldsymbol{Q_m}$ denotes the immediate capacitor charge, while $\boldsymbol{V_{in}}$ represents the instantaneous actuator voltage. This demonstrates how to compute the average power consumption in a discharge cycle by multiplying the area surrounded by the $\boldsymbol{Q_m - V_{in}}$ diagram by the discharge cycle frequency. It is vital to verify that the integral of the received data is conducted on the correct multiple of the discharge time (T), and that the reactive power in the capacitive components of the circuit does not average to zero, When utilizing numerical methods to compute this integral [9].

Selecting the Appropriate Monitor Capacitor

Fig.2 depicts the corresponding electrical circuit for the DBD system. In the parallel plane DBD, according to Fig.3, there are two "off plasma" and two "on plasma" phases during a complete cycle of the applied voltage. The reactor functions like two capacitors in series, when it is in the "off plasma" or capacitor phase,. These capacitors can store charge from the dielectric layer, C_{diel}, and gas gap discharge, C_{gap}, via an applied voltage or accumulated charges via plasma discharge. Kirchhoff's principles are used to calculate the total capacitance of the "DBD cell," C_{cell}, comprised of these two components [9].

$$\frac{1}{C_{Cell}} = \frac{1}{C_{diel}} + \frac{1}{C_{gap}} \quad (4)$$

For simple geometries like ours, approximate C_{diel} and C_{gap} values can be calculated. For a parallel plate capacitor, $C = \varepsilon_r \varepsilon_0 A / d$, where ε0 is the dielectric constant of free space, which is equal to $1/36\pi \times 10^9$, εr is the relative dielectric constant of the dielectric, which in our system Quartz is used and it is equal to 4.5, A is the area, which according to the circular structure of the electrodes is equal to πr^2, the radius of the electrodes is 4 mm, and d is the dielectric thickness, which is 2 mm for quartz and the air gap is equal 5mm. In principle, this relationship should express an acceptable value for reactor capacitors. This technique ignores edge effects, which can be substantial in speci reactor geometries. According to the given values and formula (4), $C_{cell} = 144pF$.

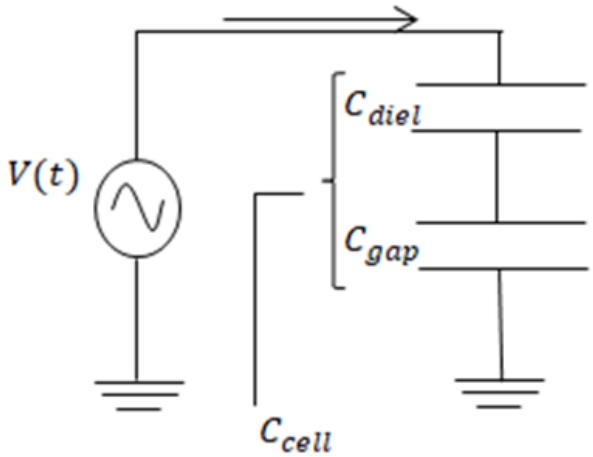

Fig.2. Equivalent circuit of DBD system

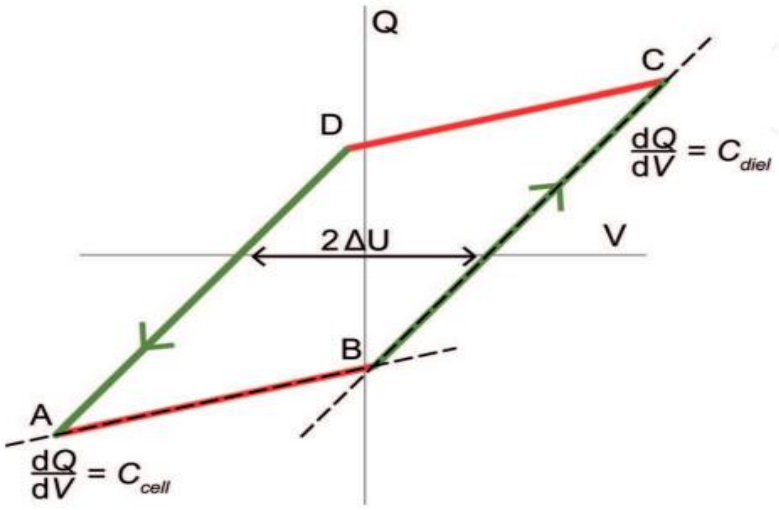

Fig.3. An ideal Q-V diagram with a distinctive parallelogram form. 'Plasma off' elements are red, whereas 'plasma on' elements s are green. The green elements' arrows show the path of time [9].

To apply the Q-V technique, an appropriate capacitor must be chosen. The amount of monitor capacitor required is determined by the C_{cell} reactor's capacity. The monitor capacitor's capacitance should be significantly more significant than the reactor's capacitor capacity ($C_m \gg C_{cell}$). In general, a ratio of C_m / C_{cell} between $100/1$ to $10000/1$ is appropriate [9]. This capacitor has an average value of 220nF, based on the value of the reactor capacitor $C_{cell} = 144pF$.

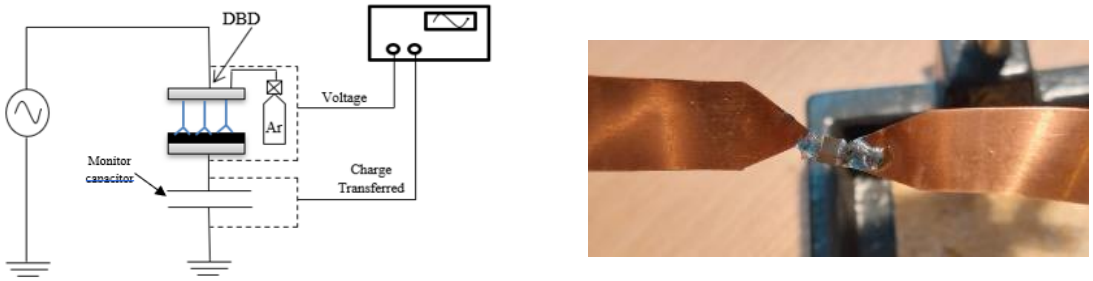

(a) (b)

Fig. 4. (a) The experimental design of the DBD actuator with the monitor capacitor, (b) An SMD monitor capacitor coupled to a copper strip.

If $C_m \gg C_{cell}$, nearly all the voltage delivered to the reactor and monitor capacitor drops across DBD and the corresponding circuit in Fig. 2. is valid, However, the monitor capacitor is not exposed to high voltages. A voltage across a parallel resistor or a Rogowski inductor can be used in place of a monitor capacitor. Instead of integrating the current in a capacitor, this approach measures it directly from the DBD to the ground. Q(t) can be obtained using the temporal accumulation of i(t) in post-processing. Because string discharges occur concurrently with currents whose amplitudes rapidly grow in the sub-nanosecond range, this method ideally requires a measurement device with a wide bandwidth and a fast sample rate to prevent measurement mistakes. The accumulation on a capacitor has the advantage that no load inside the reactor is disregarded, allowing for more precise power measurements despite the probe and oscilloscope's low bandwidth (and sampling speed) [9].

And finally, some reactor geometries feature a weak ground electrode, making it difficult the monitor capacitor, shunt resistor, or coil to connect. For example, the "ground" electrode may be electrically floating, or the current could pass via a variety of potential paths, such as plasma jets impacting the surface, before reaching the ground. In such situation, utilize the Rogowski coil to measure the direct current, between the voltage generator and the actuator, on the high voltage line. However, because unwanted discharge or inadvertent occurrence of high voltages in measuring instruments must be avoided, this method introduces additional engineering and safety issues. These issues can be resolved with diligence. Corona discharge should be avoided on sharp metal edges, whereas arc discharge should be avoided in the air gaps between the high-voltage line and coil. By covering and filling any sharp edges and air holes with materials with increased breakdown strength, such as paraffin, as described in [6], the issue can be resolved.

Experimental Structure

Fig.4 shows the experimental structure of the DBD actuator with the monitor capacitor. The electrodes are steel tablets with an 8-centimeter diameter. The distance between the electrodes is 5 millimeters. The dielectric is composed of quartz with a thickness of 1 mm. Fig.5 depicts an experimental schematic of the circuit used to calculate the monitor's voltage and load. In contrast, this project makes use of 350 watts of power. Time variations in voltage were monitored using the Tektronix P6015A high voltage.

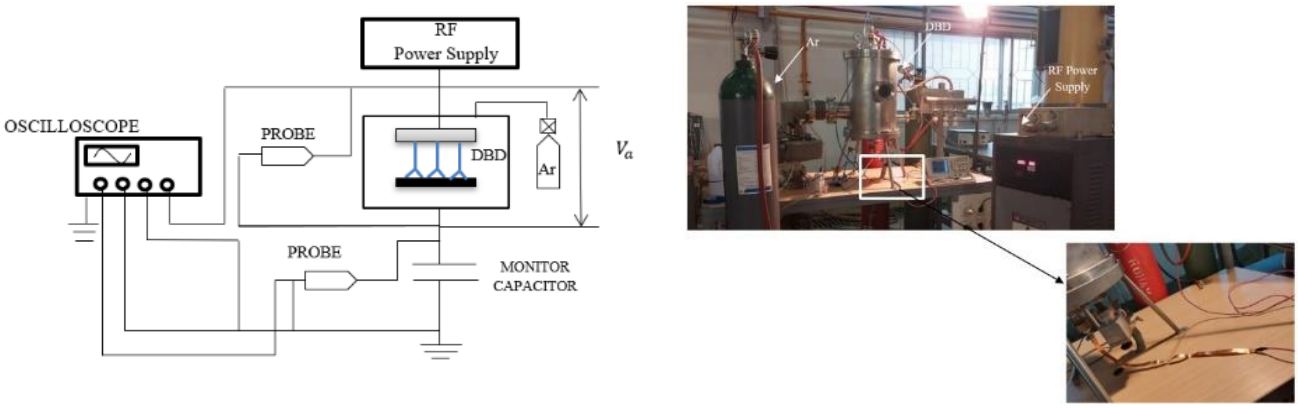

(a) (b)

Fig. 5. (a) Schematic of the test structure to detect the voltage, and then the charge of the monitor capacitor, (b) Test structure

Results and Discussion

The nature of the current signal, which is made up of huge spikes superimposed on a low-amplitude current, compels the data-gathering equipment to become an inescapable source of mistakes in current-based DBD actuator power measurements. The problem might be fixed by employing data-collecting equipment with greater bit resolution combined with higher-quality analog hardware capable of performing with appropriate SNR but High-speed equipment is uncommon in the market. on the other hand, for correct time comparisons, contemporaneous measurements are required rather than statistical comparisons between the current technique and the monitor capacitor, increasing the project's technological complexity. It is difficult to replicate the same operating circumstances using one configuration for the current approach and another for the capacitor method [1]. As a result, the monitor capacitor technique was used to assess the selection power, and the results were compared to those from previous studies.

To perform measurements with greater accuracy, multiple steps are required to minimize the parasitic inductor, parasitic capacitor, conduction interference, radiation interference, and transmission line effects [1].

A giant copper sheet should serve as the ground plate. The copper sheet has only one connection to the ground (via a separate laboratory ground line). All components are arranged on the copper sheet. Ground lines from components or probes (high voltage probe, monitor circuit ground, etc.) are connected to the ground plane. These measures aim to prevent ground loops and carried noise while establishing the reference ground potential to the greatest extent practicable. The foil protector is also attached to the ground plane and exposed to the usage of foil on all sensitive monitor circuits, and the probe tip to reduce noise generated by plasma discharges on the actuator.

To minimize parasitic induction, use flat conductors and copper rather than round conductors.

To study high-frequency sparks, data was collected using high-speed oscilloscopes.

We chose a monitor capacitor with low inductance and minimal load leakage. The ceramic chip capacitor (SMD 1206) is used in this project. This capacitor has the benefit of being compact and having no conduction channels (Fig. 4(b)). It is preferable to use an LCR meter to measure the capacity of the monitor capacitor and the completed monitor circuit, as measured values may differ from those provided by the manufacturer. Furthermore, the monitor circuit can exhibit excess capacity, resulting in inaccuracies in estimating the absolute value of Q (t) [9].

The findings obtained for monitor capacitor voltage and load, and the Lissajous plot are presented below.

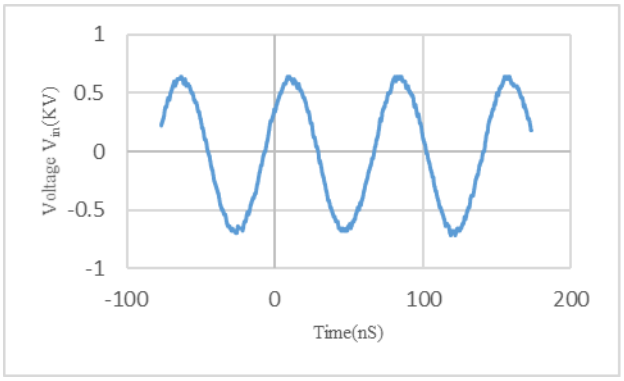

Fig.6. Time changes of input voltage

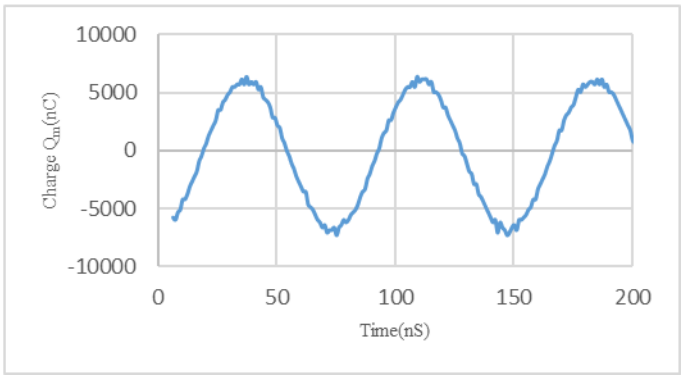

Fig.7. Time changes of monitor capacitor charge

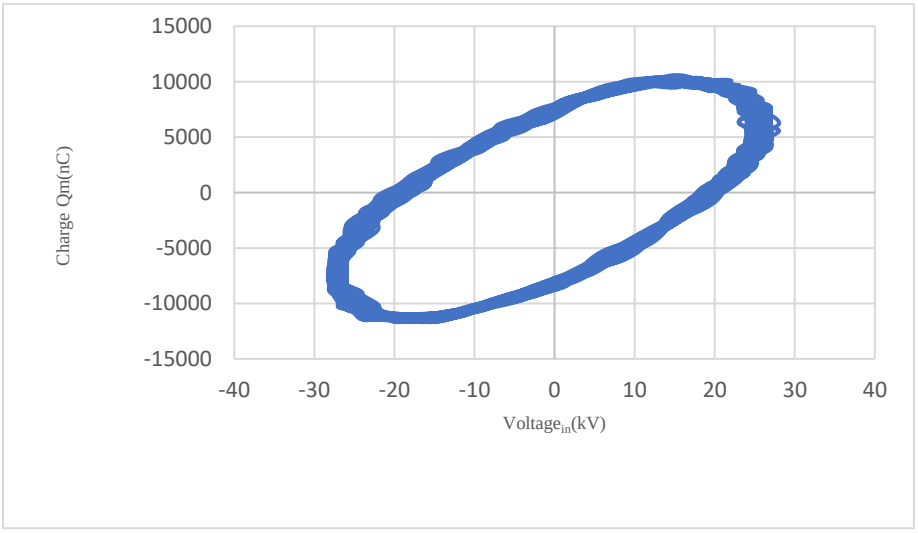

Fig.8. Lissajous curve

Equation (3) calculates plasma power consumption by computing the area under the Lissajour curve in Fig.8, which is 33 watts for the tested system. This figure is consistent with prior estimates of the dielectric barrier discharge plasma's power consumption (for example, [10]).

Conclusions

Atmospheric pressure is one of the most essential sources of plasma sources, so understanding its power consumption is critical. The fundamental issue with power measurement in dielectric barrier discharge plasma drive is the current signal, which has a short width but a high amplitude. The capacitor monitor methodology is one of the most effective approaches for calculating plasma power. In this article, the capacitor monitor method is used to quantify the driving power of a dielectric barrier discharge plasma at atmospheric pressure using argon gas and a 13.56 MHz radio frequency power source. The previous methods' power measurements reveal that the monitor capacitor method is highly accurate and reliable.

References

[1] Ashpis , David E. Laun, Matthew C. and Griebeler, Elmer L. (2017). Progress Toward Accurate Measurement of Dielectric Barrier Discharge Plasma Actuator Power. AIAA JOURNAL, Vol. 55, No. 7.

[2] Manley, T. C. (1943). The Electric Characteristics of the Ozonator Discharge. Journal of the Electrochemical Society, Vol. 84, No. 1, pp. 83–96.

[3] Wagner, H.-E. Brandenburg, R. Kozlov, K. V. Sonnenfeld, A. Michel, P. and Behnke, J. F. (2003) The Barrier Discharge: Basic Properties and Applications to Surface Treatment. Vacuum, Vol. 71, No. 3, pp. 417–436.

[4] Borcia, G. Anderson, C. A. and Brown, N. M. D. (2003). Dielectric Barrier Discharge for Surface Treatment: Application to Selected Polymers in Film and Fibre Form. Plasma Sources Science and Technology, Vol. 12, No. 3, pp. 335–344.

[5] Thomas, F. O. Corke, T. C. Iqbal, M. Kozlov, A. and Schatzman, D. (2009). Optimization of Dielectric Barrier Discharge Plasma Actuators for Active Aerodynamic Flow Control. AIAA Journal, Vol. 47, No. 9, pp. 2169–2178.

[6] Peeters, FJJ. Yang, R. van de Sanden MCM. (2015). The relation between the production efficiency of nitrogen atoms and the electrical characteristics of a dielectric barrier discharge. Plasma Sources Science and Technology, 24:045006

[7] Banerjee, AM. Billinger, J. Nordheden, KJ. Peeters, FJJ. (2018). Conversion of CO2 in a packed-bed dielectric barrier discharge reactor. Journal of Vacuum Science & Technology A Vacuum Surfaces an Film, 36

[8] Falkenstein, Z. Coogan, JJ. (1999). Microdischarge behaviour in the silent discharge of nitrogen - oxygen and water - air mixtures. Journal of Physics D: Applied Physics, 30:817-825

[9] Butterworth,T. and Peeters, T. (2019). Atmospheric Pressure Plasma - From Diagnostics to Applications, intechopen.

[10] Hołub, M. (2012). On the measurement of plasma power in atmospheric pressure DBD plasma reactors. International Journal of Applied Electromagnetics and Mechanics 39, p. 81–87.

ICNST 2024
International Conference on Nuclear Science and Technology
6- 8 MAY 2024 | Isfahan, Iran

Planting Carbon in Tungsten by Plasma Focus Device for Use in the First Wall Materials of Fusion Facilities (Paper ID: 1057)

Amir Raeisdana[1*] , Davood Sohrabi[1] , Mehdi Bakhshzad Mahmoudi[1] , Maryam Akbari Nasaji[1] ,Noushin Pishbin[1]

[1]Plasma and Nuclear Fusion Research School, Nuclear Science and Technology Research Institute, Atomic Energy Organization of Iran, Tehran, Iran
araeisdana@aeoi.org.ir

Abstract

Tungsten is one of the main candidates for making the first wall of fusion reactors. By implanting carbon in tungsten, its resistance and hardness increases. In this research, the 115 kJ dense plasma focus device (DPF) is used to plant carbon ions in the tungsten substrates. This device emits high-energy ions of 10 keV-1 MeV and with a flux of 10^{16} ions/cm^2 in each shot in the direction of the device axis to the tungsten target so it is a suitable option for ion implantation. Five tungsten substrates in 2cm×2cm dimensions with 1mm thickness were located at a distance of 20cm from the place where the pinch is formed. The experiments are carried out in 2 mbar of the methane gas pressure and 15 kV of the charging voltage. Graphite disc was installed on the anode head for increasing the flux of carbon ions. X-ray diffraction (XRD), scanning electron microscopy (SEM) and Vickers hardness test are used to study the surface of treated samples. SEM analysis indicates 28% of carbon in the tungsten sample. XRD analysis shows the formation of tungsten-carbide phases. Micro Vickers Tester demonstrates an increase of 6.7 MHV in hardness after carbon implanting.

Key Words: Ion Implantation, Plasma Focus Device, Tungsten Hardness, XRD Analysis, Micro Vickers Tester, SEM Analysis

Introduction

Dense plasma focus device can be used as a source of high energy and high intensity of ions. Ion implantation can be carried out for various ion beams and various targets using this device [1-8]. N. Ziveh and M. Habibi implanted carbon in tungsten using the 4.5 kJ plasma focus device and XRD and SEM analysis demonstrated the formation of nanocarbon on the tungsten [9]. In their research, atomic force microscopy (AFM), the surface morphology of the deposited films at various numbers of focus shots at the zero-degree angular position were tested. The AFM results showed by increasing the number

of focus shots, the crystal defects of carbon structures are reduced [9]. Shaista Zeb et al was employed the dense plasma focus device with neon filling gas at 1 mbar of pressure for the deposition of amorphous DLC films. The high purity graphite was inserted at the tip of the tapered anode which served as a carbon source. The EDX results and SEM cross-sectional views of samples showed that the substrates placed closer to the anode axis have higher carbon content as compared to those placed away from anode axis whereas carbon content decreases with increasing axial distances from anode tip [10].

Experimental setup

The IR-MPF-100 dense plasma focus device (144μF, 40kV, 115kJ) was used for the experiments. 24 capacitors (each one has 6 μF of capacitance) are placed in parallel that leads to 144 μF of capacitance. Figure 1 shows the experimental setup. Anode, cathode and the vacuum vessel are located in the downward direction. The graphite disc in the diameter of 5cm and the thickness of 3mm is installed on the anode head that increases the rate of carbon ions (see Figure 2). Five tungsten substrates in 2cm×2cm dimensions with 1mm thickness were located at a distance of 20 cm from the anode tip. Figure 3 shows the tungsten samples before and after of carbon implantation. The location of the tungsten target, the graphite disc and the diagnostic systems are seen in the Figure 1 schematically.

90 shots were carried out by the 115kJ dense plasma focus device by using the methane gas. Experiments were carried out in the working condition of V=15 kV (E=16.2 kJ) and p=2 mbar. After each 5 shots, the chamber is vacuumed and the fresh methane gas is injected. After ending the experiments, samples were sent for three important analyses contains: XRD, SEM and hardness analysis. Useful analyses are listed in Table 1.

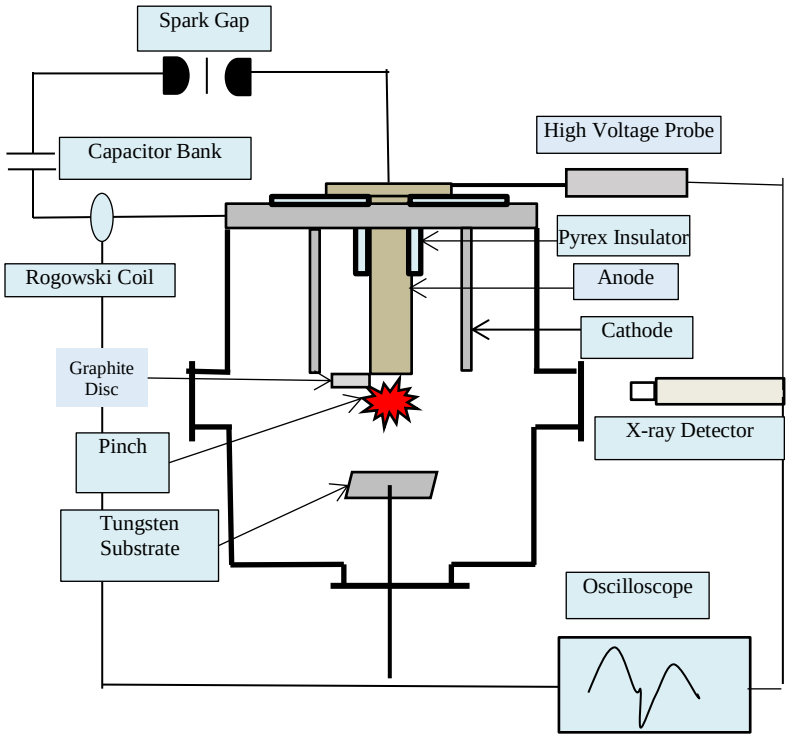

Figure 1. Experimental setup for carbon implantation on the tungsten substrate

Table 1. List of useful analysis after the carbon implantation and deposition on the tungsten

Analyze Name	Results
XRD	Atomic and molecular structure of a crystal
SEM	Surface topography and composition of the sample
AFM	Mechanical properties of the sample, stiffness or adhesion strength and electrical properties such as conductivity or surface potential
RBS	Composition and depth measurement

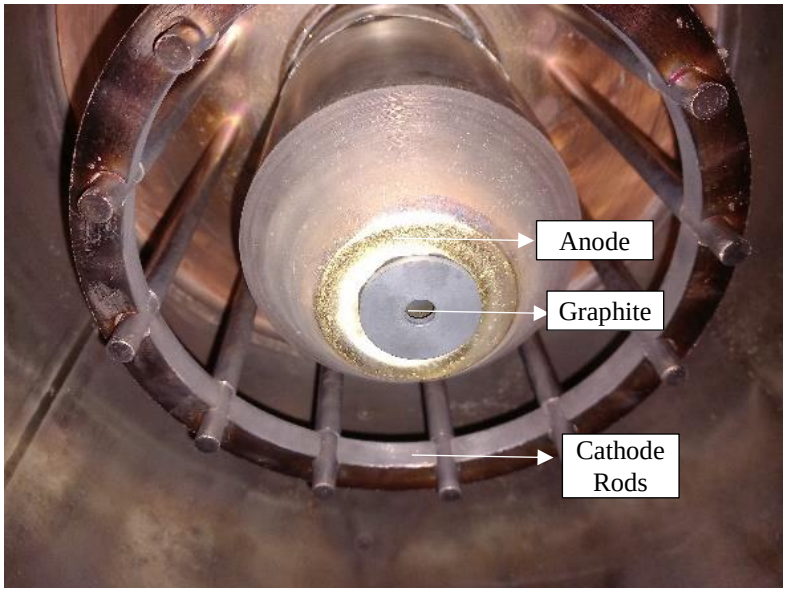

Figure 2. Graphite disc was installed on the anode head for increasing the dose of carbon ions implantation

Figure 3. Five tungsten substrates were located on the feedthrough at 20cm distance from anode head. Left: before irradiation and right: after irradiation.

Results and Discussion

XRD spectra indicates the formation of the tungsten carbide (WC) compound in the sample (Figure 4). Regarding to the sputtering of Cu and Zn from the anode head, copper zinc composite is seen in the XRD

spectra. Table 2 shows the visible compounds and their reference codes in the sample. Next analysis is the Vickers hardness testing. Vickers analysis was done for three points of samples after and before of carbon irradiation. The results indicate the average increasing of 6.4 MHV in the hardness of tungsten after the carbon implantation (Table 3).

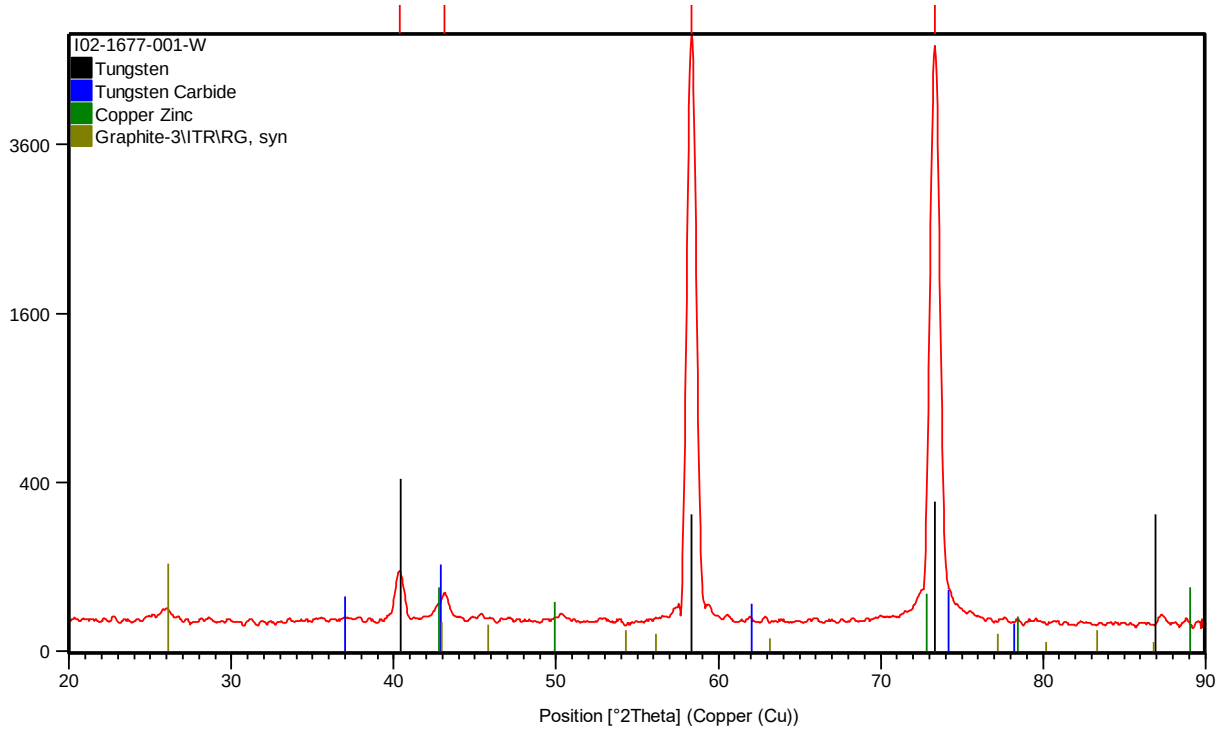

Figure 4. XRD spectra of the tungestan substrate after carbon ions implantation

Table 2. XRD analysis indicates WC and CuZn composites in the sample

Visible	Ref. Code	Score	Compound Name	Chemical Formula
*	00-001-1203	41	Tungsten	W
*	00-020-1316	16	Tungsten Carbide	W C1-x
*	00-006-0657	Unmatched Strong	Copper Zinc	Cu Zn
*	00-026-1079	4	Carbon	C

Table 3. Hardness comparison between irradiated substrate and reference sample for three points and their average

	point 1 hardness (MHV)	point 2 hardness (MHV)	point 3 hardness (MHV)	average hardness (MHV)
Reference Sample	516.6	513.8	513.8	514.8
Irradiated Sample	517.4	525.4	521.7	521.5

SEM analysis is used to examine the surface morphology, particle size and size distribution of the carbon grains deposited on the surface of the substrate. The obtained micrographs are shown in Figure 5. The Figure 5-a indicates the surface morphology in the resolution of 100 µm. This Figure shows the uniform distribution of the carbon bulks. Figures 5-d and 5-c show the surface morphology in the resolution of 10 µm and 20 µm respectively. Figure 5-b shows the carbon particle dimensions. The largest carbon particle is seen in the size of 1.5 µm. The detected elements by using SEM analysis are indicated in

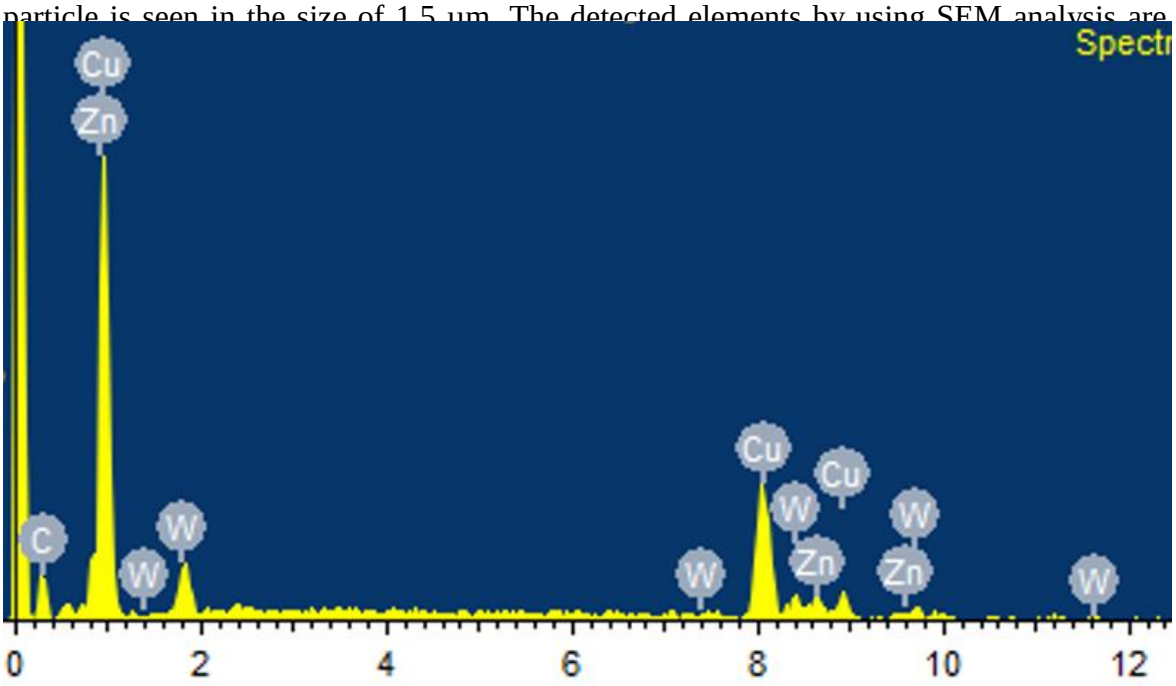

Figure **6**. C, Cu, Zn and W peaks are seen in the

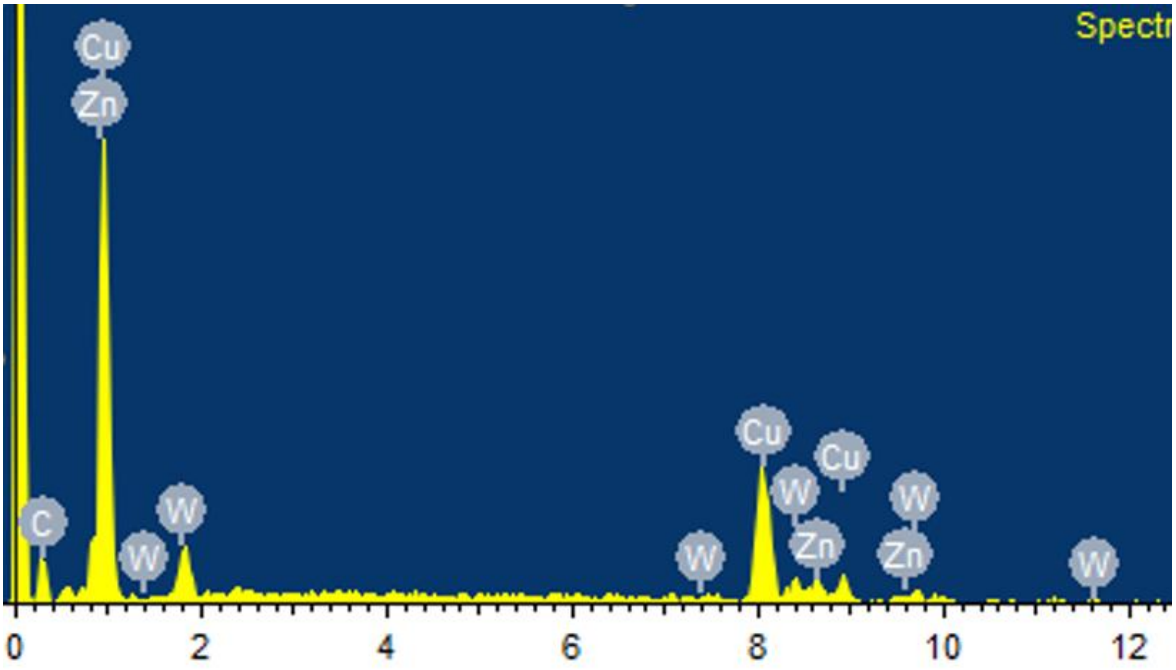

Figure **6**. The weight percent and atomic percent of the detected elements are listed in Table 4. The SEM analysis demonstrates the carbon atomic percent of 67% and the carbon weight percent of 26% in the tungsten substrate.

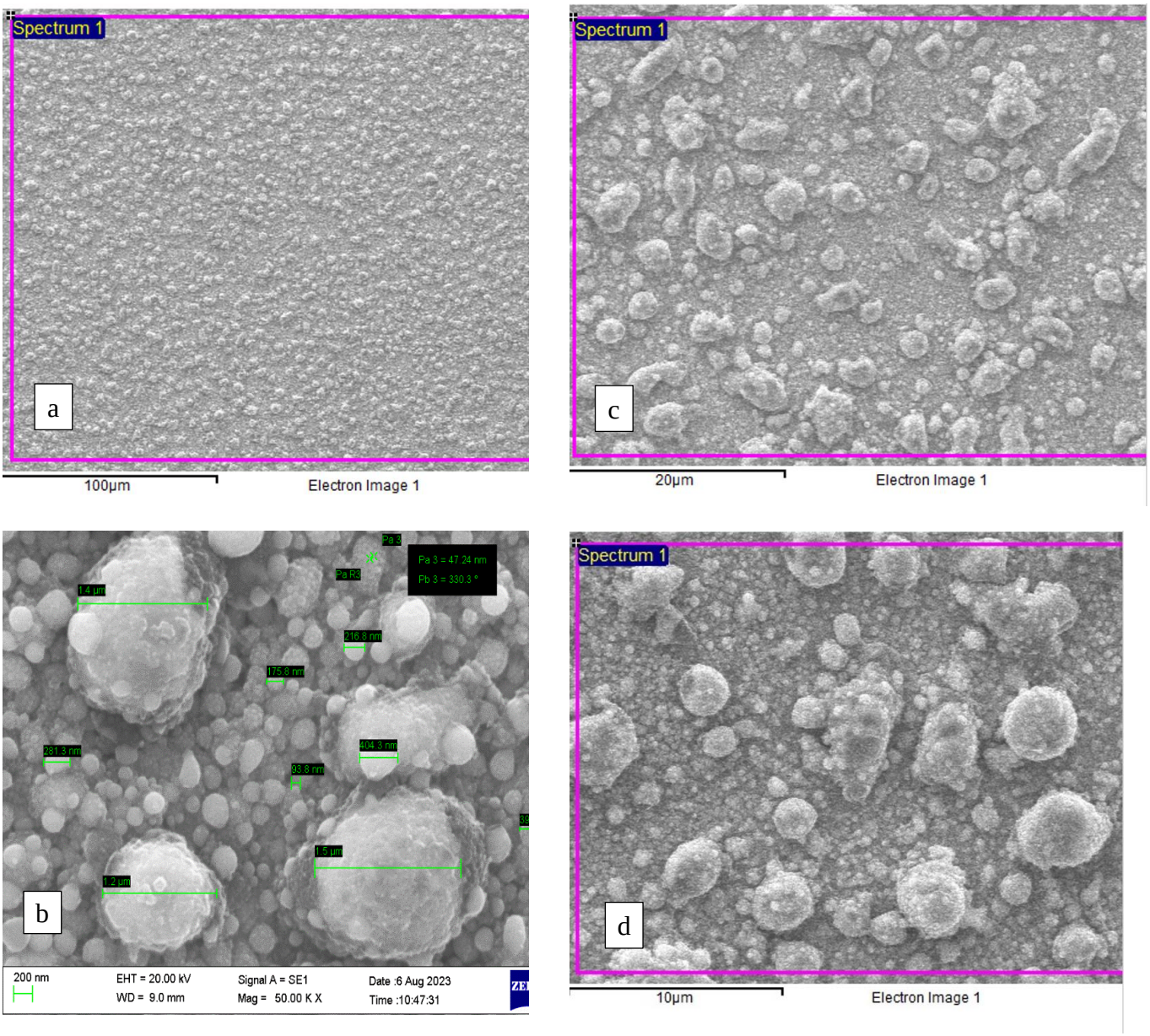

Figure 5. The SEM analysis shows a) the uniform distribution of carbon bulks on the tungsten substrate, b) The bulks size is seen in the figure, c) picture in 20µm of resolution and d) picture in 10µm of resolution

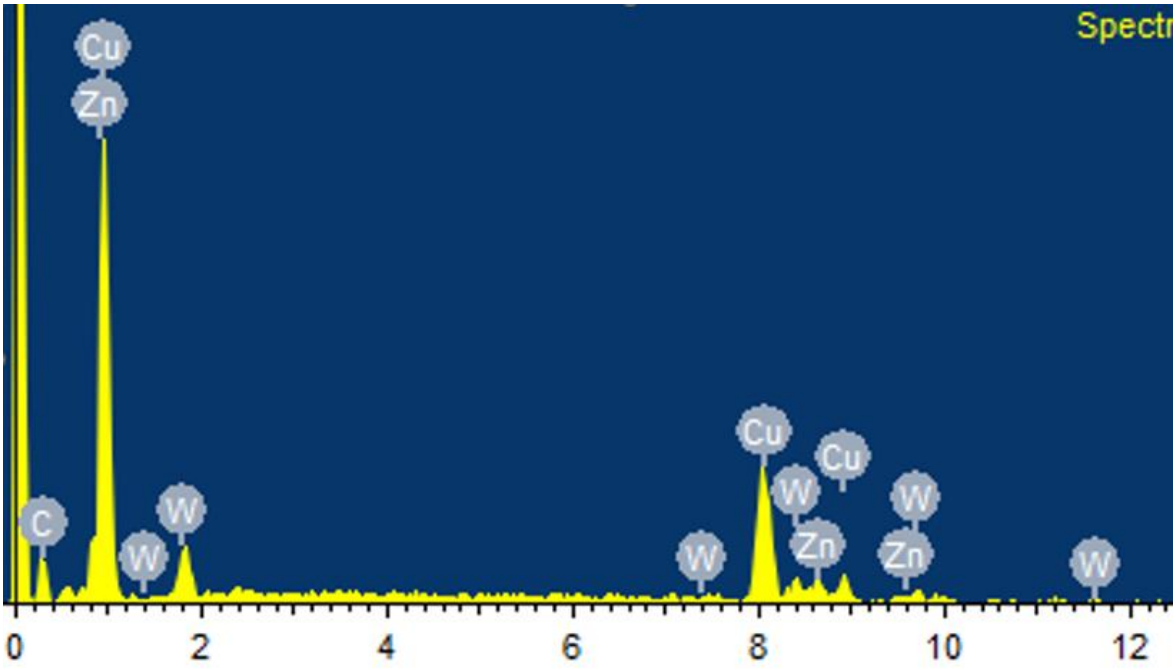

Figure 6. Carbon peak is seen in the SEM analysis

Table 4. Weight percent and atomic percent of carbon, copper and tin on the tungsten substrate from SEM analysis

Element	Atomic %	Weight %
C	67.89	26.57
Cu	25.63	53.05
Zn	4.77	10.16
W	1.71	10.23

Conclusion

The method of carbon implantation and carbon deposition on the tungsten substrate is presented by using the dense plasma focus device. The graphite disc was installed on the anode head. The 90 DPF shots by using methane gas are done. The XRD analysis and SEM analysis indicate that carbon was successfully planted on the tungsten substrates. The SEM analysis results 67% of carbon in atomic percent and 26% of carbon in the weight percent. The XRD spectra shows the formation of WC composites in the sample. The Vickers hardness test demonstrates increasing of hardness equal to 6.7 MHV after carbon implantation on the tungsten substrates.

References

[1] Jamil Siddiqui et al, "Effect of deposition parameters on structural and mechanical properties of niobium nitride synthesized by plasma focus device", Chin. Phys. B Vol. 24, No. 6 (2015)

[2] M. Shafiq et al, "Pulsed ion beam-assisted carburizing of titanium in methane discharge", Chin. Phys. B Vol. 19, No. 1 (2010)

[3] Ali Hussnain et al, "Study of Structural and Mechanical Properties of WN/a-Si3N4 Hard Coatings Grown by Plasma Focus", J Fusion Energ 34:435–442 , (2015)

[4] Z. A. Umar et al, "Hard TiCx/SiC/a-C:H nanocomposite thin films using pulsed high energy density plasma focus device", Nuclear Instruments and Methods in Physics Research B, Volume 301 pages 53–61, (2013)

[5] I. A. Khan, "Role of charge particles irradiation on the deposition of AlN films using plasma focus device", Journal of Crystal Growth, volume 317, pages 98–103, (2011)

[6] Tousif Hussain et al, "Synthesis of nanostructured multiphase (Ti,Al)N/a-Si3N4 thin films using dense plasma focus device", Nuclear Instruments and Methods in Physics Research B, volume 269 pages 1951–1955, (2011)

[7] A. Guldamashvili et al, "Mechanical Properties of Tungsten Implanted with Boron and Carbon Ions" Journal of Materials Science and Engineering A 7 (3-4) 82-88, (2017)

[8] Ming Xu et al, "Mechanical properties of tungsten doped amorphous hydrogenated carbon films prepared by tungsten plasma immersion ion implantation" Surface & Coatings Technology, Volume 203 , Pages 2612–2616, (2009)

[9] N. Ziveh, M. Habibi "The impact of carbon shot number on the morphology of deposited carbons on tungsten" 27th Iranian Nuclear Conference, Pages 1-7, (2021)

[10] Shaista Zeb et al, "Deposition of Diamond-like Carbon Films using Graphite Sputtering in Neon Dense Plasma", Plasma Chem Plasma Process, Volume 27, Pages 127–139(2007)

ICNST 2024
International Conference on Nuclear Science and Technology
6- 8 MAY 2024 | Isfahan, Iran

The effect of rotation on the growth rate management of magneto-Rayleigh-Taylor instability of stratified plasma in the Cartesian coordinate (Paper ID: 1068)

Masoumparast Katek-Lahijani M-A.*, Khoshbinfar S.

Physics Department, Faculty of Sciences, University of Guilan, 41335-1914, Rasht, Iran

Abstract

The effect of applying plasma rotation and static external magnetic field in plasma with power density dependence on the growth rate of Rayleigh-Taylor instability (RTI) was studied analytically. The plasma is assumed to be an incompressible layer enclosed between two parallel planes located at z=0 and z=h. According to the linear perturbation theory, the dispersion relation for ideal MHD equations was derived with the rotation effect under suitable boundary conditions. In the rotating case ($\Omega \neq 0$), the final dispersion relation shows the effect of the simultaneous combination of the horizontal magnetic field (ω_{fx}^{*}) and the constant angular velocity (Ω) of the plasma on the growth rate of the RTI. Here, the growth rate of the instability depends on the horizontal component of the magnetic field (ω_{fx}^{*}), plasma rotation (Ω), and dimensionless parameter $\lambda^{*} = \lambda L_D$ (where λ is constant and L_D is the density-scale length). The maximum instability occurs at the value of λ^{*}=-0.5. Compared with the corresponding non-rotating case results, the latter shows that the simultaneous combination of rotation and a static external magnetic field improves the management of the instability growth rate.

Keywords: plasma rotation, magneto-Rayleigh-Taylor instability, stratified plasma, power law density gradient, axial magnetic field

1. Introduction

Rayleigh-Taylor instability (RTI) has attracted the attention of researchers because of its decisive role in space and astrophysical phenomena such as solar corona heating, supernova explosion, and crab nebula explosion, as well as its key role in inertial confinement fusion (ICF), and laser-plasma interaction[1-2]. This instability usually occurs due to the constant acceleration of gravity at the interface of two fluids with different densities that are on top of each other or in contact with each

* E-mail: m.a.masoomparast@gmail.com

other in the gravitational field. The direction of this acceleration, whose value is constant, is always from the lighter fluid to the heavier fluid or from top to bottom $\left(\vec{a}=-\vec{g}\right)$. Specifically, RTI occurs when the density gradient and pressure gradient have opposite signs; therefore, the general condition of instability will be as $\vec{\nabla}\rho_0\cdot\vec{\nabla}p_0<0$ [3-4].

Using appropriate, innovative techniques, researchers try to mitigate the RTI growth rate in ICF [5-6]. Several physical mechanisms can affect the growth rate of RTI, such as density gradient effects and ablative stabilization. The magnetic field also accelerates the stabilization of the RTI, and the presence of an applied external magnetic field may relax the plasma parameters [7]. In this way, the ions experience a large rotational force with a constant angular velocity and move along the direction of $\vec{E}\times\vec{B}$ [8]. The compression of plasma by self-magnetic fields, known as the pinch effect, makes it possible to study high-density and high-temperature plasma under laboratory conditions. To produce such plasmas, Z-pinches are widely used as powerful sources of soft X-rays and suitable drivers for magnetized targets in ICF. Due to the high energy densities typical of the final stage of compression, the studies on Z-pinches are in the mainstream of the research on ICF. A key challenge in magneto-inertial fusion as well as Z-pinch devices is achieving stable compression of the pinched plasma. It determines the maximum achievable final values for plasma density and temperature [9-10]. The main issue with stable implosion is magneto-hydrodynamic (MHD) instability, the most dangerous type of which is the magneto-Rayleigh-Taylor (MRT) instability.

RTI may be suppressed by applying the external magnetic field or by tuning the plasma density profile [11]. In the first case, the stabilization process is such that the magnetic shear between the axial magnetic field inside the Z-pinch and the azimuthal magnetic field outside increases the stability of the implosive plasma shell and suppresses the growth of MRT instability [11]. The mitigation of the MRT instability may be considered by the linear MHD theory, and it is shown that the compression is effectively stabilized by a relatively weak initial axial magnetic field $\left(B_z=0.4(T)\right)$[12]. The appropriate applied magnetic field may prevent the radial energy loss by electron thermal conductivity which improves the quality of the ignition and burn stages [12]. This

was first observed in the Omega laser facility, where an axial magnetic field as large as 8 Tesla increased the hot spot temperature and the target efficiency from 15% to 30% [13]. It is estimated that strong seed magnetic fields improve ignition performance through proper magnetic thermal conduction [14]. They can also effectively trap DT ions and alpha particles and increase the collision frequency and finally fusion efficiency. In addition to improving the overall performance of the target, the presence of a suitable magnetic field causes a change in the perturbation growth process, so that the magnetic tension through the Lorentz force can suppress the RTI [14]. In the second method, MRT instabilities can grow or decrease depending on the initial plasma density. For plasma a power-law density profile, the growth rate of perturbations is predicted to be relatively slow and non-exponential [15]. The power density characteristic provides conditions under which the boundary between the magnetic field and the plasma does not accelerate toward the pinch axis as the density gradient increases, and exponentially growing MRT instabilities are suppressed. Considering the initial density in a stratified plasma as a function of the radial coordinate ($\rho(r) \propto r^{-n}$; $n \geq 1$), it is observed that close to the stagnation moment, the changes in density decrease rapidly with an increase in the aspect ratio. For $n = 1$, we see a slight decrease in acceleration, which has a low stability effect. For $n = 2$, we will have zero accelerations, where the growth of the perturbation is reduced but still noticeable. Finally, for $n = 3$ the reverse acceleration, we have almost no linear mass change near the stagnation, which is about a five-fold reduction in the amplitude of the perturbation compared to the uniform case n=0. For a limited total plasma mass, the parameter *n* is considered to be greater than 2 [15-16]. Suppression of RTI by inverse acceleration is a strong and purely hydrodynamic effect. According to numerical simulations by Velikovich *et al.*, stable compression of a pinch plasma may be established when the plasma density increases faster than r^{-3} [10]. Reduction of RTI using axial power density was first reported in 1996 by the Sandia National Laboratory (SNL)[14]. Unlike the radial power-law density profile, in the axial case, the RTI may reduce or even suppress, at the cost of reducing the hydrodynamic efficiency. Applying the power-law density of the fuel strongly affects the quality of the final fusion and changes the target ignition, and burn stages completely, which is far away from the standard method in ICF. The increase in the exponent, *n*, of the nonlinear density profile

leads to the control of the acceleration rate and the continuous improvement of the target energy gain [15-17].

In addition to static external magnetic fields and initial plasma density dependence, theoretical studies of rotating fluids show that rotation about an axis perpendicular to the direction of acceleration can suppress the growth rate of the RTI [18]. The RTI impact on the performance of inertial fusion energy has prompted new research about the effect of plasma rotation on the growth rate of instability. The rotation imposes a restoring force on fluid elements that move perpendicular to the axis of rotation which follows a curved path (Coriolis force). The presence of the Coriolis force allows the fluid to support inertial wave motions (similar to rotational, internal gravity waves supported by the density gradient). Therefore, it has a stabilizing effect on unsteady fluid flows by suppressing the velocity gradients parallel to the axis of rotation [18-22]. In this regard, many studies have been conducted based on analytical calculations and simulations, so that the effect of horizontal and vertical magnetic fields separately or simultaneously, considering the effect of rotation or without it, on the RTI of non-uniform plasma assuming different physical conditions such as compressibility, viscosity, density dependence, etc., were investigated for plasma in planar and cylindrical geometry [19]. In most of these studies, plasma density dependence was considered constant, linear, and exponential [22-24]. In recent years, by applying a static external magnetic field and also considering a nonlinear distribution function of the fuel density, researchers have achieved new approaches to improve the quality of inertial fusion [9]. In the most recent experimental studies, the effect of self-generated rotation on plasma in a Z-pinch implosion was investigated by applying an axial magnetic field [25]. In this study, self-generated plasma rotation using a cylindrical implosion with the application of a pre-embedded axial magnetic field was demonstrated for the first time using precise spectroscopic measurements that are highly resolved in both time and space. The direction of rotation depends on the direction of the axial magnetic field. Its velocity is comparable to the maximum implosion velocity, which significantly affects the force and energy balance throughout the implosion stage. If the rotation speed is comparable to the implosion velocity, the centrifugal forces will have a significant effect on the force and energy balance. In addition, the large rotation shear can exert a stabilizing effect on the plasma instabilities. This effect is consistent with observations in other rotating plasma experiments. These

observations are of particular importance for understanding the implosion dynamics in magnetic Z-pinch configurations designed for fusion purposes in the Mag-LIF approach or for radiation sources [25]. In another study that deals with the stabilization of RTI on the inner surface of an imploding shell with the help of rotation, it was shown that such rotation significantly affects the dynamics of the implosion through centrifugal force and reduces the instability. This result could be essential for magnetic plasma compression in general and specifically for the Mag-LIF approach in ICF [26].

The above-mentioned features on the dynamics of RTI instability motivate us to investigate the combined effect of a static external magnetic field with exponential dependence as well as the initial power density distribution function with power 3 on the linear growth rate of RTI. In this research, which was carried out in the form of analytical calculations in the framework of linear perturbation theory by considering the basic ideal MHD equations for incompressible, rotating, and non-viscous stratified fluid in planar geometry and by linearizing this set of equations, we derive perturbation equations. Then, by solving the perturbation equations in the Cartesian coordinate system, we obtain the general dispersion relation. This equation shows the effect of a static external magnetic field on the linear growth rate of the RTI. In general, the equations developed in planar geometry are easier to proceed with and analyze problems, and at the same time, they apply to many physical scenarios; therefore, in the current research, we used planar geometry.

The rest of the paper is organized as follows. Section 2, is devoted to the detailed description of the theoretical framework of the present paper for the rotating case. An ordinary differential equation (ODE) for the RTI, including the rotation effect, with an initial power density profile, in a uniform external magnetic field, is obtained in Sec. 2. In Sec. 3, the effect of magnetic field gradient and initial power density, on the linear growth rate in the RTI for rotating case, is studied. Finally, some conclusions and remarks are given in Sec. 4.

2. Theoretical Framework

In this section, an ideal incompressible magnetized plasma fluid including electrons and singly charged ions is considered. For mathematical simplicity, the dissipation effects arising from resistance and viscosity are ignored in our study.

In this research, the strata of incompressible and inviscid plasma with a certain thickness enclosed between two fixed parallel planes with coordinates z=0 and z=h are considered as a fluid of electrons and immobile ions, and the plasma is immersed in a static external magnetic field. Incompressible fluids in a magnetic field are considered regardless of viscosity, surface tension, and heat transfer, these fluids are described by ideal MHD equations. In the Cartesian coordinate system, the ideal MHD equations with the additional term describing the plasma rotation are written as follows:

$$\rho\frac{\partial\vec{U}}{\partial t}=-\vec{\nabla}p+\rho\vec{g}+2\rho\left(\vec{U}\times\vec{\Omega}\right)+\frac{1}{\mu_0}(\vec{\nabla}\times\vec{B})\times\vec{B} \quad (1)$$

$$\vec{\nabla}\cdot\vec{U}=0 \quad (2)$$

$$\frac{\partial\vec{B}}{\partial t}=\vec{\nabla}\times(\vec{U}\times\vec{B}) \quad (3)$$

$$\frac{\partial\rho}{\partial t}+(\vec{U}\cdot\vec{\nabla})\rho=0 \quad (4)$$

The quantities $\vec{U}$, p, $\vec{B}$, ρ, and $\vec{\Omega}$ show the velocity vector, thermal pressure, magnetic field vector, density, and plasma angular velocity vector, respectively. Similar to the non-rotating plasma case, to check the stability of the system using the standard linearization method, we first linearize the above equations [27]. For this, we consider some physical quantities with perturbation relative to the equilibrium state:

$$p=p_0+p_1,\quad \rho=\rho_0+\rho_1,\quad \vec{B}=\vec{B}_0+\vec{B}_1,\quad \vec{U}=\vec{U}_0+\vec{U}_1$$

In the above relations $\vec{U}_0$, p_0, $\vec{B}_0$ and ρ_0 respectively, the equilibrium state of the velocity vector, pressure, magnetic field vector, and density; Also $\vec{U}_1$, p_1, $\vec{B}_1$ and ρ_1 are the perturbed part of the velocity, pressure, magnetic field, and density vector, respectively. While $\vec{U}_1=\left(u_{x1},u_{y1},u_{z1}\right)$,

$\vec{B}_1 = (B_{x1}, B_{y1}, B_{z1})$, $\vec{g} = (0,0,-g)$, $\vec{\Omega} = (\Omega,0,0)$ and the fluid is arranged in horizontal strata; The density ρ_0 is only a function of the vertical coordinate z $(\rho_0 = \rho_0(z))$ and $\vec{B}_0 = B_{x0}(z)\vec{e}_x$. Figure (1) shows a general view of the geometry of the problem.

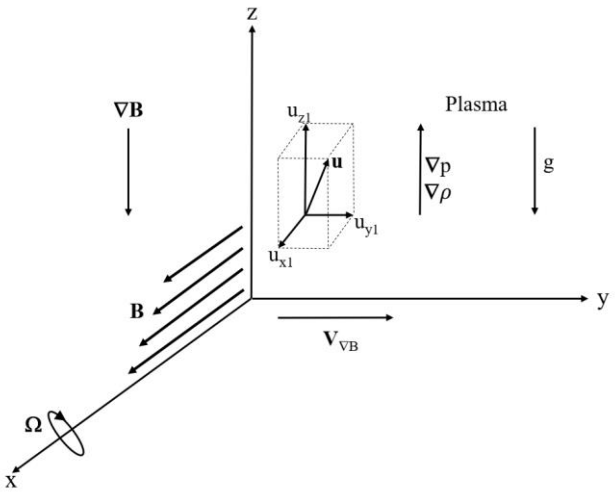

Fig. 1. Field and plasma geometry in ideal MHD problem; The quantities $\vec{B}, \vec{u}, \vec{g}, \vec{\Omega}, \vec{V}_{\nabla B}, \nabla\vec{B}, \nabla p$ and $\nabla\rho$ are the magnetic field, equilibrium flow velocity, gravitational acceleration, angular velocity, Magnetic field gradient drift velocity, Magnetic field gradient, pressure gradient, and density gradient, respectively.

Similar to the non-rotating case, to linearize the basic equations of the problem, we use normal mode analysis and obtain the general differential equation in the z component of velocity (u_z):

$$i\omega\left(\frac{d}{dz}\left(\rho_0\frac{du_z}{dz}\right)-\rho_0 k^2 u_z\right)+\frac{gk^2u_z}{i\omega}\frac{d\rho_0}{dz}+\frac{4\Omega^2}{i\omega\left(1+\frac{B_{x0}^2k_x^2}{\mu_0\rho_0 i^2\omega^2}\right)}\times\frac{d}{dz}\left(\rho_0\frac{du_z}{dz}\right)+$$
$$+\frac{B_{x0}^2k_x^2}{\mu_0 i\omega}\left(\frac{d^2}{dz^2}-k^2\right)u_z+\frac{2B_{x0}k_x^2}{\mu_0 i\omega}\frac{dB_{x0}}{dz}\frac{du_z}{dz}=0 \qquad (5)$$

The obtained differential equation, which is based on the z component of fluid velocity (u_z), shows the effect of magnetic field and rotation on the RTI of stratified plasma.

3. Dispersion Relation and Discussions

In this section, with the help of linearized equation (5), the dispersion relation is derived for the rotating case. We consider the incompressible continuity of the stratified plasma layer, which is as thick as h. The stratified plasma is enclosed between two rigid boundaries, where the initial density distribution function is defined as a power of 3, and the static external magnetic field is defined as the following exponential:

$$\rho_0(z) \propto z^3 \tag{6}$$

$$B_0(z) \propto \exp(z); \qquad 0 \le z \le h \tag{7}$$

By inserting the above relations and considering the horizontal component of Alfven velocity $\upsilon_{f_x}^2 = B_{x0}^2(0)/\mu_0\rho_0(0)$ and also $u_{z1} = \sin\left((n\pi/h)z\right)\exp(\lambda z)$ as the general solution of the differential equation of relation (5), we obtain the following set of equations in terms of $\sin\left((n\pi/h)z\right)$ and $\cos\left((n\pi/h)z\right)$:

$$\omega^2\left(z^3\left(\frac{n\pi}{h}\right)^2 - 3\lambda z^2 - \lambda^2 z^3\right) + 3z^2 g k^2 + \frac{4\Omega^2}{1 - \frac{\upsilon_{fx}^2 \exp\left(z/L_D\right)k_x^2}{\omega^2}} \times \left(-z^3\left(\frac{n\pi}{h}\right)^2 + 3\lambda z^2 + \lambda^2 z^3\right) +$$
$$+\upsilon_{fx}^2 L_D^3 \exp\left(z/L_D\right)k_x^2\left(\lambda^2 - \left(\frac{n\pi}{h}\right)^2 - k^2\right) + \upsilon_{fx}^2 L_D^2 k_x^2 \lambda \exp\left(z/L_D\right) = 0 \tag{8}$$

$$\omega^2\left(-3z^2\left(\frac{n\pi}{h}\right) - 2\lambda z^3\left(\frac{n\pi}{h}\right)\right) + \frac{4\Omega^2}{1 - \frac{\upsilon_{fx}^2 \exp\left(z/L_D\right)k_x^2}{\omega^2}} \times \left(3z^2\left(\frac{n\pi}{h}\right) + 2\lambda z^3\left(\frac{n\pi}{h}\right)\right) +$$
$$+2\left(\frac{n\pi}{h}\right)\upsilon_{fx}^2 L_D^3 k_x^2 \lambda \exp\left(z/L_D\right) + \left(\frac{n\pi}{h}\right)\upsilon_{fx}^2 L_D^2 k_x^2 \exp\left(z/L_D\right) = 0 \tag{9}$$

In relations (8) and (9), the parameters λ and L_D represent the perturbation wavelength and the density-scale length, respectively. To investigate the effect of magnetic field and rotation, we normalized the general dispersion relation by using the following dimensionless values, where $\omega_{pe}^2 = \rho e^2\left(m_e^2\varepsilon_0\right)^{-1}$ is plasma frequency.

$$\omega^{*2}=\omega^2/\omega_{pe}^2,\quad \omega_{f_x}^{*2}=\upsilon_{f_x}^2/\omega_{pe}^2L_D^2,\quad \Omega^*=\Omega/\omega_{pe},\quad \lambda^{*2}=\lambda^2L_D^2,\quad h^{*2}=h^2/L_D^2,\quad k^{*2}=k^2L_D^2,$$
$$g^*=g/\omega_{pe}^2L_D,\quad \omega_{pe}=\left(\rho_0e^2/m_e^2\right)^{1/2},\quad z^*=z/L_D$$

As a result, considering $\omega^*=\omega_r^*+i\gamma$ and $\omega_r^*=0$ (stable oscillations), we obtained the following dispersion relation for the normalized growth rate (γ):

$$\gamma^4+\gamma^2\left[\omega_{fx}^{*2}k_x^{*2}\exp\left(z^*\right)\left\{1+\frac{-\lambda^{*2}+\left(\frac{n\pi}{h^*}\right)^2+k^{*2}-\lambda^*}{z^{*3}\left(\frac{n\pi}{h^*}\right)^2-3\lambda^*z^{*2}-\lambda^{*2}z^{*3}}\right\}-\frac{3z^{*2}g^*k^{*2}}{z^{*3}\left(\frac{n\pi}{h^*}\right)^2-3\lambda^*z^{*2}-\lambda^{*2}z^{*3}}+4\Omega^2\right]+$$
$$+\omega_{fx}^{*2}k_x^{*2}\left\{\frac{\omega_{fx}^{*2}k_x^{*2}\exp\left(2z^*\right)\left\{-\lambda^{*2}+\left(\frac{n\pi}{h^*}\right)^2+k^{*2}-\lambda^*\right\}}{z^{*3}\left(\frac{n\pi}{h^*}\right)^2-3\lambda^*z^{*2}-\lambda^{*2}z^{*3}}-\frac{3z^{*2}g^*k^{*2}\exp\left(z^*\right)}{z^{*3}\left(\frac{n\pi}{h^*}\right)^2-3\lambda^*z^{*2}-\lambda^{*2}z^{*3}}\right\}=0 \qquad (10)$$

To investigate the simultaneous effect of the horizontal magnetic field and rotation on the growth rate of RTI of the considered system, equation (10) has been numerically solved, so that γ is a function of the dimensionless value of the horizontal component of the magnetic field $\left(\omega_{fx}^*\right)$. k^* is the normalized perturbation wave number relative to the spatial change rate and $\lambda^*=\lambda L_D$ is the normalized perturbation wavelength relative to the spatial change rate, where λ is a constant value and L_D is the density-scale length. In the figures below $k_x^{*2}=0.2k^{*2}$, $h^*=1, n=1$, $z^*=1$, $\lambda^*=-0.5$ and $g^*=10$. In these figures, the normalized growth rate (γ) changes according to the normalized wave number $\left(k^*\right)$. In Figure (2), the growth rate of instability has been plotted in terms of wave number in the absence of rotation $(\Omega=0)$.

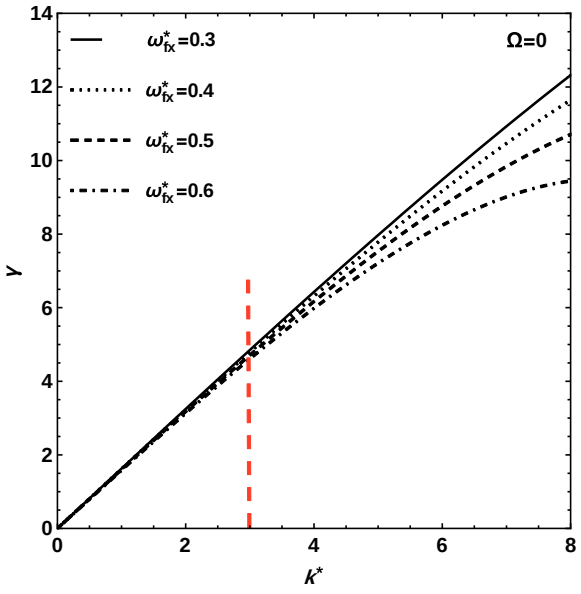

Fig. 2. The growth rate (γ) versus wave number (k^*) at $\Omega = 0$ in variation of magnetic field (ω_{fx}^*).

Based on this, we observe that by increasing the wave number to a certain value, all four curves with a constant slope on a common asymptotic line are increasing the growth rate of instability, linearly with the wave number. From this wave number onwards, the system will behave non-linearly so that each curve is separated by different slopes. The lowest slope belongs to the highest intensity of the magnetic field, therefore the role of the magnetic field in stabilizing the growth rate of the instability is well evident in the number of waves greater than 3.

From a physical point of view, according to the linear theory, when the disturbance wave number increases, the disturbance wavelength decreases, and the growth rate of the instability increases. As the rate of instability growth increases, the amplitude of the disturbance increases exponentially with time, and as a result, the energy of the disturbance wave also grows. Therefore, with the help of plasma rotation, we can minimize this range of disturbance [25-26].

Therefore, in Figure (3), the growth rate of RTI is plotted in terms of the normalized wave number in the presence of rotation $(\Omega = 0,3,9,12,60)$ for a specific magnetic field with intensity $\omega_{fx}^* = 0.5$.

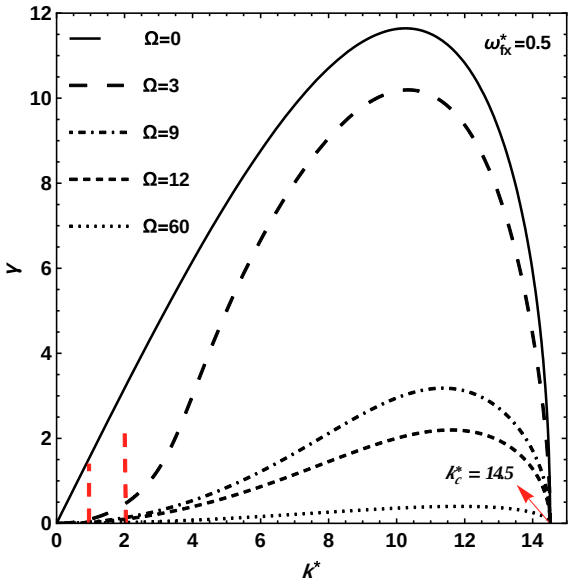

Fig. 3. The growth rate (γ) versus wave number (k^*) at $\omega_{fx}^* = 0.5$ in variation of angular velocity (Ω).

We can see that in small wave numbers, increasing the angular velocity from 3 to 60, the growth rate of instability will have a different behavior in each curve. So that the threshold wave number (k_{th}^*) changes from $k_{th}^* = 1$ to $k_{th}^* = 2$ with the increase of Ω. After this threshold wave number, we will see an increase in the growth rate of instability with a different slope. This rising slope becomes gentler at higher angular velocities and then reaches the peak. As it is clear from Figure (3), at $\Omega = 9$, the height of the peak of the growth rate reaches the lowest value. From here on, we see the maximum elongation in the two curves at $\Omega = 12$ and $\Omega = 60$, respectively. In these two curves, the growth rate is quasi-stable and stable, respectively, and we will no longer worry about the destructive effects of instability on the system. Finally, at $\Omega = 60$, we reached a very small threshold amplitude for the growth rate, which was completely suppressed with a gentle slope at the critical wave number $(k_c^* = 14.5)$ and reached full stability.

In Figure (4), the growth rate of RTI is plotted in terms of wave number in the presence of rotation with a magnitude of $\Omega = 3$, for different values for the horizontal magnetic field $(\omega_{fx}^* = 0.3, 0.4, 0.5, 0.6)$.

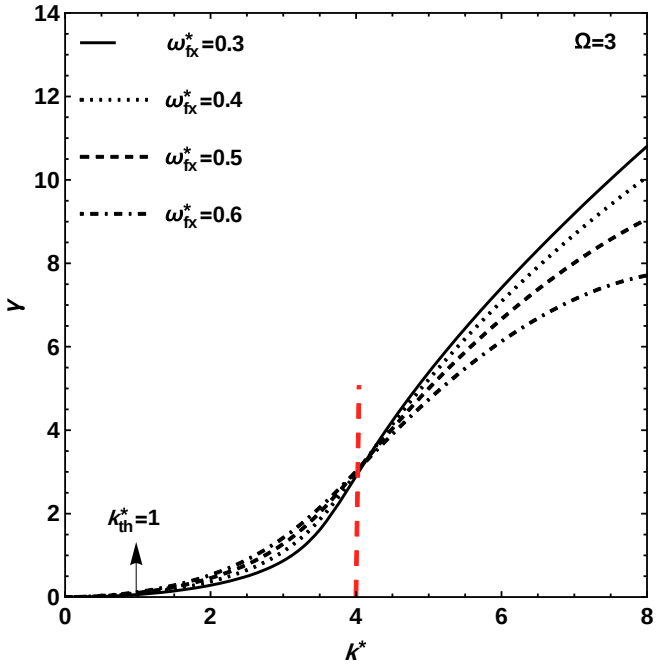

Fig. 4. The growth rate (γ) versus wave number (k^*) at $\Omega = 3$ in variation of magnetic field (ω_{fx}^*).

We can see that up to wave number 1 (threshold wave number), the system is in a completely stable state, and from $k_{th}^* = 1$ to $k^* = 4$, we will witness a quasi-stable state. From this value onwards, we see a non-linear behavior, so that the amplitude of the growth rate of instability is increasing with a certain slope for each of the curves.

Figure (5), in the form of a convenient summary, shows a comparison between the non-rotating and rotating modes. In this figure, the growth rate of RTI is plotted in terms of wave number, in the presence of horizontal and vertical components of the magnetic field for the non-rotating state, and also in the presence of constant rotation and horizontal magnetic field for the rotating state.

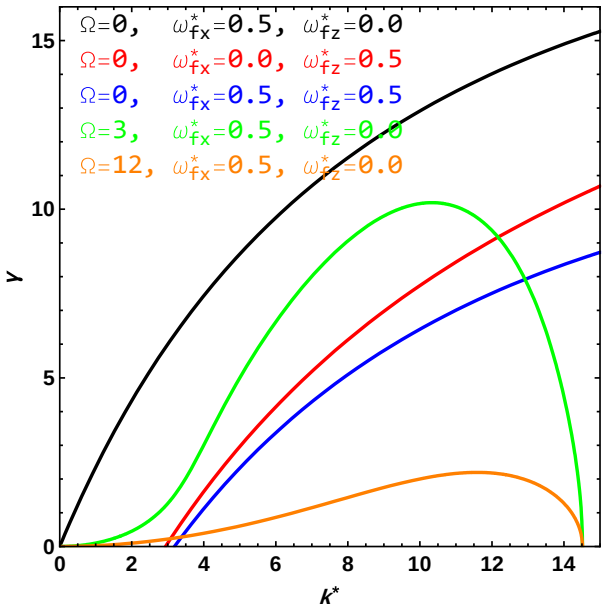

Fig. 5. The growth rate (γ) versus wave number (k^*) for non-rotating $(\Omega = 0)$ and rotating $(\Omega \neq 0)$ cases.

The results of the non-rotating case have been presented in an article before[27]. In this article, it was observed that at long wavelengths, the vertical component of the magnetic field has a stronger effect than the horizontal component of the magnetic field. This effect can also be seen in Figure (5) so that the threshold wave number starts from the value of 3 with the help of the vertical component of the magnetic field. But in short wavelengths, the opposite is the case, that is, the horizontal component of the magnetic field will have a stronger effect than the vertical component of the magnetic field. This component of the magnetic field gradually reduces the slope of the growth rate of instability and reduces its range[27].

According to Figure (5), for the rotational mode, the simultaneous application of plasma rotation and the horizontal component of the magnetic field plays an important and stabilizing role in managing the growth rate of the RTI. We observe that the horizontal component of the magnetic field has a vital ability to stop the linear growth rate of the instability for large wave numbers (short wavelengths). On the other hand, plasma rotation is effective for small values of wave number (long wavelengths). Therefore, by comparing the results, we find that the presence of rotation in long wavelengths has a stronger effect than the vertical component of the magnetic field.

4. Conclusions

In the non-rotating case, the simultaneous effect of the horizontal and vertical components of the static external magnetic field on the linear growth rate of RTI in stratified plasma was analyzed analytically in planar geometry. According to the previously obtained results, it is concluded that applying plasma power density along with horizontal and vertical external magnetic fields plays an important and stabilizing role in managing the growth rate of RTI. Our investigation showed that the maximum instability occurs at $\lambda^* = -0.5$. At long wavelengths, the vertical component of the magnetic field has a stronger effect than the horizontal component of the magnetic field. Still, at short wavelengths, the opposite is the case. However, in the rotating case, the simultaneous effect of rotation and static external horizontal magnetic field on the growth rate of RTI in stratified plasma was investigated analytically. For this purpose, the plasma density function was considered a power with 3 and the static external magnetic field as an exponential. According to the obtained results, it is concluded that applying plasma power density along with rotation and horizontal external magnetic field plays an important and stabilizing role in managing the growth rate of RTI. Our investigation showed that the horizontal component of the magnetic field has a vital ability to stop the linear growth rate of the instability for large wave numbers (short wavelengths). On the other hand, plasma rotation is effective for small values of wavenumber (long wavelengths). Therefore, by comparing the results, we find that the presence of rotation in long wavelengths has a stronger effect than the vertical component of the magnetic field and can be a suitable substitute for it. For the optimal control of RTI, it was observed that the simultaneous combination of the horizontal component of the static external magnetic field and the angular velocity (rotation effect) gives the system a better stability state.

References

S. Chandrasekhar, “Hydrodynamic and hydromagnetic stability”, *Oxford: Clarendon Press,* (1961).

R.A. Goldston and P. H. Rutherford, “Introduction to plasma physics”, *Institute of Physics,* (1997).

P. K. Sharma; A. Tiwari; S. Argal and R. K. Chhajlani, "Rayleigh Taylor instability of two superposed compressible fluids in un-magnetized plasma", *Journal of Physics*, **534(1)**, 012054, (2014); DOI: https://doi.org/10.1088/1742-6596/534/1/012054.

S. Atzeni and J. Meyer-ter-vehn, "The Physics of Inertial Fusion", *Oxford: Clarendon Press*, pp. (4-6, 11-13, 33-36, 38-41, 76, 389, 399), (2004).

R. Betti; M. Umansky; V. Lobatchev; V. N. Goncharov and R. L. McCrory, "Hot-spot dynamics and deceleration-phase Rayleigh-Taylor instability of imploding inertial confinement fusion capsules", *Physics of Plasmas*, **8(12)**, 5257, (2001); DOI: https://doi.org/10.1063/1.1412006.

B. L. Yang; L. F. Wang; W. H. Ye and C. Xue, "Magnetic Field Gradient Effects on Rayleigh-Taylor Instability with Continuous Magnetic Field and Density Profiles", *Physics of Plasmas*, 18, 072111, (2011); DOI: https://doi.org/10.1063/1.3609773.

B. Dolai and R. P. Prajapati, "The rotating Rayleigh-Taylor instability in a strongly coupled dusty plasma", *Physics of Plasmas*, **25(8)**, 083708, (2018); DOI: https://doi.org/10.1063/1.5041088.

S. A. Slutz; M. C. Herrmann; R. A. Vesey; A. B. Sefkow; D. B. Sinars; D. C. Rovang; K. J. Peterson and M. E. Cuneo , "Pulsed-power-driven cylindrical liner implosions of laser preheated fuel magnetized with an axial field", *Physics of Plasmas*, **17(5)**, 056303, (2010); DOI: https://doi.org/10.1063/1.3333505.

V. I. Oreshkin; R. B. Baksht; R. K. Cherdizov; E. V. Oreshkin; N. A. Ratakhin; A. G. Rousskikh; A. V. Shishlov; V. A. Vankevich and A. S. Zhigalin, "Studies on the implosion of pinches with tailored density profiles", *Plasma Physics and Controlled Fusion*, **63(4)**, 045022, (2021); DOI: https://doi.org/10.1088/1361-6587/abe959.

R. K. Cherdizov; R. B. Baksht; V. A. Kokshenev; V. I. Oreshkin; A. G. Rousskikh; A. V. Shishlov; D. L. Shmelev and A. S. Zhigalin, "Effect of tailored density profiles on the stability of imploding Z-pinches at microsecond rise time megaampere currents", *Plasma Physics and Controlled Fusion*, **64(1)**, 015011, (2021); DOI: https://doi.org/10.1088/1361-6587/ac35a5.

A. G. Rousskikh; A. S. Zhigalin; V. I. Oreshkin; V. Frolova; A. L. Velikovich; G. Yu. Yushkov and R. B. Baksht, "Effect of the axial magnetic field on a metallic gas-puff pinch implosion", *Physics of Plasmas*, **23(6)**, 063502, (2016); DOI: https://doi.org/10.1063/1.4953048.

C. A. Walsh; S. O'Neill; J. P. Chittenden; A. J. Crilly; B. Appelbe; D. J. Strozzi; D. Ho; H. Sio; B. Pollock; L. Divol; E. Hartouni; M. Rosen; B. G. Logan and J. D. Moody, "Magnetized ICF

implosions: Scaling of temperature and yield enhancement", *Physics of Plasmas*, **29(4)**, 042701, (2022); DOI: https://doi.org/10.1063/5.0081915.

C. A. Walsh; R. Florido; M. Bailly-Grandvaux; F. Suzuki-Vidal; J. P. Chittenden; A. J. Crilly; M. A. Gigosos; R. C. Mancini; G. Pérez-Callejo; C. Vlachos; C. McGuffey; F. N. Beg and J. J. Santos, "Exploring extreme magnetization phenomena in directly driven imploding cylindrical targets", *Plasma Physics and Controlled Fusion*, **64(2)**, 025007, (2022); DOI: https://doi.org/10.1088/1361-6587/ac3f25.

A. L. Velikovich; F. L. Cochran and J. Davis, "Suppression of Rayleigh-Taylor instability in Z-pinch loads with tailored density profiles", *Physical review letters*, **77(5)**, 853, (1996); DOI: https://doi.org/10.1103/PhysRevLett.77.853.

A. L. Velikovich; F. L. Cochran and J. Davis, "Stabilized Z-pinch loads with tailored density profiles", *AIP Conference Proceedings*, **409(1)**, 549, (1997); DOI: https://doi.org/10.1063/1.53832.

S. Khoshbinfar, in *The 3rd Conference of plasma engineering and plasma Physics*, (UT, Tabriz, Iran, 2015), pp. 316-319, (In Persian).

S. Khoshbinfar and M. A. Masoumparast, "Stabilization of magneto-Rayleigh-Taylor instability in a Plasma with Power density Gradient", *Journal of Nuclear Science and Technology (JONSAT)*, **45(1)**, 99, (2024); DOI: https://doi.org/10.24200/nst.2023.1285.1836.

K. A. Baldwin; M. M. Scase and R. J. Hill, "The inhibition of the Rayleigh-Taylor instability by rotation", *Scientific reports*, **5(1)**, 1, (2015); DOI: https://doi.org/10.1038/srep11706.

M. M. Scase; K. A. Baldwin and R. J. Hill, "Rotating Rayleigh-Taylor instability", *Physical Review Fluids*, **2(2)**, 024801, (2017); DOI: https://doi.org/10.1103/PhysRevFluids.2.024801.

P. K. Sharma; A. Tiwari and S. Argal, "Effect of magnetic field on the Rayleigh Taylor instability of rotating and stratified plasma", *Journal of Physics: Conference Series*, **836(1)**, 012009, (2017); DOI: https://doi.org/10.1088/1742-6596/836/1/012009.

M. M. Scase and R. J. Hill, "Centrifugally forced Rayleigh–Taylor instability", *Journal of Fluid Mechanics*, **852**, 543, (2018); DOI: https://doi.org/10.1017/jfm.2018.539.

M. M. Scase; K. A. Baldwin and R. J. Hill, "Magnetically induced Rayleigh-Taylor instability under rotation: Comparison of experimental and theoretical results", *Physical Review E*, **102(4)**, 043101, (2020); DOI: https://doi.org/10.1103/PhysRevE.102.043101.

C. Samulski; B. Srinivasan; M. J.-E. Manuel; R. Masti; J. P. Sauppe and J. Kline, "Deceleration-stage Rayleigh–Taylor growth in a background magnetic field studied in cylindrical and Cartesian geometries", *Matter and Radiation at Extremes*, **7(2)**, 026902, (2022); DOI: https://doi.org/10.1063/5.0062168.

G. A. Hoshoudy, "Rayleigh-Taylor Instability in Magnetized Plasma", *World Journal of Mechanics*, **4**, 260, (2014); DOI: https://doi.org/10.4236/wjm.2014.48027.

M. Cvejić; D. Mikitchuk; E. Kroupp; R. Doron; P. Sharma; Y. Maron; A. L. Velikovich; A. Fruchtman; I. E. Ochs; E. J. Kolmes and N. J. Fisch, "Self-generated plasma rotation in a Z-pinch implosion with preembedded axial magnetic field", *Physical review letters*, **128(1)**, 015001, (2022); DOI: https://doi.org/10.1103/PhysRevLett.128.015001.

J. Huneault; D. Plant and A. J. Higgins, "Rotational stabilization of the Rayleigh–Taylor instability at the inner surface of an imploding liquid shell", *Journal of Fluid Mechanics*, **873**, 531, (2019); DOI: https://doi.org/10.1017/jfm.2019.346.

M. A. Masoumparast and S. Khoshbinfar, "Growth rate of magnetic Rayleigh-Taylor instability in plasma with power-law density profile", *The 29th Iranian Nuclear Conference*, (SBU, Tehran, Iran, 2023), INC29-1061, (In Persian).

ICNST 2024
International Conference on Nuclear Science and Technology
6- 8 MAY 2024 | Isfahan, Iran

Commissioning and initial testing of microwave interferometer diagnostic system of Alvand tokamak for electron plasma densitometry (Paper ID: 1078)

Noori E.[1*], Rostamifard D.[1], Seyedhabashi M.M.R.[1], Seddighi F.[1], Raeisdana A.[1], and Sadeghi Y.[1]

[1]*Plasma and nuclear fusion research school, Nuclear Science and Technology Research Institute (NSTRI), Tehran, Iran*

Abstract

The information on the main parameters of tokamak plasma, such as line averaged electron density (linear integral of electron density) and temporal disturbance spectrum of electron density, are essential to understand the physics and to perform control procedures of tokamak. Microwave interferometry is one of the most efficient and accurate diagnostic facilities in determining the electron density of tokamak. Alvand tokamak has a single-channel microwave interferometer diagnostic system to measure the electron density of the plasma. For many years, due to the failure of interferometer components, this diagnostic system has not been able to be used for plasma densitometry of the tokamak. In this article, by introducing the characteristics and elements of the microwave interferometer of Alvand tokamak, the results of the initial test of plasma densitometry of Alvand tokamak for RF discharge and a typical shot of the tokamak, after the repair and commissioning of the interferometer system, are presented. It was found that the measured values of the plasma density are in good agreement with the density ranges reported in the technical sheets of Alvand tokamak.

Keywords: Plasma diagnostics, Microwave interferometer, Plasma density, Alvand tokamak

Introduction

Tokamak diagnostic methods consist of various systems including direct-contact diagnostic facilities for determination of edge plasma characteristics and remote diagnostic techniques to study the central plasma parameters such as density, temperature and types of radiation of rays and particles, which are variable and extensive according to the needs and purpose of the system in question. In this regard, a significant number of plasma diagnostic systems have been developed in

connection with the measurement and analysis of the electromagnetic radiation of the central tokamak plasma. The reason for this remarkable development of plasma diagnostic systems which are based on electromagnetic waves propagation in tokamak is that the plasma of tokamaks has a very high temperature, which practically makes it impossible to receive information of central plasma parameters using the direct-contact diagnostic facilities. In addition, using remote sensing diagnostic techniques which are based on wave propagation, causes the least disturbance in the plasma, which consequently reduces the error in measurement of the plasma parameters. Considering the plasma density range of tokamak, diagnostic systems which are based on microwave propagation are of special importance in determining the characteristics of tokamak plasma. The use of microwave interferometric method is known as one of the most efficient and accurate methods in determining the electron density of tokamak plasma which is being used in various tokamaks around the world [1, 2, 3]. Alvand is a small size tokamak that is used for educational purposes in the Plasma and Nuclear fusion research school of the Nuclear Science and Technology Research Institute (NSTRI). This tokamak is equipped with a homodyne microwave interferometer system to measure the electron density [4]. The main purpose of the present article is Commissioning, settting up, and performing initial test of microwave interferometer diagnostic system of Alvand tokamak for measurement of plasma density.

Physical Description of Microwave Interfrometer

The operation of a microwave interferometer in a tokamak is based on measurement of the phase difference created by propagation of linearly-polarized wave in the range of millimeter inside the tokamak plasma. As it is shown in Fig. 1, there is a plasma with a certain length (L) in the path of the measuring branch of the interferometer.

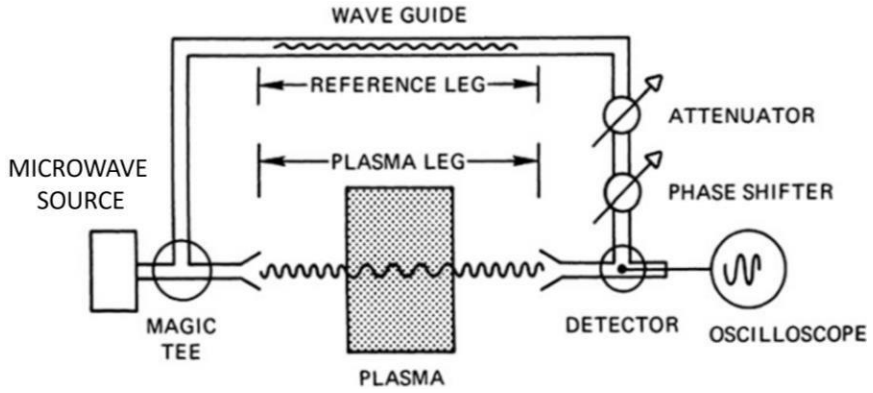

Fig. 1. A simple representation of a heterodyne microwave interferometer

Generally speaking, the density of tokamak plasma is non-uniform in tokamak. Therefore, the refractive index of the plasma is not uniform and has spatial distribution. Such changes in the refractive index of measuring branch of the interferometer, causes phase difference between the measuring and reference branches of the interferometer. If the measuring wave propagates in a magnetized plasma like a tokamak and its propagation direction and electric field are respectively perpendicular ($K \perp B_T$) and parallel ($E \parallel B_T$) to the magnetic field of the tokamak torus, it causes the propagation of ordinary wave in the plasma. Assuming that collision effects are negligible in tokamak plasma, then the relationship between plasma refractive index and plasma density is written as follows [2, 3].

$$N(x) = \sqrt{1 - \frac{n_e(x)}{n_c}} \tag{1}$$

The dispersion relation of ordinary wave propagation in plasma is

$$\omega^2 = \omega_p^2 + ck^2 \tag{2}$$

where k and ω are the wave number and frequency of the electromagnetic wave and ω_p is defined as plasma frequency which is related to the plasma density as

$$\omega_p = \left(n_e e^2 / m_e \varepsilon_0\right)^{1/2} \approx 56.42\sqrt{n_e} \tag{3}$$

where m_e, e, and ε_0 are respectively, the rest mass of electron, electric charge of electron, and vacuum permittivity. It should be noted that the plasma density at center of tokamak is maximum and therefore, for particular value of plasma density, known as critical density, we have $\omega = \omega_p$. For density values greater than the critical density ($n_e > n_c$), the wave will not propagate inside the plasma. In this case, it is said that the cut-off phenomenon has occurred in the plasma. The critical density can be defined as

$$n_c[\mathrm{m}^{-3}] \equiv \frac{\omega^2 m \varepsilon_0}{e^2} \approx \frac{f^2[Hz]}{80.6} \tag{4}$$

here f is the frequency of the propagating wave. Thus, phase changes can be expressed in terms of plasma density (electron density) as follows

$$\Delta\phi = \frac{\omega}{c}\int \left[\left(1 - \frac{n_e}{n_c}\right)^{1/2} - 1\right] dl \tag{5}$$

For situation where $n(x) \ll n_c$, or in other words, the frequency of the wave which is propagates in the plasma is much higher than the cutoff frequency of the plasma, the refractive index of the plasma can be approximated as follows

$$N \approx 1 - \frac{1}{2}\left(\frac{n_e}{n_c}\right) \tag{6}$$

Due to the non-uniformity of the density, the linear average of the plasma density in the direction of the central chord of the tokamak cross-section is defined as

$$\langle n_e \rangle = \frac{\int_0^L n_e(x) dl}{L} \tag{7}$$

Finally, the line-averaged plasma density of tokamak can be calculated as follows [2, 3].

$$\langle n_e[\mathrm{cm}^{-3}] \rangle = \frac{1.18 \times 10^6[\mathrm{GHz}]}{L[\mathrm{cm}]} F \tag{8}$$

Where F is the number of displaced interferometric fringes.

Experimental Setup and Results

Generally speaking, the microwave interferometer of Alvand tokamak consists of four main parts [4, 5]. The block diagram of the main parts of the microwave interferometer system of Alvand tokamak is described in Fig. 2.

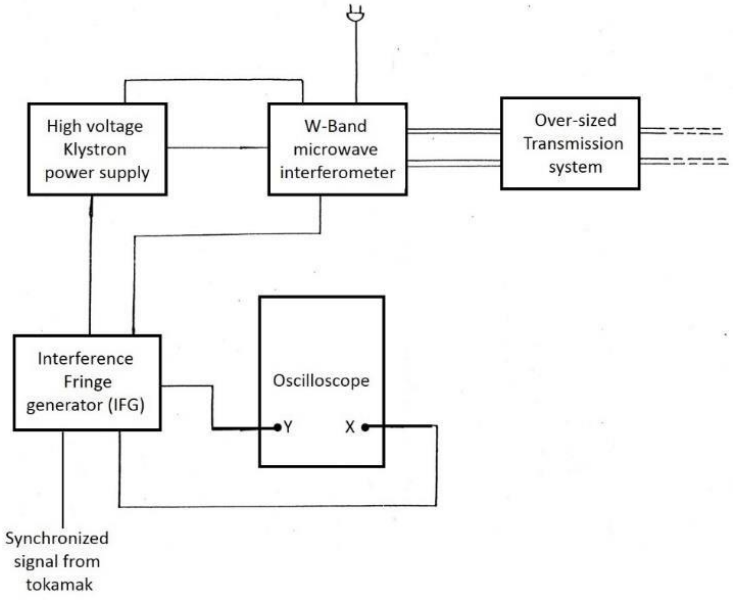

Fig. 2. Schematic view of microwave interferometer of Alvand tokamak

As it is shown in the Fig. 2, microwave interferometer system of Alvand tokamak consists of four main parts including: reflex klystron power supply which produces the required high voltage of the klystron, W- band microwave box which consists of the reflex klystron and microwave elements, over-sized transmission system including the waveguides and associated transmission components, and interference fringe generator (IFG) which provides the wave modulation signals as well as reference fringes. The physics of the interferometer that will be used in Alvand tokamak is based on the measurement of the phase change of the microwave beam that passes through the plasma of the tokamak. The results of initial test of the sawtooth wave modulation and null fringes, without

consideration of microwave source and plasma, which are produced by the interferometer fringe generator (IFG) part of Alvand tokamak interferometer are shown in Fig. 3.

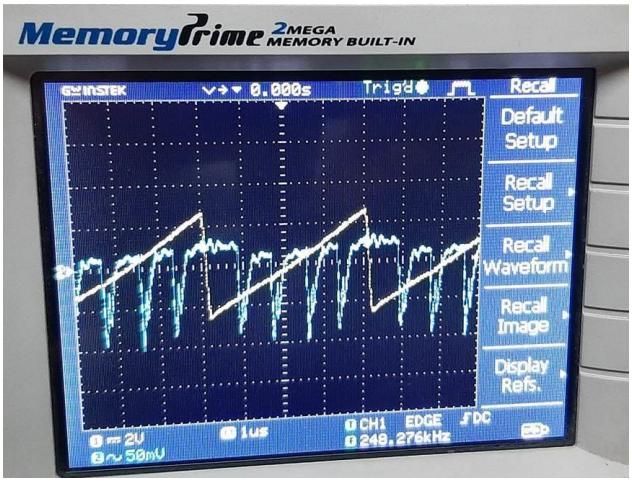

Fig. 3. Output of the sawtooth wave modulation null fringes produced by IFG part

After the initial performance test of the main components of the interferometer, the pre-startup stage was performed. At this stage, after turning on the klystron and launching the wave in a back-receive closed path, the fringes were recorded in black and white form on the oscilloscope as was shown in Fig. 4.

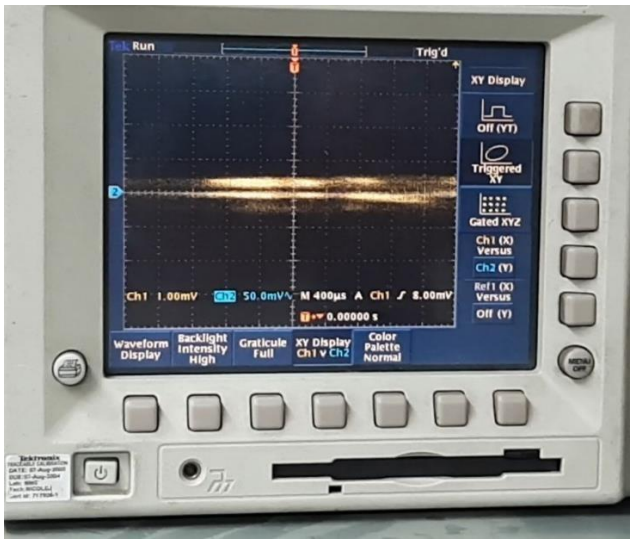

Fig. 4. Microwave interferometer fringes for a send-receive closed path

After completing the pre-setup stage of the interferometer, the electron density of the Alvand tokamak plasma was measured during a typical shot of the tokamak. Fig. 5 shows the results of loop voltage and plasma current in a typical shot of Alvand tokamak.

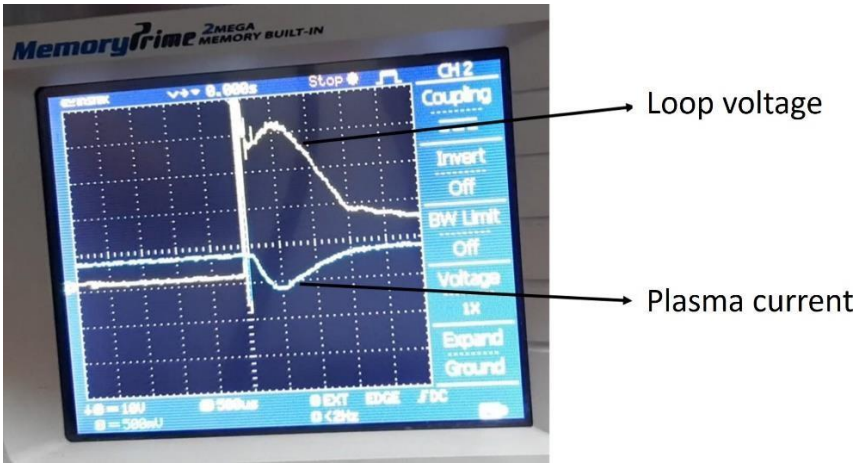

Fig. 5. Loop voltage and plasma current of typical shot of Alvand tokamak

The working frequency of the reflex klystron used in the microwave interferometer system of Alvand tokamak is 105 GHz. The plasma length of the Alvand tokamak is about 22 cm. In the case of the interfrometer system of Alvand tokamak, the output of the phase difference can be observed as black-withe firnges in the osciloscope. The displacement of one white fringe to the next white finge is equal to 2π. Since the distance of two secssesive white finges is scaled in the osciloscope. The fringe displacement of a withe finge can be measured as fraction of 2π and hence, the phase difference is determined. The amount of interference fringes displacement was obtained

$\Delta F \approx 1.0$ in a typical shot of Alvand tokamak which is associated with $\Delta\varphi \approx 1.0 \times 2\pi$. Using Eq.

6, the calculated line averaged density for a typical shot of Alvand tokamak is calculated as

$$\langle n_e \rangle \approx 3.3 \times 10^{12} \mathrm{cm}^{-3}$$

which is in agreement with the nominal density range of Alvand tokamak [4].

Conclusion

In this article, the results of the preliminary test of microwave interferometer of Alvand tokamak measurement of the line averaged plasma density during a typical shot of tokamak were presented. After conducting preliminary tests to ensure the accurate operation of the interferometer system, the pre-startup process of the interferometer was performed without consideration of the plasma. In the next step, considering the plasma presence, the initial test of the microwave interferometer was performed in a typical shot of the tokamak. It was found that the measured line averaged plasma density range is in good agreement with the reported nominal plasma density of Alvand tokamak.

References

H. J. Hartfuss and T. Geist, "Fusion Plasma Diagnostics with mm-Waves", Wiley- VCH (2013).

C. A. J. Hugenholtz, "Microwave interferometer and reflectometer techniques for thermonuclear plasmas", PhD thesis, Technical University Eindhoven (1990).

M. Varavin, et.al. "Study for the microwave interferometer for high densities plasmas on COMPASS-U tokamak", Fusion Engineering and Design 146, 1858 (2019).

Technical manual of microwave interferometer of Alvand tokamak, Volume I&II.

Ghorannevisse. M, and Avakian. M, "Interferometry measurement of line average electron density in Alvand IIC tokamak", Journal of Infrared, Millimeter, and Terahertz Wave 14, 17-22 (1993).

Effective parameters on the stochastic heating of electrons during interaction of long laser pulse with Hydrogen atoms (Paper ID: 1079)

Zohreh Dehghani, Elnaz Khalilzadeh*, and Amir Chakhmachi

Plasma and Nuclear Fusion Research School, Nuclear Science and Technology Research Institute, Tehran, Iran

Abstract

The motion of the electron in the presence of two counter-propagate electromagnetic waves in an under-dense plasma has been studied by Mendonca. He has shown that the stochastic heating happens if the condition $a_1 a_2 \geq 1/16$ is met for two counter-propagating electromagnetic waves. In which, a_1 and a_2 are the normalized vector potential amplitudes of these waves. Stochastic heating is one of important mechanism which plays a significant role in the heating of the plasma electrons. In this paper, the simulation study of effective parameters on the stochastic heating of electrons during interaction of long laser pulse with Hydrogen atoms is investigated. This is done by using the kinetic Particle-In-Cell (PIC) simulation code. For this purpose, the self-consistent evolutions of the laser pulse via the time–space Fourier transforms of transvers vector potential are investigated for different parameters of the laser and produced plasma (the field-ionized plasma). The results of our simulations represented that the when the laser pulse and the field-ionized plasma parameters (such as the laser pulse amplitude, Hydrogen atoms density, and the rise time of pulse) are selected so that a weak space charge field is formed, the backscattered Raman radiations can provide the necessary condition for occurring the chaos and stochastic heating of electrons.

Keywords: Stochastic heating, Long laser pulse, Particle-In-Cell

Introduction

The study of laser-plasma interaction is one of the fastest growing fields in present-day physics. In this regard, considerable progress has been made in understanding the physics of plasma heating due to its potential applications including fast ignition in ICF, proton acceleration, x ray lasers, and laser wakefield accelerators[1-4]. At relativistic intensities, collisionless heating of electrons

by laser radiation takes place via several heating mechanisms such as resonance heating, vacuum heating, inverse bremsstrahlung heating, and $J \wedge B$ heating [5-8]. Stochastic heating [9] by counter-propagating electromagnetic waves is other important mechanism which plays a significant role in the heating of plasma electrons. Mendonca show that chaos happens if the condition $a_1 a_2 \geq 1/16$ is met for two crossed electromagnetic waves. In which, a_1 and a_2 are the normalized vector potential amplitudes of these waves [9]. Many studies have been done theoretically and experimentally on the stochastic heating with using two crossed laser pulses. The PIC simulation results indicate that, in plasma at moderate densities such as a few percent of the critical density and when the under-dense plasma region is large enough, even with a single intense laser pulse only in plasma, the Raman backscattered and side-scattered waves can grow to a sufficiently high level to serve as intersecting pulse and trigger the electron stochastic motion [10-15].

When a strong laser pulse is propagated into a low-density gaseous medium, plasma is formed by the field ionization. Although, in many works the stage of ionization and plasma formation is not considered, but it has been shown that density fluctuations during ionization can be very effective in laser pulse evolutions through changes in scattering of radiation in plasma [16-18]. Since, as mentioned above, the Raman backscattering plays a key role in the occurrence of chaos, and also parametric instabilities (including Raman instability) can be commonly seeded by density fluctuations during gas ionization, it is expected that it can strongly influence the stochastic heating threshold of the electrons.

In this paper, the simulation study of effective parameters on the stochastic heating of electrons during interaction of long laser pulse with Hydrogen atoms is investigated. This is done by using the kinetic Particle-In-Cell (PIC) simulation code. For this purpose, the self-consistent evolutions of the laser pulse via the time–space Fourier transforms of transvers vector potential are investigated for different parameters of the laser and produced plasma (the field-ionized plasma).

Simulation parameters

Simulations have been performed by Smilei PIC code [19]. This code is a relativistic electromagnetic particle code that runs in the parallel platform. It elaborately includes the physics of atomic ionization according to the ADK model [20]. The density of Nitrogen atoms is $n_0 = 0.01 n_{cr}$, $0.02 n_{cr}$ and $0.003\ n_{cr}$ (n_{cr} is the critical density) which are in the spatial interval of $x = [85-220]\mu m$. Step like density is considered for the neutral Nitrogen atoms and for the ions and electrons in the pre-plasma case. Simulation box length is considered to be $[0-270]\mu m$ with spatial resolution $dx \approx 0.01 \times 2\pi\ \mu m$ per wavelength and there are 48 particles per cell. The laser pulse at wavelength $1\mu m$ and P polarization propagates with trapezoidal time profile along the x-direction. The pulse envelope used in our simulations, includes three duration time [PL_1, PL_2, PL_3]. It grows with PL_1, rests constant with PL_2, and drops with PL_3. The normalized laser intensity $a_0^2 \cong I\lambda_\mu^2 / 1.37 \times 10^{18}$ is selected as $a_0 = 1, 2,$ and 3. Reflecting conditions for particles and open-boundary condition for electromagnetic fields are utilized. The parameters of the quantities, position x, the electric field E_x, longitudinal momentums p_x, and vector potential a_y are normalized to c/ω_0 (ω_0 is the laser frequency), $\omega_0 m_e c/e$, $m_e c$, and $e/m_e c^2$, respectively.

Simulation results and discussions

In Fig. 1, a_y (the transverse vector potential indicated by the blue line), E_x (the produced wake-field indicated by the red line), n_x (the electron density indicated by the green line) and p_x (the momentum indicated by the black dot) are depicted for density $n_0 = 0.01\ n_{cr}$ (Hydrogen atoms), $a_0 = 1$, and laser pulse [140, 120, 140]fs in (a) the field-ionized plasma and (b) the pre-plasma at time 480 fs. It is emphasized that in Fig. 1(a) Hydrogen atoms are considered neutral, which are quickly ionized by the strong laser pulse and, in Fig. 1(b), a uniform plasma is considered by default. It is clear from the electron density diagram (green curve in Fig. 1(a)) that due to the high intensity laser pulse, Hydrogen atoms are quickly ionized. Despite the fact that the laser pulse rapidly ionizes Hydrogen atoms, there are significant differences in the electron phase space

between Fig. 1(a) and Fig. 1(b). It is clear that nothing special has happened in the case where the laser pulse propagate in the pre-plasma. On the other hand, in the previous work, using the Fourier analysis of the radiations produced during ionization, it has been revealed that there is Raman backscatter radiation produced by the strong initial noise, which can provide the necessary conditions for the occurrence chaos [9]. Mendonca show that chaos happens if the condition $a_1 a_2 \geq 1/16$ is met [9]. In this case, the Raman backscattered wave is considered as a second electromagnetic wave propagating in the opposite direction of original electromagnetic wave [15].

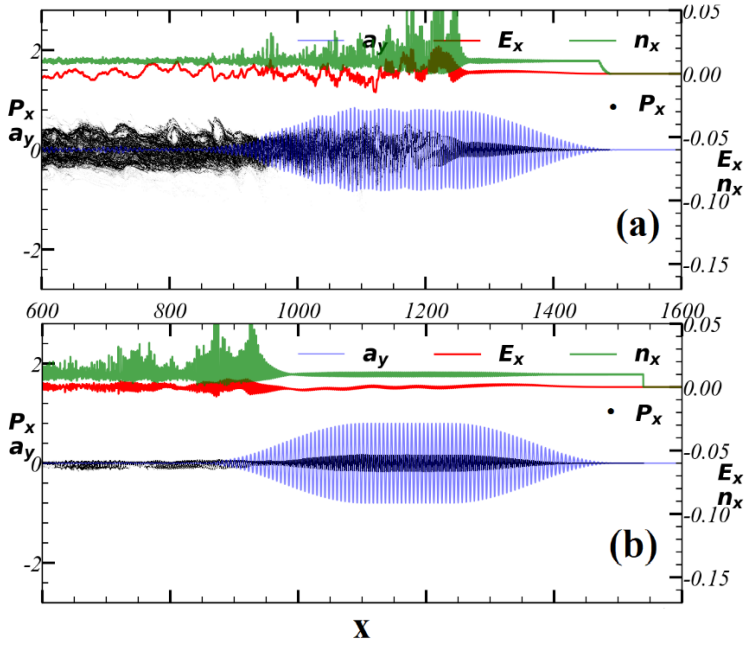

Fig. 1: The simulation results for a_y (the transverse vector potential indicated by the blue line), E_x (the produced wake-field indicated by the red line), n_x (the electron density indicated by the green line) and p_x (the momentum indicated by the black dot), for the laser pulse [140, 120, 140]fs, Hydrogen atoms density $n_0 = 0.01\ n_{cr}$, and $a_0 = 1$ at t=480 fs: Panels (a) and (b) correspond to the laser pulse propagating through the field-ionized plasma and the pre-plasma, respectively.

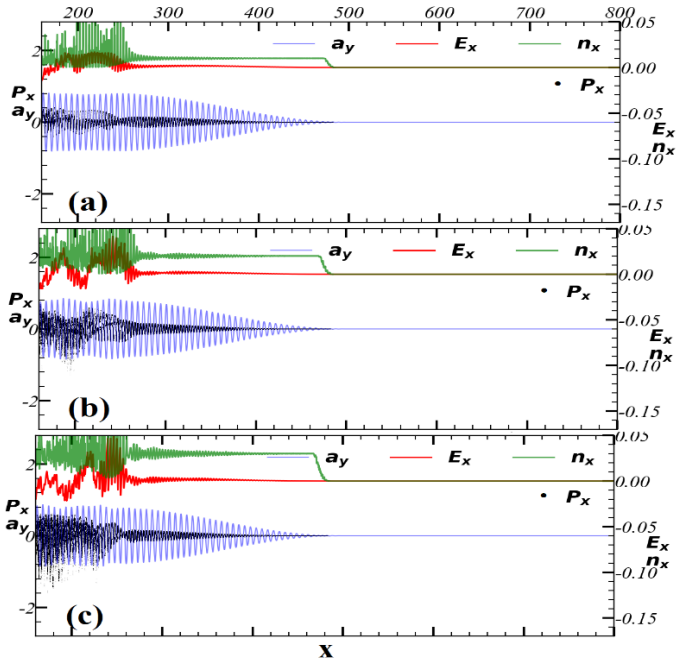

Fig. 2: The simulation results for a_y, E_x, n_x and p_x for pulse [140, 120, 140]fs, the Hydrogen atoms densities (a) $0.01n_{cr}$, (b) $0.02n_{cr}$, and (c) $0.03\ n_{cr}$ and for $a_0 = 1$ at t=250 fs.

Therefore, considering the phase space in Fig. 1(a), and low space charge electric field amplitude, it seems that the cause of the phase space disturbance is the occurrence of chaos.In the following, influence of the pulse amplitude, the pulse rise-time, and the plasma/gas density variation on the stochastic heating of electrons are investigated in this section.

In order to illustrate the density effect of Hydrogen atoms on the produced Raman backscattered radiation, a_y, E_x, n_x and p_x are plotted in Fig. 2 for pulse [140, 120, 140]fs, the gas densities (Hydrogen atoms) (a) $0.01n_{cr}$, (b) $0.02n_{cr}$, and (c) $0.03\ n_{cr}$ and for $a_0 = 1$ at t=250 fs. It is clearly seen in Fig. 3, that by increasing the density, the Raman instability can onset from upper level noise and the Mendonca criterion is satisfied sooner. Consequently, the stochastic heating mechanism can begin earlier. To show this, the self-consistent evolutions of pulse (a_y) in the ($k-\omega$) dispersion maps are investigated in Fig. 3 for the same parameters as in Fig. 2. On the other hand, analyzing the ($k-\omega$) dispersion map show that Raman backscattering phase matching conditions for the backscattered radiation is satisfied. According to this phase matching relation, the frequency and the wave number of Raman backscattered wave must satisfy relation

$\omega_{bs} \approx -\omega_0 + \omega_p$ and $k_{bs} \approx +k_0 - \omega_p / c$ (the "*bs*" and "0" refer to the Raman backscattering radiation and the incident laser pulse, respectively). The backscattered modes specified by arrow in Fig. 3. As it is clear in this figure, with the increase in the density of Hydrogen neutral atoms, the intensity of Raman backscattered radiation increases. Since this radiations play a major role in the occurrence of chaos, the results of Fig. 2 are completely justified.

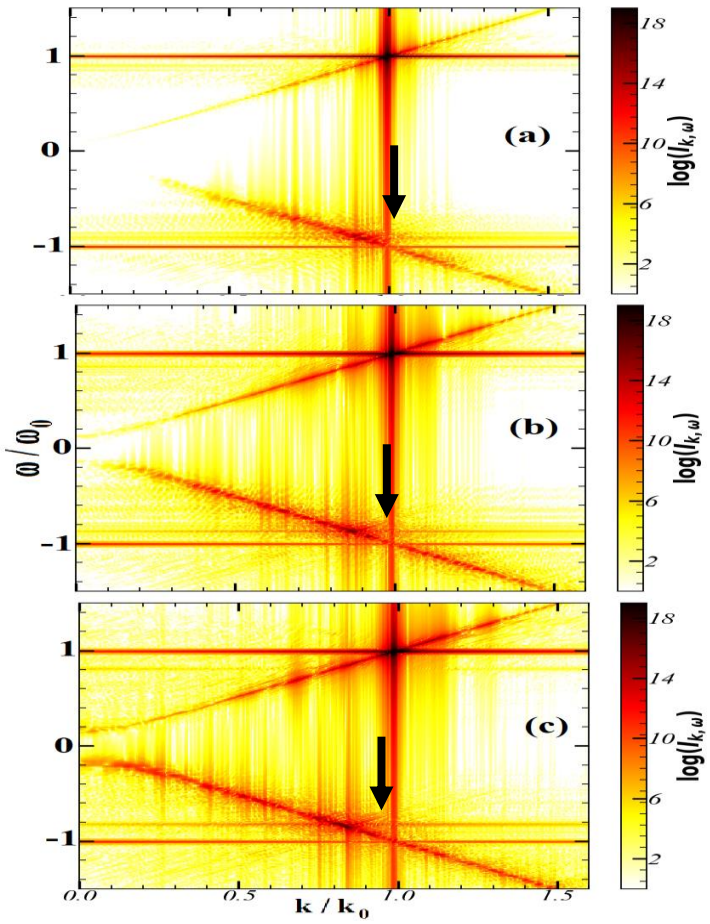

Fig. 3: (k – ω) dispersion maps for the field-ionized plasma for the laser pulse [140, 120, 140]fs, the Hydrogen atoms densities (a) $0.01 n_{cr}$, (b) $0.02 n_{cr}$, and (c) $0.03\ n_{cr}$ and for $a_0 = 1$ at t=250 fs.

In Fig. 4, influence of the pulse amplitude variation on stochastic heating are examined for field-ionized plasma. In this figure, the self-consistent evolutions of pulse (a_y) in the (k–ω) dispersion maps are investigated for Hydrogen atoms density $n_0 = 0.01\ n_{cr}$ and laser pulse [140, 120, 140]fs at time 250 fs. The vector potential varies as (a) $a_0 = 1$, (b) $a_0 = 2$ and (c) $a_0 = 3$. The simulation results

indicates that chaos in phase space can be start faster by increasing the laser pulse amplitude. In fact, the Raman backscattered wave grows from the stronger seed amplitude.

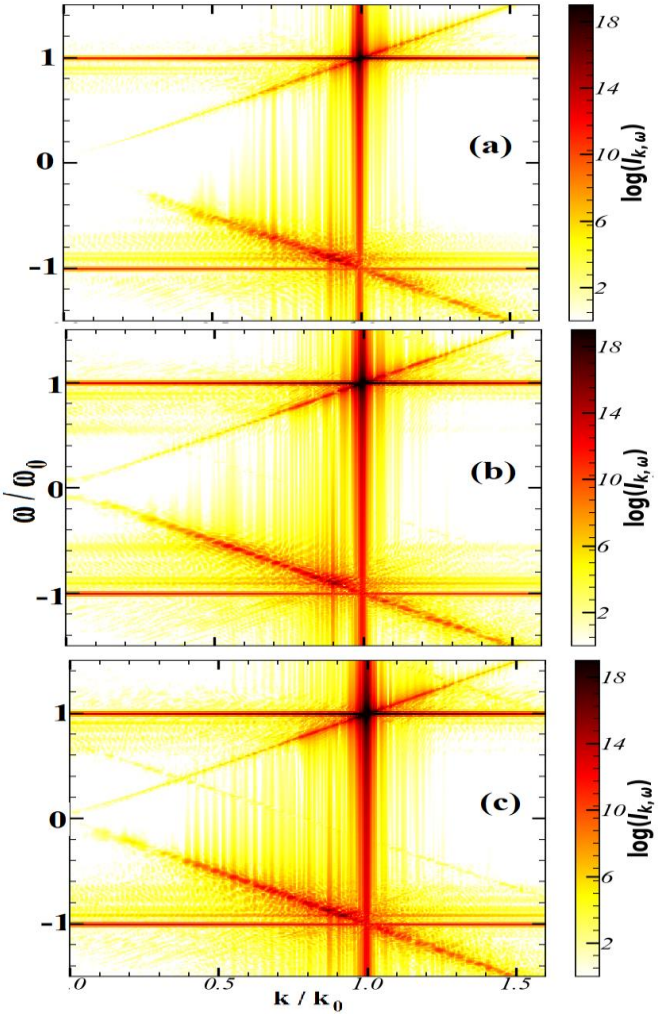

Fig. 4: (k – ω) dispersion maps for the field-ionized plasma for the laser pulse [140, 120, 140]fs, the Hydrogen atoms density $0.01n_{cr}$ and (a) $a_0 = 1$, (b) $a_0 = 2$ and (c) $a_0 = 3$ at t=250 fs.

To show the effect of the shape of the laser pulse on the intensity of the Raman backscattered radiations in the laser pulse interaction with the field-ionized plasma the self-consistent evolutions of pulse (ay) in the (k−ω) dispersion maps are studied in Fig. 5. In these simulation experiments, the laser pulse rise-time duration is varied as (a)140 fs, (b)100 fs and (c)60 fs. Also, the Hydrogen atoms density, the pulse length, and the pulse vector potential amplitude are $n_0 = 0.01\ n_{cr}$,

$L_p = 400\ fs$, and $a_0 = 1$, respectively. As it is clear in this figure, by reducing the rise-time of the laser pulse, we see a decrease in the intensity of the Raman backscattered radiations. This means that as the rise-time of the laser pulse decreases, the threshold for the occurrence of chaos decreases. In fact, since time duration of flat-top segment decreases by rise-time increment, reaching to Mendonca condition is delayed by increasing the rise-time of pulse.

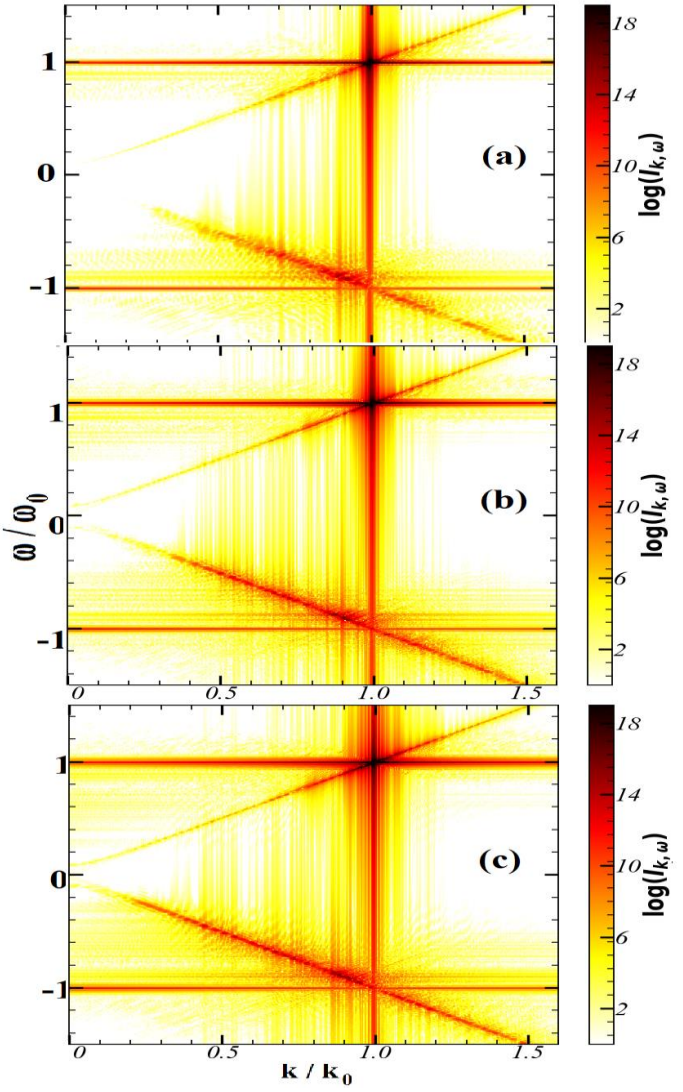

Fig. 5: (k – ω) dispersion maps for the field-ionized plasma for the laser pulse with the rise-time (a)140 fs, (b)100 fs and (c)60 fs, the Hydrogen atoms density $0.01n_{cr}$ at t=250 fs.

References

[1] G. Varillon, J. M. Clarisse, A. Couairon, Phys. Rev. E. **103**, 023211 (2021).

[2] L. A. Gizzi, G. Cristoforetti, F. Baffigi, F. Brandi, G. D'Arrigo, A. Fazzi, L. Fulgentini, D. Giove, P. Koester, L. Labate, G. Maero, D. Palla, M. Romé, M. Russo, D. Terzani and P. Tomassini, Phys. Rev. Research **2**, 033451 (2020).

[3] S. Singh, R. Versaci, A. Laso Garcia, L. Morejon, A. Ferrari, M. Molodtsova, R. Schwengner, D. Kumar, and T. Cowan, Review of Scientific Instruments **89**, 085118 (2018).

[4] S. Barzegar, A. R. Niknam, Scientific Reports **8**, 11 (2021).

[5] T. Taguchi, T.M. Antonsen Jr., H.M. Milchberg, Phys. Rev. Lett. **92**, 205003 (2004).

[6] F. Brunel, Phys. Rev. Lett. **59**, 52 (1987).

[7] P.J. Catto, R.M. More, Phys. Fluids **20**, 704 (1977).

[8] W.L. Kruer, K. Estabrook, Phys. Fluids **28**, 430 (1985).

[9] J. T. Mendonca and F. Doveil, J. Plasma Phys. **28**, 485 (1982).

[10] Z. M. Sheng, K. Mima, Y. Sentoku, M. S. Jovanovic, T. Taguchi, J. Zhang, and J. Meyer-ter-Vehn, Phys. Rev. Lett. **88**, 055004 (2002).

[11] P. Zhang, N. Saleh, C. Chen, Z. M. Sheng, and D. Umstadter, Phys. Plasmas **10**, 2093 (2003).

[12] E. Khalilzadeh, J. Yazdanpanah, J. Jahanpanah, A. Chakhmachi and E. Yazdani, Phys. Plasmas **22**, 113115 (2015).

[13] E. Khalilzadeh, A. Chakhmachi and J. Yazdanpanah, *Plasma Phys. Control. Fusion* **59**, 125004 (2017).

[14] E. Khalilzadeh, A. Chakhmachi and J. Yazdanpanah, Optik **218**, 165249 (2020).

[15] E. Khalilzadeh, M. J. Jafari, & A. Chakhmachi, Physics of Plasmas, 28(7) (2021).

[16] W. Mori and T. Katsouleas, Phys. Rev. lett. **69**, 3495 (1992).

[17] D. Gordon, B. Hafizi, P. Sprangle, R. Hubbard, J. Penano, and W. Mori, Phys. Rev. E **64**, 046404 (2001).

[18] C. Schroeder, E. Esarey, C. Geddes, C. Toth, B. Shadwick, J. Van Tilborg, J. Faure, and W. Leemans, Physics of Plasmas **10**, 2039 (2003).

[19] J. Derouillat, A. Beck, F. Pérez, T. Vinci, M. Chiaramello, A. Grassi, M. Flé, G. Bouchard, I. Plotnikov, N. Aunai, J. Dargent, Computer Physics Communications **222**, 351 (2018).

[20] M. V. Ammosov, N. 8. Delone, and V. P. Kraino, Zh. Eksp. Teor. Fiz. **91**, 2008 (1986).

Electron acceleration by a Gaussian laser pulse in magnetoplasma (Paper ID: 1088)

M. R. Jafari Milani

Photonics and Quantum Technologies Research School, NSTRI, Tehran, Iran

Abstract

In this paper, electron acceleration by a circularly polarized Gaussian laser pulse in a magnetized plasma is investigated. The coupled differential equations of energy and motion of electrons are established and solved numerically. The variation of the magnetic field and plasma density effect on the electron acceleration for both right and left-handed circularly polarized laser pulse are studied. It is observed that the right-handed (RH) polarization causes an increase in the strength of the electron acceleration while the left-handed (LH) polarization causes a decrease in the strength of the electron acceleration in the magnetized plasma. It has been observed that the RH polarization is more suitable for higher energy gain. It is also found that for the RH (LH) polarization of the laser, increasing the magnetic field increases (decreases) the acceleration of the electrons. It was also shown that for a certain laser wavelength, electron acceleration occurs more easily in low plasma densities.

Keywords: electron acceleration, laser-plasma interaction, ponderomotive force.

Introduction

In recent decades, propagation of laser beam in plasma has received a lot of attention due to its many applications in nuclear fusion, plasma accelerators, X-ray lasers, THz radiation generation and the generation of high harmonics [1-4]. Because of the ionized state and nonlinear nature of plasma, it can sustain extremely high laser intensities. During high intensity laser pulse propagation through an underdense plasma numerous types of nonlinear process can be occurred due to the ponderomotive force effects. Acceleration of particles to high energies is one of the important aspects in the laser-plasma interaction, because the plasma medium has unique characteristics that can be used for acceleration [4]. The laser pulse can accelerate the electrons to high energies in many ways. It can cause ponderomotive acceleration [5]. In the intraction of laser pulse with an electron, the laser pressure in the ascending pulse front pushes forward electron on

its way and the pressure of radiation pushes the electron backward in the descending part of the pulse. As a result, the electron does not get net acceleration. However, if after being accelerated the electron leaves the interaction zone before being decelerated, it will have gained the energy. The magnetic field also has a key role in the acceleration of the electron in the plasma. The magnetic field can be self-generated or externally applied in laser-plasma acceleration. In case one utilizes a circularly polarized laser with intensity 19 W/cm^2, it can create axial magnetic field about 7 MG [6].

In this paper, the acceleration of electrons due to the axial ponderomotive force of the circularly polarized Gaussian laser pulse in a magnetized plasma has been studied. Calculating the energy gained by electrons in the laser field, the effect of magnetic field, plasma density and polarization state of laser (right and left-handed polarization) on the energy of electrons have been discussed.

Basic Equations

Assuming that a high-intensity laser pulse with a limited spot size with circular polarization is propagated in a magnetized plasma $B_0\hat{z}$ with density n_0 along the z axis, the laser field is defined as follows [7]:

$$\vec{E} = \left(\hat{x} \pm i\hat{y}\right) A\left(t - \frac{z}{\eta_g c}\right) \exp\left(-i\omega\left(t - \frac{\eta z}{c}\right)\right) \tag{1}$$

The upper sign (+) corresponds to right-handed (RH) polarization and the lower sign (-) corresponds to left-handed (LH) polarization. The amplitude of the Gaussian laser pulse is given as follows:

$$A^2 = A_0^2 \exp\left(-\frac{(t - \frac{z}{\eta_g c} - t_0)^2}{\tau^2}\right) \tag{2}$$

In the above equation, $\eta_g c = \eta c / (1 + \omega_p^2 \omega_c / 2\omega(\omega \mp \omega_c)^2)$ is the group velocity of the laser pulse [7], η is the plasma refractive index, m, e is the mass and electron charge, $\omega_p = 4\pi e^2 n_e / m_e$ is the

plasma frequency, τ is the pulse width, and $\omega_c = eB_0 / m_e c$ is the electron cyclotron frequency. Equation of electron motion in the presence of laser radiation field and external magnetic field B_0 is given below [7]:

$$\frac{dp_x}{dt} = -eE_x + \frac{ep_z B_y}{mc\gamma} - \frac{p_y \omega_c}{\gamma} \tag{3}$$

$$\frac{dp_y}{dt} = -eE_y - \frac{ep_z B_x}{mc\gamma} + \frac{p_x \omega_c}{\gamma} \tag{4}$$

$$\frac{dp_z}{dt} = -\frac{e(p_x B_y - p_y B_x)}{mc\gamma} \tag{5}$$

In the above equations, γ is the relativistic factor. By defining the electron momentum as $\vec{p} = (\hat{x} \pm i\hat{y})\, p_{0x} \exp[-\mathrm{i}\,\omega(\mathrm{t} - \mathrm{z}\,\eta / \mathrm{c})]$ and using it in Eq. (3), an equation for p_{0x} is obtained. Then, by using it in Eq. (5) and defining $P_z = p_z / m_e c$, the axial ponderomotive force is obtained as follows:

$$\vec{F}_{pz} = \frac{dp_z}{dt} = \frac{e^2 \eta \partial |\mathrm{A}^2| / \partial \mathrm{t}}{2m\gamma c[\omega(1 - \mathrm{P}_z \eta / \gamma) - \omega_c / \gamma]^2} \times \left[\left(1 - \frac{\mathrm{P}_z \eta}{\gamma}\right)^2 - \frac{\mathrm{P}_z \omega_c (1 - \eta_g \eta)}{\gamma^2 \eta_g \omega} \right] + \tag{6}$$

$$\frac{e^2 \left(1 - \frac{\mathrm{P}_z \eta}{\gamma}\right)^2 (1 - \eta_g \eta)}{2m\gamma c\omega\eta_g [\omega(1 - \mathrm{P}_z \eta / \gamma) - \omega_c / \gamma]} \frac{\partial |\mathrm{A}^2|}{\partial t} - \frac{e^2 \eta \omega_c \left(1 - \frac{\mathrm{P}_z \eta}{\gamma}\right) |\mathrm{A}^2|}{m\gamma^3 c[\omega(1 - \mathrm{P}_z \eta / \gamma) - \omega_c / \gamma]^3} \frac{d\gamma}{dt}.$$

Using the $d / dt = (\mathrm{p}_z / \mathrm{m}_e \gamma) d / dz$, the electric field of the laser pulse Eq. (1) and the corresponding magnetic field, and $Z = \omega z / c, \tau_1 = \omega\tau, \mathrm{T} = \omega \mathrm{t}, P_x = p_x / mc, P_y = p_y / mc,$ the set of equations (5)-(3) are rewritten as follows:

$$\frac{dP_x}{dZ} + \frac{\omega_c P_y}{\omega P_z} = -a \exp[-\mathrm{i}(\mathrm{T} - \mathrm{Z}\eta)] \times \left[\left(\frac{\gamma}{P_z} - \eta\right) + \frac{i(1 - \eta_g \eta)(T - \frac{Z}{\eta_g} - t_1)}{\eta_g \tau_1^2} \right], \tag{7}$$

$$\frac{dP_y}{dZ}-\frac{\omega_c P_x}{\omega P_z}=\mp a\exp[-\mathrm{i}(\mathrm{T}-\mathrm{Z}\eta)]\times\left[\mathrm{i}(\frac{\gamma}{P_z}-\eta)\mp\frac{i(1-\eta_g\eta)(T-\frac{Z}{\eta_g}-t_1)}{\eta_g\tau_1^2}\right], \tag{8}$$

$$\frac{dP_z}{dZ}=-\frac{a}{P_z}\exp[-\mathrm{i}(\mathrm{T}-\mathrm{Z}\eta)][P_x\pm iP_y]\times\left[\eta-\frac{i(1-\eta_g\eta)(T-\frac{Z}{\eta_g}-t_1)}{\eta_g\tau_1^2}\right], \tag{9}$$

$$\frac{dT}{dZ}=\frac{\gamma}{P_z} \tag{10}$$

Where $a=a_0\exp[-(T-\frac{Z}{\eta_g}-t_1)/2\tau_1^2],\ a_0=eA_0/m_ec\omega$.

Results and Discussion

Above equations depend on the electron density, spatial parameters of propagation and strength of magnetic field. These coupled equations were solved numerically using the fourth-order Runge-Kutta technique with initial conditions $P_z(0)=0.5, P_x(0)=P_y(0)=0, T(0)=0, \tau_1=30$, and γ variations which represents changes of the electron energy, were obtained. Figure (1) shows the γ parameter (electron energy) versus the dimensionless distance Z in the plasma, for two RH and LH polarizations. From Fig. (1), it can be seen that the energy obtained by electrons in RH polarization is much more than in LH polarization, and this means that electrons gain more acceleration in RH polarization.

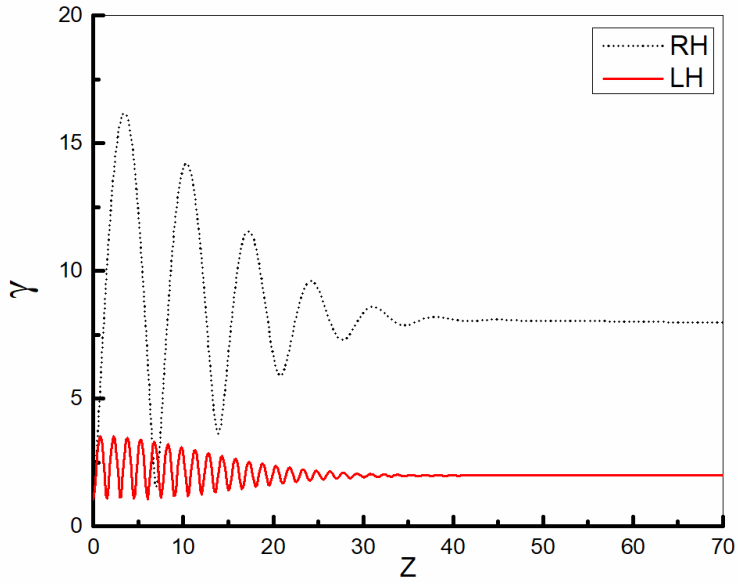

Fig. 1. Plot of γ vs Z for RH and LH polarization, $\omega/\omega_c = 2, \omega_p/\omega = 0.3, a_0 = 2.$

The reason is the intensification of the cyclotron motion of electrons in the laser field with RH polarization. Therefore, the state of polarization is very decisive for the acceleration of electrons with a laser.

Due to the laser field, the electrons experience a ponderomotive force and accelerate to higher energies. The applied magnetic field increases the amount of force $\vec{v} \times \vec{B}$ applied to the electrons and causes them to reach very high energies. As a result of the magnetic field, the laser transfers its energy to electrons through induced cyclotron resonance. In Fig. (2), the effect of plasma density (or plasma frequency) on the γ parameter for RH polarization is investigated. This figure shows that by increasing the plasma density, the value of γ, or the electron energy is decreased. Therefore, the increase in plasma density reduces the electron acceleration. In Fig. (3) the effect of ratio of laser frequency to electron cyclotron frequency ω/ω_c is investigated. Assuming constant laser frequency, Fig. (3) shows that in the case of RH polarization, decreasing ω/ω_c, or increasing the magnetic field causes more electron acceleration, while increasing the magnetic field for LH polarization decreases the electron acceleration. In RH polarization, a force is applied to the electrons and forces them to move in the direction of their cyclotron motion.

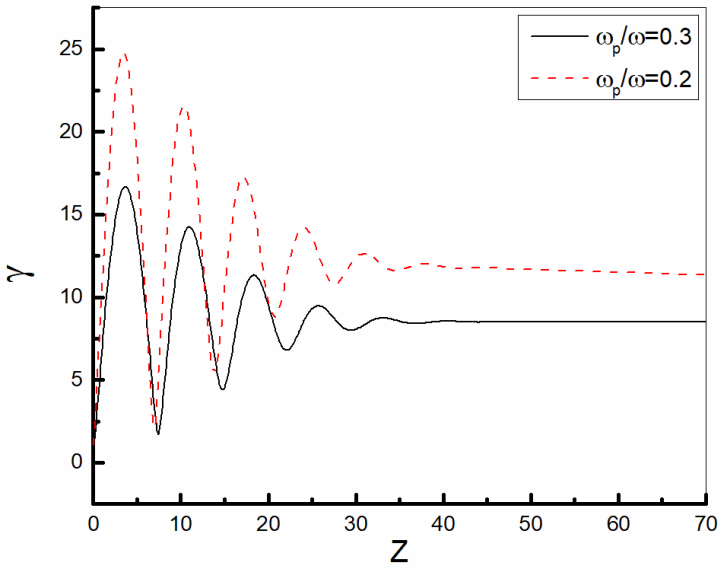

Fig. 2. Plot of γ vs Z for RH polarization, $\omega / \omega_c = 2,\ a_0 = 2.$

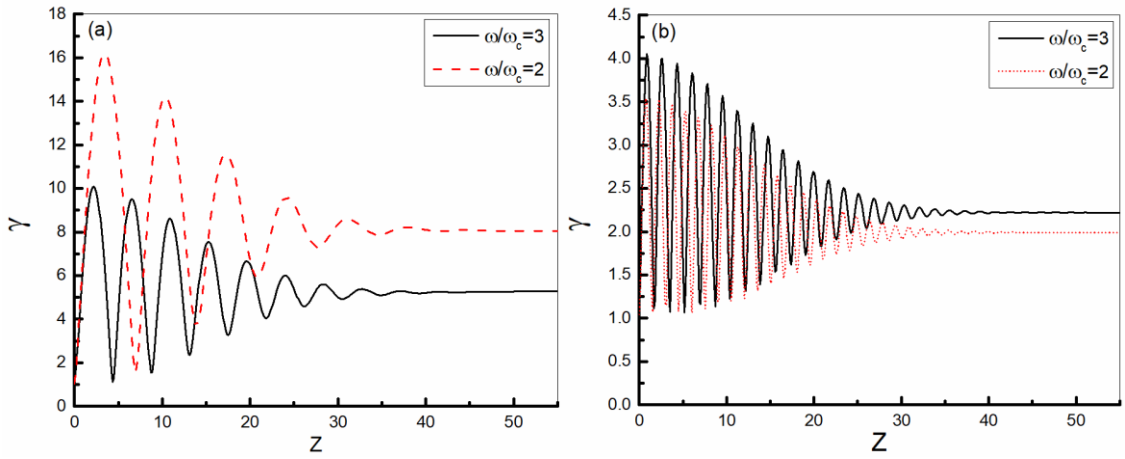

Fig. 3. Plot of γ vs Z for two different values of ω / ω_c (a) RH polarization and (b) LH polarization, $\omega_p / \omega = 0.3, a_0 = 2.$

In this state of polarization (RH), by increasing of the magnetic field strength, the transverse velocity of the electrons increases and leads to an increase the nonlinear current density in the plasma. While for LH polarization, the direction of the force applied to the electrons is opposite to

the direction of their cyclotron motion, and the transverse velocity of the electrons decreases with the increase of the magnetic field.

Conclusions

In this paper, electron acceleration in the magnetized plasma was investigated considering the nonlinear ponderomotive force of the Gaussian laser pulse. We obtained the coupled equations of motion and electron energy in the plasma and solved them numerically. It was shown that the state of polarization (Right-handed or Left-handed) of the Gaussian laser pulse plays an important role in the electron acceleration. In the magnetized plasma, for RH (LH) polarization of the laser, increasing the magnetic field causes an increase (decrease) in the acceleration of the electron. It was also shown that for a certain laser wavelength, electron acceleration occurs more easily in low plasma densities.

References

[1] H.Hora, Laser Part. Beams 27,207–22, ,(2009).

[2] P.ZHANG, J.T.HE, D.B.CHEN, Z.H.LI, Y.ZHANG, W. LAN, Phys. Rev. E 57, 3746–3752, (1998) .

[3] P. Sprangle, E. Esarey, A. Ting, and G. Joyce, Appl. Phys. Lett. 53, 2146–2148 (1988).

[4] A. Sharma and V. K. Tripathi, Phys. Plasmas 16, 043103 (2009).

[5] V. Sazegari, M. Mirzaie, and B. Shokri, Phys. Plasmas 13, 033102, (2006).

[6] Z. Najmudin, M. Tatarakis, A. Pukhov, E. L. Clark, A. E. Dangor, J. Faure, V. Malka, D. Neely, M. I. K. Santala, and K. Krushelnick, Phys. Rev. Lett. 87, 215004, (2001).

[7] X. Xia, B. Xu, L. Wang, Optik, 127, (2016).

Formation of Cr1.2Ni0.8Zr and Zr(Cr0.25Fe0.75)2 Composites by Using the Ion Beam Irradiation of Plasma Focus Device (Paper ID: 1094)

Amir Raeisdana[*1], Chapar Rasouli[1], Ehsan Noori[1], Alireza Aslezaeem[1], Mir Mohammad Reza Seyedhabashi[1]

[1]Plasma and Nuclear Fusion Research School, Nuclear Science and Technology Research Institute, Atomic Energy Organization of Iran, Tehran, Iran

araeisdana@aeoi.org.ir

Abstract

Improvement of zirconium properties by chromium and nitrogen implantation is ideal to protect the nuclear fuel rods against corrosion and secondary hydrogenation. Metallic chromium (Cr) has attracted attention as a potential coating material on zirconium alloys, to limit external cladding corrosion. In this research, high energy plasma focus device was used to plant the chromium and nitrogen ions in the zirconium substrate. Nine zirconium samples in 2cm×1cm dimensions with 1mm thickness were located at a distance of 20cm from the place where the pinch is formed. The experiments are carried out in 1.2 mbar of the nitrogen gas pressure and 17 kV of the charging voltage. Fe-Cr (85% , 15%) disc and Ni-Cr (70% , 30%) pills were installed on the anode head for sputtering of the chromium and deposition on the zirconium substrate. When the pinch plasma column decays due to various instabilities, intense and high-energy N_2 ions are accelerated towards the zirconium substrate also sputtered Cr is deposited on the substrate. XRD and XRF analysis were used to study the structural properties of the samples. XRF analysis indicates 87.81% of Zr, 3.70% of Ni, 2.09% of Cr and 1.75% of Fe in the surface of the sample. XRD spectra shows the formation of ZrN, $Cr_{1.2}Ni_{0.8}Zr$ and $Zr(Cr_{0.25}Fe_{0.75})_2$ Composites after ion implantation.

Key Words: Cr deposition on Zr, Cr-Zr-Ni-Fe Composites, Plasma Focus Device, XRD Analysis, XRF Analysis

Introduction

The plasma focus (PF) is being employed for thin film deposition because it has attractive features for deposition purposes such as: (a) deposition is done by the energetic ions and hence will be a resistant deposition, (b) deposition rate is high, (c) film adhesions to the substrate surface is generally good, (d) deposition with the different background gases is allowed and (e) deposition

on the substrate materials at the room temperature. Many experiments have been carried out based on the dense plasma focus (DPF) deposition and implantation [1] [2] [3] [4] [5].

I. A. Khan et al presented the possibility of the DPF based zirconium nitride films deposition on zirconium substrate [6]. Their characterizations were ion doses and angular position of the samples [6]. They observed zirconium nitride phases (ZrN, Zr_2N and Zr_3N_4) on zirconium substrate. The XRD spectra demonstrated that the crystallinity of zirconium nitride in the deposited film increases by increasing the nitrogen ion dose and decreases by increasing the angular position [6].

S. Javadi et al used a 1.6 kJ PF device for the synthesis of chromium films on Si(400) substrates [8]. They considered various numbers of focus shots at 0◦ angular position and at the distance of 8 cm from the top end of the anode. The XRD results showed that the intensity of Cr diffraction peaks increases with increasing the number of focus shots from 15 to 25. Their experiments demonstrated the degree of crystallinity of chromium film is decreased for the sample exposed to 35 shots [8]. AFM and SEM images presented a two-stage variation pattern for the sizes of the particles distributed on the film surface by increasing the focus shots from 15 to 25 and then to 35 [8].

Experimental Setup

The 115kJ dense plasma focus device is used for the experiments. This device has been made in the inverse structure and the direction of the anode and cathode is downward (Figure 7). This structure leads to sputtering from the anode head materials and deposition to the substrate. Fe-Cr (85% - 15%) alloy with 5cm of diameter is installed on the anode head (Figure 8). Ni-Cr (70% , 30%) pills are installed on the Fe-Cr disc for increasing in Cr deposition (Figure 9). The experiments were performed with 135 shots by using the nitrogen gas at the pressure of 1.2 mbar. The capacitors are charged up to V=17 kV (E=20.8 kJ). Nine zirconium substrates in the dimension of 2cm×1cm are installed on the feedthrough (Figure 10) 20cm away from the anode head. The chamber is vacuumed up to 10^{-2} mbar then the nitrogen gas is injected to the chamber up to optimized pressure (1.2 mbar). The nitrogen filling gas is vacuumed after 5 shots and fresh gas is

injected. The high voltage probe, Rogowski coli and NE-102 plastic scintillator are the diagnostic systems (Figure 11).

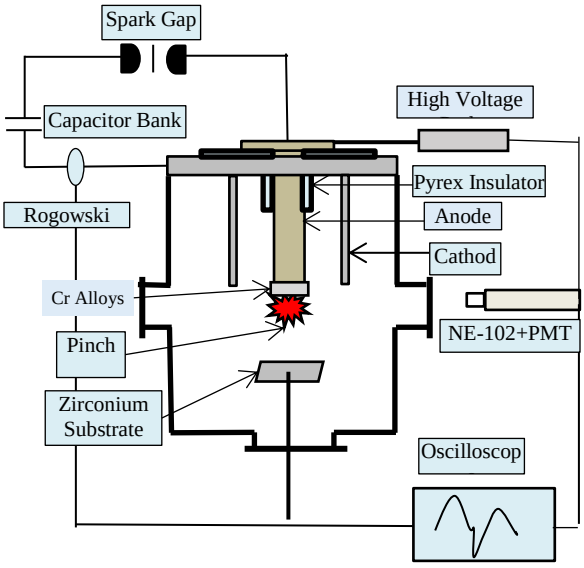

Figure 7 . Experimental setup for Cr and N implantation in the Zr

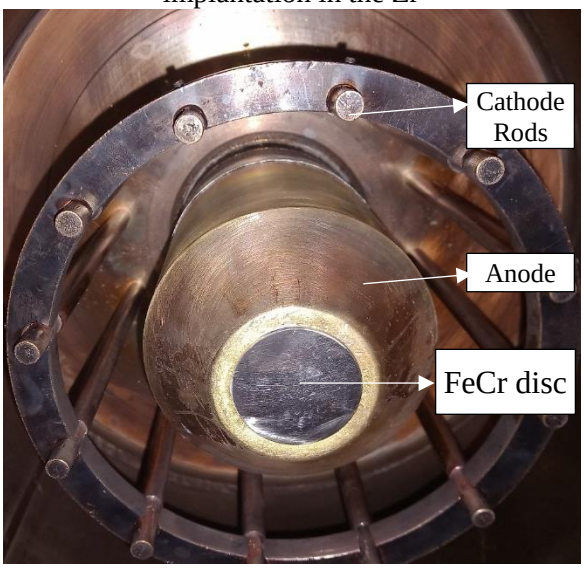

Figure 8. View from bottom to top. FeCr alloy disc was installed on the anode head

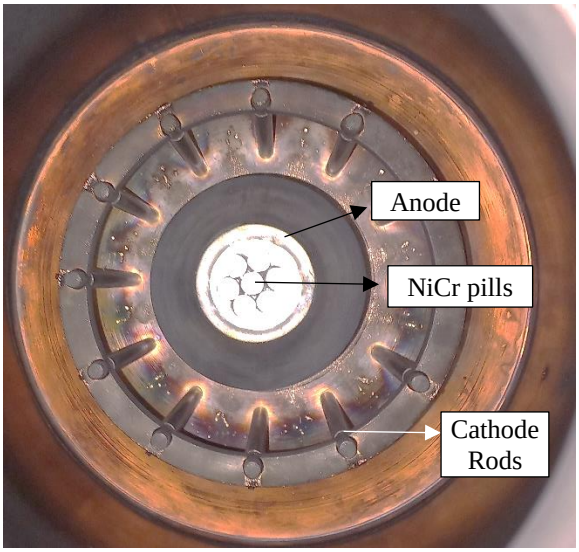

Figure 9. View from bottom to top. NiCr alloy pills were installed on the anode head

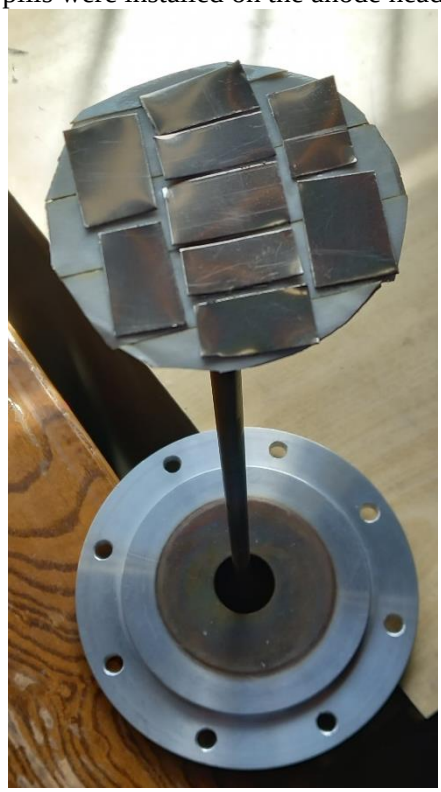

Figure 10. Nine Zr substrates were installed on the feedthroug

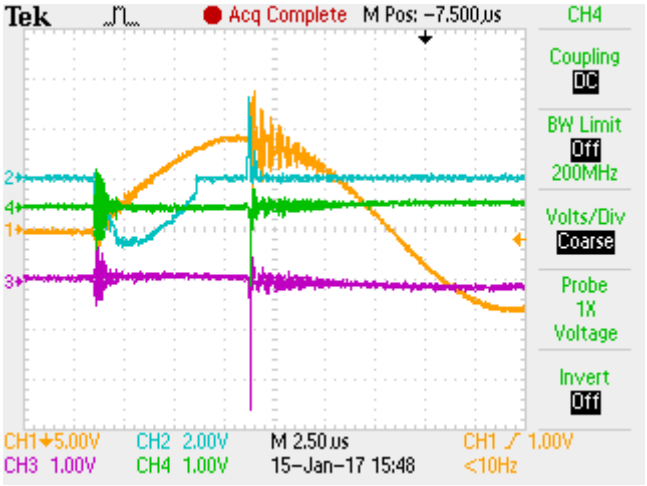

Figure 11. Chanel 1: current, Chanel 2: current derivative, Chanel 3: Plastic scintillator signal and Chanel 4: High Voltage probe.

Results and Discussion

XRF analysis indicates 2.09 % of Cr deposition on the zirconium substrate (Table 5). Ni and Fe deposition is seen in the sample due to the composite of alloys that installed on the anode head. Using of the pure chromium leads to the high deposition of Cr on the Zr substrate and eliminate the other elements.

Table 5. XRF analysis indicates Cr, Ni, Fe, Al and Zn elements in the sample

Analyte	Concentration %
Zr	87.81
Ni	3.70
Cr	2.09
Fe	1.75
Al	1.42
Zn	1.04
Other Elements	2.19

XRD analysis was used to study the structural properties of the samples. Table 6 shows the visible composites in the XRD pattern. In addition to the zirconium, composites of zirconium with nitrogen, chromium, iron and nickel are observed.

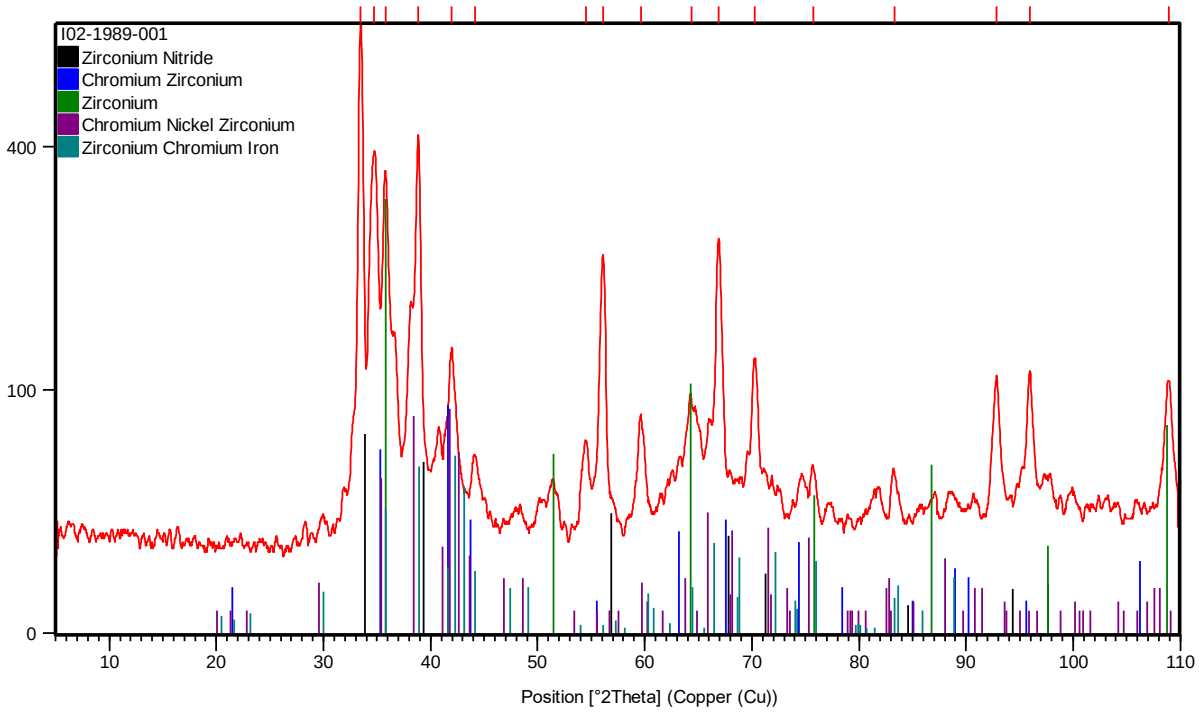

Figure 12 shows the general XRD pattern of the substrate with all observable composites. $Cr_{1.2}Ni_{0.8}Zr$ and $Zr(Cr_{0.25}Fe_{0.75})_2$ composites are observed in the

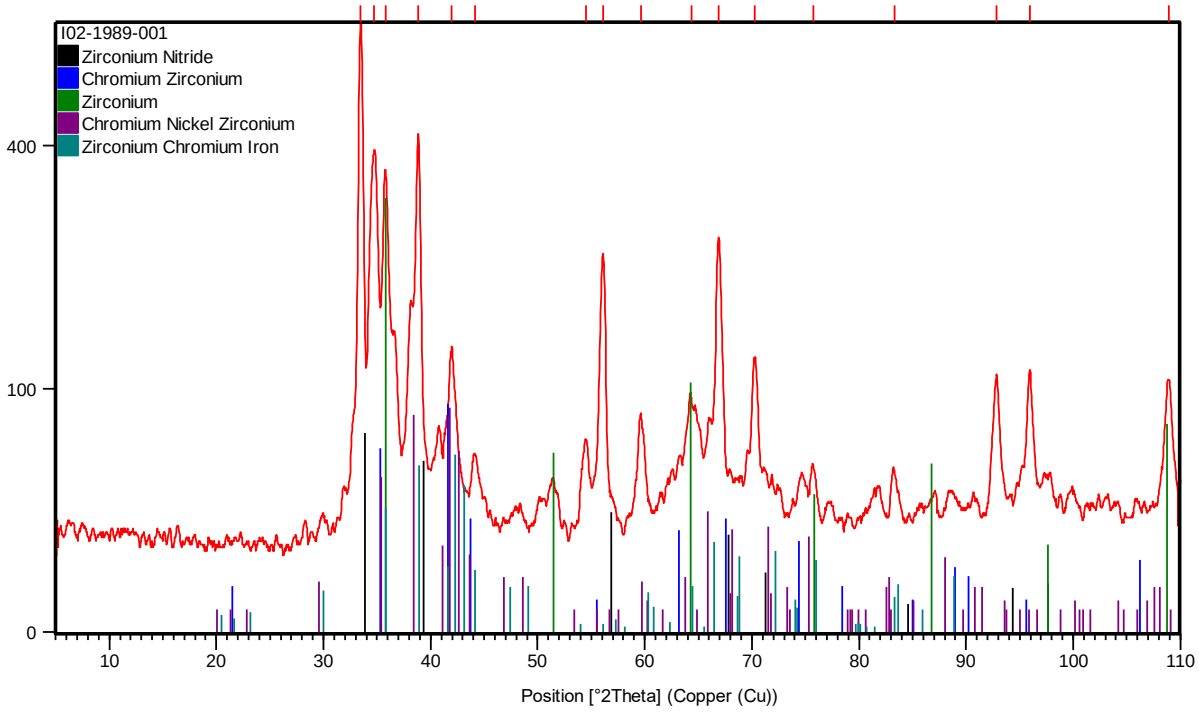

Figure 12. Figure 13, Figure 14 and Figure 15 show the reference XRD pattern of CrFeZr (reference code 01-085-2330), CrNiZr (reference code 00-048-1309) and ZrN (reference code 00-035-0753) in comparing with the sample main graph. These graphs demonstrate the formation of $Cr_{1.2}Ni_{0.8}Zr$, Zr $(Cr_{0.25}Fe_{0.75})_2$ and ZrN in the substrate.

Table 6. Visible peaks in the XRD spectra

Visible	Ref. Code	Compound Name	Chemical Formula
*	00-035-0753	Zirconium Nitride	Zr N
*	00-034-0657	Zirconium	Zr
*	00-048-1309	Chromium Nickel Zirconium	$Cr_{1.2}Ni_{0.8}Zr$
*	01-085-2330	Zirconium Chromium Iron	Zr $(Cr_{0.25}Fe_{0.75})_2$

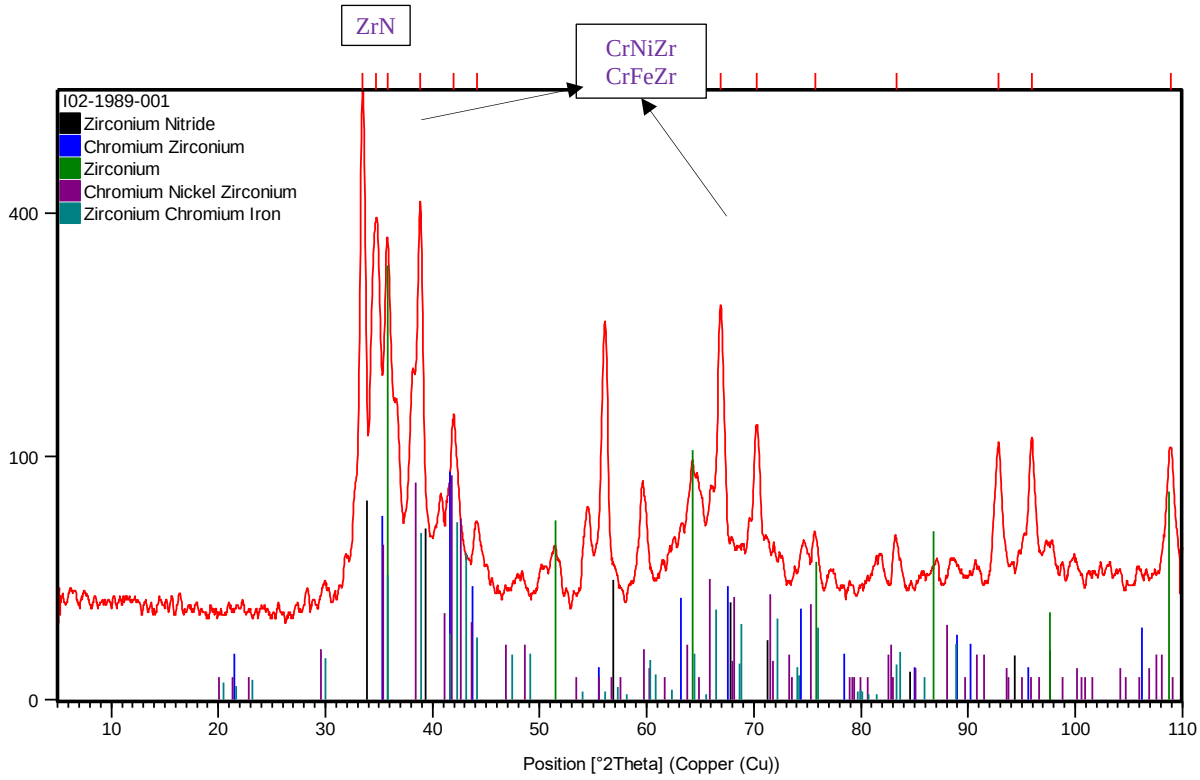

Figure 12. XRD spectra of Zr substrate irradiated by Cr and N_2 ions. Visible composites are seen in the graph.

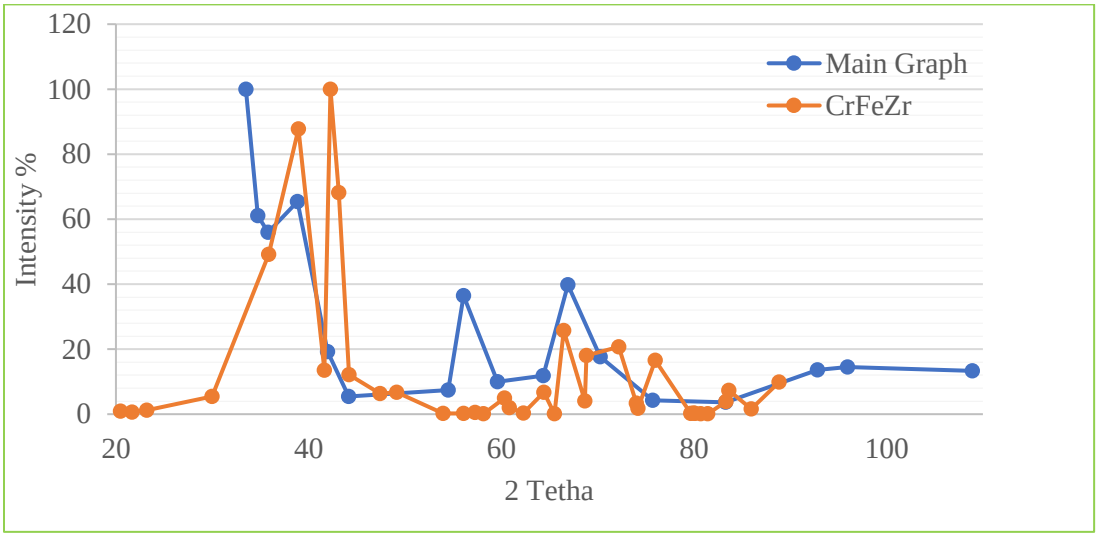

Figure 13. XRD pattern of the sample (main graph) is compared with the CrFeZr reference pattern. CrFeZr composite is seen in 2θ = 38.945° and 66.49°.

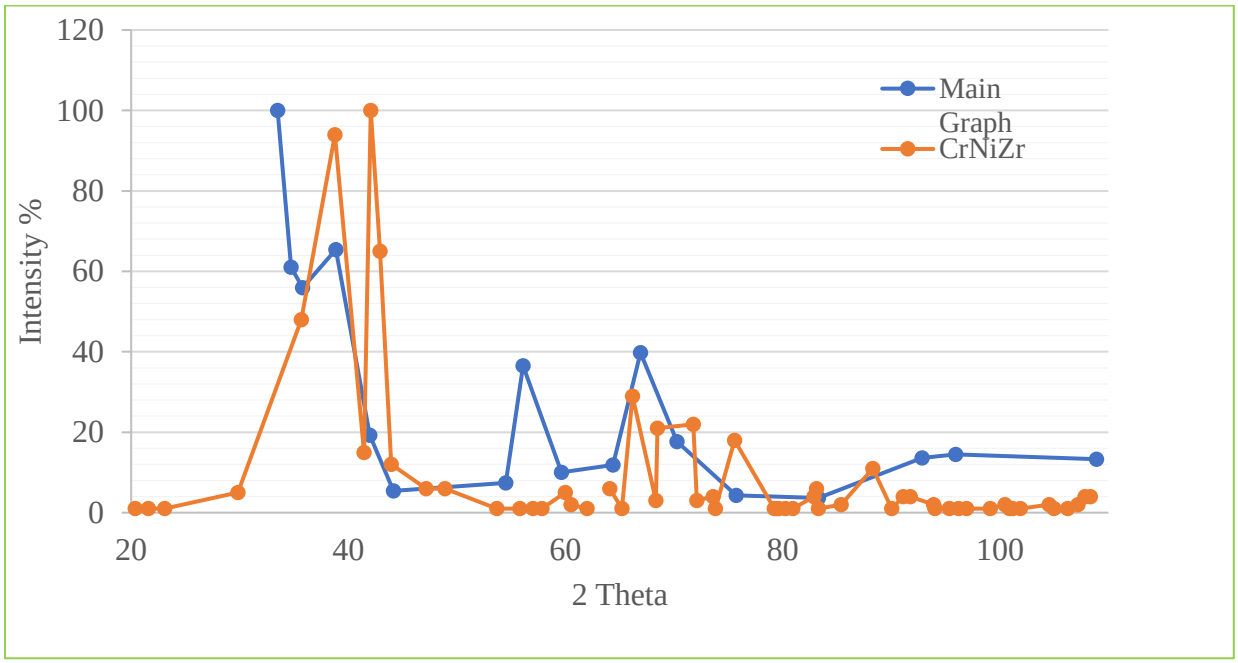

Figure 14. XRD pattern of the sample (main graph) is compared with the CrNiZr reference pattern. CrNiZr composite is seen in 2θ = 38.749° and 66.176°.

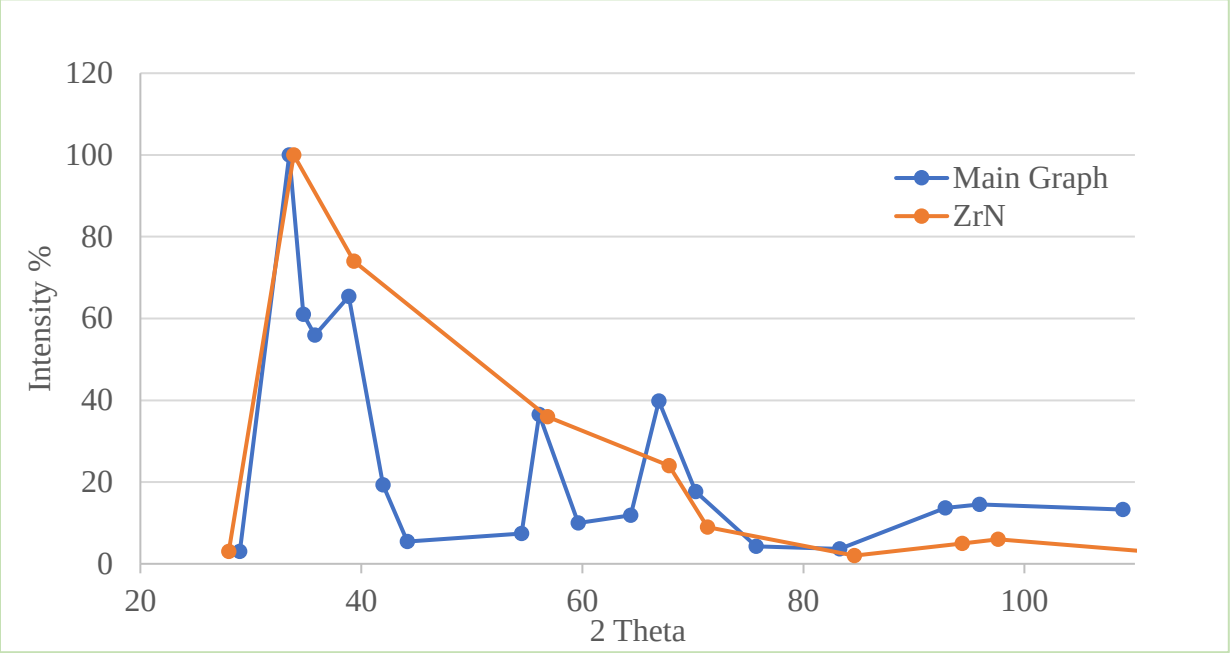

Figure 15. XRD pattern of the sample (main graph) is compared with the ZrN reference pattern. ZrN composite is seen in 2θ = 33.89°, 39.329°, 56.835° and 67.852

CrFeZr peaks overlap in 2θ = 38.945° and 66.909° with the main graph. Main overlap occurs in 2θ = 38.945° (Figure 13). CrNiZr peaks overlap in 2θ = 38.749° and 66.176° with the main graph. Main overlap occurs in 2θ = 38.749° (Figure 14). Reference XRD spectra of ZrN fit to the main graph of sample in the Figure 15. This curve indicates overlap in 2θ = 33.89°, 39.329°, 56.835° and 67.852 that main overlap is observed in 2θ = 33.89°.

Conclusion

A dense plasma focus device is applied to deposit the chromium and nitrogen thin films on the zirconium substrates at the room temperature. This device emits high-energy ions of 10 keV-1 MeV and with a flux of 10^{16} ions/cm^2 in each shot [9] [10] [11] toward the target so it is attractive for deposition on the substrate materials at the room temperature. Chromium alloys were installed on the anode head as a disc and pills. 135 shots were carried out by using the nitrogen filling gas. XRD spectra indicates nitrogen implantation and chromium deposition on the Zr substrate successfully. XRD spectra shows the formation of $Cr_{1.2}Ni_{0.8}Zr$ and $Zr(Cr_{0.25}Fe_{0.75})_2$ Composites at 2θ = 38.7° and the ZrN composite at 2θ = 33.89° . The use of pure chromium on the anode head will certainly eliminate the iron and nickel deposits on the zirconium substrate.

References

[1] M. Shirazi and e. al, "Plasma focus method for growth of molybdenum nitride thin films: Synthesis and thin film characterization," *Journal of Alloys and Compounds* , vol. 727, pp. 978-985, 2017 .

[2] M. Hassan and e. al, "Dense plasma focus ion-based titanium nitride coating on titanium," *Nuclear Instruments and Methods in Physics Research B* , vol. 267, p. 1911–1917, 2009.

[3] I. Khan and e. al, "Synthesis of nano-crystalline zirconium aluminium oxynitride (ZrAlON) composite films by dense plasma Focus device," *Applied Surface Science* , vol. 255, p. 6132–6140, 2009.

[4] M. Sadiq and e. al, "Enhanced Crystallinity of PTFE by Ion Irradiation in a Dense Plasma Focus," *Plasma Processes and Polymers,* vol. 4, p. 186–191, 2007.

[5] R. S. Rawat and e. al, "Room temperature deposition of titanium carbide thin films using dense plasma focus device," *Surface and Coatings Technology,* vol. 138, pp. 159-165, 2001.

[6] I. A. Khan and e. al, "Nitridation of zirconium using energetic ions from plasma focus device," *Thin Solid Films,* vol. 516, p. 8255–8263, 2008.

[7] A. Ryabchikov and e. al, "High-intensity chromium ion implantation into Zr-1Nb alloy," *Surface and Coatings Technology,* vol. 383, p. doi.org/10.1016/j.surfcoat.2019.125272, 2020.

[8] S. Javadi and e. al, "Investigation of structural properties of chromium thin films prepared by a plasma focus device," *PHYSICA SCRIPTA*, vol. 86, pp. doi:10.1088/0031-8949/86/02/025801, 2012.

[9] H. Bhuyan and e. al, "Ion beam emission in a low energy plasma focus device operating with methane," *J. Phys. D: Appl. Phys.,* vol. 38, p. 1164–1169, 2005.

[10] V. Damideh and e. al, "Fast Faraday cup for fast ion beam TOF measurements in deuterium filled plasma focus device and correlation with Lee model ," , vol. 24, pp. doi: 10.1063/1.4985309, 2017.," *PHYSICS OF PLASMAS,* vol. 24, p. doi: 10.1063/1.4985309, 2017.

[11] J. Moreno and e. al, "Measurements of ions emission using ToF method and CR39 SSNTD in a Small Plasma Focus device of Hundreds of Joules," *Journal of Physics: Conference Series 511,* vol. 511, pp. doi:10.1088/1742-6596, 2010.

Calculations of energy and ion beam current range necessary for the IR-DD105-M1 neutron generator to reach the yield of 105 n/s (Paper ID: 1111)

Morteza Sedaghat Movahhed[1], Alireza Aslezaeem[1*], Ali Bagheri[1], Emad Rezaei[1]

Plasma and Nuclear Fusion Research school, Nuclear Science and Technology Research Institute, Tehran -Iran

Abstract

Various applications of fusion based neutron generators such as boron neutron capture therapy and neutron activation analysis are being developed at the nuclear science and technology research institute. In this paper calculations for energy and ion current range required for 10^5 n/s in IR-DD105-M1 neutron generator which is under construction are performed. Due to high hydrogen absorption and metal hydride formation characteristic of Titanium, this metal has been selected as the target and the stopping power of deuterium ions are calculated with SRIM software. Based on the experimental data and theory a new formula with high accuracy for the D-D reaction cross sections is employed. Then the necessary voltage and current to reach 10^5 n/s is determined.

Keywords: Neutron generator, IR-DD105-M1, Nuclear fusion, Titanium, Neutron yield

Introduction

After the discovery of neutron many studies have been performed and variety of applications such as neutron radiography, neutron activation analysis, short-lived radioisotopes and explosive materials detection gradually emerged. Therefore, is opening new areas of research and developments in various technical fields e.g. aeronautics, defense industries, medicine, semi-conductor devices and so one. Generally, fission reactors and radioactive-based sources have been used as the neutron generator however, fusion base neutron generators are more attractive due to lower coast of constructions maintains and possessing lower physical dimensions that make it easy to be used in industries. In addition, they do not require nuclear materials as fuel and therefore lower security considerations are needed for them.

Despite radio isotopic neutron sources do not have the problems of lagged sized fission reactors, the have relatively low neutron flux which may not satisfy some specific solutions. Also, there are always emitting neutrons during their life time and they could not be turned-off or turned-on

immediate decisions. Therefore, they must always be placed inside a radiation shield for radiation protection standards. On the other hand, neutron generators based on nuclear fusion do not have such problems of the other methods. For example, the cost of their design and construction is much lower than the fission reactors. Due to their small size, it is possible to install and operate them in different places. they do not have nuclear waste and the required fuel is found in abundance in nature. Also, it is very easy to control the neutron flux produced by them, and by cutting off their feeding system, the whole process is turned off and neutron emission is stopped. According to the mentioned advantages, neutron production methods based on nuclear fusion are one of the bests, and many researches have been conducted on them in the world and various samples are constructed. Neutron generating devices based on accelerator and fusion are one of the best methods for stable and reliable neutron production. These types of generators have the ability to work in both continuous and pulse modes, their structure is a bit more complicated, however, their control is much easier. For this reason, prominent commercial companies in the field of producing neutron generators mostly use this type of generators to produce neutrons. In thisarticle calculations based on the experimental sufion database and the SRIM code has been used to obtain the nessecary deutron beam energy and current to reach 105 n/s as the optimum condition.

Research Theories

In neutron generator, nuclear fusion reaction takes place due to impact of energetic deuterium ion beam with a solid target. Neutron yield could be calculated as the following in case of thin target assumption where the ion beam energy does not change during the penetration:

$$(E) = N_{in}.\frac{N_{imp}.\sigma_E}{A} \qquad (1)$$

Where N_{in} is the number of deuterium ions impinging on the target surface in one second

N_{imp} is the total number on deuterium inside the target volume

σ is the fusion cross section reaction of $D(D,n)\,^3He$

A is the ion beam surface area on the target.

But in case of thick target assumption the ion beam energy decreases during the penetration therefore it is easier to devid the target thickness into several differential ones where the thin target assumption is valid in each section. Therefore, it is possible to write the neutron yield formula as the following for a beam current I_0 and initial energy of E_0:

$$Y(E) = \frac{I_0}{e}.\sum \frac{AR.N_T.A.dx_i.\sigma_{E_i}}{A} = I_0.\frac{AR.N_T}{e}.\sum dx_i.\sigma_{E_i}$$
$$\Rightarrow Y(E) = I_0.\frac{AR.N_T}{e}.\int_0^{E_0} \frac{\sigma_E}{\left(\frac{-dE}{dx}\right)_E} dE \qquad (2)$$

In which N_T is the target density

AR is the atomic fraction of deuterium inside the target

$\frac{dE}{dx}$ is the stopping power of ion beam inside the target which is assumed to be loaded with deuterium atoms.

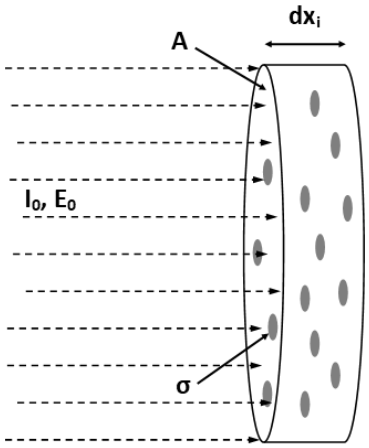

Fig.1.Differential thin sector view of the target

Finally necessary ion beam current for reaching 10^5 n/s yield could be written as the following formula:

$$I_0 = \frac{10^5}{\frac{AR.N_T}{e}.\int_0^{E_0} \frac{\sigma_E}{\left(\frac{-dE}{dx}\right)_E} dE} \qquad (3)$$

Therefore, it is possible to calculate the exact neutron yield in a beam target reaction for a known initial energy, stopping power and fusion cross section reaction to reach the specific yield of 10^5 n/s.

Calculations of fusion cross section reactions:

In D-D nuclear fusion analyses, the fusion cross section σ plays the most important roll. This quantity determines the nuclear reaction probabilities for impact of two nuclides. For a D-D reaction there are two reaction channels in which just one of them ($^2_1D + ^2_1D \rightarrow ^3_2He + ^1_0n$) ends in the neutron production. For reaction cross section of two light nuclides, it is possible to write it as the following:

$$\sigma(E_{lab}) = -16389 \times C_3 \left(1 + \frac{m_a}{m_b}\right)^2 \times \left[m_a E_{lab} \left[EXP\left(31.40 Z_1 Z_2 \sqrt{\frac{m_a}{E_{lab}}} \right) - 1 \right] \left\{ (C_1 + C_2 E_{lab})^2 + \left(C_3 - \frac{2\pi}{\left[Exp\left(31.40 Z_1 Z_2 \sqrt{\frac{m_a}{E_{lab}}} \right) - 1 \right]} \right)^2 \right\} \right]^{-1} \quad (4)$$

M_a and m_b represent the molecular mass of the target and incident beam and Z_1, Z_2 represent the atomic numbers of the target and incident beam. Here m_a=m_b=1 and Z_1=Z_2 =1

C_1, C_2 and C_3 are constant parameters that are defined in table.1. as the following:

Table1. Triple coeficents for D-D fusion cross section formula

C_1	**-60.2641**
C_2	**0.05066**
C_3	**-54.9932**

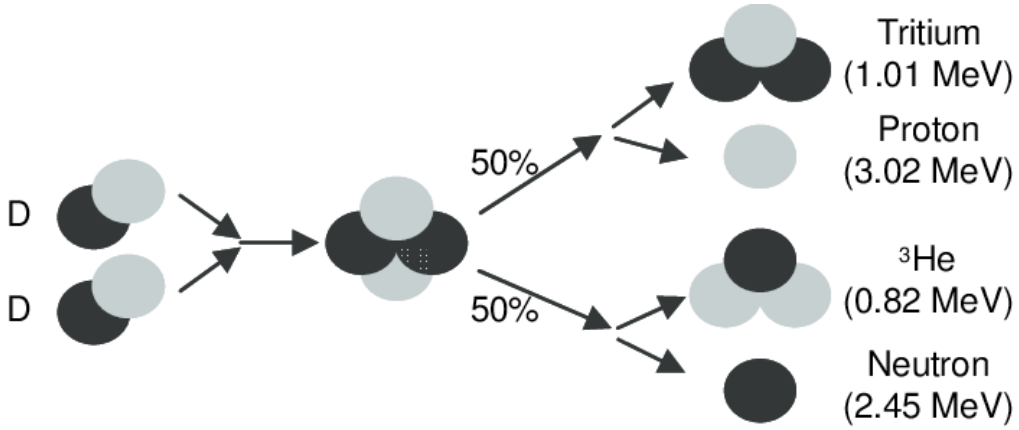

Fig.2. D-D nuclear fusion reaction

As is viewed from Fig.2. 50 percent of the D-D reactions related to the $D + D(p + T\ and\ n + {}^{3}He)$ which is representative of neutron production. Therefore, to draw on more to the reality for the fusion cross section of the mention channel a coefficient equal to 0.5 must be multiply the formula. To verify the equation.4 ENDF/B-VI from national nuclear data center has been used. As is observable on Fig.3 the errors are between 14 to 27 percent. To reduce these errors a second order equation was used to modify the final reaction cross section formula as the following:

$$\sigma(E_{lab}) = -0.5 \times \left(-1.66 \times 10^{-6} E_{lab}^{2} + 1.4 \times 10^{-3} E_{lab} + 0.8\right) \times 16389 \times 4C_3 \times \left[2E_{lab}\left[EXP\left(31.40\sqrt{\frac{2}{E_{lab}}}\right) - 1\right]\left\{(C_1 + C_2 E_{lab})^2 + \left(C_3 - \frac{2\pi}{\left[Exp\left(31.40\sqrt{\frac{2}{E_{lab}}}\right) - 1\right]}\right)^2\right\}\right]^{-1} \quad (5)$$

Data from equation (5) and ENDF/B-IV and the errors are depicted on Fig.4. Here the errors are reduced to less than 2.28 percent.

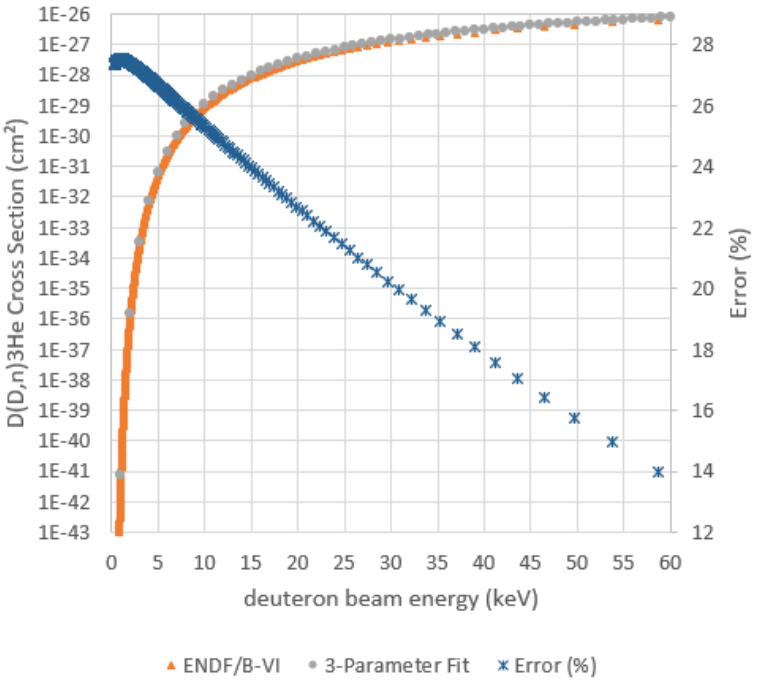

Fig.3. Obtained results of the D-D fusion cross section from equatio4 vs. ENDF/B-VI data and the errors

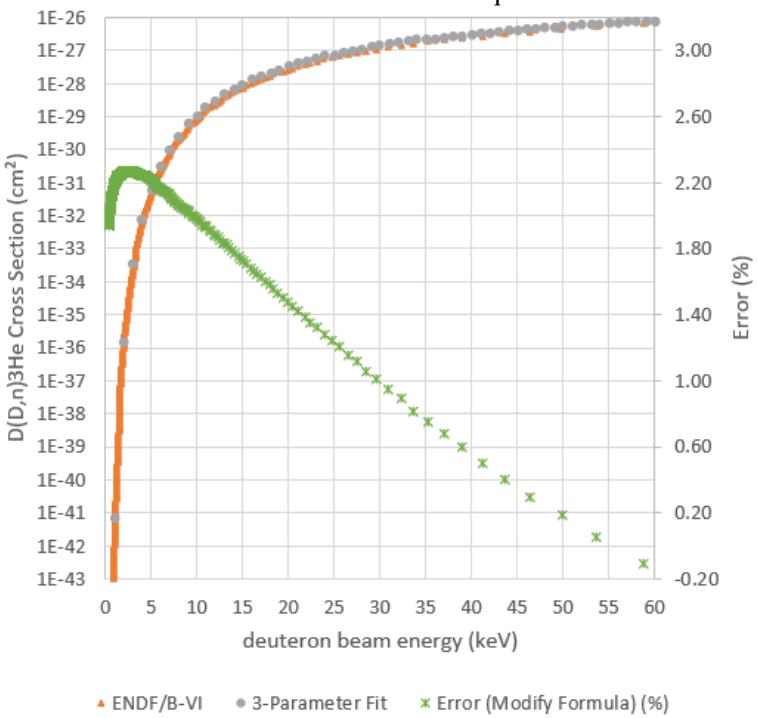

Fig.4. Obtained results of the D-D fusion cross section for equation 5 vs. ENDF/B-VI data and the errors

Stopping power of deuterium in titanium target

Another important factor for the neutron yield depends on the target capacity to retinting deuterium atoms particularly at the beginning of the beam target reaction proses while the target is not saturated, as well as the stopping power of the target for the incoming ion beam. The lower the stopping power the lower the power is loosed for the ion beam and vice versa. Since the Titanium could make metallic hydride then it is a good chois for obtaining the D-D target for neutron generators. Due to low atomic number, it has relatively lower stopping power in comparison with other metals with high atomic number. In addition, Titanium has high hydrogen to metal ration (AR) with respect to other metals. This ratio could reach to AR=2. Therefore Titanium is recognized as the most efficient metal for the neutron generation target. SRIM code has been used for the stopping power of deuterium ions in the Titanium target in the energy rang of 1 to 60keV.

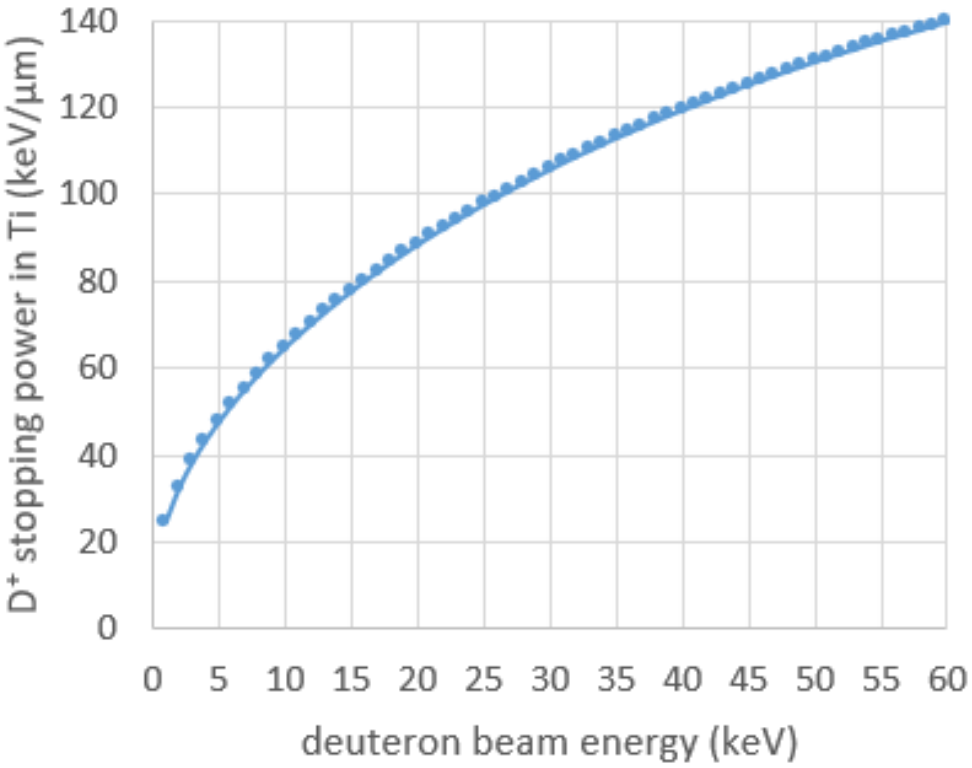

Fig.5. Stopping power of deuterium ions inside the Titanium target

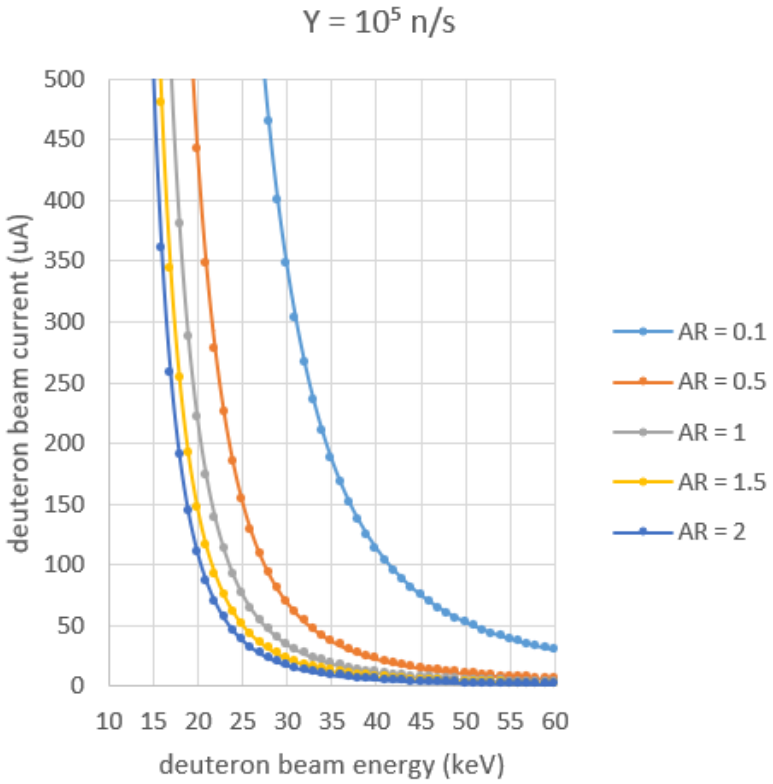

Fig.6. Necessary deuteron beam current and energy for deuterium target to reach the 105 n/s yield

Results and Discussion

Substituting the obtained formulas for the stopping power and the $D(D,n)\ ^3He$ fusion cross section reaction in the equation 5 the ion beam and energy necessary for the 10^5 n/s as a function of different AR ratios are calculated and depicted on Fig.6. As is obvious, in the worst-case scenario (AR=0.1) 10^5 n/s is reachable for the energy and ion current range of 27 to 60 keV/500 µA.

It should be noted that, even though the energy and current reduction ends in lowering the power consumption and simplified construction of ion source, the time needed for the target saturation becomes longer and makes it more difficult due to requirement of higher voltage power supply and insulation problems as lowering the ion beam current. On the other hand, reducing the voltage and increasing the current increase the power consumption of the ion source and therefore ends in more complicated ion source construction even though it lowers the saturation time and requiring simplified high voltage power supply as well as the simpler insulation considerations. Therefore, based on the limitations for IR-DD105-M1 considerations such as ion source, power supply,

cooling system, dimension of the device and the total cost, the optimized situation for the voltage and beam current in the studied ranges should be selected.

Conclusions

In this paper the required ion current and voltage reneges to achieve 10^5 n/s for the IRDD105 neutron generator was calculated. At firs a relationship between the ion-beam current and voltage to reach 10^5 n/s has been calculated. Then a three parameter formula has been used as the fusion reaction cross section of D(D,n) ^{3}He reaction and the errors are compared to ENDF/B-VI nuclear data. Because of 14 to 28 percent errors, a corrected formula is proposed to reduce the errors lower than 2.3 percent. SRIM code has been used to calculate the deuterium ion beam stopping power inside the Titanium metal as the target. After replacement of the formulas, the ion-voltage diagrams are depicted for different atomic ratios. In the end, the energy and ion current necessary to achieve 10^5 neutron/s for the IR DD105-M1 neutron generator facility calculated to be 27 keV/500µA to 60keV/30µA range.

References

[1] Adams, R., Bort, L., Zboray, R., et al. (2015). Development and characterization of a D-D fast neutron generator for imaging applications. Applied Radiation and Isotopes. 96:114–121.

[2] Bergaoui, K., Reguigui, N., Gary, C.K. et al. (2015). Prompt gamma-ray neutron activation analysis of boron using Deuterium–Deuterium (D–D) neutron generator. Radioanalytical and Nuclear Chemistry. 303:115–121.

[3] Jaakko H. Vainionpaa, Allan X. Chen, Melvin A. Piestrup, Charles K. Gary, Glenn Jones, Richard H. Pantell. (2015). Development of high flux thermal neutron generator for neutron activation analysis, Nuclear Instruments and Methods in Physics Research Section B: Beam Interactions with Materials and Atoms. 350:88-93.

[4] Gierlik, M., Borsuk, S., Guzik, Z. (2016). Swan - Detection of explosives by means of fast neutron activation analysis. Nuclear Instruments and Methods in Physics Research Section A: Accelerators, Spectrometers, Detectors and Associated Equipment. 834:16–23.

[5] Xing Z. Li, Qing M. Wei, Bin Liu. (2008). A new simple formula for fusion cross-sections of light nuclei. Nuclear Fusion. 48(12):125003.

[6] https://www-nds.iaea.org/exfor/

ICNST 2024
International Conference on Nuclear Science and Technology
6- 8 MAY 2024 | Isfahan, Iran

Comparison of Photoluminescence and Positron Annihilation Spectroscopy in Annealed Tungsten Characterization (Paper ID: 1113)

Torabi M.[1*], Kakuee O.[2], Sobhanian S.[3], Biganeh A.[2], Kouhi M.[4], vafaei R. [5]

[1] *Department of physics, Islamic Azad University, West Branch, Tehran, Iran*

[2] *Physics and Accelerators Research School, Nuclear Science and Technology Research Institute, P.O. Box 14395-836, Tehran, Iran*

[3] *Department of Atomic and Molecular Physics, University of Tabriz, Tabriz, Iran*

[4] *Department of physics, Islamic Azad University, Tabriz Branch, Tabriz, Iran*

[5] *Department of physics, Islamic Azad University, Shahindezh Branch, Tabriz, Iran*

Abstract

Positron Annihilation Spectroscopy (PAS) is a well-established technique to check the annealing quality of metals. This work aims to compare (PAS) and Photo Luminescence (PL) techniques in the characterization of well-annealed metals. For this purpose, four tungsten sample were used. First, the effect of annealing on the structure of a rolled tungsten with a purity of 99.97 **%**was investigated. Second, the tungsten sheet was divided into four pieces. The as-received sample was considered as a reference. Three samples were annealed at 700 °C, 1000 °C, and 1400 °C. Annealing was done for one hour under a vacuum of about 10^{-6} mbar. Then, PAS and PL techniques were performed to determine the defects and their structure in the samples. A comparison of the obtained results by the both PAS and PL methods indicates an increase in the size of defects and a decrease in their number under with an increase in annealing temperature. The correlation between the PAS and PL parameters were described in details. Although the PAS technique was more accurate in characterizing defects, the obtained results by the two methods were in good agreement.

Keywords: Positron Annihilation Spectroscopy, Photoluminescence, Tungsten, Annealing, Defect.

Introduction

Tungsten was recognized by ITER as a good candidate for plasma-facing material due to its unique properties such as low sputtering, high melting temperature, high thermal conductivity, low retention of hydrogen isotopes and low reactivity. Hydrogen isotopes, as the main fuel of a fusion reactor, cause severe damage to the material in contact with the tungsten surface. These damages can be considered as the most probable reason for the loss of mechanical properties of tungsten [1-3]. In fact, these damages are formed by defects in tungsten [4]. Therefore, it is important to study and recognize the defects.

The Photoluminescence (PL) analysis is an easy, non-destructive and fast technique. Although the fundamental limitation of PL analysis is its reliance on radiative events, its signals provide useful information about surface and interface quality [5]. Therefore, this method can be used to investigate the surface of fusion materials. Modifications in the structure and the formation of defects such as oxygen vacancies on the ion and γ-irradiated breeder blanket materials surface were obtained using the PL technique by Carella et al. [6].

Investigation of the surface of gold and copper using PL and observation of peak emission in both metals was reported by Mooradian [7]. Mooradian also reported the exciting optical radiation of observations electron-hole recombination of the two metals from near-Fermi energy in deep bands [7].

The modern positron annihilation spectroscopy (PAS) method can be used to obtain valuable information about metal defects. Because positrons are highly sensitive to vacancy defects in solids, this non-destructive method is capable of providing excellent quantitative and qualitative information at the atomic scale [8,9].

PAS is used to study metals because of its ability to measure some important properties that are critical to identifying the magnetic, mechanical, and electrical properties of metals. Properties such as electron momentum distribution, ratio of free electrons Z_c/metal atom, Fermi energy ε_F (usually measured in eV), and np concentration (in cm^{-3}) in the capacitance band [10].

Recent experiments examining the evolution of defect concentration and size under different annealing conditions by Positron Annihilation Lifetime Spectroscopy (PALS) [4] show that, initially, an increase in temperature leads to an increase in the size and concentration of point

defects due to recombination of migration point defects. Then, at very high temperatures, tungsten is completely recrystallized [11,12] and completely free of defects [4,13].

In this presentation, annealed tungsten is characterized by two methods, PAS and PL. The purpose of this work is to compare the PAS and PL methods

Experimental

In this work, a rolled tungsten sheet with 99.97% purity and 1 mm thickness were used. Tungsten sheet was manufactured by the Austrian company PLANSEE. Tungsten sheet was divided into 4 sample groups. The annealed samples are shown at i) 973 K with the symbol W_{01}, ii) 1273 K with the symbol W_{02}, iii) 1673 K with the symbol W_{03}, and iv) sample as-received denoted by W_{00}. The duration of the samples were annealed under the vacuum ~10^{-6} mbar was 1 h. The surface of the samples was first polished mechanically and electropolished with SiC papers from 600# to 5000# and then 2% NaOH solution, respectively. The samples were electropolished at room temperature and 8v for 30 s to 60 s.

After polishing, the samples were cleaned in an ultrasonic bath for 10 minutes with ultrapure acetone and deionized water.

The calculation of grain size before and after annealing shows a ~16 times growth in grain size with increasing temperature [14].

Positron Annihilation Spectroscopy (PAS)

PAS is a technique that provides information about defects by detected annihilation photons. When the positron enters the sample and its inelastic collision with the free electrons is thermalized after a few picoseconds. Inelastic collision of the positron with free electrons is one way of annihilation of positron. Other ways to annihilation positron include trapping at sample sites, and creating a positronium (Ps) atom by bounding to an electron.

Both the positron and the electron particle are annihilated in an inelastic collision into electromagnetic radiation. This annihilation, in the two photons case, results in the emission of

two photons with ~511 keV energy and an approximate angle of 180°. Fig. 1 shows the mechanism of PAS.

In defect, the absence of positively charged atomic nuclei creates a local adsorbent potential for the positron, which plays an effective role in trapping the positron. The dependence of different defects on changes in the momentum distributions and concentration of the annihilating electron impulse can affect the two parameters of energy spectrum and lifetime of the emitted photons in the characterization pathways. Therefore, defects at the nanometer scale and very low concentrations can be investigated. Positrons emitted from the ^{22}Na source can lose their energy to thermal energy in a few ps and diffuse to a depth of 0.1 μm in the material until the defect is trapped [15,16].

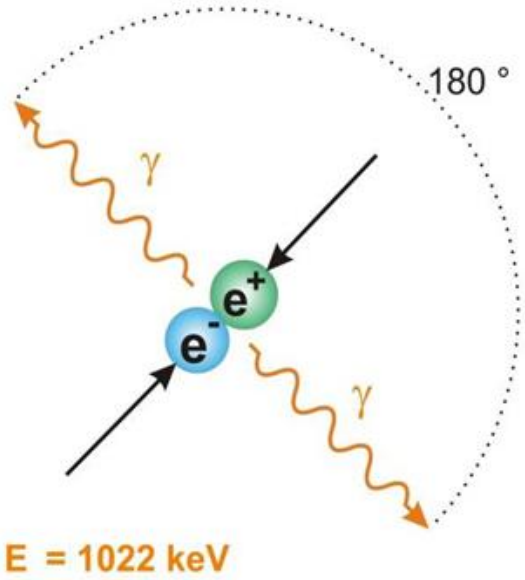

Fig. 1. mechanism of PAS [16]

Positron Annihilation Lifetime Spectroscopy (PALS) and Coincidence Doppler Broadening Spectroscopy (CDBS) are two laboratory methods of the PAS technique that were used in this work to study the structure of matter and defects.

Positron Annihilation Spectroscopy (PAS)

The density of the electrons around the positron before annihilation determines the lifetime of the positron. Therefore, to determine the type and size of defects of the material, the measurement of positron lifetime in the material can be used [9,15].

The positron lifetime is the time between emissions until the annihilation of the positron (Fig.2). The randomness of the annihilation process results in a statistical distribution over the lifetime of the positron, so it can obtain the lifetime spectra from the sum of the exponential reduction components with different intensities. The standard counts of annihilation events for the lifetime spectrum is about 10^6 [4, 16–17].

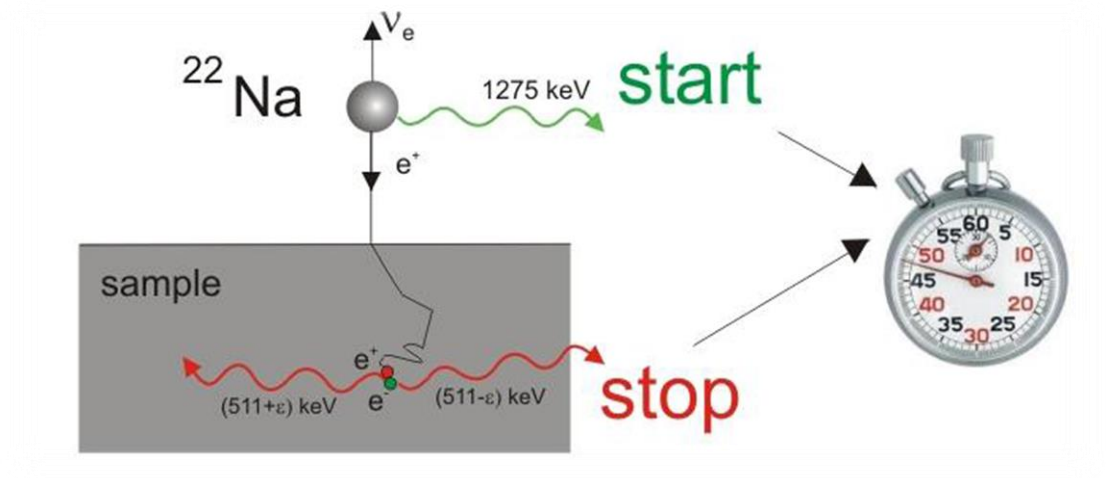

Fig. 2. Positron lifetime measurement [16]

The following equation is used to obtain the lifetime spectrum, z(t), [4]:

$$z(t) = R(t) \times \sum_{i=1}^{N+1} \frac{I_i}{\tau_i} \exp(-\frac{t}{\tau_i}) + BG \qquad (1)$$

Where BG and R(t) are constant background and time resolution function. N, I_i and, τ_i are the number of open volume defects in the matter, intensity and, lifetime of positron, respectively. τ_{ave} indicates average lifetime of a positron and is obtained from the following equation [4]:

$$\tau_{ave} = \sum_i \tau_i I_i \qquad (2)$$

Here, the lifetime of positron annihilation in defective and non-defective sample τ_{ave} and τ are expressed respectively. The duration of annihilation of the positron trapped in defects such as

micro voids, dislocations, vacancies, vacancy-impurity pairs, etc., is longer than that of the free positron in the same sample. Therefore, $\tau<\tau_{ave}$ indicates the presence of open-volume defects in the structure of a material [16-18].

Coincidence Doppler Broadening Spectroscopy

Placement of positrons and their annihilation in the vacancy sites is the basis of this method. In the laboratory, when the local positrons are annihilated by collisions with electrons to protect energy and momentum, due to the annihilating electrons primary momentum, the Doppler broadening of the 511 keV line occurs with a value $E = \pm(p_l c)/2$. Where pl is the longitudinal momentum of the electron in the direction of annihilation radiation and c is the speed of light. Doppler broadening spectroscopy technique can be a suitable method to detect the chemical nature of holes in the lattice structure. The conversion of the momentum of the sample electrons into the energy of the positron annihilation gamma radiation is the basis of this technique [19].

Two very important parameters in this method are S and W, which show the momentum distribution of core electrons at the place of electron-positron annihilation. Positron annihilation is represented by valence electrons with S-parameter and by core electrons with W-parameter. Due to the high sensitivity of S-parameter on open volume defects, this parameter shows the size and concentration of defects. The chemical environment of the positron annihilation sites is described by the parameter W [19,20].

To increase the accuracy in determining the momentum distribution of internal electrons and reduce the background radiation as much as possible, the Coincidence Doppler Broadening Spectroscopy (CDBS) method can be used by two detectors. Two HPGe detectors or one HPGe detector and one NaI(Tl) detector are placed in front of each other and the source sandwiched by the two samples is placed between them (Fig. 3). The system counts only the gamma rays that enter the two detectors coincidentally, and the background spectrum is well removed. With this method, the peak-to-Compton ratio of about 10^4 can be obtained. The highest accuracy in measuring S and W-parameters is obtained by using the coincidentally of two HPGe detectors [21]. This configuration is used in this work.

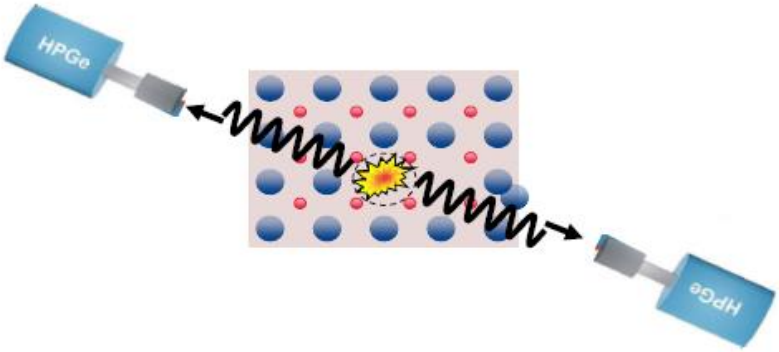

Fig. 3. configuration of Coincidence Doppler Broadening Spectroscopy [16]

Results and discussion

Coincidence Doppler Broadening Spectroscopy

Spectroscopy results of samples by CDBS are shown in Table I. In the W_{00}, W_{01}, W_{02} samples, S-parameter decreases and increases in sample W_{03}. As can be seen, the lowest value of S-parameter corresponds to samples W_{01}, W_{02}. Due to the high sensitivity of the S-parameter to open-volume defects, perhaps the increase of the S-parameter in two samples W_{00} and W_{03} can be considered as an indication of the greater number of defects in the sample W_{00} and their larger size in W_{03}.

Table 1. W- and S-parameters of the applied tungsten samples, (Error S-parameter: ± 0.001) (Error W-parameter ± 0.0003) [14]

Sample	Annealing temperature(K)	S-parameter	W-parameter
W_{00}	as-received	0.467	0.2264
W_{01}	973	0.461	0.2327
W_{02}	1273	0.458	0.2360
W_{03}	1673	0.464	0.2295

By examining the changes of W-parameter in terms of S-parameter (Fig. 4) and lining up the points on a line, it can be concluded that the trapping sites of positron and their annihilation are the same for all samples [14,22].

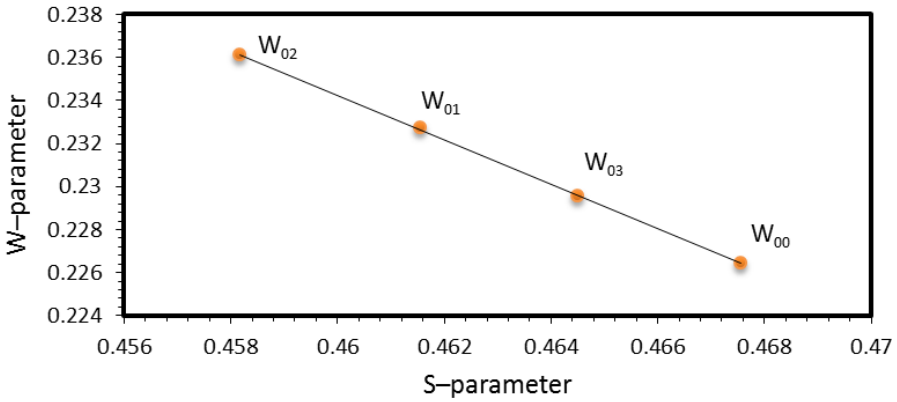

Fig. 4. The variation of W–parameter versus S–parameter [14]

Two main and distinct regions in Doppler broadening method, i) region with low momentum or $0< pl <3 \times 10^{-3}\ m_0c$, ii) region with high momentum or $6 \times 10^{-3}<pl<15 \times 10^{-3}\ m_0c$, represent the values S-parameter and W-parameter respectively [17]. Fig.5 shows a peak for all samples. Positron annihilation with 5d tungsten electrons leads to the presence of the peak in ΔE~3 keV ($pl\approx11.73 \times 10^{-3}\ m_0c$). This peak corresponds to the W-parameter [23]. Considering the inverse relationship of two parameters W and S, it can be said that in ΔE~3 keV, for all samples, S-parameter is the lowest value that an increase in temperature leads to its decrease compared to the as-received sample.

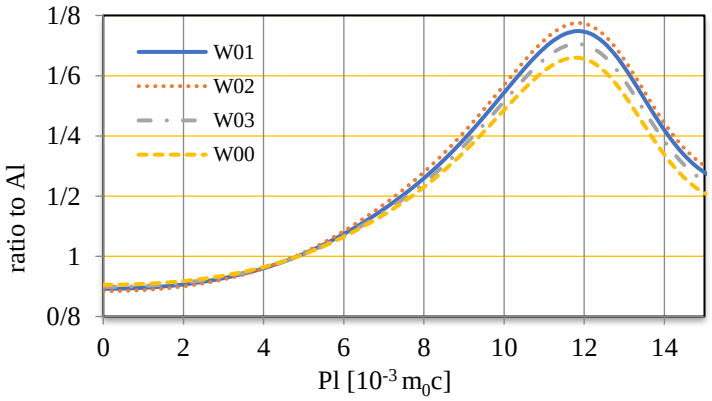

Fig.5. The measured momentum spectrum of the Doppler broadened annihilation radiation [14]

Examining the defects created on tungsten by PAS showed the evolution of the defects with increasing annealing temperature. This evolution occurs in three stages: stage I (from room temperature to ~773 K), initiation of movement of small vacancy-type defects at low temperatures; stage II (~773 K to ~1723 K), at medium temperature, first there are medium-sized defects, and

then with increasing temperature, larger defects are produced; stage III, at temperature above ~1723 K to ~2773 K, defects undergoes recovery [24].

PALS Experiment

In this measurement, the positron emitting source was ^{22}Na. The counts collected in each lifetime's spectrum, channel widths and FWHM are 10^5, 23 and 360 s, respectively. The lifetime of a positron in a defect free tungsten lattice is τ=~105 ps [25]. Direction LT-10 was the software used to solve the average positron lifetime of the spectrum. 25% of the intensity of positron annihilation in all samples is related to foil's Kapton. The results of positron annihilation lifetime spectroscopy are shown in Table 2**.**

Table 2. Results of the PALS experiment [26]

Sample	τ_1(ns)	I_1(%)	τ_2(ns)	I_2(%)	τ_{ave}(ns)
W_{00}	0.221±0.005	89.88	1.71±0.038	10±1.025	0.371
W_{01}	0.160±0.010	92.74	1.20±0.082	7±2.694	0.238
W_{02}	0.191±0.004	95.38	1.42±0.040	4.6±0.729	0.248
W_{03}	0.147±0.005	93.21	1.28±0.040	7±1.238	0.223

The effect of temperature on positron lifetime is shown in fig. 6. The highest average lifetime is related to W_{00}, which indicates a large number of small vacancy-type defects. A decrease in the average positron lifetime with increasing temperature indicates the presence of larger defects such as small cavities [14].

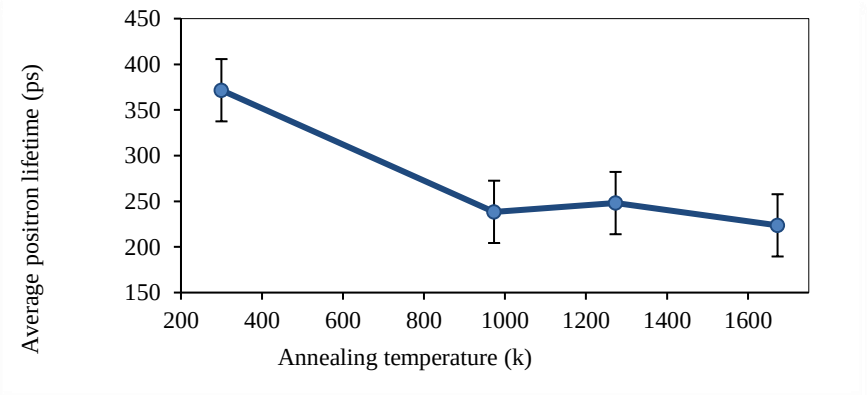

Fig.6. Graph of average positron lifetime versus temperature [14]

Photoluminescence spectroscopy

In the photoluminescence spectrometer, a Xe lamp was used as the excitation source. The surface of the samples was excited at room temperature with a wavelength of 275 nm. Photoluminescence spectra obtained from tungsten samples were shown in Fig. 7.

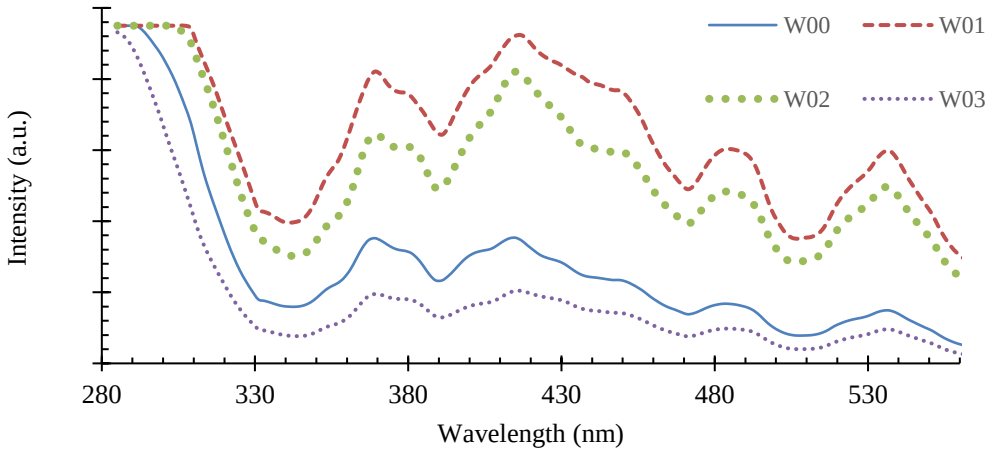

Fig.7. Photoluminescence spectra obtained from tungsten samples annealed at different temperatures [14]

The peaks obtained from the experimental data (from 285.07 nm to 307.02 nm, 369.07 nm and 381.06 nm) are in good agreement with the theoretical evaluation [14]. The observed peaks in the wavelengths of 400 to 600 nm are due to carbon impurities [14] and oxygen vacancies. It can also be seen in Fig. 7, the increase in temperature has led to a decrease in the intensity of PL emission. This result shows the increase in the size of the intrinsic defects and the formation of a large vacancy in the samples [14]. The peak broadening for higher temperatures is believed to cause by light excited holes in k-space. Minor shift in the peaks is due to the flattening of the distribution of electrons and holes [7].

Conclusion

The effect of annealing on tungsten and the characterization of defects at different temperatures were investigated by PAS and PL methods. Also, the changes in the size and number of defects caused by heat treatment were studied. By comparing both laboratory methods, the following points can be noted:

i. Severe changes in behavior, especially at 1673 K, caused by a decrease in numerical density and an increase in the size of defects.

ii. They were able to identify the type of defect.

iii. The results of both methods were in good agreement.

iv. In defect characterization (density, type and size), PAS is more accurate.

v. PL is a simple, convenient and accessible method whereas PAS is a complex method.

vi. PL can be a good alternative in the characterization of metals as a secondary method.

Acknowledgment

This research did not receive any specific grant from funding agencies in the public, commercial, or not-for-profit sectors.

References

[1] Seyedhabashi, M. M., Shafiei, S., Tafreshi, M. A., & Bidabadi, B. S. (2020). Study of surface damage and hydrogen distribution in irradiated tungsten by protons in plasma focus device. Vacuum, 175, 109249.

[2] Bolt, H., Barabash, V., Krauss, W., Linke, J., Neu, R., Suzuki, S., ... & ASDEX Upgrade Team. (2004). Materials for the plasma-facing components of fusion reactors. Journal of nuclear materials, 329, 66-73.

[3[Zhexian, Z. H. A. N. G., Wentuo, H., & Akihiko, K. I. M. U. R. A. (2015). Correlation of Microstructure Evolution and Hardening in Ion-irradiated Pure Tungsten. Journal Plasma Fusion Res. SERIES, Vol. 11, 2015.

[4] Zibrov, M. (2018). The influence of radiation, mechanical, and plasma-induced damage on deuterium retention in tungsten (Doctoral dissertation, Ghent University).

[5] Gfroerer, T. H. (2000). Photoluminescence in analysis of surfaces and interfaces. Encyclopedia of analytical chemistry, 67, 3810.

[6] Carella, E., Leon, M., Sauvage, T., & Gonzalez, M. (2014). On ion implantation and damage effect in Li2TiO3 as a fusion breeder blanket: A technological approach for degradation testing. Fusion Engineering and Design, 89(7-8), 1529-1533.

[7] Mooradian, A. (1969). Photoluminescence of metals. Physical Review Letters, 22(5), 185.

[8] Nambissan, P. M. G., & Sen, P. (1992). Positron annihilation study of the annealing behaviour of alpha induced defects in tungsten. Radiation effects and defects in solids, 124(2), 215-221.

[9] Puska, M. J., & Nieminen, R. M. (1983). Defect spectroscopy with positrons: a general calculational method. Journal of Physics F: Metal Physics, 13(2), 333.

[10] Grafutin, V. I., & Prokop'ev, E. P. (2002). Positron annihilation spectroscopy in materials structure studies. Physics-Uspekhi, 45(1), 59.

[11] Zhang, Z., Hasenhuetl, E., Yabuuchi, K., & Kimura, A. (2016). Evaluation of helium effect on ion-irradiation hardening in pure tungsten by nano-indentation method. Nuclear Materials and Energy, 9, 539-546.

[12] Zhang, Z. X., Chen, D. S., Han, W. T., & Kimura, A. (2015). Irradiation hardening in pure tungsten before and after recrystallization. Fusion Engineering and Design, 98, 2103-2107.

[13] El-Shaer, A., Abdelfatah, M., Mahmoud, K. R., Momay, S., & Eraky, M. R. (2020). Correlation between photoluminescence and positron annihilation lifetime spectroscopy to characterize defects in calcined MgO nanoparticles as a first step to explain antibacterial activity. Journal of Alloys and Compounds, 817, 152799.

[14] Torabi, M., Kakuee, O., Sobhanian, S., & Kouhi, M. (2022). Characterization Of Defects In Tungsten Samples Interested In Pfm Studies Using Positron Annihilation And Photoluminescence Spectroscopy. Surface Review and Letters, 29(04), 2250053.

[15] Wagner, A., Butterling, M., Liedke, M. O., Potzger, K., & Krause-Rehberg, R. (2018, May). Positron annihilation lifetime and Doppler broadening spectroscopy at the ELBE facility. In AIP Conference Proceedings (Vol. 1970, No. 1). AIP Publishing.

[16] Dr. Maciej Oskar Liedke / FWKK / www.hzdr.de.

[17] Brusa, R. S., Deng, W., Karwasz, G. P., & Zecca, A. (2002). Doppler-broadening measurements of positron annihilation with high-momentum electrons in pure elements. Nuclear Instruments and Methods in Physics Research Section B: Beam Interactions with Materials and Atoms, 194(4), 519-531.

[18] Ogorodnikova, O. V., Dubov, L. Y., Stepanov, S. V., Terentyev, D., Funtikov, Y. V., Shtotsky, Y. V., ... & Gutorov, K. (2019). Annealing of radiation-induced defects in tungsten: positron annihilation spectroscopy study. Journal of Nuclear Materials, 517, 148-151.

[19] Biganeh, A., Kakuee, O., Rafi-Kheiri, H., & Lamehi-Rachti, M. (2019). Development of a 2D digital coincidence Doppler broadening spectrometer. Journal of Instrumentation, 14(02), P02017.

[20] Uytdenhouwen, I., Schwarz-Selinger, T., Coenen, J. W., & Wirtz, M. (2016). Mechanical and microstructural changes in tungsten due to irradiation damage. Physica scripta, 2016(T167), 014007.

[21] Mehmandoost, K. D. A., Mahjour, S. M., & Khaghani, M. (2011). Development of a Doppler broadening positron spectroscopy setup and relative positron-electron momentum distribution measurement for commercial Al.

[22] Asgarian, S. M., Kargar, Z., & Mozaffari, M. (2017). Investigation of cation vacancies in Zinc substituted maghemite by positron annihilation lifetime and Doppler broadening spectroscopy. Applied Radiation and Isotopes, 125, 18-22.

[23] Biganeh, A., Kakuee, O., Rafi-Kheiri, H., Lamehi-Rachti, M., Sheikh, N., & Yahaghi, E. (2020). Positron annihilation lifetime and Doppler broadening spectroscopy of polymers. Radiation Physics and Chemistry, 166, 108461.

[24] Debelle, A., Barthe, M. F., & Sauvage, T. (2008). First temperature stage evolution of irradiation-induced defects in tungsten studied by positron annihilation spectroscopy. Journal of Nuclear Materials, 376(2), 216-221.

[25] Zhu, S., Xu, Y., Wang, Z., Zheng, Y., Zhou, D., Du, E., ... & Minamisono, T. (2005). Positron annihilation lifetime spectroscopy on heavy ion irradiated stainless steels and tungsten. Journal of nuclear materials, 343(1-3), 330-332.

[26] Torabi, M., Kakuee, O., Sobhanian, S., & Kouhi, M. (2022). Positron annihilation lifetime spectroscopy of annealed tungsten. Kerntechnik, 87(2), 226-229.

A comparative study for solid and gas target neutron generators (Paper ID: 1125)

Alireza. Asle Zaeem[1*], Morteza. Sedaghat Movahhed[1], Emad. Rezaei[1], Amir Raeisdana[1], Maryam. Hosseinzadeh[1]

[1]Plasma & nuclear fusion research school, Nuclear Science and Technology Research Institute (NSTRI), Tehran, Iran

Abstract

Solid target neutron generators have become area of interests due to many potential applications in industry and nuclear medicine such as prompt gamma neutron activation or BNCT. In this kind of device, a beam of deuterium is formed and accelerated up to specific energy range impinged on a solid target that is composed of deuterium or tritium atoms. This phenomenon is able to generate 2.45MeV or 14MeV fast neutrons respectively. Even though the fusion cross section of D-D reaction increases with increment of ion beam energy, besides engineering constrains such as heat removal saturation in solid targets there exist some nuclear physics constrains that limits the neutron yield. Therefore, it is worthy to have physical comparison between solid and gas targets. In this paper a code has been written to calculate the D-D neutron yield in both solid Titanium and deuterium gas targets as a function of incident deuterium beam, current and the target density. Due to high hydrogen absorption and metal hydride formation characteristic, stopping power of deuterium ions in Titanium are calculated with SRIM code and experimental fusion cross sections are employed. The results indicate that the gas target results more neutron yield in comparison with solid metal target at similar ion beam current conditions.

Keywords: Neutron generator, Deuteron beam, Solid target, Gas target

Introduction

Fusion based neutron generators have been increasingly applied in industry and nuclear medicine. These devices are tools of choice for obtaining, neutron radiography and prompt gamma neutron activation analyses for detections of explosives or nuclear materials [1-3]. Neutron generators also could be used in nuclear medicine methods such as BNCT for curing the brain tumors which are out of reach of the surgeon [4,5]. In this neutron generators an ion source and the target play the most important role. the most advantages of these kinds of neutron generatopr are portibility and no reqiuirment of fissionable materials and the ability of turning on and off based on the imideat desision. Eventhoughr the neutron yields are much lower in comparison with the fission reactor,

the attractive characteristics makes it worthwhile to perform more researches toward improvements of neutron yield in fusion bases neutron generators. In addition, increment of neutron yield might open new applications particularly in the field of isotope production for nuclear medicine imaging i.e., ^{99}Mo which is the most traditionally used radioisotope in the nuclear medicine diagnostic.

In this paper the ultimate neutron yields for the D-D fuel has been calculated based on the experimental fusion cross sections and the SRIM code for the solid deuterated target. The same approach has been used for the deuterium gas target to compare the results. Advantageous and disadvantageous of each method are discussed.

Research Theories

D-D and D-T nuclear fusion reactions are well known as the most used reactions for fusion based neutron generators to produce quasi-monoenergetic neutrons of 2.45 MeV and 14 MeV respectively. In these devices deuterium ion beam with energy levels of 60-200 keV is generated by an ion source that finally impinges on a metallic target usually composed of deuterium or tritium atoms which are loaded on a high hydrogen absorber thin film such as titanium or molybdenum on cooper surface[6]. To have estimation on the basic parameters affecting the neutron yield of a solid target neutron generator, it is logical to imagine the deutrated target as a volume containing deuterium atoms attached to the high absorber deuterium atoms such as Titanium as the main bacground material. Since the background metal atoms are able to form a limited number of chemical bonds with deuterium atoms, then the number density of deuterium atoms in the target material is proportional with target alloy density.

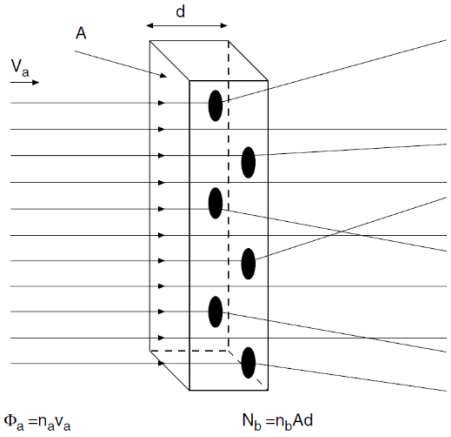

Fig(1). schematic picture of ion beam-target nuclear reaction

For a beam target reaction, laws of probability determine the reaction rate for a specific ion flux impinging on a target with specific number density of N_t as the following:

$$\dot{N} = \sigma \dot{N}_{in} \frac{N_t}{A} = \sigma \dot{N}_{in} \frac{\rho A d}{M_{Atomic} A} N_{av} \qquad (1)$$

Where σ is the nuclear fusion cros section reaction which is a sensitive function of ion beam energy, A is the ion beam area on the target surface, d is the target thickness, $M_{atomic}$is the target atomic mass, N_{av} is the Avogadro constant. If the ion beam energy decrement is not ignorable during penetration, then it is possible to write the equation (2) in a thick target scenario for Titanium target as follows:

$$\dot{N} = \sigma \dot{N}_{in} \frac{\rho A d}{M_{Atomic} A} N_{av} = \frac{N_{av} I}{eM} \int_{E_{out}}^{E_{in}} \frac{\sigma(E)}{S(E)} dE = 7.83 \times I(mA) \times Y \times 10^9 \qquad (2)$$

in which S(E) is the stopping power ($S(\mathrm{E}) = -\frac{dE}{\rho dx}$) and Y(E) defines as $Y = \int_{E_{out}}^{E_{in}} \frac{\sigma(E)}{S(E)} dE$

Therfore it is possible to write it as the following formula:

$$Y = \int_0^{E_{in}} \frac{\sigma(\mathrm{E})}{\left(\frac{dE}{dx}\right)} dE = \int_0^{L} \sigma(\mathrm{E}) dx \approx \sum_{i=1}^{N} \sigma(E_i) \Delta x_i \qquad (3)$$

in other words, neutron yield not only is proportional with the corss section values but also depends on the peneteration depth of the incident ion inside the target material. The higher penetration depth ends in the higher fuson yield. it means lower density materials e.g. gases are more efficent in neutron production rather than the high density solid targets.

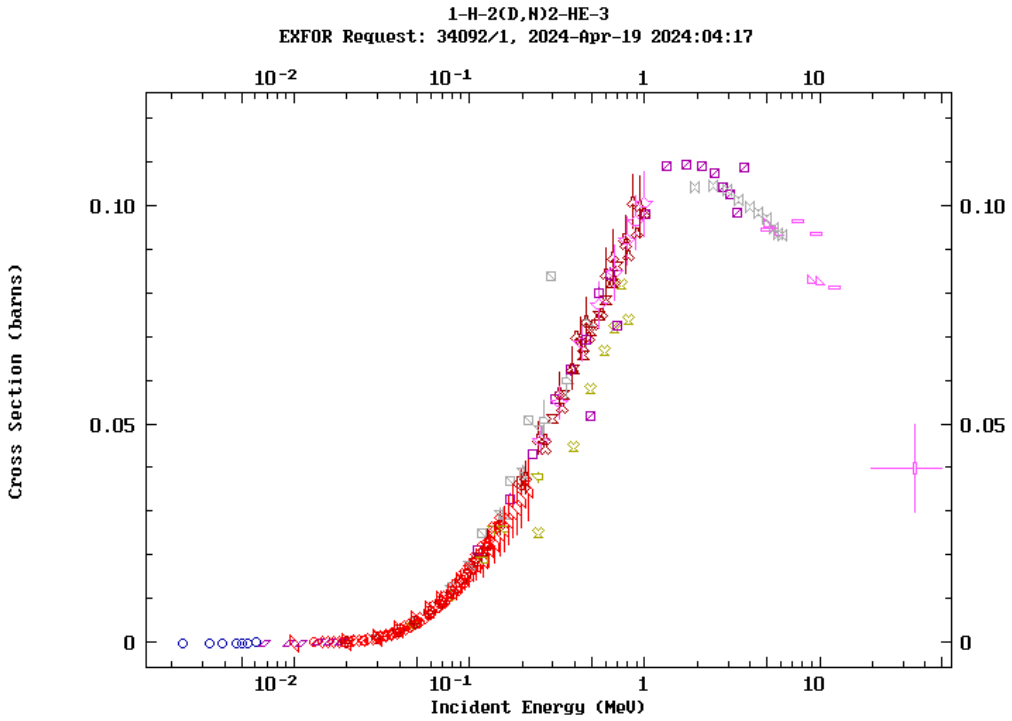

Fig (2). Experimental D(D,n)3He fusion cross section as a function of incident deutron energy

Results and discussion

Calculations of the neutron yield from equation (2) both for the solid Titanium and deuterium gas targets are performed. For these calculations SRIM code has been used for the penetration depth of deuterium ions inside the Titanium and deuterium gas as the targets. The comparative perspective of the penetration depths is depicted on Fig (3). Here the penetration depth is written in Angstrom for the solid titanium target and millimeter in gas target. In addition, ENDF experimental cross section data base is employed to write a code to calculate the neutron yield as a function of incident ion beam energy at different target densities which means different gas target pressure [7]. Fig (4) represents the calculated neutron yield as a function of deuterium ion beam energy (keV) for 1 mA of current beam and target pressure of 1000 Pa. Gas targets in neutron generators are usually in the range of 100 to 1000Pa pressure. This pressure (physically interpreted

as density) is much more than the ion source pressure ranges but much lower than the solid target densities [8,9].

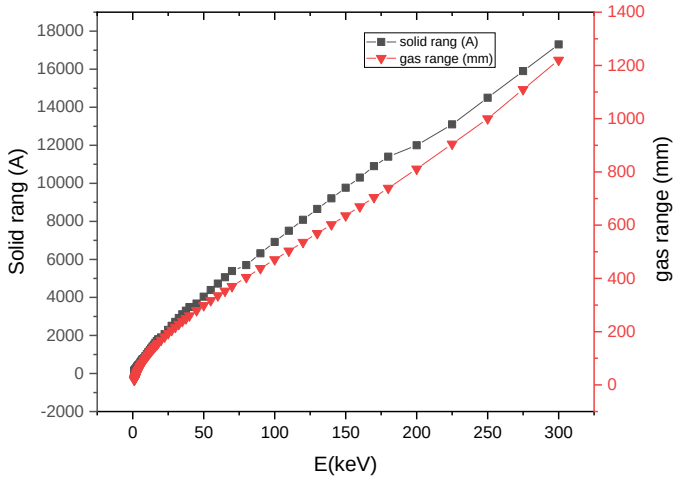

Fig(3). deutron penetration depth as a function of incident deutron enegrty for gas and Ti targets

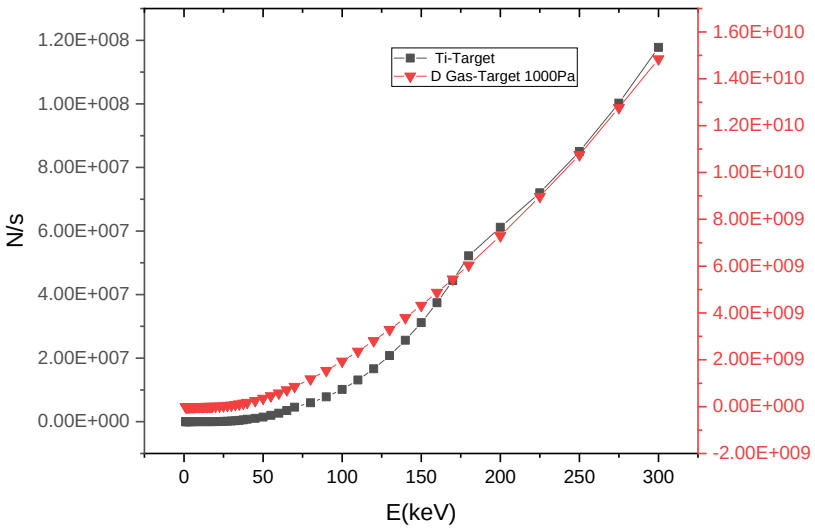

Fig.4. Neutron yield comparison for solid Titanium and deuterium gas target at 1000Pas for 1mA of deuteron beam

To have a better view of this comparison the written program was run calculate to the neutron yield ration for gas (1000Pa) and Titanium solid targets. The results indicate that the neutron yield is higher for gas target in comparison with the solid Titanium. It seems the gas targets which have

lower density are more efficient in neutron production rate, because of the lower atomic number of deuterium background atoms. Therefore, lower stopping power and the longer efficient penetration depth ends in higher neutron yield.

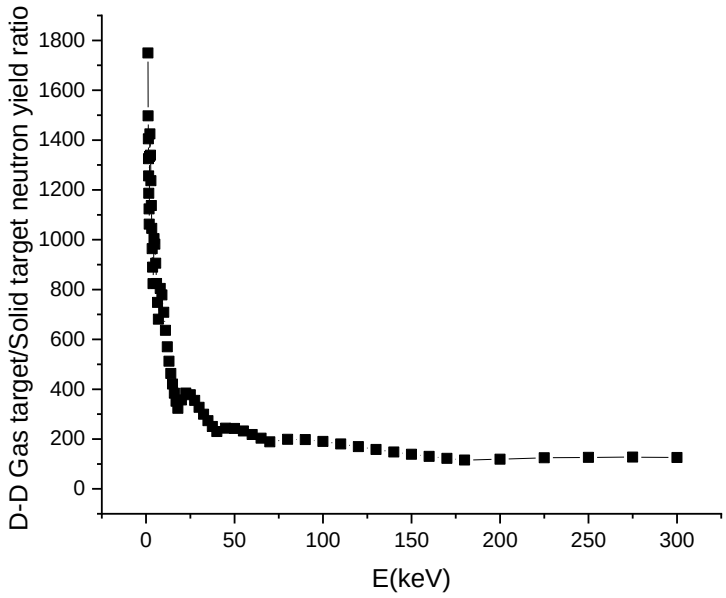

Fig.5. Neutron yield ration for gas and solid Ti target as a function of deuteron incident energy

Conclusions

Solid target neutron generators are being developed in industry and medicine. The higher the neutron yield ends in the higher quality of applications, therefore in order to taking step towards progress, a comparison study is performed between the solid and gas targets. Since in solid targets such as Titanium-as the most convenient metal- the main power loss mechanism of the incident ions is due to the background penetration environment of the target (electron clouds of the target atoms) which have relatively high atomic number, then it seems the gas target which have lower density is more efficient in neutron production rate, because of the lower atomic number of deuterium background atoms. Therefore, lower stopping power and the longer efficient penetration depth ends in higher yields. In other words, decrement of target density which ends in increment of the neutron yield. In addition, gas targets have the advantageous of no surface damage and heat removal problems however design and constructions of a gas target system with differential

pressure gradient from the ion beam generation to the target might be a challenging issue in engineering point of view that requires more delicate vacuum considerations.

References

[1] Adams, R., Bort, L., Zboray, R., et al. (2015). Development and characterization of a D-D fast neutron generator for imaging applications. Applied Radiation and Isotopes. 96:114–121.

[2] Bergaoui, K., Reguigui, N., Gary, C.K. et al. (2015). Prompt gamma-ray neutron activation analysis of boron using Deuterium–Deuterium (D–D) neutron generator. Radioanalytical and Nuclear Chemistry. 303:115–121.

[3] Jaakko H. Vainionpaa, Allan X. Chen, Melvin A. Piestrup, Charles K. Gary, Glenn Jones, Richard H. Pantell. (2015). Development of high flux thermal neutron generator for neutron activation analysis, Nuclear Instruments and Methods in Physics Research Section B: Beam Interactions with Materials and Atoms. 350:88-93.

[4] Gierlik, M., Borsuk, S., Guzik, Z. (2016). Swan - Detection of explosives by means of fast neutron activation analysis. Nuclear Instruments and Methods in Physics Research Section A: Accelerators, Spectrometers, Detectors and Associated Equipment. 834:16–23.

[5] Xing Z. Li, Qing M. Wei, Bin Liu. (2008). A new simple formula for fusion cross-sections of light nuclei. Nuclear Fusion. 48(12):125003.

[6] W.R. Wampler et al(2020). Optimization of target lifetime for production of 14 MeV neutrons, U.S. Department of Energy or the United States Government report.

[7] Masataka Furuta et al (2008). Measurements of activation cross sections of (n, p) and (n, a) reactions in the energy range of 3.5–5.9 MeV using a deuterium gas target" Annals of Nuclear Energy 35, 1652–1662.

[8] J. Guzek et al (1999). Development of high pressure deuterium gas targets for the generation of intense mono-energetic fast neutron beams, Nuclear Instruments and Methods in Physics Research B 152

[9] Wen Wang et al(2023). Design and experimental validation of differential pumped vacuum system for HINEG windowless gas target" Fusion Engineering and Design 189

Comparison the side effects of H and He ions on W and Mo surfaces due to glow discharge cleaning procedure as a primary method for wall conditioning in Damavand tokamak (Paper ID: 1150)

Sedighi F[1*], Rasouli C[1], and Iraji D[2]

[1] Plasma Physics and Nuclear Fusion Research School, Nuclear Science and Technology Research Institute, PO Box 14155-1339, Tehran, Iran

[2] Energy Engineering and Physics Department, Amirkabir University of Technology, P.O. Box 1591634311 Tehran, Iran

Abstract

Glow discharge cleaning (GDC) is a regular conditioning procedure for fusion devices such as tokamaks. Due to the low energy of ions in glow discharge plasmas, the probability of any considerable damage to the plasma-facing components was mainly ignored among researchers in the field. In this work, Tungsten (W) and Molybdenum (Mo), as the primary candidates for the plasma-facing materials in tokamaks, are considered for studies regarding the effects of the hydrogen and helium GDC procedure on these materials during a routine vacuum vessel conditioning in Damavand tokamak. After performing routine GDC using pure hydrogen and Helium, the formation of loosely attached nano-structure bundles (NSBs) on the surface of the tungsten and molybdenum samples was observed. The presence of the NSBs, which can be a source of dust, would be significant due to their possible effects on the functionality of future fusion plasma devices such as ITER. The surface modifications of specimens exposed to hydrogen and helium GDC were examined and compared using a material probe experiment and several surface analysis techniques such as SEM, and EDX. Therefore, the formation of loose nanostructures on the wall of plasma confinement vessels, due to GDC draws attention to the probable damaging effects of this phenomenon upon functionality and outcomes of tokamaks.

Keywords: glow discharge cleaning, plasma-wall interaction, nanostructures

Introduction

For numerous years, researchers have delved into the interaction between plasma and the materials they encounter, known as plasma-facing materials (PFMs), recognizing it as a critical concern in fusion devices. This exploration persists because plasma-material interactions significantly impact both the plasma itself and the PFMs. Tungsten (W), a refractory metal with a highest melting point

of all metals (TM=3695 K), distinguished by its exceptional thermal and mechanical properties, minimal sputtering yield, low activation, and satisfactory response to neutron irradiation, stands out as the leading candidate for PFMs in forthcoming fusion reactors, including ITER. Alongside W, molybdenum (Mo) has consistently been cited as a viable substitute for tungsten [1]. Nevertheless, thorough examinations into the impact of plasma ions on W and Mo surfaces have pinpointed particular performance concerns [2, 3]. The bombardment of tokamak walls by energetic ions results in the release of various low-Z and high-Z impurities into the plasma, potentially exerting detrimental effects on plasma evolution. Hence, wall conditioning plays a crucial role in eliminating impurities and enhancing plasma quality. Various methods, including baking, thin film deposition, ion cyclotron resonance, and glow discharge cleaning (GDC), are employed for wall conditioning, with GDC holding significant importance among them [4, 5]. Glow discharge plasma, a plasma regime generated by passing electrical current through a gas, arises by applying voltage across two electrodes within a vacuum chamber filled with low-pressure gas. This regime finds frequent applications, notably for vacuum vessel conditioning in tokamaks [6, 7].
During the process of glow discharge cleaning (GDC), a variety of gases including hydrogen, helium, neon, and argon are utilized, each possessing distinct characteristics and benefits.

Due to the low energy of ions within the glow discharge cleaning (GDC) procedure, the likelihood of significant damage to plasma-facing components (PFCs), typically composed of drable and resistant materials, is minimal. Consequently, there are limited reports detailing the interaction between ions in the GDC regime and PFCs. However, a sequence of investigations conducted on glow discharge cleaning (GDC) within the LHD stellarator has documented microscopic material damage[8, 9]. It should be noted that the LHD is a major experimental device located at the National Institute for Fusion Science (NIFS) in Toki, Japan. It is one of the largest and most advanced stellarator devices in the world [10]. Nevertheless, the GDC technique remains highly regarded as one of the primary wall conditioning methods in both present-day tokamaks and the forthcoming ITER reactor [11, 12].

While the prevailing belief has been that low-energy ions (below 200eV) pose negligible risk of causing significant harm to PFMs, recent reports have emerged indicating interactions between

low-energy ions and refractory materials like W and Mo, prompting concerns. These reports highlight the potential for low-energy helium ions to induce substantial changes in the surfaces of tungsten and molybdenum [13, 14]. Because of the significance attached to the interaction between low-energy ions and PFMs, substantial research efforts have been undertaken in recent years using diverse devices to investigate this issue in more detail[15-17]. Given the low energy of ions during the GDC procedure, coupled with the significant role of GDC in current tokamaks and the upcoming ITER reactor, it was deemed essential to investigate the microscopic effects of glow discharge on tungsten and molybdenum samples, the primary candidates for PFMs. The findings from experiments conducted at the Damavand tokamak are interesting and offer valuable insights into the effects of the GDC method on tungsten and molybdenum [18, 19]. Comparison of the effects of H and He ions on W and Mo surfaces due to glow discharge cleaning procedurei is discussed in this work.

Experimental

The experiments were performed at the Damavand tokamak [20]. The conventional GDC performed in Damavand tokamak includes the following steps. Initially, the rotary pumps evacuate the chamber from atmospheric pressure (~760 Torr) to approximately 40 Millitorr. In the subsequent phase, the pressure is further decreased to about 2×10^{-6} Torr using turbomolecular pumps. Gas puffing then begins, followed by the establishment of glow discharge plasma by applying voltage to electrodes positioned within the vacuum vessel. Finally, after the gas puffing procedure concludes, the substances within the tokamak are evacuated by the turbomolecular pumps, reducing the pressure to around 1×10^{-6} Torr. It should be noted that the ion flux is about $2\times10^{18}\,\frac{ions}{s.m^2}$. A standard GDC process employing hydrogen and helium, each with a purity of 99.9995%, is conducted at a pressure of 2.5×10^{-3} Torr, employing discharge parameters of 1.5 A and 450 VDC (volts of direct current). Throughout the GDC operation, the specimens maintained a temperature below 370 K, as monitored by a pyrometer. Additionally, a thermocouple was mounted on the material probe, with its tip directly exposed to the plasma.

Following the exposure of specimens to H-GDC, nanostructures were initially examined using a LEO 1455VP Scanning Electron Microscope (SEM). Subsequent to this observation, the chemical

composition of the nanostructures was analyzed utilizing Energy Dispersive X-ray Spectroscopy (EDX) coupled with SEM.

Results and Discussion

The SEM image in Figure 1 displays the Mo sample exposed to H-GDC. Nanostructures formed on the specimens exhibit incomplete coverage of the surface, resembling isolated islands. The majority of these islands measure approximately 400 μm² in area. Although the number of islands formed on the surface is not extensive, averaging around 15 per square millimeter, they collectively occupy about 0.6% of the tungsten surface.

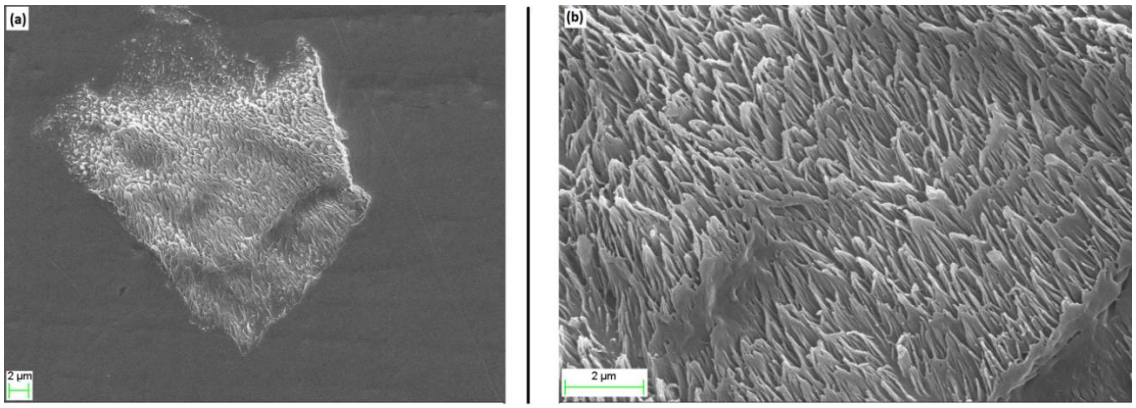

Fig. 1. (a) SEM image of nanostructures formed on molybdenum surface due to H-GDC in different magnifications (b) high magnification image

In certain experiments investigating the role of impurities on the formation of nanostructures, the tungsten surface exhibited complete coverage with a fuzzy layer. However, in this study, nanostructures were observed as isolated islands, and there was no full coverage of the sample's surface by a fuzzy layer. Additionally, as illustrated in Figure 2, an interesting phenomenon is the coexistence of blisters alongside the nanostructures. Initially, the simultaneous presence of these two phenomena (blisters and nanostructures) might suggest a potential relationship between them. However, a comparison between tungsten and molybdenum surfaces undermines the validity of this assumption. As illustrated in Figure 2, numerous blisters form on W surfaces (with diameters ranging from 0.1 to 10 μm), whereas no blisters are observed on Mo surfaces. The significant conclusion drawn from comparing W and Mo is that blisters and nanostructures are distinct phenomena that can occur independently of each other; nanostructures can form under conditions unsuitable for blister formation.

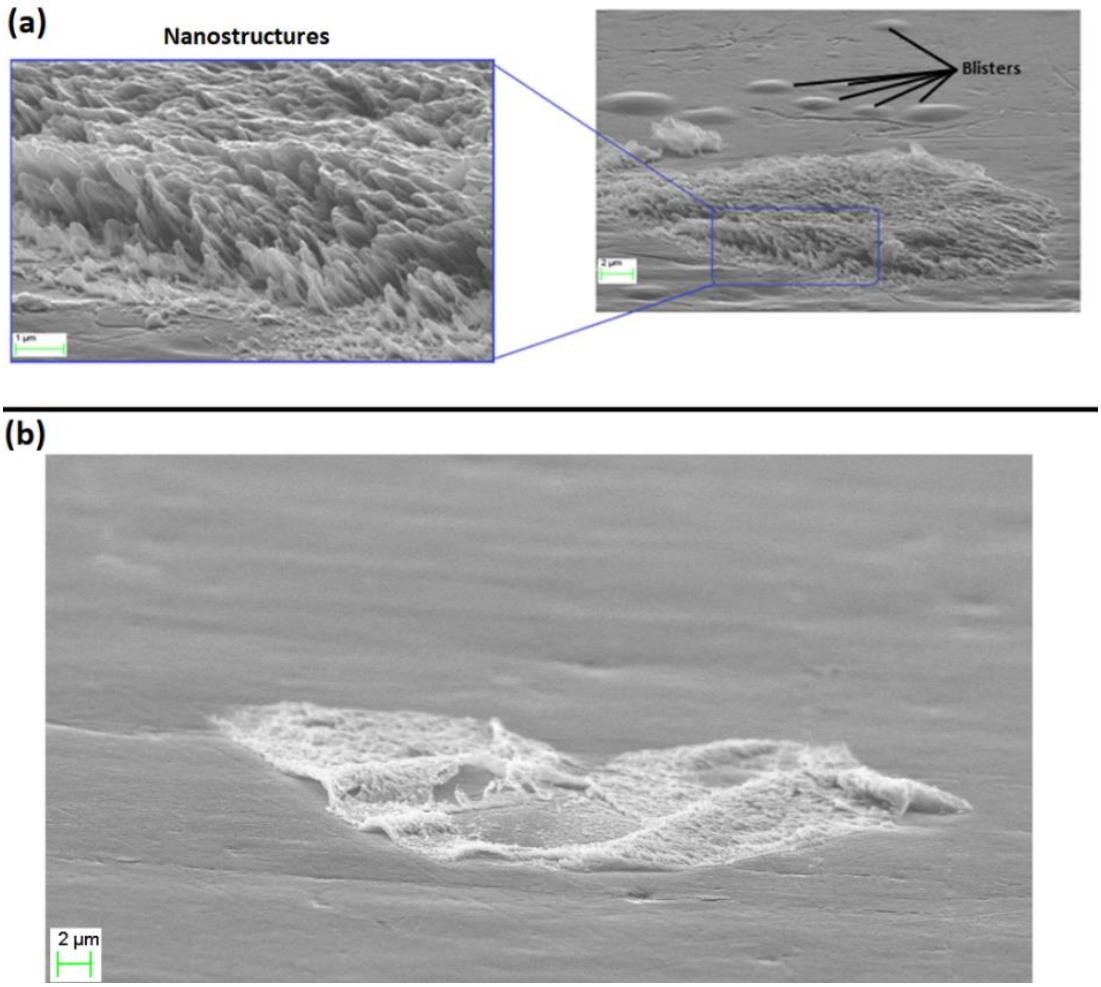

Fig. 2. (a) Coexistence of blisters alongside the nanostructures in W surface (b) absence of blisters in Mo samples

Multiple pure W and Mo specimens also underwent exposure to He-GD plasma. Figure 3 illustrates SEM images of the W sample, revealing the formation of fuzzy nanostructures on certain areas of the surface. Similar to H-GD, these nanostructures exhibit non-uniform coverage, appearing as isolated islands rather than providing complete surface coverage.

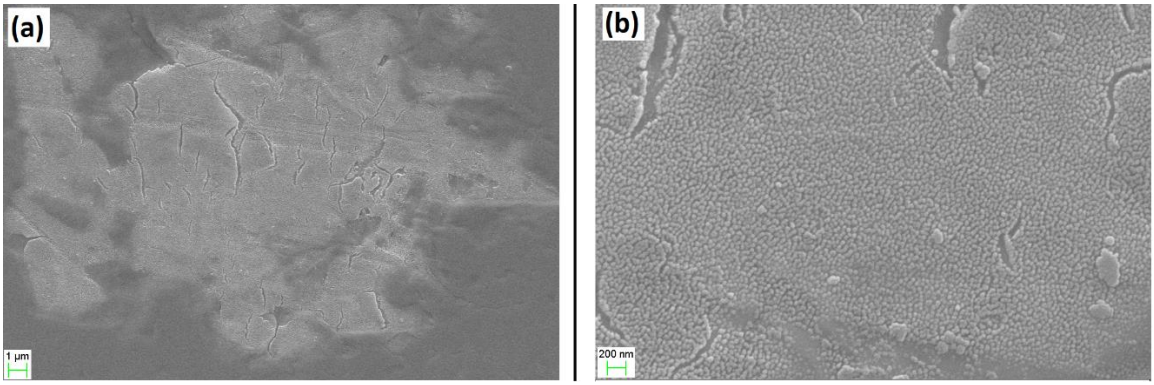

Fig. 3. (a) SEM image of nanostructures formed on tungsten surface due to He-GDC in different magnifications (b) high magnification image

Unlike the samples exposed to H-GDC, there is no trace of blisters in the specimens exposed to He-GDC. However, the formation of isolated bundles was observed in both experiments. Employing Energy Dispersive X-ray analysis (EDX), elemental analysis of these nanostructures revealed them to be composed of tungsten and molybdenum elements. Notably, the atomic composition of these nanostructures, as determined by EDX analysis, remains consistent with that of the reference sample, even in areas where these nanostructures have not developed. This observation suggests that the creation of these nanostructures may be attributed to an intrinsic effect rather than an extrinsic one. Initially, experimental results suggested that the requisite temperature for fuzz formation fell within the range of 1000-2000K [21]. However, Woller et al. observed this phenomenon occurring at lower temperatures (870-1220K) [22]. Several years thereafter, Corr et al. documented the formation of fuzzy nanostructures at 470K [23]. Consequently, the outcomes obtained from the experiment conducted in the Damavand tokamak corroborate Corr et al.'s observation of the fuzz phenomenon at low temperatures.

Conclusions

The emergence of the fuzz phenomenon in recent years has presented a novel and substantial challenge concerning the interaction of low-energy helium ions with tungsten, particularly in the context of fusion reactor construction. These fuzzy and loosely bound nanostructures pose a notable concern as they can easily detach from the tungsten surface, serving as potential sources of dust particles and impurities that could subsequently cool the plasma. Given the significance of this issue, extensive experimental investigations and simulations have been initiated to unveil its diverse characteristics. While early studies suggested that fuzz formation typically occurs under

specific conditions related to surface temperature, ion incident energy, and ion fluence, recent experimental findings have indicated their potential formation at lower temperatures and beyond these specified conditions. Despite significant research efforts thus far, the underlying mechanism of fuzz formation remains incompletely understood, highlighting the need for further experimental inquiries to attain a comprehensive understanding.

The glow discharge cleaning procedure, a primary method for vacuum vessel conditioning in fusion devices, finds widespread application in current tokamaks and is anticipated for use in future fusion reactors like ITER. At the Damavand tokamak, investigations have examined the microscopic alterations of key plasma-facing materials such as tungsten and molybdenum when exposed to hydrogen and helium ions in glow-discharge plasma. Interesting findings reveal the formation and growth of a fiber-like nanostructure on the surfaces of tungsten and molybdenum, reminiscent of the tungsten fuzz observed in tokamak divertor regions. Consequently, these investigations suggest that while glow discharge cleaning remains a crucial wall conditioning technique, it may induce unintended effects and prove detrimental to regions composed of tungsten and molybdenum, such as divertor regions. Therefore, caution is advised when employing the hydrogen and helium GDC procedure in such scenarios.

Referance

[1] R. Pitts *et al.*, "A full tungsten divertor for ITER: Physics issues and design status," *Journal of Nuclear Materials*, vol. 438, pp. S48-S56, 2013.
[2] V. Philipps, "Tungsten as material for plasma-facing components in fusion devices," *Journal of Nuclear Materials*, vol. 415, no. 1, pp. S2-S9, 2011.
[3] J. N. Brooks, L. El-Guebaly, A. Hassanein, and T. Sizyuk, "Plasma-facing material alternatives to tungsten," *Nuclear Fusion*, vol. 55, no. 4, p. 043002, 2015/03/11 2015.
[4] J. Wesson and D. J. Campbell, *Tokamaks*. OUP Oxford, 2011.
[5] Z. Khan *et al.*, "Conditioning of SST-1 Tokamak Vacuum Vessel by Baking and Glow Discharge Cleaning," *Fusion Engineering and Design*, vol. 103, pp. 69-73, 2016.
[6] M. Shimada and R. A. Pitts, "Wall conditioning on ITER," *Journal of Nuclear Materials*, vol. 415, no. 1, Supplement, pp. S1013-S1016, 2011/08/01/ 2011.
[7] G. J. M. Hagelaar, D. Kogut, D. Douai, and R. A. Pitts, "Modelling of tokamak glow discharge cleaning I: physical principles," *Plasma Physics and Controlled Fusion*, vol. 57, no. 2, p. 025008, 2014/12/22 2014.
[8] S. Masuzaki *et al.*, "Wall Conditioning in LHD," *Fusion Science and Technology*, vol. 58, no. 1, pp. 297-304, 2010.

[9] M. Tokitani *et al.*, "Initial growth phase of W-fuzz formation in ultra-long pulse helium discharge in LHD," *Nuclear Materials and Energy,* vol. 12, pp. 1358-1362, 2017/08/01/ 2017.
[10] M. Fujiwara *et al.*, "Overview of LHD experiments," *Nuclear fusion,* vol. 41, no. 10, p. 1355, 2001.
[11] P. Semwal *et al.*, "Baking and helium glow discharge cleaning of SST-1 Tokamak with graphite plasma facing components," *Journal of Physics: Conference Series,* vol. 823, p. 012061, 2017/04/19 2017.
[12] D. Kogut, D. Douai, G. Hagelaar, and R. Pitts, "Modelling the ITER glow discharge plasma," *Journal of Nuclear Materials,* vol. 463, pp. 1113-1116, 2015.
[13] S. Takamura, N. Ohno, D. Nishijima, and S. Kajita, "Formation of nanostructured tungsten with arborescent shape due to helium plasma irradiation," *Plasma Fusion Research,* vol. 1, pp. 051-051, 2006.
[14] F. Sefta, K. D. Hammond, N. Juslin, and B. D. Wirth, "Tungsten surface evolution by helium bubble nucleation, growth and rupture," *Nuclear Fusion,* vol. 53, no. 7, p. 073015, 2013.
[15] G. M. Wright *et al.*, "Comparison of tungsten nano-tendrils grown in Alcator C-Mod and linear plasma devices," *Journal of Nuclear Materials,* vol. 438, pp. S84-S89, 2013/07/01/ 2013.
[16] K. B. Woller, D. G. Whyte, and G. M. Wright, "Isolated nano-tendril bundles on tungsten surfaces exposed to radiofrequency helium plasma," *Nuclear Materials and Energy,* vol. 12, pp. 1282-1287, 2017/08/01/ 2017.
[17] Y. Ueda *et al.*, "Exposure of tungsten nano-structure to TEXTOR edge plasma," *Journal of Nuclear Materials,* vol. 415, no. 1, Supplement, pp. S92-S95, 2011/08/01/ 2011.
[18] F. Sedighi *et al.*, "Investigation of Hydrogen Glow Discharge Cleaning Side Effects on Tungsten," *Plasma Physics Reports,* vol. 47, no. 2, pp. 128-138, 2021/02/01 2021.
[19] F. Sedighi, D. Iraji, C. Rasouli, and M. Gholampour, "OBSERVATION OF MICROSCOPIC DAMAGE OF TUNGSTEN AND MOLYBDENUM SURFACES DUE TO HELIUM GLOW DISCHARGE CLEANING," presented at the 29th IAEA Fusion Energy Conference (FEC 2023), London, UK, 2023.
[20] C. Rasouli and F. Abbasi Davani, "Identification of the plasma boundary shape and position in the Damavand tokamak," *Plasma Physics Reports,* vol. 43, no. 1, pp. 1-11, 2017/01/01 2017.
[21] S. Kajita, W. Sakaguchi, N. Ohno, N. Yoshida, and T. Saeki, "Formation process of tungsten nanostructure by the exposure to helium plasma under fusion relevant plasma conditions," *Nuclear Fusion,* vol. 49, no. 9, p. 095005, 2009.
[22] K. Woller, D. Whyte, and G. Wright, "Impact of helium ion energy modulation on tungsten surface morphology and nano-tendril growth," *Nuclear Fusion,* vol. 57, no. 6, p. 066005, 2017.
[23] C. S. Corr *et al.*, "Mechanical properties of tungsten following rhenium ion and helium plasma exposure," *Nuclear Materials and Energy,* vol. 12, pp. 1336-1341, 2017/08/01/ 2017.

Simulation the plasma equilibrium in a spherical tokamak to estimate some of the basic designing parameters (Paper ID: 1164)

Moradi Zamenjani F[1*], Pirizad Hejrandoost S[2], Moazzemi Ghamsari M[2], Arjhangmehr A[3], Jafarzadeh M[4]

[1]*Nuclear engineering Department, University of Isfahan, Isfahan, Iran*

[2]*Physics Department, Kashan University, Isfahan, Iran*

[3]*Nuclear engineering Department, Shahid Beheshti University G. C, Tehran, Iran*

[4]*Physics Department, Guilan University, Guilan, Iran*

Abstract

The most basic concept in a tokamak is the plasma equilibrium which determines whether the considered plasma remains in the equilibrium condition for a reasonable time to occur fusion reaction or not. Equilibrium problem is divided into fixed and free boundary categories. These two categories determine some of the basic and necessary structural features for any kind of tokamaks like spherical and conventional tokamaks. One of the main differences between these two types of tokamaks is the larger elongation of the spherical tokamaks compared to conventional ones that arises from their compact structures. This feature causes higher plasma pressure, better stability and confinement. The elongated shape reduces instabilities too which is important in controlling process of a tokamak. In this paper, the plasma equilibrium problem in SMART, as typical spherical tokamak, is solved for fixed boundary conditions. Here the importance of some of the main parameters specially the elongation and triangularity on the safety factor and beta values of SMART is studied to estimate the optimum configuration which is the basic step in designing a tokamak.

Keywords: simulation, plasma equilibrium, spherical tokamak, designing parameters

Introduction

In a fusion reactor, strong magnetic field produced by external magnetic coils confines high temperature plasmas to keep deuterium and tritium ions close together for a reasonable long time

without colliding the confining walls consequently which results fusion reactions and produces helium and neutron as a practical source of energy of 17.6 MeV.

Because the hot reacting particles are moving along the applied magnetic field, they should to be confined in a way which cannot escape from the ends of plasma tube, so the ends must be closed. These features lead to a toroidal configuration. The most famous device in toroidal configuration is Tokamak[1]. Tokamaks are axially symmetric machines with helical magnetic fields.

Pure toroidal magnetic field causes charge separation via ∇B and curvature drift. The resulted vertical electrical field causes $\mathrm{E} \times \mathrm{B}$ drift which drive all charged particles towards the outboard side so it is necessary to apply a central current to create a poloidal magnetic field but it isn't enough magnetic field to make a complete confinement. There are two reasons for applying more poloidal magnetic field: In a tokamak there is some outward forces yielding from toroidal structure so it is necessary to add another poloidal magnetic field to overcome these forces. Another reason is the importance of plasma shape i.e., tokamaks with more elongated plasma shape same as spherical tokamaks (ST) have higher β, and tokamak with separatrix point have some advantages like decreasing the amount of impurities, avoiding transfer of impurities to plasma and extracting helium from plasmas. These last two reasons persuade us to add more poloidal magnetic field. The coils responsible to create this additional field are poloidal magnetic field coils (PF coils). The location and current of these coils are topics of the fixed and free boundary equilibrium problem. Depending on the boundary conditions to be enforced, we distinguish between two general classes of problems: (I) fixed-boundary problems in which the plasma boundary is prescribed, with magnetic flux (ψ) is constant on the boundary and one solves for magnetic flux inside the plasma, and (II) free-boundary problems where the current flowing in a set of external coils is given and one has to find magnetic flux such that the equilibrium is self-consistent with these currents [1].

After estimating the magnetic confinement designing limits by calculation of the fixed boundary equilibrium, the design and location of the coils must be optimized many times to generate the necessary magnetic field [2]. So, the fixed boundary equilibrium can be supposed as the conceptual design of magnetic coils that is the base of the detailed design. We consider only fixed-boundary

[1] Toroidal chamber with magnetic coils

problems. That is, the shape of the plasma boundary is given and $\psi = constant$ on the boundary. Furthermore, since only derivatives of ψ represent physical quantities, someone can choose $\psi = 0$ on the boundary without loss of generality [1].

Tokamaks are divided into two configurations based on the shape of the vacuum vessel. In conventional tokamaks the major radius is very larger than the minor one which causes the vessel to form like a donut while in STs the major radius is approximately equal to minor one that forms the vessel same as an apple. The difference between these two configs of vessels are shown in figure 1.

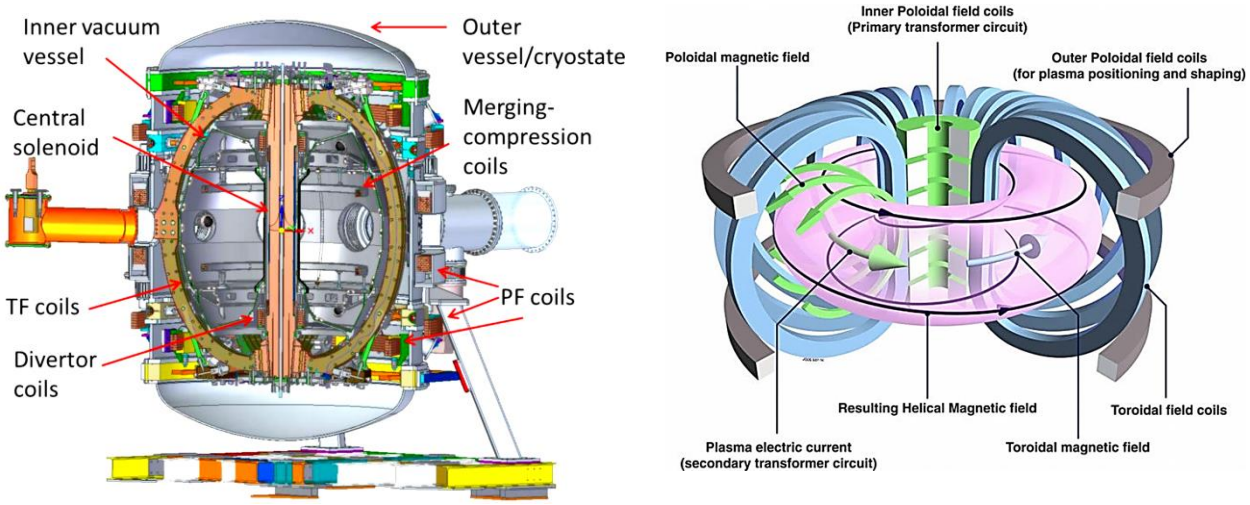

Figure 16:schematics of spherical (left) and conventional (right) tokamaks [3].

As it can be seen in figure 1, One of the main differences between these two types of tokamaks is the larger elongation of the STs compared to conventional ones which arises from their compact structures. This feature causes higher plasma pressure, better stability and confinement. The elongated shape reduces instabilities too which is an important factor in controlling processes of tokamaks. While these kinds of tokamaks have many advantages but there are some weaknesses in designing STs which most of them resulted from the compact structure, for example there is a low space to locate many coils and necessary devices in central area of the vessel that create high magnetic field and currents in the space. So, the structural designing of STs is a crucial point.

In this paper, by solving the fixed boundary problem in numerical method, the influence of the elongation and triangularity on the equilibrium of SMART is studied. The Grad–Shafranov (GS) equation is solved and flux surfaces are obtained. At the end, an optimum overall design is suggested.

Research Theories

The Magnetohydrodynamic (MHD) equilibrium in the tokamak are described by GS equation. In general, this is a nonlinear elliptic partial differential equation derived from the ideal MHD equations. There are numerous extensive works in the literature for solving GS equation for the fixed and free boundary problems in the tokamak using the finite element, finite difference, spectral, boundary element and other mesh-based methods [4].

The GS equation is derived from the steady state ideal MHD equations in cylindrical coordinates (R, Z, φ) with the assumption of toroidal symmetry $(\partial/\partial\varphi = 0)$ and static plasma $(v = 0)$ it can be written as follows [4, 5]:

$$-\left\{R\frac{\partial}{\partial R}\left(\frac{1}{R}\frac{\partial\psi}{\partial R}\right)+\frac{\partial^2\psi}{\partial Z^2}\right\} = \mu_0 R^2\frac{dp(\psi)}{d\psi} + I(\psi)\frac{dI(\psi)}{d\psi} \equiv \mu_0 R J_\phi \qquad (1)$$

where J_ϕ is the toroidal component of the current density and μ_0 is the magnetic permeability of free space. The magnetic flux ψ in Eq. (1) is the poloidal flux ψ_p normalized by 2π, i.e.,

$$\psi = \frac{1}{2\pi}\int_{s_p} \mathbf{B}\cdot\mathbf{n}ds_p \qquad (2)$$

where B is the magnetic field and n is the unit normal to a surface element, ds_p, as shown in Fig. 2(a). In Eq. (1) $p(\psi)$ is the pressure as a function of ψ and $I(\psi)$ is the poloidal current function defined by

$$I(\psi) = \int_{s_p} \mathbf{J}\cdot\mathbf{n}ds_p \qquad (3)$$

where J is the current density. The quantity $\psi \equiv \psi(R, Z)$ gives the equilibrium profile of the plasma in the geometry under consideration. The boundary of the plasma surface for spherical, elongated and D- shaped cross section is determined as $x = 1 + \varepsilon\cos(\theta + \alpha\sin\theta)$, $y = \varepsilon\kappa\sin\theta$ where θ is the

poloidal angle in toroidal coordinate ($0 < \theta < 2\pi$), κ is the elongation, $\alpha = sin^{-1}(\delta)$ defines the plasma triangularity and ε is the inverse aspect ratio [6].

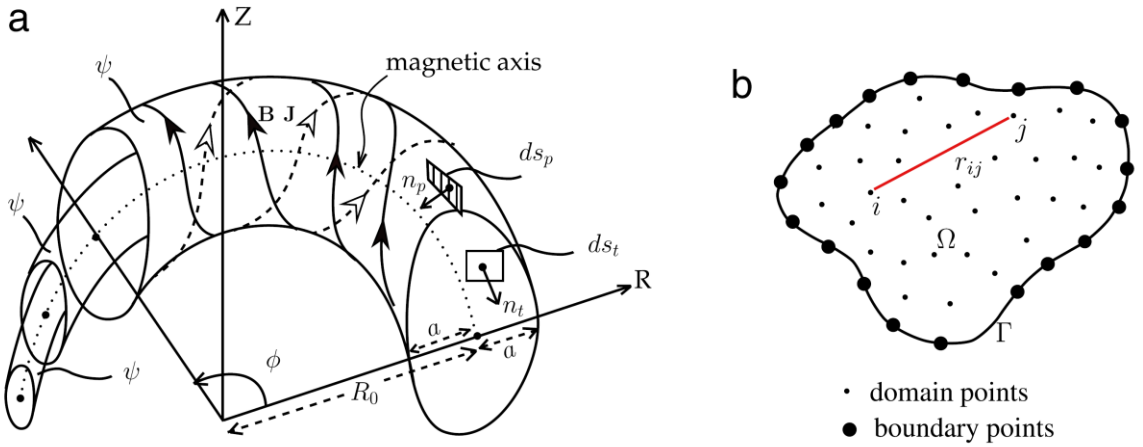

Figure 17. (a) A torus showing flux surfaces ($\psi = constant$) on which B and J lie, (b) a schematic representation of domain and boundary on a poloidal cross-section [4].

These are constant concepts and relationships for any kinds of tokamaks as well as STs. The low aspect ratio of STs is an interested feature causes high beta while the compact structure is a challenge too. SMART**2**, as a famous ST located in university of Seville in Spain, is a new spherical machine that is currently under construction. SMART will explore both positive and negative triangularities ($-0.6 < \delta < 0.6$), high elongation ($\kappa < 2.3$) and single/double null divertor plasmas [7].

[2] SMall Aspect Ratio Tokamak

Figure 18: SMART cross section with negative triangularity plasma [7]

The SMART operation will cover three phases. The first phase aims to test the machine and obtain first plasmas. The second one will focus on the demonstration of the machine capabilities (increasing I_p, B_t and τ), the addition of a neutral beam injector (NBI) for plasma heating and the integration of new diagnostics. Third phase will study plasmas with fusion-relevant parameters, similar to those of the main existing ST experiments and with the possibility of studying negative triangularity plasmas. Table 1 shows the basic parameters and different phases of SMART [5].

Table 7 SMART operation phases [8]

	Simulation parameters	First phase	Second phase	Third phase
1	Major radius (m)	0.4	0.4	0.4
2	Minor radius (m)	0.25	0.25	0.25
5	triangularity	0.38	0.44	0.52
6	Plasma current (kA)	30	100	500
7	Magnetic field (T)	0.1	0.3	1
8	Confinement time (MA)	20	100	500

Following, GS equation for SMART as a candidate of STs category is solved numerically for different configuration to study the stability parameters.

Experimental

Newton Raphson method is a way to quickly find a good approximation for the root of real-valued function. It uses the idea that a continues and differentiable function can be approximated by a straight-line tangent to it. In this paper Newton Raphson method applying Fortran is used through TASK[3] [9, 10] code. TASK solve the GS equation for SMART in fixed boundary manner to estimate some of the basic designing parameters, then the results are compared to choose the best structure. In reality and at the next step that isn't the subject of this paper the obtained results will be rechecked and optimized many times to determine accurate and specific parameters.

TASK is an open source code developed in Kyoto university, Japan. It has some interesting features like Modular structure, unified standard data interface, various heating and current drive schemes included of electron cyclotron, lower hybrid, ion cyclotron and NBI heating methods. It has a high portability so that the most of library routines is included. It can be paralleled using MPI library and can be extended to toroidal helical plasmas.

TASK's modular structure is included of EQ/EQU module to solve GS equation in fixed/ free condition, TR module for analyzing various kinds of transport models, WR module to simulate the ray tracing and beam tracing problems, WM modules for analyzing the full wave problems, FP module to study heating and current drive issues and DP to study the wave dispersion topics.

Here EQ module is used to simulate fixed boundary equilibrium in plasma of SMART. For solving equilibrium equation, the listed values in table 2 are used:

$$p(\psi) = p_0(1-\psi_N^{\mathrm{PR0FR0}})^{\mathrm{PR0FP0}} + p_1(1-\psi_N^{\mathrm{PR0FR1}})^{\mathrm{PR0FP1}} + p_2(1-\psi_N^{\mathrm{PR0FR2}})^{\mathrm{PR0FP2}} \quad (3)$$

$$I(\psi) = B \times R_0 + I_0(1-\psi_N^{\mathrm{PR0FR0}})^{\mathrm{PR0FF0}} + I_1(1-\psi_N^{\mathrm{PR0FR1}})^{\mathrm{PR0FF1}} + I_2(1-\psi_N^{\mathrm{PR0FR2}})^{\mathrm{PR0FF2}} \quad (4)$$

Table 8:initial value of parameters

parameter	Initial value	parameter	Initial value
p_0	0.64	PR0FP0	1.5
p_1	0	PR0FP1	1.5

[3] Transport Analyzing System for tokamaK

p_2	0	PR0FP2	2
I_0	1	PR0FF0	1.5
I_1	0	PR0FF1	1.5
I_2	0	PR0FF2	1.5
PR0FR0	1		2
PR0FR2	2		

Even though fixed boundary problem is easier to solve, it determines the boundary of plasma by a reasonable accuracy so it presents a rough estimation about PF coils. By this kind of simulation, we can see whether flux surfaces are generated or not that is a criterion topic in designing a tokamak. More over the flux surfaces and quality factor that are focused in this paper, many other parameters can be determined through EQ module, these are poloidal and toroidal beta values, current density, plasma pressure and temperature, poloidal current function and etc.

In table 3, the parameters based on the geometrical features of SMART (minor, major and blanket radius) are listed:

Table 9: basic designing parameters of SMART

	fixed parameters	value
1	Major radius (m)	0.4
2	Minor radius (m)	0.25
3	Minor blanket radius (m)	0.35
4	Aspect ratio	1.6
	suggested parameters	value
5	elongation	1
6	triangularity	0.38
7	Magnetic field (T)	0.1
8	Plasma current (MA)	0.1

In the figure 4, the flux surfaces that are obtained based on the fixed and suggested parameters listed in the table 3 are shown.

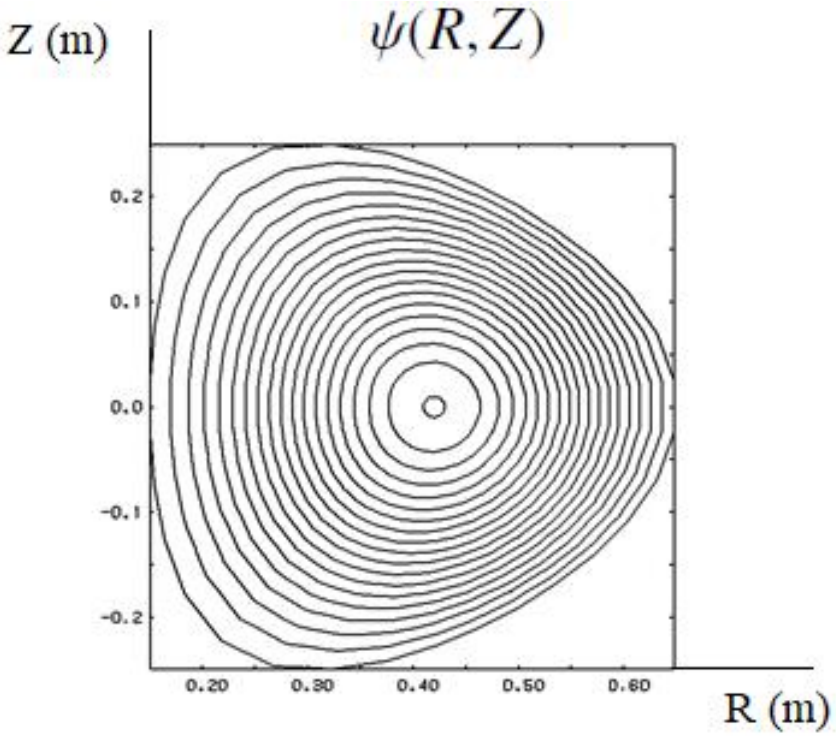

Figure 19: simulated flux surfaces based on the table 3 for SMART

As shown in Table 1, at the third phase of SMART, the magnetic field is increased alongside the increasing of triangularity and elongation, but in table 3 another configuration is suggested that generate the equilibrium condition and is applicable too. By considering these parameters, the equilibrium is achieved through applying very less magnetic fields and plasma current compared to the third phase.

Another geometrical configuration is considered and listed in table 4.

Table 10: basic designing parameters of SMART

	fixed parameters	value
1	Major radius (m)	0.4
2	Minor radius (m)	0.25
3	Minor blanket radius (m)	0.35
4	Aspect ratio	1.6
	suggested parameters	value
5	elongation	2
6	triangularity	0.52
7	Magnetic field (T)	0.1
8	Plasma current (MA)	0.1

The flux surfaces that are obtained based on the fixed and suggested parameters listed in the table 4 are shown in figure 5.

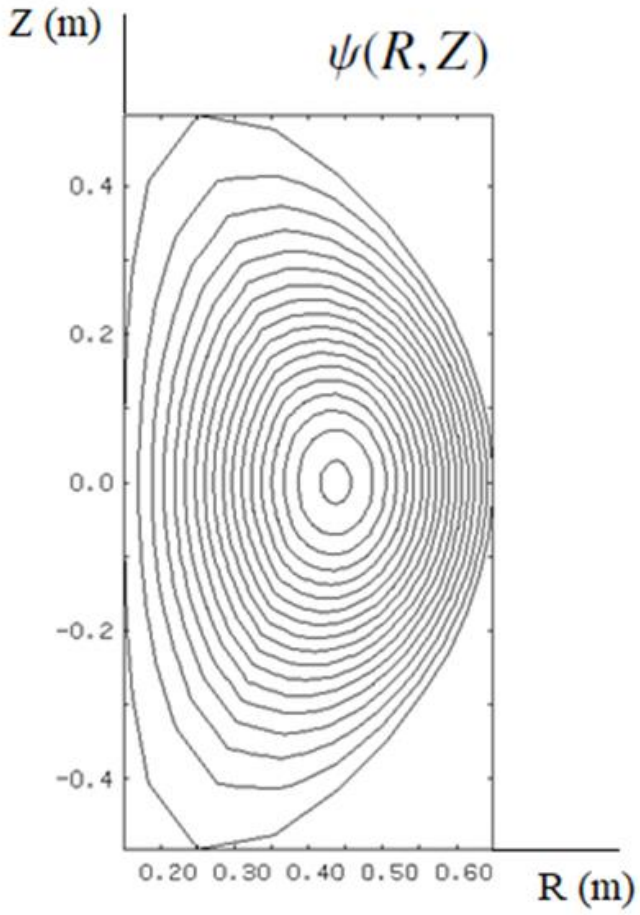

Figure 20: simulated flux surfaces based on the table 4 for SMART

To investigate the influence of the elongation and triangularity on the plasma parameters, two configurations of SMART tokamak based on the two suggested parameters of SMART (see Table 3, 4) are compared and the resulted quality factor in these two mentioned configurations is shown in figure 6.

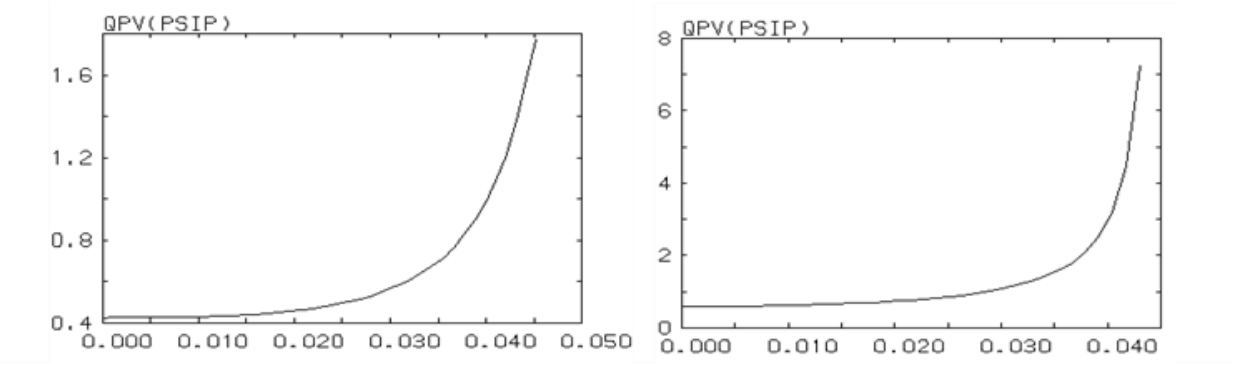

Figure 1: Normalized quality factor in two configurations, right) the first suggested and left) the second suggested parameters

Another quantity that is studied is the beta value. The poloidal and toroidal beta values, elongation and triangularity are defined as below [11]:

$$\beta_{toroidal} = \frac{\int pdV/V}{B_0^2/2\mu_0}, \quad \beta_{poloidal} = \frac{(1/S)\int_S pdS}{B_{\theta a}^2/2\mu_0}, \quad \frac{(1+\delta)^2}{\varepsilon\kappa^2} = \psi_{yy}(1+\varepsilon,0)\psi(1+\varepsilon,0) \qquad (5)$$

where V, S and $\psi_{yy}(1+\varepsilon,0)$ are the volume, surface of the plasma and the outer equatorial point curvature respectively. As mentioned later, the poloidal and toroidal beta values as well as axis and surface quality factors can be obtained by TASK code which are listed in table 5.

Table 11: obtained beta and quality for in two suggested configurations

	Suggested configuration	Simulated parameters	Obtained values
1	Elongation=1	Toroidal Bate values	7.502×10^{-2}
2	Triangularity=0.38	Poloidal beta values	1.191×10^{-1}
3	Magnetic field (T)=0.1	Axis quality factor	4.196×10^{-1}
4	Plasma current (MA)=0.1	Surface quality factor	1.770
1	Elongation=2	Toroidal Bate values	6.764×10^{-2}
2	Triangularity=0.52	Poloidal beta values	2.535×10^{-1}
3	Magnetic field (T)=0.1	Axis quality factor	5.706×10^{-1}
4	Plasma current (MA)=0.1	Surface quality factor	7.231

Results and Discussion

Simulations show that by using new suggested structures the equilibrium condition will be satisfied by applying very lower amounts of magnetic field and plasma current. In the suggested configs (see table 3, 4) while the magnetic field is 10% less than the magnetic field and plasma current is 20% less than the plasma current in the third phase of SMART (see table 1) the equilibrium is achieved and has a high-quality factor and beta values. By applying a magnetic field 30% less than

the second phase of SMART, the equilibrium condition is satisfied but the triangularity should be decreased.

Simulations show higher poloidal beta values by applying higher amounts of elongation and triangularity so that by increasing the elongation 2 times the poloidal beta values increase more than two times. As shown, quality factor is very sensitive to elongation and triangularity too but the interesting point is that the surface quality factor will be increased strongly so that by increasing the elongation 2 times and triangularity 1.3 times, the quality factor multiplied by more than 4.

Conclusions

Showing more desirable plasma parameters same as high beta values and quality factors in the presence of very lower magnetic fields and plasma currents in more elongated structures with higher triangularity verifies the capability of the STs, but more elongated shapes causes more instabilities that disrupt the plasma and terminate the discharge. It means that an optimized elongation value is needed which can be found at first by solving the free boundary equilibrium and using some optimization procedures secondly.

References

[1] Pataki, A. (2013). et al. A fast, high-order solver for the Grad–Shafranov equation. Journal of Computational Physics 243: 28–45 29.

[2] Garabedian, P R. (2008). Three-dimensional analysis of tokamaks and stellarators, Proc Natl Acad Sci U S A,105(37):13716-9.

[3] Gryaznevich, M. (2019). Theoretical and experimental studies of confinement in high field STs. EPTC, Ghent, Belgium.

[4] Nath, D. and Munish, P. (2015). Computation of Fixed Boundary Tokamak Equilibria Using a Method Based on Approximate Particular Solutions. Journal of Applied Physics, 107(11):113302. Computers & Mathematics with Applications 70:1220-1233.

[5] Wesson, J and Campbell, D. (2011). Tokamaks, OUP Oxford.

[6] Noori, E, Sadegi, Y and Ghorannevis, M. (2016). Application of poloidal beta and plasma internal induvtance in determination of input power time of Damavand tokamak. J theor Appl Phys.

[7] Segado-Fernandez, J and Mancini, A. (2023). Analysis and design of the central stack for the SMART tokamak, Fusion Engineering and Design 193(18):113833

[8] Mancini, A and Ayllon-Guerola, J. (2021) Mechanical and electromagnetic design of the vacuum vessel of the SMART tokamak.

[9]. http://bpsi.nucleng.kyoto-u.ac.jp/.

[10]. User Manual of the TASK Code .(2022).

[11] Freidberg, J, P. Cerfon, A. Lee, J. P. (2015). Tokamak elongation-How much is too much? Part 1. theory. Journal of Plasma Physics 81.

Numerical Investigation of nonlinear landau-damping using Semi-Lagrangian Vlaov-Poisson code (Paper ID: 1244)

Razavinia S.N[1*], Jamali S., Jazayeri S.M. [2]

[1] *Plasma Physics and Nuclear Fusion Research School, Nuclear Science and Technology Research Institute*

[2] *Department of Physics, Iran University of Science and Technology, Tehran*

Abstract

The Vlasov–Poisson system of equations is an important model for describing collisionless plasma. The kinetic description of collisionless plasma is provided by the nonlinear set of Vlasov-Maxwell and Vlasov-Poisson (in the electrostatic case) equations. In this paper, the Vlasov-Poisson equations have been numerically solved in one dimension using the Backward Semi-Lagrangian method, which is a subset of phase space-based methods. Phase space-based methods, which directly solve the hyperbolic partial differential Vlasov equation (PDE) in phase space, are free of numerical noise. In this method, the characteristic curves of the Vlasov equation have been traced backward in time for one time step, and the values of the distribution function at the origin of characteristics have been interpolated using the values on the grid points at the previous time step. The 1D1V periodic Vlasov-Poisson code has been utilized to investigate linear and non-linear Landau damping, which involves the damping of small oscillations in collisionless plasma. The effect of applied nonlinearity on Landau damping has been studied using the Vlasov-Poisson code. The results indicate that in the case of linear Landau damping, the amplitude of the electric field decreases exponentially, and the kinetic energy of electrons increases as time progresses. The damping rate depends on the perturbation wave number. In the nonlinear case, the electrostatic energy of the wave exhibits oscillatory behavior and periodically exchanges energy with electrons.

Keywords: Vlasov-Poisson equations, Landau damping, Semi-Lagrangian method

Introduction

Vlasov equation, which describes the collective motion of a collisionless plasma has a wide range of applications for studying collisionless plasma and the propagation of charged particle beams. In collisionless plasmas coulomb interaction between charged particles have been approximated by a mean field which in electrostatic case computed from Poisson equation and in electromagnetic case computed from Maxwell equations [1]. There are various methods for numerical solution of

hyperbolic PDE[4] Vlasov equation, that nonlinearly coupled to Poisson or Maxwell equations [2]. These methods are categorized into particle-based [3] and grid-based methods, each of them has multiple subsets. For instance, grid-based methods are divided into two categories: Eulerian solvers [4] based on finite volume or discontinuous Galerkin method and Semi-Lagrangian methods [5]. Most of the time numerical solution of Vlasov-Poisson equations have been performed using PIC[5] methods, that have Lagrangian nature and estimate plasma by limited number of super particles. In spite of simplicity, robustness and scalability, these methods suffer from numerical noise which caused by the limited number of super particles. However, numerical noise due to approximating plasma by super particles could be avoided by direct integration of Vlasov equation on phase space. These approaches have Eulerian nature. Another advantage of direct Vlasov solvers is detailed information of distribution function in phase space. Numerical solution of Vlasov equation in 6-dimensional phase space (3-D configuration space and 3-D velocity space) is computationally expensive and therefore need huge computer resources and parallel computing [6]. Semi-Lagrangian methods trying to take advantage of both PIC and Eulerian methods. In basic form of Semi-Lagrangian methods, which called Backward Semi-Lagrangian (BSL) method, characteristics of Vlasov equation are integrated backward in time, then an interpolation procedure has been done to find distribution function at the origin of characteristic curves [5]. Landau damping is one of the main and important issues in plasma physics. The importance of investigation and analysis of Landau damping have two aspects: first, this phenomenon establishes a connection between collective behavior and single-particle behavior in plasma. On the other hand, in studies related to plasma transport, reduced fluid models that include kinetic effects such as nonlinear Landau damping, are of great importance [7]. During linearization and analytical solution of the Vlasov equation some important aspects of Landau damping have been lost, therefore the use of numerical solutions of the Vlasov equation is of great importance for studying this phenomenon. In this paper we use Backward Semi-Lagrangian algorithm to develop 1D1V Vlasov-Poisson code in C++ language. This code has been used to investigate linear and nonlinear Landau damping. First Vlasov-Poisson system of equations introduced, then numerical algorithm described and finally numerical results are presented.

[4] Partial Differential Equation
[5] Particle In Cell

Vlasov-Poisson equations

Kinetic equation of a system in which collective effects dominate binary collisions is Vlasov equation. In Vlasov plasma, plasma parameter $n\lambda_D^3$ is large, for instance, value of plasma parameter for fusion plasma is in the range of $10^7 - 10^9$ and for space plasma is larger than 10^{10}. Vlasov equation is a hyperbolic partial differential equation, in which collisional effects are introduced through the average electromagnetic fields. In electrostatic case, which considered here, this field is computed from Poisson equation. In this manuscript, we use one-dimensional Vlasov-Poisson equations to study Landau damping. The assumptions considered in this problem are introduced in the following. Vlasov equation is only written for electron distribution function and ions are considered as a fixed homogeneous, neutralizing background with density of n_0. Time is normalized to the inverse of electron plasma frequency ω_{pe}^{-1}, length is normalized to Debye length λ_D , momentum is normalized to $m_e v_{th}$ and density is normalized to n_0. Dimensionless Vlasov equation has the following form:

$$\frac{\partial f(x,p,t)}{\partial t} + p\frac{\partial f(x,p,t)}{\partial x} + E(x,t)\frac{\partial f(x,p,t)}{\partial p} = 0 \qquad (1)$$

In this equation, $f(x,p,t)$ is electron distribution function in phase space and $E(x,t)$ is the self-consistent electrostatic field, computed from Poisson equation. In equation (2), $\varphi(x,t)$ is electric potential and $\rho(x,t)$ represents the electron charge density, which is computed from electrons distribution function.

$$\frac{\partial^2 \varphi(x,t)}{\partial x^2} = -\frac{\partial E(x,t)}{\partial x} = \rho(x,t) - 1 \qquad (2)$$

$$\rho(x,t) = \int f(x,p,t)dp \qquad (3)$$

Equations (1) and (2) are nonlinearly coupled through electron charge density. Periodic boundary conditions are imposed in x and p directions.

Numerical Approach

We use Backward Semi-Lagrangian method to solve the system of equations (1) and (2) which coupled nonlinearly. Basic idea of BSL method is using the invariance of distribution function

along characteristic curves of Vlasov equation. In this method, phase space grid is fixed in time (Eulerian approach), and Vlasov equation is integrated backward in time along its characteristic curves (Lagrangian approach). Then, the value of distribution function on phase space grid points is computed using cubic spline interpolation. The characteristic curves of Vlasov equation are defined by the following set of ordinary differential equations:

$$\begin{aligned} \frac{dx}{dt} &= p \\ \frac{dp}{dt} &= E(x,t) \end{aligned} \qquad (4)$$

Computational grid is constructed by introducing a finite set of mesh points $(x_i)_{i=1,\ldots,N_x}$, $(p_j)_{j=1,\ldots,N_p}$ in phase space. In summary, different steps of Backward Semi-Lagrangian code for solving equations (1) and (2) are as follows:

1- Initializing distribution function on phase space grid $f(x_i, v_j, t=0)$ and calculating charge density $\rho(x_i, v_j, t=0)$ using equation (3).

2- Computing electric field using the solution of the Poisson equation (equation (2)).

3- Solving characteristic curves of Vlasov equation (equation (4)) which ends at x_i to find starting point of them.

4- Computing distribution function at starting point of characteristics using cubic spline interpolation.

Semi-Lagrangian method has an implicit nature. Since the method is equivalent to solving the characteristics of Vlasov equation, in this method integration along x or p are nothing but Lagrangian advections. In Semi-Lagrangian method, time step is not restricted by Courant condition ($|U\,\Delta t/\Delta x| < 1$), but by the deformational Courant number ($\|(\partial U/\partial x)\Delta t\| < 1$), which is often less restrictive [5]. In fact, in this scheme characteristics of Vlasov equation could be stably integrated with Courant numbers that far exceed unity. The accuracy of Semi-Lagrangian methods can be achieved by less computational cost, compared to explicit Eulerian methods, since this

scheme can use larger time steps than Eulerian ones, but the price to pay is to reconstruct a regular grid using interpolation.

Simulation of Nonlinear Landau Damping

Nonlinear Landau damping was first predicted analytically by Landau in 1946 [8]. Subsequently, this phenomenon has been observed experimentally [9] and numerically [10] in various physical systems. Classical Landau damping occurs in the interaction of a plasma wave with warm plasma. Electrons that move with velocities close to the phase velocity strongly interact with wave, and depending on their initial phase in plasma wave, they could be accelerated or decelerated. The average velocity of electrons which are closed to resonance, approaches the phase velocity of wave. The total energy of resonance electrons increases if the number of electrons that moving at velocities lower than the wave's phase velocity is greater than the number of electrons that moving at velocities higher than the phase velocity of wave. In this phenomenon, due to wave-particle interaction, electrostatic energy of wave reduces exponentially (linearly in logarithmic scale). In order to gain a physical insight to the value of basic parameters of plasma in Landau damping problem, the reader can refer to reference [11] and the experimental work in reference [9], in which collisionless damping of electrostatic waves have been studied in a plasma with density of $5\times10^{8}[cm^{-3}]$, temperature of $12\pm3eV$ and Debye length of about $1mm$. In order to study this behavior using Vlasov code, we introduce a small perturbation to the Maxwellian distribution function. Initial distribution function is defined as $f(x,p,t=0)=\frac{1}{\sqrt{2\pi}}\exp(-\frac{p^2}{2})(1+\alpha\cos(kx))$. That k is the wave number and α is the amplitude of initial perturbation (nonlinearity). Amplitude of initial perturbation, that appear in the initial distribution function ($f(x,p,t=0)$) determines linear or nonlinear regime (except for longer times that explained in the following). Perturbed initial distribution function would change electron charge density in equation (3), by changing charge density, electric field in right hand side of equation (4) (characteristic curves) also changes. In linear Landau damping, the amplitude of perturbation is sufficiently small, therefore, oscillatory term in electric field at the right-hand side of equation (4) is small and exponential term is dominant. We consider a periodic plasma with a length of $L=2\pi/k$. Only electrons are moving, while ions form a homogeneous neutralizing background. To observe linear Landau damping, the

size of velocity computational domain should be greater than the phase velocity $v_\phi = \omega/k$, which ω is wave frequency and computed using the normalized dispersion relation $\omega^2 = 1+3k^2$. The number of grid points along x direction is $N_x = 256$, and the number of grid points along p direction is $N_p = 256$. The time step of simulation is set to $\Delta t = 0.1$, and the spatial step size is set to $\Delta x = L/N_x$. Figure 1(a) shows time evolution of electrostatic wave energy per plasma length $\varepsilon(t) = \frac{1}{2L}\int E_x^2(x,t)dx$ for a given wave number $k\lambda_{De} = 0.3$ and a very small perturbation $\alpha = 0.001$. According to Landau's theory, we expect that field amplitude decreases exponentially over time. The damping rate $\gamma = \frac{\pi}{2}\omega_{pe}^2 \frac{\omega}{k^2 n_0}\left(\frac{\partial f_0(v)}{\partial v}\right)_{v_\phi}$, calculated using linear theory, depends on the derivative of equilibrium distribution function with respect to velocity in the vicinity of the phase velocity [12]. Calculated analytical damping rate for given wave number and the introduced distribution function is $\gamma = 0.0259\omega_{pe}$. As we can see in the relation of initial distribution function, Landau damping problem has two dimensionless parameters: strength of nonlinearity α and wave number k. The damping rate depends on the wave number and time $\tau = \alpha^{-1/2}$. Linear Landau damping is valid for times up to $t < \tau$ and for longer times, independent of initial perturbation, it will be intrinsically nonlinear [1]. Theoretical studies indicate that after the initial Landau damping, due to periodic exchange of energy between electrons that trapped in plasma potential and wave, the wave amplitude oscillates in time. As we can see in figure 1(a), in linear regime electric field decreases exponentially with time. In nonlinear regime, the amplitude of perturbation is not small anymore and therefore, oscillatory term in electric field plays a significant role. According to equation (4), temporal evolution of electron velocities depends on electric field. Therefore, behavior of electric field, that affected by the amplitude of initial perturbation, determines evolution of electron velocities over time. For instance, in nonlinear Landau damping, the particles that travel relative to the wave will trap in potential well of the wave. The trapped electrons will be bounced back and forth in the potential well, causing fluctuating amplitudes of the wave. Figure 1 (b) shows that by increasing the initial perturbation to a value of $\alpha = 0.01$, until time $t\omega_{pe} \approx 60$ the wave amplitude decreases exponentially. After this time, the amplitude of oscillations tends to a constant value. Therefore, Landau damping does not continue indefinitely,

and after the initial damping, it takes the form of oscillations with a relatively constant amplitude. In Figure 2, time evolution of average kinetic energy of electrons and electrostatic wave energy for initial perturbation $\alpha = 0.1$ are compared. Normalized average kinetic energy of electrons is defined as $K(t) = \frac{1}{2L}\int p^2 f(x,p,t)dxdp$. This perturbation leads to nonlinear Landau damping.

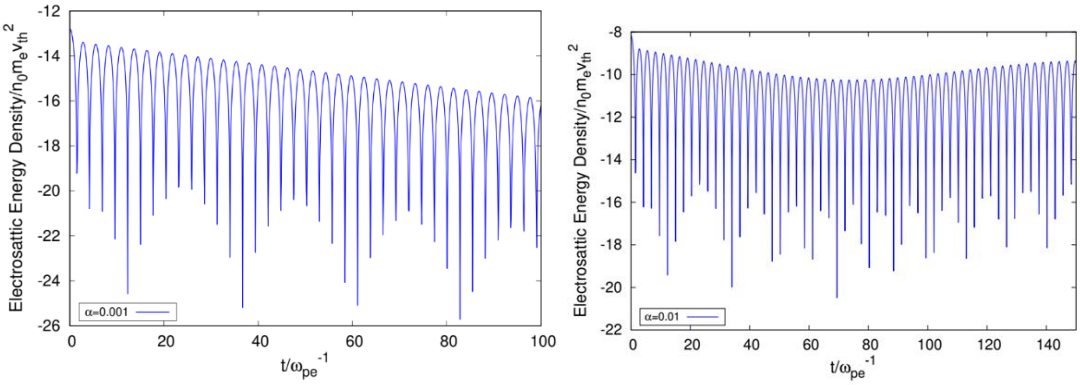

(a) (b)

Fig. 1. Time evolution of electrostatic energy for $k\lambda_{De} = 0.3$ (a) $\alpha = 0.001$ (b) $\alpha = 0.01$ in logarithmic scale

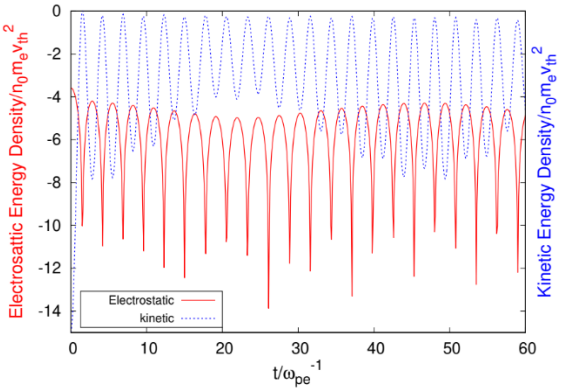

Fig. 2. Time evolution of electrostatic energy (red) and kinetic energy (blue) for $k\lambda_{De} = 0.3$ and $\alpha = 0.1$ in logarithmic scale

As a result, we observe that electrostatic energy of wave oscillates around a constant value. We can see energy exchange between electrons and wave. At points where kinetic energy of electrons reaches its maximum value, the electrostatic energy reaches its minimum value. In fact, at these points, electrons gain energy from wave, and their kinetic energy increases. In the next phase, the

kinetic energy of electrons decreases, and the electrostatic energy increases. This energy exchange between electrons and wave leads to the oscillation of electrostatic wave around a constant value.

The results are in agreement with reference [13], in which a structure-preserving Particle-in-Cell algorithm have been used for solving the electrostatic Vlasov-Poisson systems. Time evolution of electrostatic energy of wave in linear Landau damping case is in agreement with the results in reference [14], in which Vlasov-Poisson system of equations have been solved numerically by using a new particle-in-cell method, that is 4th-order accurate in both space and time.

Conclusions

In this paper Vlasov-Poisson system of equations have been solved numerically. Numerical solution of Vlasov equation that coupled to Poisson or Maxwell equation plays an important role in simulation of space plasma, laser-plasma interaction and magnetically confined fusion plasma. Here, we solve Vlasov-Poisson equations using Semi-Lagrangian method. This method, is free from numerical noise and due to direct integration of Vlasov equation along its characteristics, there is no limitations on time step size. One of the disadvantages of grid-based methods is their requirement to huge computer resources for six-dimensional(3D3V) problems in phase space. This problem could be avoided using parallel computing and efficient algorithms. Here, we use Semi-Lagrangian 1D1V Vlasov-Poisson periodic code for numerical investigation of Landau damping. Simulation results indicate that in linear Landau damping, the amplitude of the electrostatic wave exponentially decreases over time, while the kinetic energy of electrons increases. The damping rate depends on the perturbation wave number. In non-linear Landau damping, the electrostatic energy exhibits oscillatory behavior, and electrostatic wave periodically exchanges energy with electrons. In future works we would extend dimensions of the code in order to investigate two dimensional problems. Moreover, we would study long time behavior of nonlinear Landau damping by using efficient parallel algorithms.

References

[1] J. Buchner, (2007) Vlasov-code simulation. Advanced Methods for Space Simulations, edited by H. Usui and Y. Omura, pp. 23–46.

[2] E. Sonnendrucker, (2013) Numerical methods for the Vlasov equation. Max-planck institute Lecture notes.

[3] C. K. Birdsall, A. B. Longdon, (1986) Plasma physics via computer simulation. McGraw-Hill, New York.

[4] E. Pohn , M. Shoucri, G. Kamelander, (2005) Eulerian Vlasov codes. Computer Physics Communications 166 ,81–93.

[5] E. Sonnendrücker, J. Roche, P. Bertrand and A. Ghizzo, (1999) The semi-Lagrangian method for the numerical resolution of the Vlasov equation. J. Comput. Phys. 149, 201– 220.

[6] K. Kormann, K. Reuter and M. Rampp, (2019) A massively parallel semi-Lagrangian solver for the six-dimensional Vlasov–Poisson equation. The International Journal of High Performance Computing Applications Vol. 33(5) 924–947.

[7] G. Manfredi, (1997) Long-Time behavior of nonlinear landau damping. Phys. Rev. Lett 79, 2815-2818.

[8] L.D. Landau, (1946) On the vibrations of the electronic plasma. J. Phys (USSR) 10 25-34.

[9] J. H. Malmberg and C.B.Wharton, (1964). Colliosionless damping of electrostatic plasma waves, Phys. Rev. Lett. 13 184.

[10] R. R. J. Gagne and M. M. Shoucri, (1977) A splitting scheme for the numerical solution of a one-dimensional Vlasov equation" J.Comput. Phys 24 445.

[11] Chen, Francis F. (1984). Introduction to Plasma Physics and Controlled Fusion II . , 10.1007/978-1-4757-5595-4

[12] F. Valentini (2005), Nonlinear Landau damping in nonextensive statics. Physics of Plasmas. 12, 072106.

[13] DS Finn, MG Knepley, JV Pusztay, MF Adams, A numerical study of Landau damping with PETSc-PIC, in Applied Mathematics and Computational Science, 2023.

[14] Myers, A.; Colella, P.; Straalen, B. Van (2017). A 4th-Order Particle-in-Cell Method with Phase-Space Remapping for the Vlasov--Poisson Equation. SIAM Journal on Scientific Computing, 39(3), B467–B485.

ICNST 2024
International Conference on Nuclear Science and Technology
6- 8 MAY 2024 | Isfahan, Iran

The comparative study of helium-generated direct and indirect cold atmospheric plasma effects against human skin cancers: An in vitro study (Paper ID: 1250)

Bakhtiyari-Ramezani M. [1*], Baniasadi M. [2]

[1*] Plasma Physics and Nuclear Fusion Research School, Nuclear Science and Technology Research, Institute (NSTRI), Tehran, Iran
[2] Plasma Technology Development Company, Tehran, Iran

Abstract

Skin cancer is one of the most prevalent cancer types globally and is broadly categorized as nonmelanoma skin cancer (NMSC) and melanoma. Malignant melanoma is the third common type of skin cancers, and stands out as the most aggressive and deadly form of cancer. When melanoma detects in its early stages, surgical excision can often lead to a complete cure. However, for advanced-stage tumors, the prognosis tends to be poor, necessitating the use of additional therapies like chemotherapy or immunotherapy. It's worth noting that systemic therapies can result in severe side effects in healthy tissues and frequently yield unsatisfactory outcomes. Therefore, there is a growing need for innovative therapeutic approaches and the implementation of localized treatments through extensive clinical studies. One hopeful advancement is cold atmospheric plasma (CAP) technology, that displays specificity for *in vitro* and *in vivo* therapy of different malignancies, leading to the creation of a novel studies in medication named "plasma oncology". In this research, our objective was to explore the effect of our CAP device composed of helium in two approaches of direct and indirect on human wild type A-375 malignant melanoma cell viability compared with normal human epidermal melanocyte in the cellular phases. IC_{50} dose was determined by MTT assay. Our results showed CAP treatment in both direct and indirect approaches have a selective killing effect on A-375 melanoma cell lines at its IC_{50} dose while, provide superior safety for its counterpart normal fibroblast AGO-1522 cell lines.

Keywords: Cold atmospheric Plasma, Helium plasma, Plasma medicine, Melanoma, Cancer

Introduction

The skin, constituting approximately 15% of an adult's total body weight, is the body's largest organ and is contained of three layers: the epidermis, the dermis, and the subcutaneous tissue (1). It carries out numerous crucial functions, including shielding the body against external chemical physical, chemical, and biological threats, preventing excessive water loss, and contributing to thermoregulation. The thickness of these layers varies significantly, depending on the body's geographic location and anatomy (2). The remarkable rate of cell proliferation in the epidermis, which is frequently exposed to physical and chemical hazards, has led to an exceptionally high incidence of skin cancers (3). Skin cancer is one of the most prevalent cancer types globally and is broadly categorized as nonmelanoma skin cancer (NMSC) and melanoma. Determining the precise incidence of skin cancer poses challenges due to the absence of clear diagnostic criteria and underreporting. Nevertheless, numerous epidemiological studies have presented evidence of a rising occurrence of both nonmelanoma skin cancer (NMSC) and melanoma in recent decades (4).

Melanoma stands out as the most aggressive and deadly form of cancer, and the primary treatment of choice is surgical excision. When detected in its early stages, surgical excision can often lead to a complete cure. However, for advanced-stage tumors, the prognosis tends to be poor, necessitating the use of additional therapies like chemotherapy or immunotherapy (5). It's worth noting that systemic therapies can result in severe side effects in healthy tissues and frequently yield unsatisfactory outcomes. Therefore, there is a growing need for innovative therapeutic approaches and the implementation of localized treatments through extensive clinical studies.

In recent times, there have been noteworthy advancements in the realm of CAP engineering and science. Innovative CAP sources have been established, characterized by precise temperature control, ensuring that they operate at temperatures below 40 ℃. This breakthrough has made it possible to safely apply plasma to both human bodies and animal. Over the past decade, a pioneering field known as plasma medicine has emerged, seamlessly integrating principles from plasma physics, life sciences, and clinical medicine (6, 7).

While the effectiveness of cold atmospheric pressure plasma therapy in human subjects with skin cancer remains somewhat constrained, findings from in vitro experiments and animal models of

skin cancer strongly indicate that CAP therapy holds significant potential for future clinical applications in the treatment of skin cancer (8, 9).

In addition to the noted therapeutic benefits of plasma on melanoma, SCC, and BCC, it is important to acknowledge that the anti-tumor potential of CAP can be modulated by various factors, including treatment duration, gas source composition, supply voltage, and gas flow rate. Furthermore, the diverse range of CAP devices in use leads to variations in the composition and concentration of plasma components, encompassing charged particles, electrons, UV light, reactive species, and heat (10). Consequently, comparing the outcomes of different CAP studies becomes challenging and, in some cases, impractical. As a result, there is a growing interest and active research focus on optimizing CAP design and treatment parameters to ensure its efficacy and selectivity in targeting different organisms and cell types. In this context, we are conducting an investigation into the therapeutic potential of our innovative CAP technology in treating melanoma in the in vitro phase.

Material AND Methods

Experimental procedures

This study was planned and implemented in cell line part.

Cell culture

In this study, A-375 melanoma cell line was gotten from Pasteur Institute of Iran and cultured in monolayers utilizing RPMI 1640 Glutamax supplemented with fetal bovine serum 10% and 1% antibiotic at 90 % humidity, 37ºC, and 5% CO2. The cells were seeded in 96 well cell culture plates, each containing 2500 cells for all the concentrations and the control group.

Plasma Jet source

Plasma Technology Development Company (Tehran, Iran) provided plasma sources for this research **Figure 1. a**. Previous work mentioned details of the plasma source, configuration, and OES spectroscopy results (10).

Plasma treatment of cancer cells

The two treatment strategies were adopted in this study as follow: direct plasma treatment and indirect plasma treatment. In the direct method, the plasma jet was used directly against the cells in the medium (**Figure 1. b and c**). In the indirect method, cold plasma was first irradiated to the culture medium and then the cells were added to the culture medium All experimental setup was performed at a 4 cm distance from the well plate (10). The cell lines were classified into 6 groups including: (a) Model group of A-375 melanoma cells with no treatment; (b) The A-375 melanoma cells which treated by direct helium CAP; (c) The A-375 melanoma cells which treated by indirect helium CAP; (d) The untreated normal fibroblast AGO-1522 cells; (e) The normal fibroblast AGO-1522 cells which treated by direct helium CAP; (f) The normal fibroblast AGO-1522 cells which treated by indirect helium CAP.

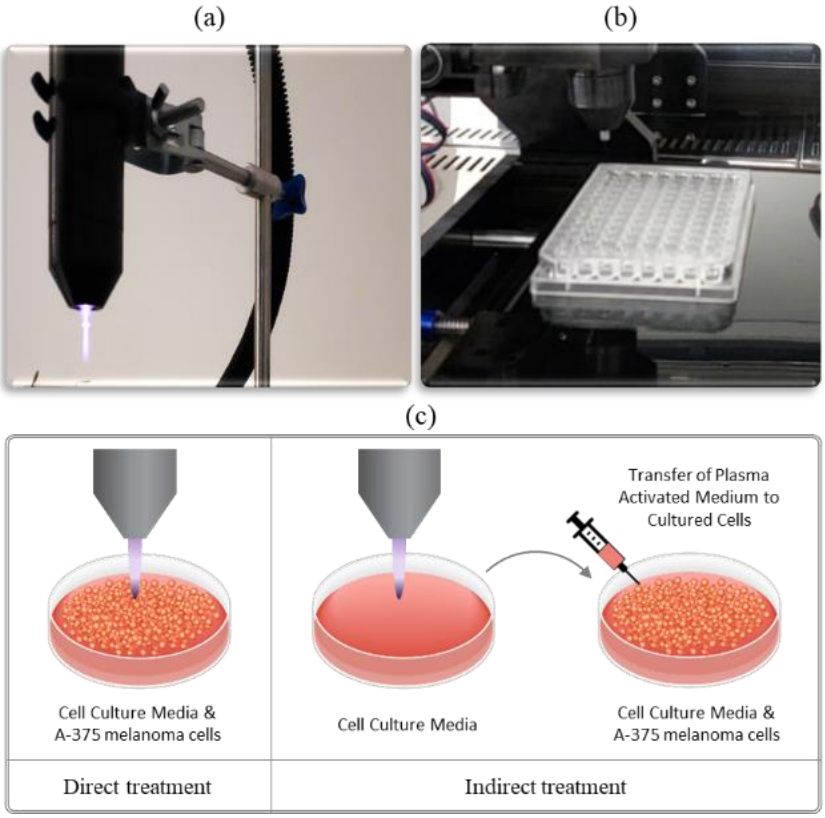

Fig 21. a. Illustration of plasma source, b. Plasma treatment of cells, c. Direct and Indirect methods of treatment

Cell viability assessment

After up to passage 7, melanoma cells were detached with trypsin-EDTA 0.25% and seeded into a 96-well polystyrene microplate at 5×10^3 cells per well along with 100 μL of culture media. The cells were cultured for 24 hours to ensure stability and suitable cell adhesion. The condition media was removed, and in order to the dead cell's elimination, single wash with PBS was performed. Renewed condition media was added. In order to the IC50 dose of CAP determination, cells were treated by CAP for 90, 120, 150, 180, and 210 seconds, in two approaches of direct and indirect. Then, cells were incubated at 37 °C for 24-, 48-, and 72-hours post-treatment (10). Then, the cell viability was assessed by MTT (3-(4,5-Dimethylthiazol-2-Yl)-2,5-Diphenyltetrazolium Bromide) assay at 24, 48, and 72 hours after treatment according to the manufacturer's protocol. After washing the cells with PBS, 100 μL of MTT solution was added, and cells were incubated 3-hour in a humidified incubator at 37 °C with 5% CO_2 concentration. Then, the unreacted MTT solution was removed from all wells, and 100 μL of DMSO solvent (0.4% HCl in anhydrous isopropanol) was gently placed directly into each well. The measurement was taken either after 10 minutes or within half an hour using a microplate reader at an absorbance of 570 nm, following a 30-second linear shaking. For accuracy, the entire set of experiments was performed three times.

Statistical data analysis

The study provides descriptive statistics as means ± standard errors. The Shapiro-Wilk test was investigated in order to assess the normality of the quantitative data distribution. In cases where the data distribution was obtained by normality, data transformation methods including inverse distribution functions and Box-Cox transformations (11) were performed. To assess the variables among various study groups, one-way analysis of variance and Bonferroni's post hoc test were performed. The statistical difference level was set at $p < 0.05$, and all data analysis was performed using SPSS Statistics 27.0.

Results

The growth-inhibitory effects of CAP on human A-375 melanoma and normal fibroblast AGO-1522 cells

To assess the optimal exposure time for direct and indirect helium CAP therapy, we evaluate the viability of A-375 melanoma cells at five exposure times: 90, 120, 150, 180, and 210 seconds. We performed the assessment after 24, 48, and 72 hours of continuous cultivation after the exposure by the MTT assay. The results exhibited the cell death rate, influencing by both the duration of cultivation after treating and the exposure time. The IC_{50} values at 48 and 72 hours after treatment further validate the consistent toxicity of direct helium gas. The best exposure times were 70.15 and 138 seconds at the 48-hour post-treatment time point for direct and indirect helium CAPs, respectively, based on the calculated IC_{50} values (Figure 2). Because the IC_{50} value for direct helium CAP was attained after 48 hours of treatment (15.41 seconds), which was outside of plasma treatment times range, we done additional MTT tests with exposure times of 30, 45, 60, 75, and 90 seconds after 48 hours of continuous cultivation. The results showed that the IC_{50} value for helium CAP jet after 48 hours of cultivation is 70.15 second.

The influence of the IC_{50} dose of the helium CAP on normal fibroblast AGO-1522 cells was also evaluated. The cell viability of AGO-1522 cells was 94.76% for direct helium, and, 95.98% for indirect helium and no significant difference was observed.

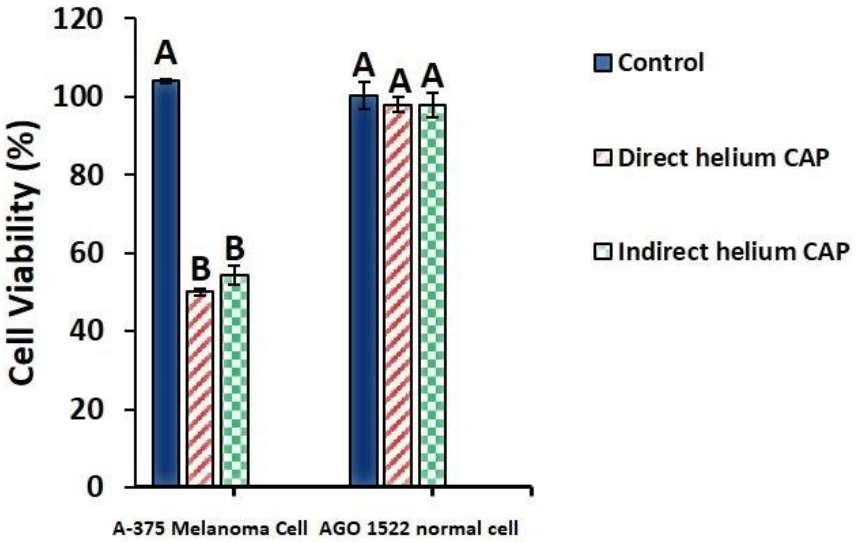

Fig 2. Treatment of A-375 melanoma cells and normal fibroblast AGO 1522 cells with IC_{50} dose of helium CAP directly and indirectly.

Discussion

Skin malignancies are one of the most prevalent cancers. In the Islamic Republic of Iran, skin cancer also is the most prevalent cancer, with a male-to-female ratio of 1.6, observed in the 70th and 80th decades of life (12). The prevalence of malignant melanoma increased in the last decades in many parts of the world. The prevalence of this malignancy has tripled in the last 40 years, that has been more than any other malignancies (13, 14). Disability, Cosmetic problems, and high costs of it, especially its long-term form, cause this cancer to be a general health problem in many countries (16). Although malignant melanoma only comprises 4% of all cancers, but it is the cause of death in about 79% of types of malignancy which shows that the current treatments have been less effective (15). Therefore, novel methods and therapeutic targets are necessary for melanoma cancer management (16, 17).

In recent years, advances in technologies have led to the possibility of new physical interventions in different fields, including dermatology, sterilization, wound healing, dentistry, sterilization, medical applications, and clinical oncology (18, 19). The considerable interests are received in Cold Atmospheric Plasma, which shows specificity for in vitro and in vivo treatment of different malignancies, in combination with other common treatments or alone, leading to the creation of a new field in medicine named "plasma oncology" (20, 21).

The current study aims to assess efficacy and safety of helium CAP on human A-375 melanoma cells in compared with fibroblast normal cells. The optimal exposure times were 70.15 and 138 seconds at the 48-hour post-treatment time point for direct and indirect helium gases, respectively, based on the calculated IC_{50} values. This data approves previous researches (22, 23) , which demonstrated the effect of CAP on cell death, influencing by the duration of cultivation after treating and the exposure time.

One of the challenges in presenting a novel therapeutic method is verifying its safety for healthy cells. It is essential to mature therapies that specifically diminish damage to healthy tissues while effectively abolishing tumor cells (24, 25). The physical and chemical characteristics of CAP have made it a unique tool in various medical field such as oncotherapy. Studies have shown that all anticancer effects of cold plasma are mediated through reactive oxygen and nitrogen species

(RONS), both in vivo and in vitro (28, 29). These compounds activate the signaling cascade that ultimately leads to the death of cancer cell. Unlike common cancer treatments such as chemotherapy and radiotherapy, which also destroy healthy cells and therefore have many side effects, plasma therapy destroys cancer cells without harming healthy cells (30).

As we know, the anticancer effect of CAP is through increasing reactive oxygen species, causing oxidative stress and finally cell death. Although the mechanism of the selective action of cold plasma on cancer cells is not precisely known, some hypotheses have been proposed so far. One of the possible mechanisms is the difference in the basal levels of reactive oxygen species in cancer and healthy cells. Studies have shown that cancer cells have higher amounts of reactive oxygen species in the basal state than healthy cells. It leads to their greater sensitivity to reactive oxygen species produced by plasma. Another model suggests that cancer cells have more aquaporin channels on their surface and hydrogen peroxide produced by plasma diffuses into cancer cells faster, which increases ROS in cancer cells (31, 32). Some studies also stated that CAP-cell interaction leads to lipid peroxidation, which causes the formation of cell membrane pores and allows further diffusion of ROS and RNS. Because cancer cells have lower cholesterol levels, they are more susceptible to peroxidation and death (33, 34).

Our data revealed that CAP treatment in both direct and indirect approaches have a discerning killing effect on A-375 melanoma cell lines at its IC_{50} dose, providing superior safety for its counterpart normal fibroblast AGO-1522 cell lines. Confirmation of our results, many studies have also highlighted that CAP does not damage normal cells where applied at proper dosages, introducing CAP as a selective treatment mood for killing cancer cells (26, 27).

Conclusions

The purpose of this study, the use of a non-thermal helium plasma-based direct and indirect was to treat selectively in human wild type A-375 malignant melanoma cell as compared with normal human epidermal melanocyte in the cellular phases. Following a plasma exposure, IC_{50} dose in the cell death of melanoma after 48 hours of cultivation was obtained 70.15 second. Also, the results obtained out studies exhibited that both direct and indirect approaches have a selective killing effect on A-375 melanoma cell lines, meanwhile, this method did not showed toxicity on normal

fibroblast AGO-1522 cell lines. The results confirm that the cold atmospheric plasma can be used as a potential treatment for melanoma, however, more preclinical studies with a larger sample size are needed to draw accurate conclusions.

References

1. Dehdashtian A, Stringer TP, Warren AJ, Mu EW, Amirlak B, Shahabi L. Anatomy and Physiology of the Skin. Melanoma: a modern multidisciplinary approach. 2018:15-26.

2. Kolarsick PA, Kolarsick MA, Goodwin C. Anatomy and physiology of the skin. Journal of the Dermatology Nurses' Association. 2011;3(4):203-13.

3. Gordon R, editor Skin cancer: an overview of epidemiology and risk factors. Seminars in oncology nursing; 2013: Elsevier.

4. Rogers HW, Weinstock MA, Feldman SR, Coldiron BM. Incidence estimate of nonmelanoma skin cancer (keratinocyte carcinomas) in the US population, 2012. JAMA dermatology. 2015;151(10):1081-6.

5. Lugowska I, Teterycz P, Rutkowski P. Immunotherapy of melanoma. Contemporary Oncology/Współczesna Onkologia. 2018;2018(1):61-7.

6. Yousfi M, Merbahi N, Pathak A, Eichwald O. Low-temperature plasmas at atmospheric pressure: toward new pharmaceutical treatments in medicine. Fundamental & clinical pharmacology. 2014;28(2):123-35.

7. Braný D, Dvorská D, Halašová E, Škovierová H. Cold atmospheric plasma: A powerful tool for modern medicine. International journal of molecular sciences. 2020;21(8):2932.

8. Arndt S, Wacker E, Li YF, Shimizu T, Thomas HM, Morfill GE, et al. Cold atmospheric plasma, a new strategy to induce senescence in melanoma cells. Experimental dermatology. 2013;22(4):284-9.

9. Pasqual-Melo G, Nascimento T, Sanches LJ, Blegniski FP, Bianchi JK, Sagwal SK, et al. Plasma treatment limits cutaneous squamous cell carcinoma development in vitro and in vivo. Cancers. 2020;12(7):1993.

10. Bakhtiyari-Ramezani M, Nohekhan M, Akbari ME, Abbasvandi F, Bayat M, Akbari A, Nasiri M. Comparative assessment of direct and indirect cold atmospheric plasma effects, based on helium and argon, on human glioblastoma: an in vitro and in vivo study. Scientific Reports. 2024;14(1):3578.

11. G S. Normalize data in SPSS software. Statistical tutorials and software guides. Retrieved January, 12, 2022 2021. Available from: 2021 [Available from: https://graphpad.ir/transform-data-to-normal-distribution/.php.

12. Mohammadi M, Mirzaei M, Ahmadi A. Comparing of the Epidemiology of Skin Cancer in the Kurdistan and Yazd in 2012. SSU_Journals. 2015;23(4):2118-26.

13. Erdei E, Torres SM. A new understanding in the epidemiology of melanoma. Expert review of anticancer therapy. 2010;10(11):1811-23.

14. Schadendorf D, van Akkooi AC, Berking C, Griewank KG, Gutzmer R, Hauschild A, et al. Melanoma. The Lancet. 2018;392(10151):971-84.

15. Allen DC. Histopathology reporting. Springer.

16. Chen Z, Simonyan H, Cheng X, Gjika E, Lin L, Canady J, et al. A novel micro cold atmospheric plasma device for glioblastoma both in vitro and in vivo. Cancers. 2017;9(6):61.

17. Chen Z, Cheng X, Lin L, Keidar M. Cold atmospheric plasma discharged in water and its potential use in cancer therapy. Journal of Physics D: Applied Physics. 2016;50(1):015208.

18. Keidar M, Shashurin A, Volotskova O, Ann Stepp M, Srinivasan P, Sandler A, Trink B. Cold atmospheric plasma in cancer therapy. Physics of Plasmas. 2013;20(5).

19. Thakor AS, Gambhir SS. Nanooncology: the future of cancer diagnosis and therapy. CA: a cancer journal for clinicians. 2013;63(6):395-418.

20. Yadav DK, Adhikari M, Kumar S, Ghimire B, Han I, Kim M-H, Choi E-H. Cold atmospheric plasma generated reactive species aided inhibitory effects on human melanoma cells: An in vitro and in silico study. Scientific reports. 2020;10(1):3396.

21. Alimohammadi M, Golpour M, Sohbatzadeh F, Hadavi S, Bekeschus S, Niaki HA, et al. Cold atmospheric plasma is a potent tool to improve chemotherapy in melanoma in vitro and in vivo. Biomolecules. 2020;10(7):1011.

22. Gjika E, Pal-Ghosh S, Kirschner ME, Lin L, Sherman JH, Stepp MA, Keidar M. Combination therapy of cold atmospheric plasma (CAP) with temozolomide in the treatment of U87MG glioblastoma cells. Scientific Reports. 2020;10(1):16495.

23. Bekeschus S, Ispirjan M, Freund E, Kinnen F, Moritz J, Saadati F, et al. Gas plasma exposure of glioblastoma is cytotoxic and immunomodulatory in patient-derived GBM tissue. Cancers. 2022;14(3):813.

24. Yan D, Wang Q, Malyavko A, Zolotukhin DB, Adhikari M, Sherman JH, Keidar M. The anti-glioblastoma effect of cold atmospheric plasma treatment: Physical pathway vs chemical pathway. Scientific reports. 2020;10(1):11788.

25. Yousfi M, Merbahi N, Pathak A, Eichwald O. Low-temperature plasmas at atmospheric pressure: toward new pharmaceutical treatments in medicine. Fundamental & Clinical Pharmacology. 2014;28(2):123-35.

26. Iseki S, Nakamura K, Hayashi M, Tanaka H, Kondo H, Kajiyama H, et al. Selective killing of ovarian cancer cells through induction of apoptosis by nonequilibrium atmospheric pressure plasma. Applied Physics Letters. 2012;100(11).

27. Shashurin A, Keidar M, Bronnikov S, Jurjus R, Stepp M. Living tissue under treatment of cold plasma atmospheric jet. Applied Physics Letters. 2008;93(18).

28. Keidar M, Yan D, Beilis II, Trink B, Sherman JH. Plasmas for treating cancer: Opportunities for adaptive and self-adaptive approaches. Trends in biotechnology. 2018;36(6):586-93.

29. Khalili M, Daniels L, Lin A, Krebs FC, Snook AE, Bekeschus S, et al. Non-thermal plasma-induced immunogenic cell death in cancer. Journal of physics D: Applied physics. 2019;52(42):423001.

30. Mali SB. Role of Cold atmospheric plasma in cancer management. Oral Oncology Reports. 2024;9:100133.

31. Keidar M. Plasma for cancer treatment. Plasma Sources Science and Technology. 2015;24(3):033001.

32. Ma Y, Ha CS, Hwang SW, Lee HJ, Kim GC, Lee K-W, Song K. Non-thermal atmospheric pressure plasma preferentially induces apoptosis in p53-mutated cancer cells by activating ROS stress-response pathways. PloS one. 2014;9(4):e91947.

33. Xu K, Yin N, Peng M, Stamatiades EG, Shyu A, Li P, et al. Glycolysis fuels phosphoinositide 3-kinase signaling to bolster T cell immunity. Science. 2021;371(6527):405-10.

34. Galluzzi L, Vitale I, Aaronson SA, Abrams JM, Adam D, Agostinis P, et al. Molecular mechanisms of cell death: recommendations of the Nomenclature Committee on Cell Death 2018. Cell Death & Differentiation. 2018;25(3):486-541.

ICNST 2024
International Conference on Nuclear Science and Technology
6- 8 MAY 2024 | Isfahan, Iran

Simulation of the effect of magnetic field profile generated by permanent magnets on plasma density in ECR plasma source using Comsol multiphysics (Paper ID: 1253)

Razavinia, S.N[1*], Jamali, S

[1] *Plasma Physics and Nuclear Fusion Research School, Nuclear Science and Technology Research Institute*

Abstract

The development of high-density plasma sources, which provide high deposition rate, is one of the requirements for plasma processing of microelectronics devices. Electron cyclotron resonance (ECR) plasma sources have the ability to achieve high degree of ionization at low gas pressures. ECR plasma sources that use permanent magnets to produce the required magnetic fields for ECR condition are significantly more compact than systems equipped with electromagnets. In this paper we have simulated the evolution of ECR plasma in COMSOL Multiphysics 6.1. The magnetic fields no current module (MFNC) of COMSOL computes the magnetic flux density of permanent magnets. The results have been used in plasma module to compute plasma conductivity tensor. The electron number density and energy density are computed by solving drift-diffusion equation in plasma module, while high-frequency component of the electric field is calculated in frequency domain using electromagnetic wave frequency domain module (EMW). ECR plasma source that simulated here uses four NdFeB block magnets to create ECR surfaces inside plasma chamber. We have investigated the effect of the magnetic field profile on plasma density. Different profiles of the magnetic field inside the chamber have been achieved by changing the arrangement and polarization of permanent block magnets around plasma chamber. Profile of magnetic field inside chamber, plasma density and potential for three different cases have been computed and compared. Taking into account that higher plasma density is suitable for increasing the deposition rate in plasma processing, the best arrangement has been achieved.

Keywords: ECR plasma source, COMSOL Multiphysics, permanent magnet, plasma density

Introduction

Electron Cyclotron Resonance (ECR) plasma sources are magnetized plasmas, in which plasma is produced in a chamber by properly choosing the strength of external magnetic field and frequency of microwave energy source. Resonant condition for electrons can be obtained by setting up the

microwave frequency to be in resonance with gyration frequency of electrons around external magnetic field lines. In contrast to inertial confinement fusion (ICP) and helicon sources, the excitation source for an ECR plasma is in the microwave range. In ECR plasma sources, a right hand circularly polarized wave, which excited at microwave frequency (mostly 2.45 GHz), propagates along dc magnetic field lines in resonance condition (87.5 mT). Energy of wave is absorbed by collisionless heating mechanism [1]. ECR plasma sources have various applications in plasma processing such as etching [2,3] and deposition processes [4,5]. Generally, electromagnetic coils have been used for generation of ECR condition, however, in some cases permanent magnets could be used for generation of ECR condition. Plasma source which is generated by this technique is called Permanent Magnet Electron Cyclotron Resonance (PMECR) source [6]. Using permanent magnets instead of electromagnets have several advantages including simplicity and cost-effectiveness, reduction of power consumption, compactness of system, stability and durability. However, this technique has limitation in magnetic field control and flexibility. Development of numerical modelling of ECR sources, that provide the standard geometry of reactor for plasma processing applications, have been started since 1990s [7]. Monte-Carlo methods [8], PIC methods [9], quasi-neutral particle models [10] and fluid models [11] have been used for studying different aspects of ECR plasma sources. In this manuscript we have used COMSOL Multiphysics for numerical simulation of ECR plasma source, which sustained by permanent magnets. The purpose of this simulation is to find the best magnets arrangement for creating a plasma that is appropriate for plasma processing applications. Usually, two chambers have been used for plasma enhanced chemical vapor deposition using ECR plasma source, one for plasma generation and the other for processing of substrate. Here, we use one chamber instead of two chambers. Several parameters affect the downstream motion of plasma, that produced in discharge chamber, toward processing chamber (substrate is located in this chamber), such as creating pressure difference between two chambers, profile of magnetic field inside discharge chamber and etc. Moreover, profile of magnetic field affects the locations of resonance surfaces (plasma produced resonantly at resonance surfaces) inside plasma chamber and plasma density, that plays an important role in plasma processing applications. By changing arrangement and polarization of magnets around plasma chamber different profiles of magnetic field have been achieved inside it. Here, we investigate the effect of three different profile of magnetic field on plasma density and potential. In the next section ECR plasma source introduced, then a brief

description about numerical model, that used in COMSOL, has been presented. Finally, we represent numerical results and conclusions.

ECR plasma source

In ECR plasma sources, plasma is produced by applying electromagnetic waves in the frequency range of 300MHz-10GHz to a gas and in the presence of magnetic field in resonance condition. The effect of magnetic field on breakdown electric field at microwave frequencies, which ultimately led to the creation of ECR plasma sources, was first studied by Lax [12] in the 1950s as a method for characterizing confined plasma. The idea of using this technique for plasma production was proposed in the early 60s for research on plasma acceleration [13] and fusion plasma. In ECR plasma, electrons absorb energy from injected microwave power in resonance conditions. In the presence of a uniform and static magnetic field, electrons will move in a circular motion (if initial axial velocity is non-zero) along magnetic field lines due to the Lorentz force. The angular frequency of this motion is $\omega_c = eB/m$ and its radius is $r_c = mv/eB$, which v is electron velocity perpendicular to magnetic field lines. This circular motion in vacuum and without collisions will not give energy to electrons. When the microwave electric field with angular frequency of ω is added to the system, the path of electrons will change. The resonance condition is occurred when $\omega = \omega_c$. As a result, electrons rotate in phase with right hand side circularly polarized wave and continuously gain energy from electromagnetic wave. Therefore, electrons gain sufficient energy to ionize the background gas [1]. For the microwave frequency of 2.45 GHz, the resonance effect occurs when the magnetic field is equal to 875 Gauss.

Numerical simulation

In ECR plasma source simulated in this manuscript, microwave with a frequency of 2.45 GHz will enter the cylindrical plasma chamber through WR340 rectangular waveguide. Cylindrical plasma chamber with 10 cm diameter surrounded by four neodymium 10cm×5cm×1cm block permanent magnets (NdFeB). In magnetic field no currents (MFNC) module of COMSOL, static magnetic field that produced by permanent magnets computed by solving following equation:

$$H = -\nabla V_m$$
$$B = \mu_0 \mu_r H \quad (1)$$

Where V_m is magnetic scalar potential and μ_r is relative permeability of magnet. After computing profile of magnetic field, it used to calculate plasma conductivity in plasma module. High-frequency component of the electric field is solved in the frequency domain and by using electromagnetic wave frequency domain module (EMW). In plasma module drift-diffusion equation are solved and the results are plasma density and temperature. Simulation parameters are as follow: Input power 500-Watt, temperature 300 kelvin, background pressure 10^{-3} mbarr, and initial electron density $10^{14} m^{-3}$. The schematic of simulated model has been represented in Figure 1. Reactions of Ar gas that considered in the simulation are presented in Table 1, while cross-section of these reactions is plotted in Figure 2. Boundary conditions are represented in Table 2.

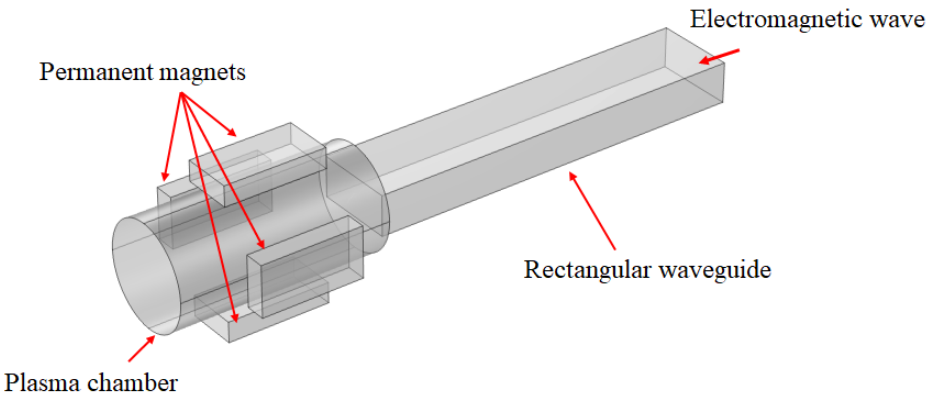

Fig. 1. Schematic of the simulated model of ECR plasma source.

Table 1. Reactions of Ar that considered in the simulation

Collision type	Reaction
Elastic	e+Ar=>e+Ar
Excitation	e+Ar=>e+Ars e+Ars=>e+Ar
Ionization	e+Ar=>2e+Ar+ e+Ars=>2e+Ar+

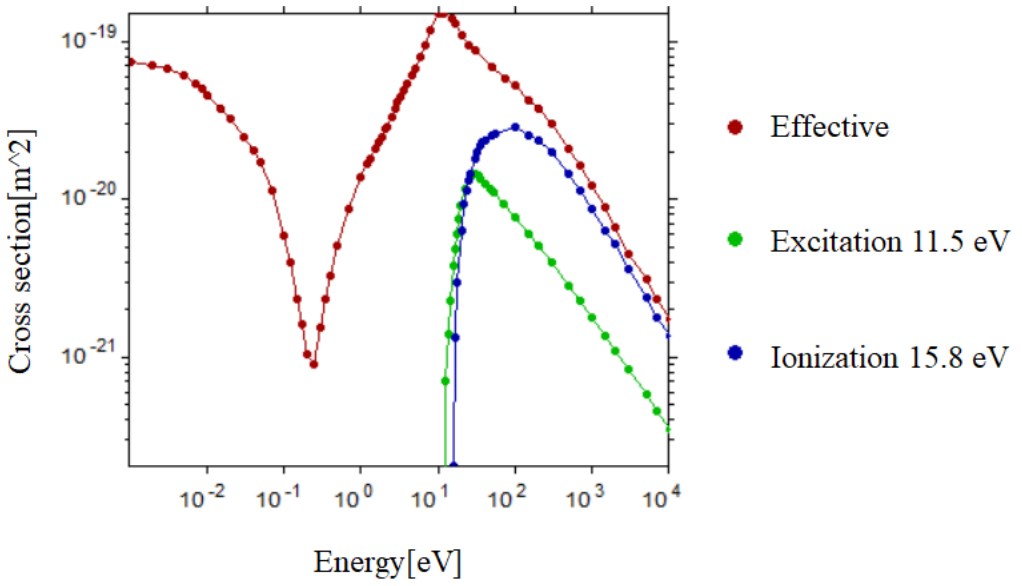

Fig. 2. Cross-section of Ar reactions that considered in the simulation

Table 2. Boundary conditions of simulation

Boundary condition	Domain
Perfect Electric conductor	Waveguide, Walls of plasma chamber
Ground	Walls of plasma chamber

In Figure 3 profile of magnetic fields and ECR surface, which produced by 4 block magnets are plotted in a cut plane in y-z plane and x = 0.115m. ECR surfaces with magnetic field value of 87.5 mT denoted by red line. Different arrangements of magnets are represented in Figure 3. In this figure north pole of magnets denoted by red surface while south pole denoted by blue surface, for instance arrangement 1 is achieved by setting opposite poles in front of each other. Arrangement 2 is described in Figure 3(b) and arrangement 3 described in Figure 3(c). In Figure 4, magnetic field profile and electron density along y axis (radius of chamber) and in 8.5 cm distance from electromagnetic field entrance, have been plotted for three different arrangements of block magnets. In Figure 5, magnetic field profile and electron density along x axis (symmetric axis of plasma chamber) at 2 cm distance from cylinder center have been plotted.

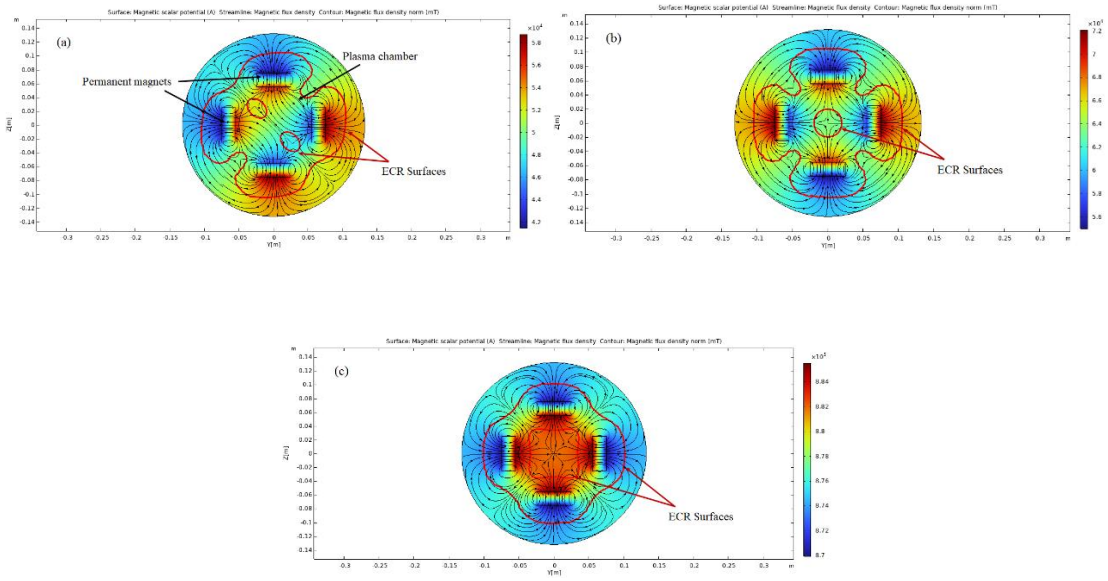

Fig. 3. Magnetic field profile for (a) arrangement 1, (b) arrangement 2 and (c) arrangement 3 of magnets. North pole of magnets denoted by red surface while south pole denoted by blue surface.

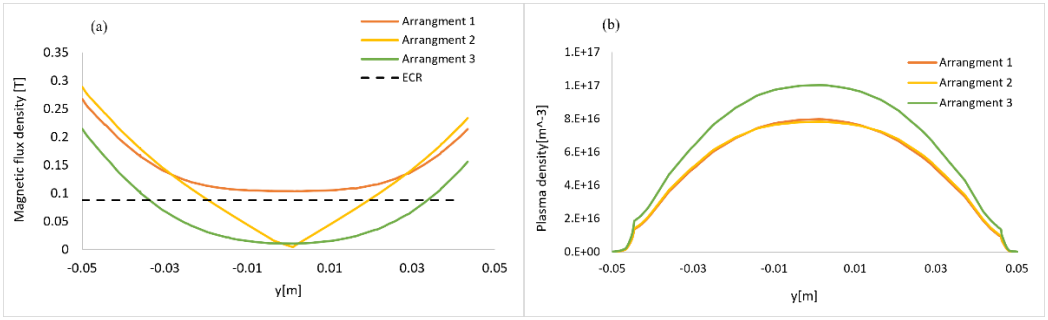

Fig. 4. (a) Magnetic field profile inside plasma chamber along y axis for three different arrangements of magnets. ECR location denoted by dashed line. (b) Plasma density inside plasma chamber along y axis for three different arrangements of magnets at $t = 3.98 \times 10^{-6} s$.

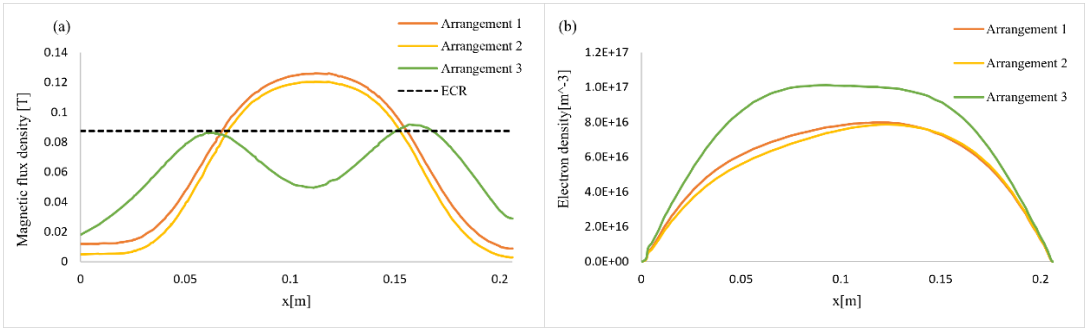

Fig. 5. (a) Magnetic field profile inside plasma chamber along x axis for three different arrangements of magnets. ECR location denoted by dashed line. (b) Plasma density inside plasma chamber along x axis for three different arrangements of magnets at $t = 3.98 \times 10^{-6} s$.

In Figure 6, Plasma density in x-y plane inside chamber have been plotted for different arrangement of magnets. Plasma potential in x-y plane inside chamber have been plotted in Figure 7.

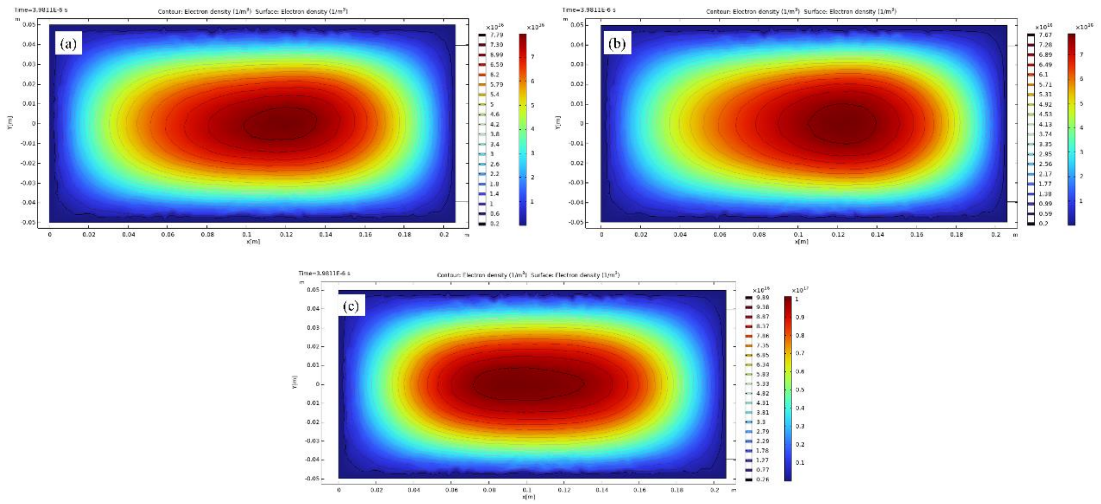

Fig. 6. Plasma density inside plasma chamber in x-y plane for (a) arrangement 1, (b) arrangement 2 and (c) arrangement 3 of magnets at $t = 3.98 \times 10^{-6} s$.

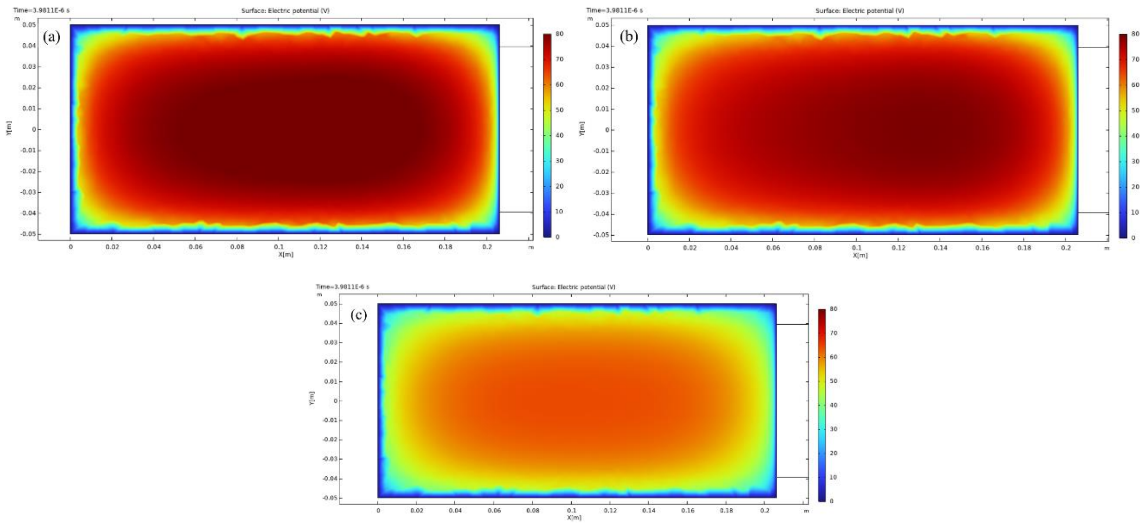

Fig. 7. Plasma potential in x-y plane for (a) arrangement 1, (b) arrangement 2 and (c) arrangement 3 of magnets at $t = 3.98 \times 10^{-6} s$.

Results and Discussion

According to Figure 3 and Figure 4 (a) arrangement 2 construct a localized and symmetric ECR surface inside plasma chamber that magnetic field is zero at the center of chamber, while in arrangement 1 two localized ECR surface near the walls of chamber are produced and magnetic field strength at the center of chamber is 0.12 tesla. ECR surface in arrangement 3 is located near chamber walls and magnetic field strength at the center of chamber is about 0.01tesla. By moving along chamber radius in y direction at z=0 and x=0.115 m, ECR condition does not achieved in arrangement 1, while in arrangement 2 and 3 it achieved at radius 1.8 cm and 3.3 cm respectively. Magnetic field profile along symmetric axis of chamber in x direction that been plotted in Figure 5 (a) is a bell-shaped curve for arrangement 1 and 2, while it is a two-peak curve for arrangement 3. The peak electron density in Figure 5 (b), for three different arrangement is $7.9 \times 10^{16} m^{-3}$, $7.8 \times 10^{16} m^{-3}$ and $10^{17} m^{-3}$, respectively. Critical density for 2.45 GHz ECR source is about $7.5 \times 10^{16} m^{-3}$, therefore beyond this density mechanism of power absorption from electromagnetic wave has been changed from ECR absorption. According to Figure 5 (b), peak electron density for arrangement 1 and 2 is located near the entrance of electromagnetic wave, while for arrangement 3 it is located at the other side of chamber. It can also be observed in different panels of Figure 6. We can observe from Figure 7 that, plasma potential in arrangement 3 is lower than two other arrangements. Moreover, plasma potential in arrangement 2 is lower than arrangement 1. For applications such as deposition using ECR plasma, the lower plasma potential in front of the substrate is favorable. In fact, plasma potential determines the energy with which the ions impinge on the substrate, therefore in the case where plasma potential is lower less damage has been caused by ion bombardment.

Conclusions

In this paper COMSOL Multiphysics has been used for investigating the effect of magnetic field profile on plasma density in ECR plasma source. ECR plasma source that simulated in this

manuscript, has been designed for processing applications. Higher plasma density is favorable for processing applications, since higher deposition rates have been achieved at higher plasma densities. Plasma density required for plasma processing using ECR source is in the range of $10^{17}-10^{18} m^{-3}$ at low pressures $10^{-4}-5\times10^{-3} Torr$. This condition can be achieved using the profile of magnetic field in arrangement 3.

Here, we use four neodymium block permanent magnets for generation of resonance ECR surfaces in plasma chamber. The advantages of using permanent magnets instead of electromagnetic coils for generation of ECR surface are simplicity, cost-effectiveness, reduction of power consumption, compactness of system and stability and durability. ECR plasma source which is an electrodeless discharge, has a wide range of applications in plasma processing. Plasma density has important effect on deposition rate for deposition process which aided by ECR plasmas. In this paper, we have changed profile of ECR surfaces inside plasma chamber by changing the arrangement and polarity of magnets around the chamber. Three different arrangements have been considered and profile of magnetic field inside plasma chamber, plasma density and potential have been computed for each case and compared with each other. The results show that plasma density and potential are controlled by the profile of magnetic field. Best magnets arrangement (arrangement 3 in this paper) results in higher plasma density and lower plasma potential.

References

[1] M. A. Lieberman, et al., (2005). Principles of Plasma Discharges and Materials Processing. New Jersey: Wiley.

[2] Castrischer, G., Kretschmer, K.-H., Lorenz, G., & Kessler, I. (1990). Reactive Etching with ECR Plasma Source. Micro System Technologies 90, 366–371.

[3] J. T. C. Lee, (1996). A comparison of HDP sources for polysilicon etching. Solid State Technol., vol. 39, no. 8, pp. 63–69.

[4] J. Wang. (2017) .Novel Concepts in the PECVD Deposition of Silicon Thin Films: from Plasma Chemistry to Photovoltaic Device Applications. Plasma Physics [physics. plasm-ph]. Université Paris Saclay (COmUE).

[5] D. B. Bonneville, et al., (2021). Low-Temperature and Low-Pressure Silicon Nitride Deposition by ECR-PECVD for Optical Waveguides. Appl. Sci., 11(5), 2110.

[6] A. Saproo and T. D. Mantei,(1995), Performance and modeling of a permanent magnet electron cyclotron resonance plasma source. Journal of Vacuum Science & Technology A 13, 883.

[7] Hagelaar, G. J. M., Makasheva, K., Garrigues, L., & Boeuf, J.-P. (2009). Modelling of a dipolar microwave plasma sustained by electron cyclotron resonance. Journal of Physics D: Applied Physics, 42(19), 194019.

[8] Weng, Y., & Kushner, M. J. (1992). Electron energy distributions in electron cyclotron resonance discharges for materials processing. Journal of Applied Physics, 72(1), 33–42.

[9] Gopinath, V. P., & Grotjohn, T. A. (1995). Three-dimensional electromagnetic PIC model of a compact ECR plasma source. IEEE Transactions on Plasma Science, 23(4), 602–608.

[10] M. Lampe, G. Joyce, W. M. Manheimer, and S. P. Slinker (1998) .Quasi-neutral particle simulation of magnetized plasma discharges: general formalism and application to ECR discharges, IEEE Trans. Plasma Sci. 26, 1592.

[11] Hemmers, D., David, M., Kempkens, H., & Uhlenbusch, J. (1998). Self-consistent modelling of overdense plasmas in ECR discharges. Journal of Physics D: Applied Physics, 31(17), 2155–2164.

[12] B. Lax, et al. (1950). The Effect of Magnetic Field on the Breakdown of Gases at Microwave Frequencies. J. Appl. Phys., 21(12): 1297.

[13] D. B. Miller, et al., (1964). Experiments with an electron cyclotron resonance plasma accelerator. AIAA Journal, Vol 2, No 1.

Effect of non-thermal plasma on treating strong wastewaters from polyester manufacturing industry (Paper ID: 1257)

Bakhtiyari-Ramezani M. [1*], Mohammadi F. [2], Ziveh N. [2], Ghassempour H. [2]

[1*] Plasma Physics and Nuclear Fusion Research School, Nuclear Science and Technology Research Institute (NSTRI), Tehran, Iran
[2] Plasma Technology Development Company, Tehran, Iran

Abstract

In the present paper, the effect of atmospheric pressure plasma (APP) on the treatment of strong wastewaters from polyester manufacturing industry has been studied using a dielectric barrier discharge (DBD) generator. The treatment process was carried out on the experimental samples of real wastewaters for 0, 10, 30, 45, 60, 90 and 120 minutes, and the effect of APP on the reduction of chemical oxygen demand (COD) was investigated. We showed that plasma had the ability to destroy unsaturated polyester chains, fatty acids and alcohol compounds. The data resulted from plasma treatment indicated that the 60-minutes treatment time contributed to the reduction of the COD parameter by about 80%, which means the parameter decreased from 25000 ppm to 4611 ppm. According to the obtained results, it was found that treatment times longer than 60 minutes increased the amounts of COD. The plasma effect on TDS, EC, temperature and pH parameters was also investigated. According to the results, plasma did not seem to have a great impact on the pH, TDS and EC value of the wastewater after plasma treatment for two hours, while the temperature increased significantly (near to 40 degrees) after treatment process for one hour, and then it remained constant afterwards.

Keywords: non-thermal atmospheric plasma, polyester manufacturing industry wastewater, treatment, chemical oxygen demand (COD)

Introduction

Chemical and petrochemical industries consume a considerable amount of water processes, and unfortunately they generate approximately 70 % of pollution wastewater including hazardous and dangerous products [1,2]. The high strength wastewater including various additives and detergents containing softening agents, antioxidant, surfactant, wetting agents, detergent and antiseptic are

produced by polyester manufacturing industry [3-5]. Many of these compounds are non-biodegradable, toxic, hazardous, and represent priority hazardous pollutants [6].

In recent years, industrial effluents including pollutants are often discharged into the natural environment, along with sewage. However, toxic materials presented in industrial wastewaters may prevent the biological activity of the treatment plant biomass, causing process upsets and making their way into the waters [7]. The toxic pollutants can volatilize from sedimentation tanks, bar racks, and sewers before biodegradation, resulting that those contaminants can aggregate in sludge to create hazard risks for plant or human health or the environment [8].

In order to decompose hazardous organic compounds and to overcome these limitations of conventional methods, pretreatment at the source of industrial effluents and especially effluents from polyester production industries is required before discharge into central treatment plant [9,10].

In order to solve this problem, the eco-friendly advanced oxidation technology like cold plasma technology have been extensively investigated for the polutants degradation [11,12], photo-Fenton techniques [13], photocatalysis [14,15], ozonation [16], electrochemical reactions [17], irradiation technology [18,19] or a combination of these for pretreatment at the source of polyester manufacturing industry wastewaters. These methods are perforemed under mineralization, decomposing different organic contaminants into compounds of intermediates, carbon dioxide, and water. In addition, it has been confirmed that these techniques proved the remarkable potential to remove toxic derivatives and recalcitrant materials in water system [20]. As a result, the complete oxidation process as an alternative approach has attracted solid amount of attention to treat wastewater in such a way that techniques of photocatalysis and UV/ozone may not provide [21]. As huge challenges of industrial wastewater treatment are emerging, atmospheric pressure plasma (APP)-assisted AOPs technology, therefore exhibits a more viable and alternative advanced oxidation processes (AOPs) option for the solution [22].

The non-thermal technique as an APP technology is one of the newest techniques, containing a reactive mix of positively and negatively charged ions, OH radicals, $O\cdot$, O_3, H_2O_2, NO^-, NO_2^-, neutral particles, UV radiation and electromagnetic waves. These produced components are

collectively combined to generate reactive agents [23]. In particular, the advantage of APP includes OH radicals' generation and reactive species [24]. Furthermore, it is an economical, eco-friendly, and easy-to-use technology at room temperature and atmospheric pressure, which is able to eliminate various toxic components found in wastewater [22, 25,26].

As mentioned before, strong wastewater from polyester manufacturing industry had very dangerous organic compounds and high COD. Therefore, discharching of this wastewater into the central treatment plant before the pretreatment, causes disruption in the treatment process. So far, studies have been conducted on the treatment of wastewater from polyester industries. However, no study has been done on the use of cold plasma in the pretreatment of this type of wastewater and reducing the amount of COD to the standard level for discharching into the central treatment plant. Therefore, in this paper, the effects of cold plasma pretreatment on polyester wastewater treatment and the analysis of its mechanism on COD removal has been investigated.

Experimental

The wastewater was obtained from one of the polyester production companies located in industrial city of Kaveh (**S_0**), 100 km southeast of Tehran, and the initial conditions are displayed in Table 1. The polyester wastewater treatment (**S_0**) was carried out using an atmospheric pressure plasma (APP) system, which is shown in Table 2.

Table 1. Characterization of the real polyster wastewater

COD (ppm)	25000
EC (µs/cm)	1620
TDS (ppm)	1028
pH	2.6

Table 2. Different times of non-thermal plasma (NTP) treatment for polyester wastewater

Sampels code	
S_0	Real polyster wastewater
S_1	Plasma for 10 min
S_2	Plasma for 30 min
S_3	Plasma for 45 min
S_4	Plasma for 60 min
S_5	Plasma for 90 min
S_6	Plasma for 120 min

Figure 1 illustrates the schematic configuration of designed atmospheric pressure plasma (APA) in this study for polyester wastewater treatment, which comprised four main parts; water falling film system, cooling water circulator, power supply and wastewater tank. The efficiency of the APP reactor on a real wastewater sample was assessed by measuring the total dissolved solids (TDS) chemical, oxygen demand (COD), and electrical conductivity (EC). For this purpose, about ten liters of wastewater was poured into the device tank and circulated through falling film system for APP treatment under room temperature and pressure. The value of voltage and frequency was set to 15 kV and 8 kHz, respectively. At the desired times, 50 mL of wastewater was taken from the outlet valve of the APP device for COD, TDS, and EC measurements. In addition to these indicators, the temperature and pH of the circulating wastewater were also measured at different treatment times. An infrared thermometer (FC-IR202) and a digital pH meter (FiveEasy pH meter F20-std-Kit) were used to record the temperature and pH of samples, respectively, during the plasma treatment. COD calculation was carried out using a HACK model DRB200/HACK(DR6000). TDS and electrical conductivity (EC) were analyzed using a HACK-based probe model HQ440d multi.

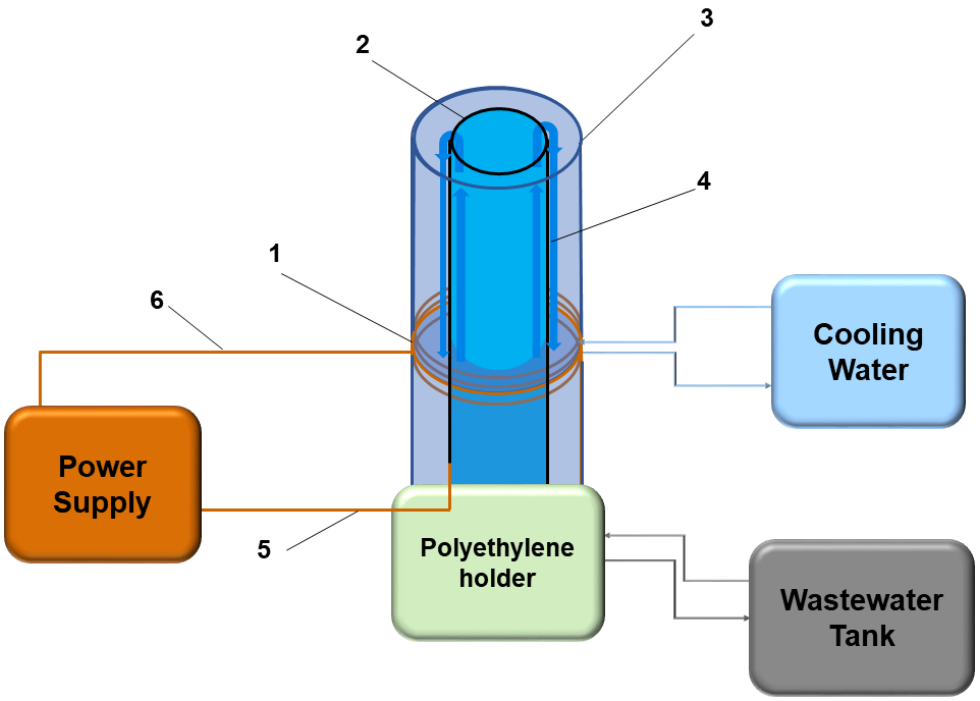

Fig. 1. Schematic illustration of used atmospheric pressure plasma (APP) system in this study. Numbers 1-6 referred to coil electrode, style tube electrode, quartz, water falling film, High voltage and low voltage connection, respectively.

Results and Discussion

The obtained results are summarized in Figure 2 as a bar chart. The samples are labeled Sn, where n= 0-6 corresponded to samples of 0, 10, 30, 45, 60, 90 and 120 minutes treated with APP, respectively (see Table 2).

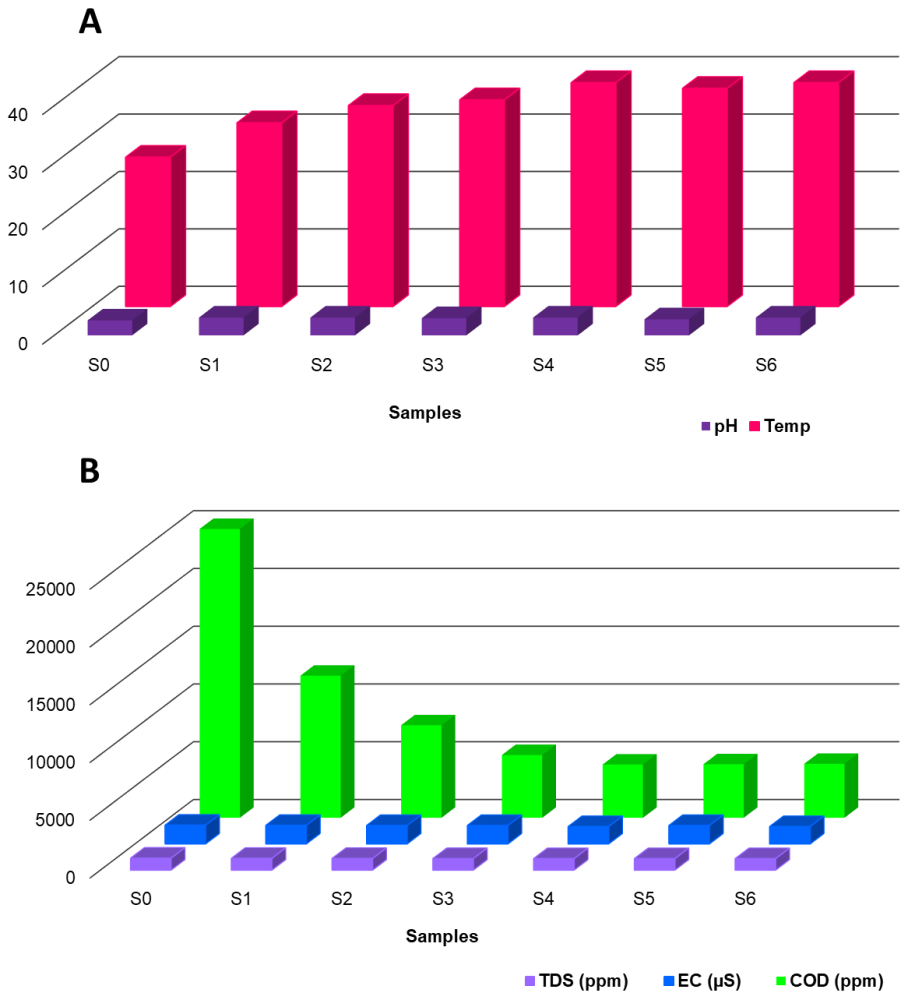

Fig. 2. Variations of (A); temperature and pH; (B) COD, TDS and EC of the wastewater as a function of circulation time in APP (**S_0**= 0 min, **S_1**= 10 min, S2= 30 min, **S_3**= 45 min, **S_4**= 60 min, **S_5**= 90 min and **S_6**= 120 min).

As revealed in Figure 2-A, the pH of the wastewater does not change significantly during the treatment process, while the temperature of the wastewater shows a relatively significant increase (near to 40 degrees) after treatment process for one hour. After that, the temperature remains almost constant and below 40 degrees with increasing plasma treatment time. This constancy of temperature is considered an important advantage, since one of the most important characteristics of cold plasma technology in the field of wastewater treatment, is its low temperature in order to increase the lifetime of electrodes and other equipment. As demonstrated in Fig. 2-B, APP cannot reduce the TDS and EC value of the wastewater after treatment for two hours. APP is able to reduce the COD of wastewater more than 50 % (from 25000 to 12300 ppm) after only 10 minutes of plasma treatment. Interestingly, employing longer treatment time of 30 and 45 minutes, the wastewater's COD reduced by more than 67 % and 78 %, respectively. The best COD reduction of 81 % (from 25000 to 4611 ppm) resulted for S4, while with increasing treatment time for more than one hour (S5 and S6), COD value remains relatively constant. The proposed mechanism of APP-based strong polyester wastewater treatment including possible reactions taking place under plasma treatment is given in Figure 3. Briefly, the rush of the $OH^{\bullet}$ radical is the main phatway for the degradation of organic contaminates. Long chain pollutants break down into smaller compounds by electrophilic addition of $OH^{\bullet}$, or by the hydroxylation of ester bond. Many intermediates have also been reported during the oxidative degradation in plasma processes. Scheme 1 demonstrated the different reactive species (RS) generated during APP treatment and their involvement in the decomposition of long chain compounds and mineralization of small organic compounds [27].

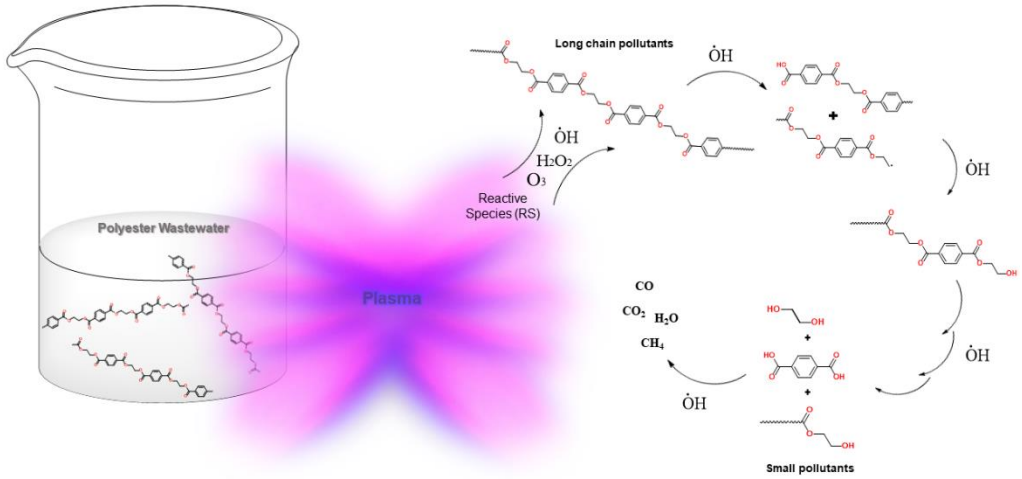

Fig. 3. The possible mechanism of APP-based polyester wastewater treatment.

Conclusions

To treat wastewater, the application of atmospheric pressure plasma (APP) system has gained significant attention due to its ability to eliminate a wide range of contaminants. High densities of reactive mixture of negatively and positively charged ions, along with reactive species like H_2O_2, O_3, O·, OH^-, NO^-, NO_2^-, neutral particles, electromagnetic waves, and UV radiation are generated, making decomposion of micro-pollutants available within a shorter time. The strong wastewater resulted polyester manufacturing industry is a type of waste which contains dangerous organic compounds and high COD. Therefore, discharching this wastewater into the central treatment plant before the pretreatment, causes disruption in the treatment process. Consequently, it is necessary to focus on the pretreatment of this wastewater. Despite the great effect of APP technology in the treatment of all types of wastewater, so far few studies have been reported for the application of this technology in the treatment and pre-treatment stages of polyester industry wastewater to reduce the COD parameter. In the current study, the effects of cold plasma pretreatment on polyester wastewater treatment and the analysis of its mechanism on COD removal have been investigated. According to the obtained results, plasma did not have a great impact on the pH, TDS and EC values of the wastewater after treatment for two hours, while the temperature of the wastewater showed a relatively significant increase (near to 40 degrees) after treatment process

for one hour. After that, the temperature remained almost constant and below 40 degrees with increasing plasma treatment time. Plasma could reduce the COD of wastewater more than 50 % (from 25000 to 12300 ppm) after only 10 minutes of plasma treatment. Interestingly, by employing longer treatment time of 30 and 45 minutes, the wastewater COD was reduced more than 67 % and 78 %, respectively. The best COD reduction of 81 % (from 25000 to 4611 ppm) resulted for 60 minutes plasma treatment, while with prolongation of treatment time more than one hour, COD value remained relatively constant.

References

[1] Tolba, A., Alalm, M. G., Elsamadony, M., Mostafa, A., Afify, H., & Dionysiou, D. D. (2019). Modeling and optimization of heterogeneous Fenton-like and photo-Fenton processes using reusable Fe_3O_4-MWCNTs. Process Safety and Environmental Protection, 128, 273-283.

[2] Tawfik, A., & Elsamadony, M. (2017). Development of dry anaerobic technologies of bio-waste and unlock the barriers for valorization. Optimization and Applicability of Bioprocesses, 267-282.

[3] Mahmoud, M., Elreedy, A., Pascal, P., & Tawfik, A. (2017). Hythane (H_2 and CH_4) production from unsaturated polyester resin wastewater contaminated by 1, 4-dioxane and heavy metals via up-flow anaerobic self-separation gases reactor. Energy Conversion and Management, 152, 342-353.

[4] Mahmoud, M., Ismail, S., & Tawfik, A. (2018). Post-treatment of anaerobic effluent containing 1, 4-dioxane and heavy metals via auto-aerated down-flow hanging luffa (ADHL) system. Process Safety and Environmental Protection, 117, 22-32.

[5] Yang, X. (2009). Interior microelectrolysis oxidation of polyester wastewater and its treatment technology. Journal of Hazardous Materials, 169(1-3): 480-485.

[6] Osama, R., Awad, H. M., Ibrahim, M. G., & Tawfik, A. (2020). Mechanistic and economic assessment of polyester wastewater treatment via baffled duckweed pond. Journal of Water Process Engineering, 35, 101179.

[7] Ren, S. (2004). Assessing wastewater toxicity to activated sludge: recent research and developments. Environment international, 30(8):1151-1164.

[8] Manual, W. M. O. A. (1988). United states environmental protection agency. Government Institutes Inc, 1-5.

[9] Office of Water—United States Environmental Protection Agency. (2005). EPA's National Pretreatment Program, 1973–2003: Thirty Years of Protecting the Environment. Water Encyclopedia, 1, 798-801.

[10] Caffaro-Filho, R. A., Morita, D. M., Wagner, R., & Durrant, L. R. (2009). Toxicity-directed approach of polyester manufacturing industry wastewater provides useful information for conducting treatability studies. Journal of hazardous materials, 163(1):92-97.

[11] Wang, N., Chen, D. Z., & Zou, L. S. (2015). Influence of non-thermal plasma pre-treatment on the scaling characteristics of viscous oil wastewater during evaporation. Applied Thermal Engineering, 75, 779-788.

[12] Duan, L., Li, J., Shang, K., Na, L., & Wu, Y. (2015). Enhanced biodegradability of coking wastewater by gas phase dielectric barrier discharge plasma. Separation and Purification Technology, 154, 359-365.

[13] Ameta, S. C., & Ameta, R. (Eds.). (2018). Advanced oxidation processes for wastewater treatment: emerging green chemical technology. Academic press.

[14] Vaiano, V., Iervolino, G., Rizzo, L., & Sannino, D. (2017). Advanced oxidation processes for the removal of food dyes in wastewater. Current organic chemistry, 21(12):1068-1073.

[15] Vaiano, V., & Iervolino, G. (2018). Facile method to immobilize ZnO particles on glass spheres for the photocatalytic treatment of tannery wastewater. Journal of colloid and interface science, 518, 192-199.

[16] Saeid, S., Tolvanen, P., Kumar, N., Eränen, K., Peltonen, J., Peurla, M., & Salmi, T. (2018). Advanced oxidation process for the removal of ibuprofen from aqueous solution: A non-catalytic

and catalytic ozonation study in a semi-batch reactor. Applied Catalysis B: Environmental, 230, 77-90.

[17] Garcia-Segura, S., Lanzarini-Lopes, M., Hristovski, K., & Westerhoff, P. (2018). Electrocatalytic reduction of nitrate: Fundamentals to full-scale water treatment applications. Applied Catalysis B: Environmental, 236, 546-568.

[18] Bisht, B., Bhatnagar, P., Gururani, P., Kumar, V., Tomar, M. S., Sinhmar, R., & Kumar, S. (2021). Food irradiation: Effect of ionizing and non-ionizing radiations on preservation of fruits and vegetables–a review. Trends in Food Science & Technology, 114, 372-385.

[19] Pricaz, M. A. R. I. A., & Uţă, A. C. (2015). Gamma radiation for improvements in food industry, environmental quality and healthcare. Rom J Biophys, 25(2):143-162.

[20] García, M. C., Mora, M., Esquivel, D., Foster, J. E., Rodero, A., Jiménez-Sanchidrián, C., & Romero-Salguero, F. J. (2017). Microwave atmospheric pressure plasma jets for wastewater treatment: degradation of methylene blue as a model dye. Chemosphere, 180, 239-246.

[21] Thirumdas, R., Sarangapani, C., & Annapure, U. S. (2015). Cold plasma: a novel non-thermal technology for food processing. Food biophysics, 10, 1-11.

[22] Zeghioud, H., Nguyen-Tri, P., Khezami, L., Amrane, A., & Assadi, A. A. (2020). Review on discharge Plasma for water treatment: Mechanism, reactor geometries, active species and combined processes. Journal of Water Process Engineering, 38, 101664.

[23] Bakhtiyari-Ramezani, M., Nohekhan, M., Akbari, M. E., Abbasvandi, F., Bayat, M., Akbari, A., & Nasiri, M. (2024). Comparative assessment of direct and indirect cold atmospheric plasma effects, based on helium and argon, on human glioblastoma: an in vitro and in vivo study. Scientific Reports, 14(1), 3578.

[24] Iervolino, G., Vaiano, V., & Palma, V. (2019). Enhanced removal of water pollutants by dielectric barrier discharge non-thermal plasma reactor. Separation and Purification Technology, 215, 155-162.

[25] Li, S., Dang, X., Yu, X., Abbas, G., Zhang, Q., & Cao, L. (2020). The application of dielectric barrier discharge non-thermal plasma in VOCs abatement: A review. Chemical Engineering Journal, 388, 124275.

[26] Gururani, P., Bhatnagar, P., Bisht, B., Kumar, V., Joshi, N. C., Tomar, M. S., & Pathak, B. (2021). Cold plasma technology: advanced and sustainable approach for wastewater treatment. Environmental Science and Pollution Research, 1-21.

[27] Szilvia, K., Sandor, T., Lorand, R., Miklos, M., Emília, C., & Zolt, K. (2020). Degradation phenomena on atmospheric air plasma treatment of polyester fabrics. Surfaces and Interfaces 22, 100826.

ICNST 2024
International Conference on Nuclear Science and Technology
6- 8 MAY 2024 | Isfahan, Iran

Redesign of Alborz tokamak toroidal magnetic field system (Paper ID: 1265)

Mazloom H[1], Ghasemi M[2], Amrollahi R[1], Mirzaei H[3*], Kashani Z[1]

[1]Department of Energy Engineering and Physics, Amirkabir University of Technology, Tehran, Iran
[2]Department of Nuclear Engineering, Central Tehran Branch, Islamic Azad University, Tehran, Iran
[3]Physics and Accelerator Research School, NSTRI, P.O. Box 14395-836, Tehran, Iran

Abstract

Alborz Tokamak's design and construction program started in 2013 in the fusion laboratory of Amirkabir University of Technology. In the first phase, this tokamak was put into operation in 2019. At the moment, the redesign of magnetic systems is considered. Since one of the influencing factors on the plasma confinement time is the size and flattop of the toroidal magnetic field, in this phase, the increase of the toroidal magnetic field has been considered. The toroidal field coil system consists of 16 rectangular-shaped coils. These copper cable conductors have 5 cm width and 6 mm thickness. The toroidal magnetic field system provides a 0.85 T magnetic field at the plasma axis. This value will be increased in the new plan. In the present study, according to the ability to supply the capacitor bank, the electric circuit, and the magnetic field have been simulated and redesigned using PSpice and COMSOL Multiphysics software, respectively. Consequently, the maximum magnetic field, capacity, and maximum voltage of the improved capacitor bank have been determined.

Keywords: Alborz tokamak, toroidal magnetic systems, power supply

1.Introduction

Fusion will be one of the most important sources of energy in the future. At the time of writing this paper, electrical energy production from nuclear fusion has not yet been done practically. But one of the most important and main methods that is a candidate for producing energy from fusion is called Tokamak [1]. The first tokamak was designed and constructed in the 1950s, at the Kurchatov Institute of Moscow. After that, tokamaks developed significantly.

The first tokamak machine in Iran was prepared in 1994 from the Russian Kurchatov Institute and launched in the Atomic Energy Organization of Iran. This machine, named Damavand, is a small

tokamak (a = 7 cm, R = 36 cm) with an elongated plasma cross-section. Also, the IR-T1 tokamak purchased by Islamic Azad University from China in 1994. This machine has a main radius R = 0.45 m and a minor radius a = 0.125 m. Taban tokamak was the first tokamak that was completely designed and built in Iran and has a circular cross section with a main radius of 0.45 and a minor radius of 0.15 m. This tokamak was built and launched in the fusion laboratory of the Faculty of Physics and Energy Engineering of Amirkabir University of Technology. In this laboratory, other tokamak, named Alborz tokamak, has been designed and constructed. This device is a D-shaped tokamak with The main and minor radius of 0.45 and 0.15m, respectively.

The electromagnetic system of a tokamak consists of toroidal field (TF) system, ohmic heating (OH) system and equilibrium field (EF) system [2]. The Alborz tokamak are shown in fig. 1. Toroidal field (TF) coils are responsible for producing the most important magnetic field in a tokamak. The purpose of producing this field is to confine and control the plasma stability.

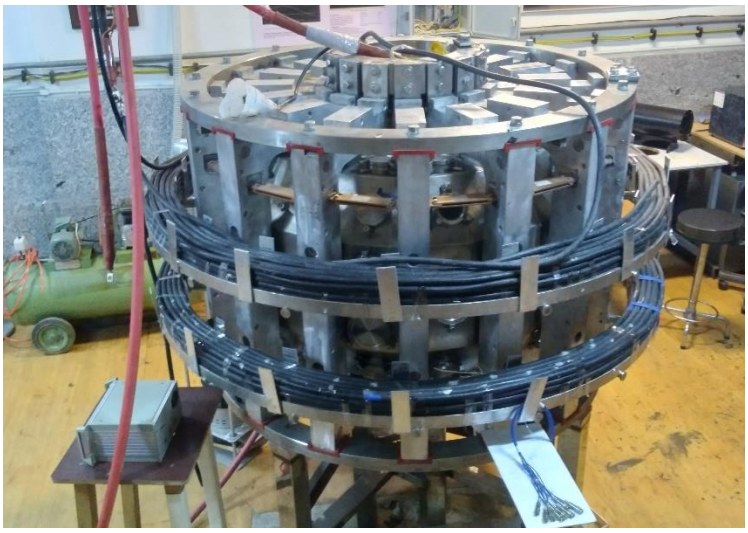

Fig. 22. A view of Alborz Tokamak

Alborz tokamak has 16 TF coils [2]. The material of the coils is 99.99% copper. Currently, the power source of the TF coils is a capacitor bank with a capacity of 40mF and a maximum voltage of 3kv [3], which leads to a field production of about 0.3T in the center of the plasma. In this paper, we are going to present a plan to redesign these coils and increase their production field. This plan includes increasing the capacity of the capacitor bank.

In part 2, the Alborz tokamak and its TF coils have been presented in detail. In part 3, using Pspice software, the electrical simulation of the TF system has been performed in two states, before and after the redesign. Based on the results obtained from section 3 and using COMSOL Multiphysics software, the magnetic field before and after the redesign has been calculated in section 4. Finally, in section 5, we discuss the results of the redesign plan.

2. Specifications of Alborz Tokamak

2.1. Main characteristics of Tokamak

Alborz Tokamak is a small size tokamak with a D-shaped cross section of the vacuum vessel. The main radius of the tokamak, R, is 0.45m and its minor radius, a, is 0.15m[1]. The vacuum vessel (VV) of Alborz Tokamak has been constructed of 316 stainless steels, with 3 mm thickness. This vessel consists of four parts that have been connected [1] and can host 0.5 m3 of plasma. 63 access ports have been installed in this chamber for plasma diagnostic systems, auxiliary heating equipment, Vacuum system, gas injection system., etc.

In this tokamak, the required toroidal field to confine and control the plasma stability [4] is provided by 16 coils wrapped around the vacuum vessel in the poloidal direction. The following presents the toroidal field (TF) coils in more detail.

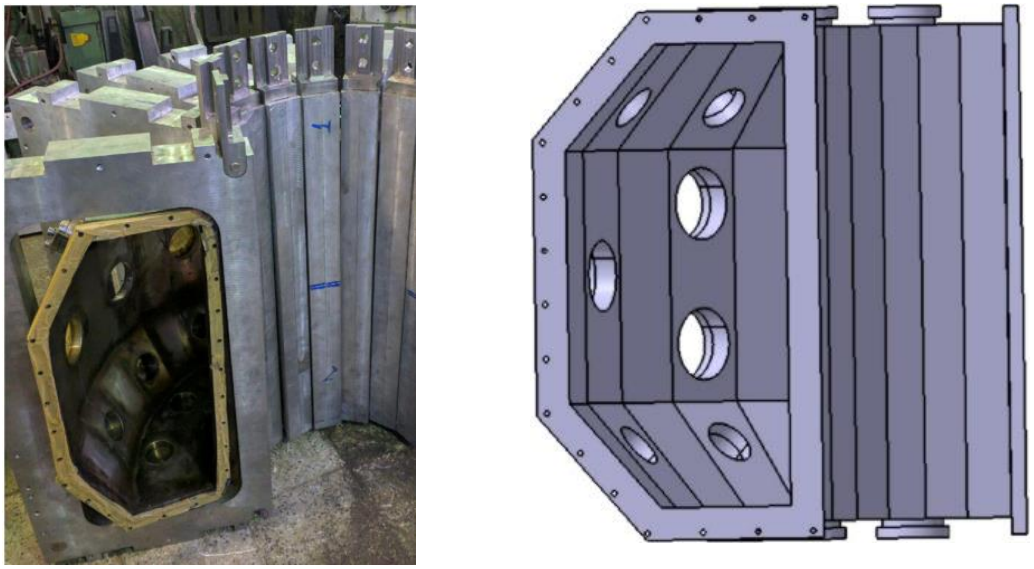

Fig. 23. Cross section view of Alborz vacuum vessel

In this tokamak, a central solenoid (CS) is used for the ohmic heating method. This coil has 195 turns [1] placed in the center of the tokamak. The position of CS is such that the passage of an electric current that varies with time, according to Faraday's principle, induces an electric field in the toroidal direction of the tokamak in the plasma, which starts the plasma current and heats the plasma.

Alborz tokamak is also equipped with poloidal coils. These coils are wrapped around the vacuum vessel in the toroidal direction, which produces a magnetic field in the poloidal direction. This poloidal field shapes the plasma and controls its position [1].

The power sources of all these magnetic field systems are capacitor banks with different capacities.

Alborz Tokamak also has other parts such as vacuum system, pre-ionization system, gas injection system, etc. Table 1 lists the main parameters of Alborz tokamak.

Table 12. main parameters of the Alborz tokamak

Major radius (m)	**0.45**
Minor radius (m)	**0.15**
Aspect ratio	**3**
Edge safety factor	**3**
Plasma volume (m^3)	**0.5**
material of the vacuum vessel	**SS 316L**

2.2. TF coils and its power supply

2.2.1 Coils

As mentioned, the Alborz tokamak has 16 Toroidal magnetic Field (TF) coils wrapped around the vacuum vessel symmetrically. Therefore, the angle between two adjacent coils is 22.5 degrees. These coils are responsible for producing the toroidal field which plays the main role in plasma confinement. Each coil in this tokamak has 10 turns, with a total of 160 TF winding turns[2].

The coils are made of copper sheets with a purity of 99.99% and a thickness of 5 mm[2]. Their width is 6 cm, which creates a cross-sectional area of 300 mm^2.

All 16 coils are electrically connected in series, so the current passing through them is equal. The current passing through them is supplied by the TF power source, which we will explain in the next section.

The electrical resistance and approximate inductance of the coils are obtained from equations (1) and (2).

$$R = \rho \frac{l}{A} \qquad (1)$$

$$L_{TF} = \mu_0 N^2 \left[R - (R^2 - a^2)^{1/2}\right] \qquad (2)$$

Where, ρ is the specific resistance of the coil material (copper), l is the total length of the coils, A is the cross-sectional area of the coil, μ_0 is the vacuum permeability constant, N is the number of turns, and R and a are the major and minor radii, respectively.

From these relations, the approximated resistance and inductance are obtained as 27 mΩ and 0.83 mH, respectively. However, the practical measurements of these values give results of 29 mΩ and 1.85 mH, respectively. The specifications of TF coils are reported in Table 2.

Table 13. TF system parameters.

Cross section (mm*mm)	**5*50**
Number of coils	**16**
Number of turns of each coil	**10**
Total number of turns	**160**
Material	**copper 99.99%**
Inductance (mH)	**1.85**
Resistance (mΩ)	**29**

2.2.1 power supply of TF coils

In Alborz tokamak, the capacitor bank has been considered as the power source of the magnetic field systems. The capacitor bank of the toroidal field system has a capacity equal to 40 mF, which can be charged up to 3 kv. Therefore, the maximum energy stored in the TF capacitor bank can be obtained from equation (3).

$$\mathbf{W} = \frac{1}{2}\,\mathbf{c}\,v^2 \qquad (3)$$

where *W* is the energy of the capacitor bank, *c* is the capacity of the capacitor bank and *v* is the maximum charged voltage of the capacitors. In this case, the maximum energy stored in the bank is 180 kJ.

This bank is connected to TF coils by thyristor. By applying a pulse to the thyristor, the thyristor acts like a switch and closes, which discharges the energy of the capacitor bank in the TF coils. In this circuit system, a diode is used in parallel with the TF coils as a shunt to prevent the energy discharged in the coils from returning to the capacitors. In Table 3, you see the power supply specifications of TF coils.

Table 14. TF power supply parameters.

Capacity (mF)	**40**
Charge voltage level (kV)	**Maximum 3**
Maximum stored energy (kJ)	**180**
Charging current (A)	**2**
Transformer	**3 phases (primary 380 V - secondary 3 kV)**

3. Electric Circuit Simulation

The electric circuit of TF capacitor bank discharge can be simulated in simulation software such as PSpice. In this section, we use this software to simulate the discharge circuit of the TF capacitor bank in two stages before and after upgrading the TF system. Finally, the obtained results, including the maximum passing current, pulse length, etc. have been compared for both stages before and after the redesign. It is worth mentioning that, the plan only includes increasing the capacity of the TF capacitor bank. In this way, the capacity has been developed from 40mF to 60mF.

In simulating the discharge circuit of the TF bank with PSpice software before the redesign, the values of the Table 2 and 3 have been used. In the software, a switch as a thyristor has been used,

which closes at the desired time. In addition, the stray circuit includes a diode and a resistor paralleled with the inductor. The simulated circuit is shown in Fig. 3.

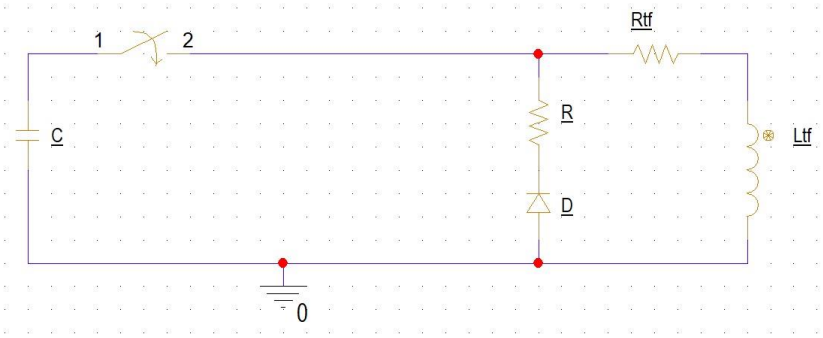

Fig. 24. The simulated electrical circuit of the TF system

The obtained current after running the program can be seen in Fig. 4. It is clear from this figure that the amount of current in the first positive peak is around 10.5kA. Also, the length of each pulse is about 54ms. The flat-top length of the current is important. It means the time interval when the current has passed 90% of its maximum value, reached its peak and returns to 90% of its maximum value again. According to the figure, this value is around 8ms. In Section 4 we use these values to observe the induced field before the redesign.

Since the plan is limited to increasing the capacity of the capacitor bank from 40mF to 60mF, therefore, to simulate the discharge circuit of the capacitor bank after the redesign, it is enough to increase the equivalent capacity value from 40mF to 60mF in the software and run the program again. Fig. 4 shows the waveforms of current passing through TF coils.

From the waveform, it is clear that in this case, the maximum current at its positive peak reaches about 12.6 kA. Also, the flat-top length of the current is about 10ms, both of them have increased compared to the state before the redesign. In section 4, these values are used to simulate the induced toroidal magnetic field.

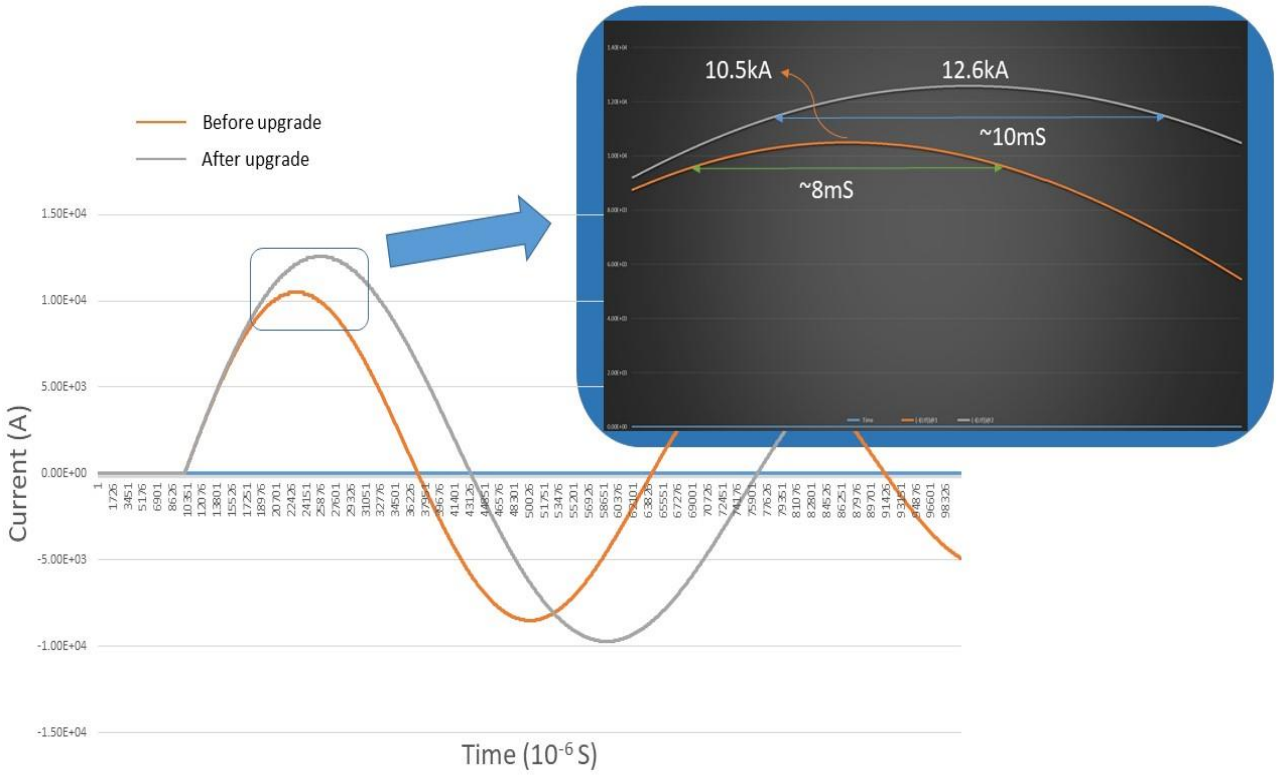

Fig. 25. Current waveform of TF coils before and after upgrad.

4. Magnetic Field Calculation and Simulation

In the previous section, the waveform of the TF coil current before and after the system redesign has been calculated. In the present section, the magnetic fields produced by these coils have been studied. The magnetic fields produced by the coil current can be calculated by using Biot–Savart law. The toroidal field in the center of the tokamak can be obtained from below simplified equation (4).

$$B = \mu_0 \frac{NI}{2\pi R} \qquad (4)$$

where I is the current passing through the coils, N is the number of turns and R is the major radius of the tokamak.

In this paper, COMSOL Multiphysics simulation software has been also used to simulate the toroidal field. In this software, after defining the geometry of the coils and their material, we define the entire geometry as a coil and set other parameters according to Alborz Tokamak's toroidal coils. Finally, the magnetic field can be simulated.

The Redesign Plan that has been carried out finally led to an increase in the current. Therefore, the difference between the two states before and after the redesign is equivalent to changing the current of the coils.

First, we use equation (4) to obtain the field befor redesign in the center of the plasma in a theoretical way. According to the results of section 3, the maximum field in the center of the plasma will be around 0.75T. Fig. 5 also shows the simulation results of the toroidal field before the redesign using Comsol software, which is in good agreement with the mentioned calculation.

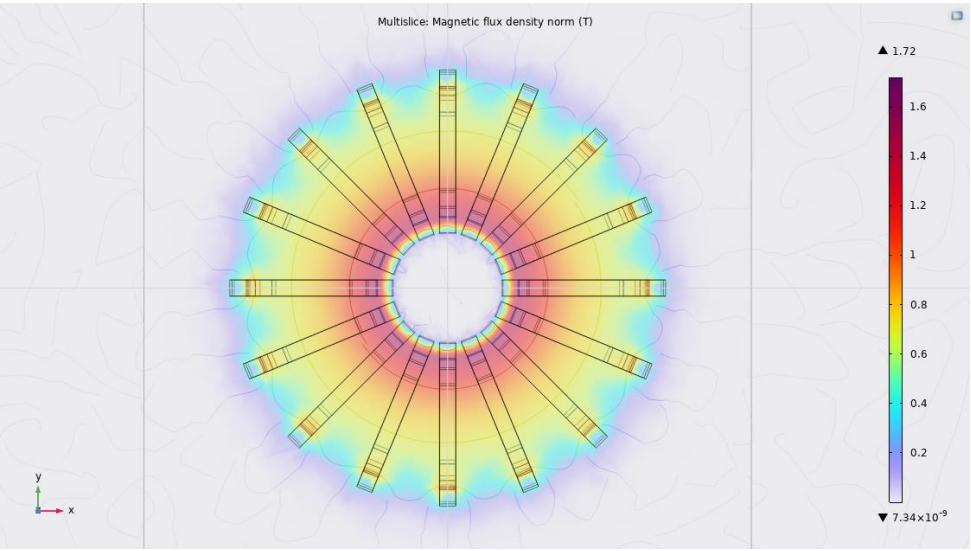

Fig. 26. Magnetic field of TF coils simulated with Comsol software (before upgrading)

In section 3, we saw that after increasing the capacity of the TF capacitor bank, the current through the coils increased and reached the value of 12.6kA. Now, in theoretical calculations and software simulation, we replace the new current value with the previous value and get the TF field again.

According to equation (4), and by placing the new value of the current in this equation, the field in the plasma center is about 0.9T, which shows an increase of 0.15T compared to the state before

the redesign. Fig. 6 shows the TF field after system redesign. The agreement between theoretical and simulation results can be seen again.

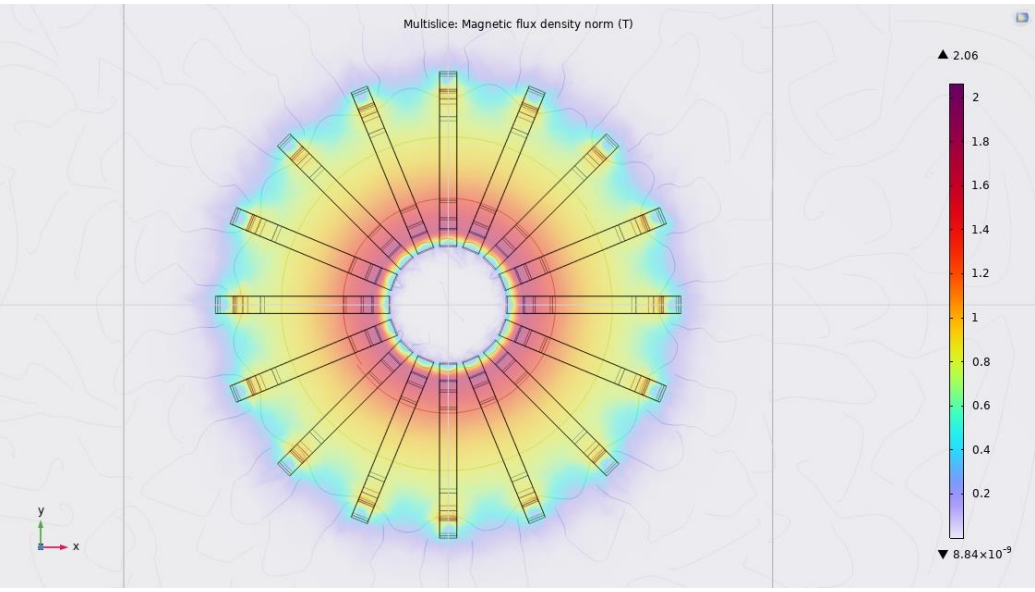

Fig. 6. Magnetic field of TF coils simulated with Comsol software (after upgrading)

Conclusion

Alborz Tokamak is a small size tokamak with a D-shaped cross section of the vacuum vessel. The main radius of the tokamak is 0.45m and its minor radius is 0.15m. This device has 16 Toroidal magnetic Field (TF) coils wrapped around the vacuum vessel symmetrically. These coils are responsible for producing the toroidal field which plays the main role in plasma confinement.

Currently, the redesign of TF magnetic systems has been considered as the redesign phase. Since one of the influencing factors on the plasma confinement time is the amount and flattop of the toroidal magnetic field, in this phase, the increase of the toroidal magnetic field has been considered. The present redesign plan only includes increasing the capacity of the TF capacitor bank. In this way, the capacity has been developed from 40mF to 60mF.

This plan provides the field 0.9T in the plasma center, which shows an increase of 0.15T compared to the state before the redesign. The amount of current in the first positive peak before redesign is around 10.5kA which reaches about 12.6 kA after that. Also, the flat-top length of the current was about 8ms and reached about 10ms.

References

1. Amrollahi, R., et al., *Alborz tokamak system engineering and design.* Fusion Engineering and Design, 2019. **141**: p. 91-100.

2. Koohestani, S. and R. Amrollahi, *TF coil structure in Alborz Tokamak, from design to mounting.* Fusion Engineering and Design, 2018. **137**: p. 104-111.

3. Mardani, M., R. Amrollahi, and S. Saramad, *Preliminary Design of Alborz Tokamak.* Journal of fusion energy, 2012. **31**: p. 175-178.

4. Walker, M.L., et al. *Introduction to tokamak plasma control*. in *2020 American Control Conference (ACC)*. 2020. IEEE.

ICNST 2024
International Conference on Nuclear Science and Technology
6- 8 MAY 2024 | Isfahan, Iran

Investigation of Metamaterials Application for Deuteron-Deuteron Tokamak Gamma and Neutron Shielding (Paper ID: 1281)

Yassin Heydarizade[1], Arezoo Riahi[1], Mohammad Reza Rezaie[1]

1. Faculty of Modern Sciences and Technologies, Graduate University of Advanced Technology, Kerman, Iran

Abstract

The development of materials for shielding of gamma and neutron radiation is an important aspect in nuclear fusion technology. Personnel of tokamak are exposed to radiation hazards due Gamma ray and neutron particles form plasma and shield material. Recently, tungsten metamaterials introduced for Gamma ray and neutron shielding. This article investigates the application of old and new metamaterials for shielding abilities in tokamaks. For method validation by Geant4 simulation, the neutron spectrum produced by Deuteron-Deuteron (D-D) in plasma interaction was compared with experimental studies. After 98% validation between experimental and simulation result, the gamma ray spectrum production in different types of metamaterials with interaction of D-D neutrons has been calculated by Geant4 toolkit. Finally, the gamma and neutron shielding property of old and new metamaterials was investigated. Result was shown the Graphene/WC and Graphene/W_2B metamaterials in comparison to other materials have the highly effective in shielding neutron and gamma rays in D-D tokamaks. The advantages of Graphene/W_2B and Graphene/WC metamaterials due low neutron and Gamma ray leakage is because their thermal conductivity coefficient than other material.

Keywords: Power Shielding, Tokamak, D-D Plasma, Metamaterial, Neutron, Gamma

1. Introduction

Recently, there have been a significant increase in discussions about tokamaks and their possibility as a source of carbon-free energy [1-3]. Deuteron-tritium (D-T) or deuteron-deuteron (D-D) plasma are the main part of tokamaks. By interaction of plasma particles, fast neutrons produce that impact with shielding materials and gamma rays create in tokamak structure. the secondary neutron and gamma ray have potential to cause harm and genetic mutations for tokamak employees. The annual effective dose depends on the type of reactor and tokamak. Hence, it is crucial to consider the annual effective dose of these particles must be in order to keep the physical

health of the personnel. The limitation level of annual effective dose of neutrons for personnel in reactors and tokamaks is 20-50 mSv/year[4-6] .But radiological dose is lower than 1 mSv/year [6-9] and environmental neutron dose is 1-5 mSv/year [10-12].The gamma rays can be successfully stopped by some material like lead ,concrete construction etc. Metamaterials have been increasingly developed for a wide range of uses in recent years as neutron shielding material [13]. Metamaterials are synthetic components that exhibit special characteristics due to their unique geometric structure and material composition. Investigators have been interested in the development of neutron and gamma shields for reactors and tokamaks for a lengthy period. Yearly, many reports are published on the development of new shields for neutrons and gamma Rays for tokamak structures and fusion research [14, 15].

In 2021, Chen et al. developed novel shields to monitor neutron and gamma rays in tokamaks [16]. The design focused on improved protective performance while minimizing both volume and shielding mass that utilizing by Monte Carlo method and the Geant4 toolkit [17]. Result was shown that the Polyethylene borate and lead was as a good material for neutron and gamma shielding for TCV tokamak [18]. Hassanpour et al study a metamaterial composed of Graphene and hexagonal boron nitride (hBN) as a potential shield for neutrons by MCNPx simulation [19].

The main purpose of this study by evaluation the 11 materials and metamaterials, is introduce a new shield for neutrons and gamma rays in tokamaks. The metamaterials that will investigate is include Graphene/B_4C [20], Graphene/hBN [21], Graphene/W_2B [22], Graphene/WB [23], and Graphene/WC [24]. The materials that will investigate is include concrete [25], boron (B) [26], calcium (Ca) [27], sodium (Na) [28], phosphorus (P) [29], and tungsten (W) [30]. This research was done using version 10.0.2 of the Geant4 toolkit. The Geant4 toolkit offers developed particle tracking and transport abilities. The overall structure of the study takes the form of seven sections, including the second part is concerned with the material and methodology used by Geant4 toolkit. The Third section will calculate the neutron production spectrum in a tokamak plasma. The fourth Section will validate the simulation neutron spectrum in D-D plasma. A comparison between the materials and metamaterials shields will do in final section that is as bellow.

2. Materials and Method

The current study utilizes the Geant4 toolkit for tokamak simulation. In the "DetectorConstruction" class was defined the material, geometry, and electromagnetic fields for this matter. In the initial stage, a 1 cm^3 cylinder is selected as the target. The source is then positioned at 1 cm distance from target. The source and target materials are specifically chosen as deuterium for simulating the neutrons created by the collision of deuterium nuclei. The Geant4 geometry was shown in Figure 1. The file known as "Run manager" is utilized for extracting the neutrons production, the yield and energy spectrum of secondary particles, and their location around target and tokamak shield. The next stage, is designed for simulation of internal environment of the tokamak, where the plasma is located with temperature exceed 20 eV [31]. The detail of used material and metamaterial such as temperature, density, and pressure was shown in Table 1. The design of first neutron shielding around the plasma has immense significance. For comparison of neutron shielding power, the thickness of all material was chosen as 80 cm. The magnetic field is applied to the geometry to improve the reliability of the simulation model compared to the real model. Figure 2 shows a final simulation geometry of tokamak components, displaying their spatial arrangement from multiple perspectives. The physics model of simulation can be found in the "PhysicsList" class. The "QGSP-BERT-HP" is used as the basic physics model and is suitable for produce secondary particles that interact with nuclei.

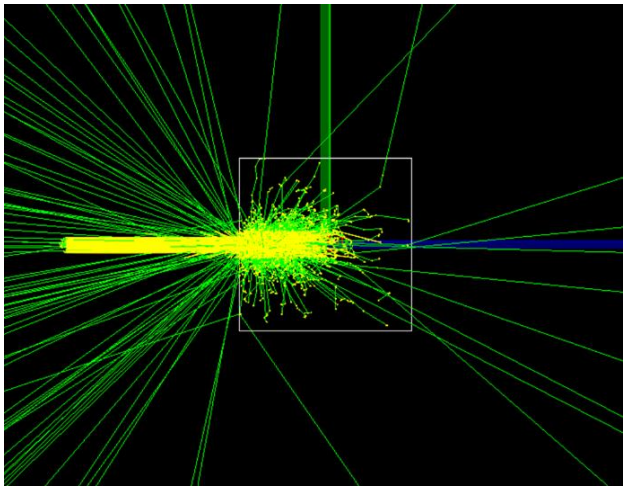

Figure 1: The simulated geometry of D-D interaction.

Table 1: The information of materials and metamaterials

Materials and Graphene (Gr) Metamaterials											
Density g/cm^3	B	Ca	Concrete (CON)	Na	P	W	Gr/B_4C	Gr/hBN	Gr/W_2B	Gr/WB	Gr/WC
	2.5	1.55	2.3	0.97	1.82	19.3	2.52	2.1	15.97	15.6	15.63

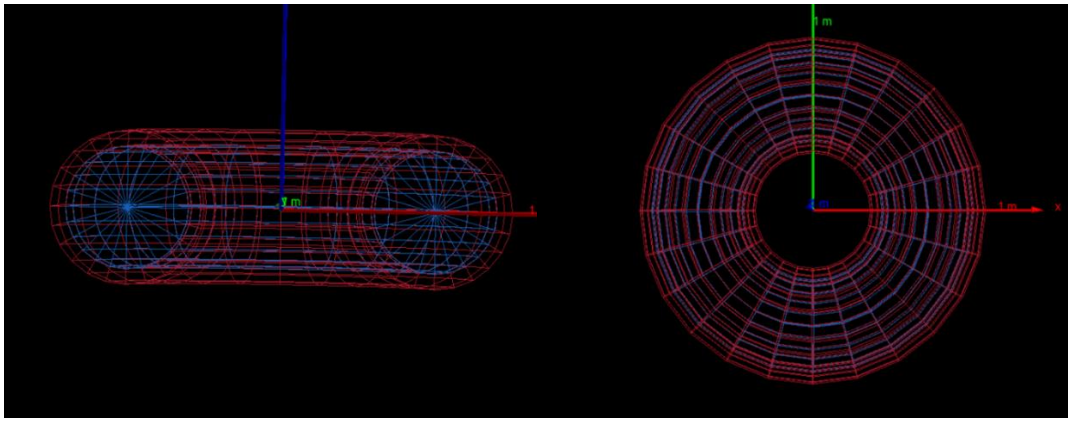

Figure 2: A perspective of the tokamak, including the interior and exterior shielding.

The equation 1 show the one of the reactions for neutron generation in D-D tokamak plasma interaction [32].

$$D + D \rightarrow {}^{3}He(0.82) + n(2.45) \qquad (1)$$

Always collision between D-D produce neutrons with energy spectrum that can be exited from magnetic field of tokamak and generate radiation hazard for employers. by analyzing of Geant4 data using Excel and Origin Pro software, it can be extracted the gamma Rays spectrum and secondary particles production in tokamak shielding material by interaction of neutrons.

Result and Discussion

Calculation of the spectrum of neutrons produced in plasma

According of Table 2, the energy range of D-D particles is reported to be between 1.22 - 7.98 MeV. The neutron spectrum corresponds to the energies mentioned in Table 2 shows in Figure 3. The spallation process in the Geant4 toolkit affects the generation of secondary particles in high energy. The Figure 3 results shows the energy of neutrons have Gaussian distribution that

maximum energy and FWHM of it is a function of deuterons energy in D-D plasma. The energy of the produced neutrons is twice the energy of D-D collisions. Similar of previously result, by increasing of the maximum energy of neutrons, the FWHM of distinction increase [33].

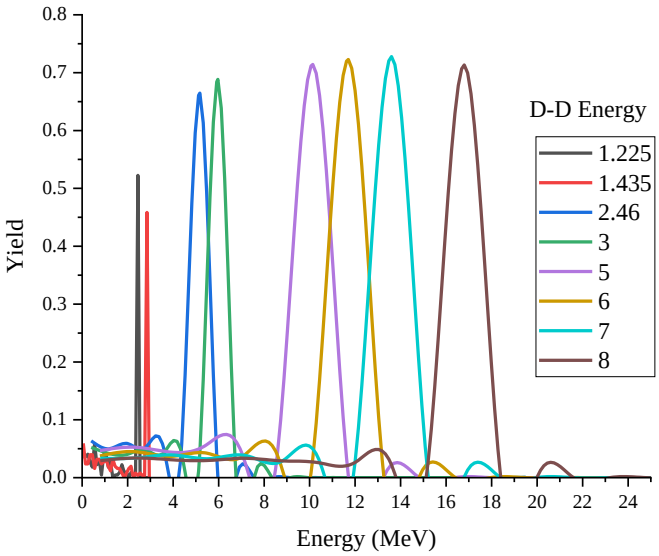

Figure 3: Neutron spectrum energy as a function of in D-D plasma collision energies

Table 2: Comparison of Geant4 simulation and practical result [35] of neutrons main energy production in D-D plasma collision .

D-D energy (MeV)	Main energy of neutrons (MeV)	Main energy of neutrons obtained from Geant4 toolkit (MeV)
2.46	5	5.174
2.87	5.5	5.978
6	8.5	11.7
6.98	9.5	13.6
7.98	10.5	16.8

It is important to mention that the KSTAR [34], EAST [35], and ITER [36] tokamaks utilize D-D plasma with an energy of 2.45 MeV. The ITER [37], HL-2A [38], and JT-60 [39] tokamaks use D-D plasma with an energy of 8 MeV. Therefore, in the next, simulation result was done only with 2.45 and 8 MeV plasma energy. Hence, the validation and verification of the code is the most crucial aspect in the simulation and modeling function. In the next section for validation and

verification of the code, was done the comparison of the simulation and practical result of neutron production in FTU tokamak.

3. Validation of Geant4 toolkit in calculation of D-D plasma neutron spectrum

This section presents the validation process of the Geant4 toolkit for neutron production in tokamak and neutron generator. The figure 4 shows the neutron spectrum produced by the collision of D-D plasma with 2.45 MeV energy in FTU tokamak and NGM-17 neutron generator [40]. The data of these reactors were modeled in Geant4 toolkit. In Figure 4, the red and yellow lines display simulation result of neutron spectrum for FTU tokamak and NGM-17 neutron generator respectively that 95% validation with the experimental result. Therefore, the Geant4 toolkit can be used for calculating neutron spectrum generated by different D-D energy.

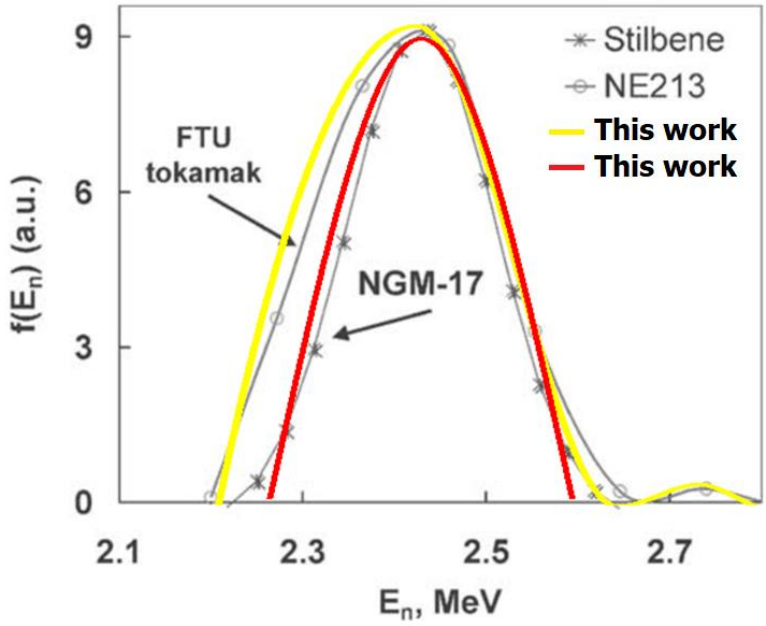

Figure 4: The neutron spectrum in D-D plasma interaction FTU tokamak and NGM-17 neutron generator[40]. Yellow and red lines show the simulation result for FTU tokamak and NGM-17 neutron generator.

4. Neutron Shielding of metamaterials for D-D tokamak comparison with other materials

In this section the neutron shielding power of Gr/B_4C, Gr/hBN, Gr/W_2B, Gr/WB and Gr/WC metamaterial was compared with B, Ca, Concrete, Na, P and W material that result was shown

in figures 5 and 6 for D-D plasma with 2.45 and 8 MeV energy respectively. Figures 5 was shown that for D-D plasma with 2.45 MeV energy, the Na, W and Ca materials are the best shielding between materials and Gr/W_2B, Gr/WB and Gr/WC are the best shielding between metamaterials.

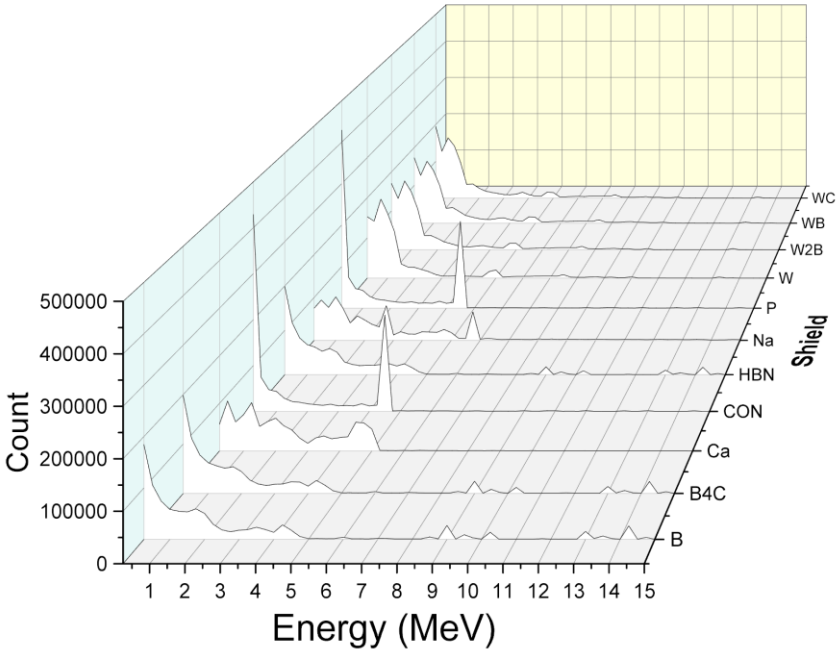

Figure 5: The neutron spectrum after tokamak with different shields for D-D plasma with 2.45 MeV energy

Figures 6 was shown that for D-D plasma with 8 MeV energy, the P and W are the best shielding between materials and Gr/W_2B, Gr/WB and Gr/WC are the best shielding between metamaterials

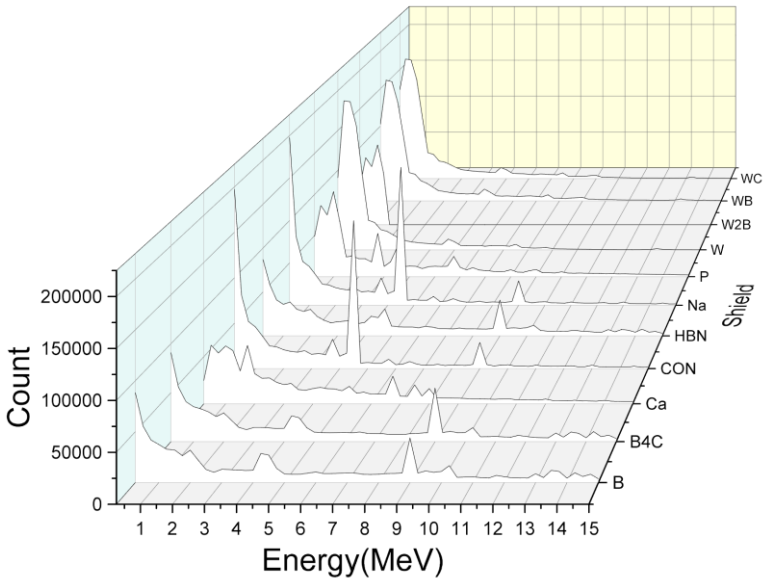

Figure 6: The neutron spectrum after tokamak with different shields for D-D plasma with 8 MeV energy

Based on the results given in Figures 5 and 6, it can be inferred that boron-based shields metamaterial such as W_2B are more effective in providing safeguards against D-D plasma with an energy of 2.45 and 8 MeV with comparison of other material and metamaterial. Therefore, it is suggested to use graphene/W2B shield as the most effective neutron shielding for tokamak.

5. Gamma Shielding of metamaterials for D-D tokamak comparison with other materials

Two cases can generate gamma rays in tokamaks: a) Deuterons that escapes from the plasma and hit with the Tokamak body. b) Neutron Particles that emitted by plasma, hit with the Tokamak body. Due to the deuteron collision in the D-D plasma environment, gamma rays can be generated. The potential for gamma ray production in D-D plasma at various energy has been explored using the Geant4 toolkit that result presented in Figure 7.

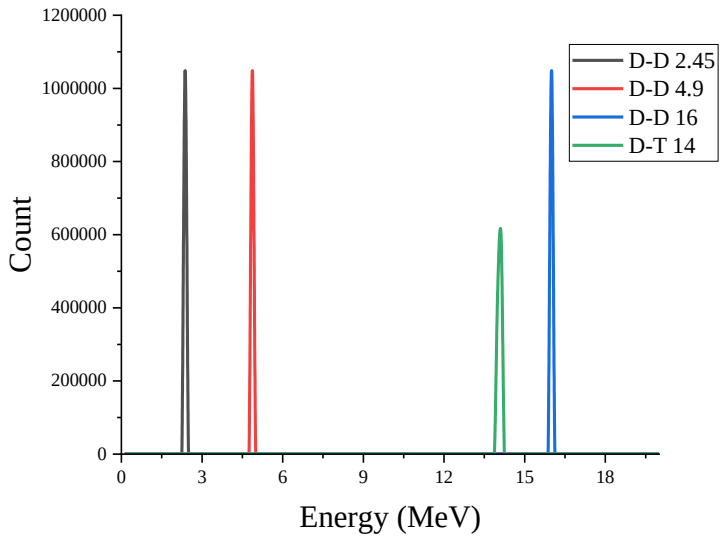

Figure 7: The gamma spectrum generated by D-D plasma fusion interaction for total different energies

According of Fig 7 result, it can be found that by decreasing the energy of deuteron particles in the plasma, the gamma ray energy was decreased. The Gamma ray spectrum resulting by plasma deuteron particles in energy levels of 1.225 and 8 MeV with a body has been used for power shielding calculation of materials and metamaterials in case A that result was shown in figures 8 and 9 respectively.

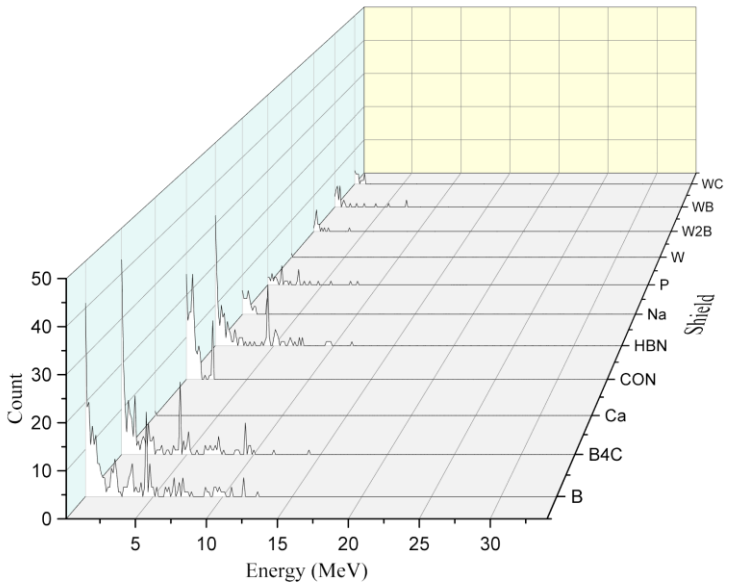

Figure 8: Transmission spectrum of gamma ray produced in 1.225 MeV D-D plasma collision with materials and metamaterial shield

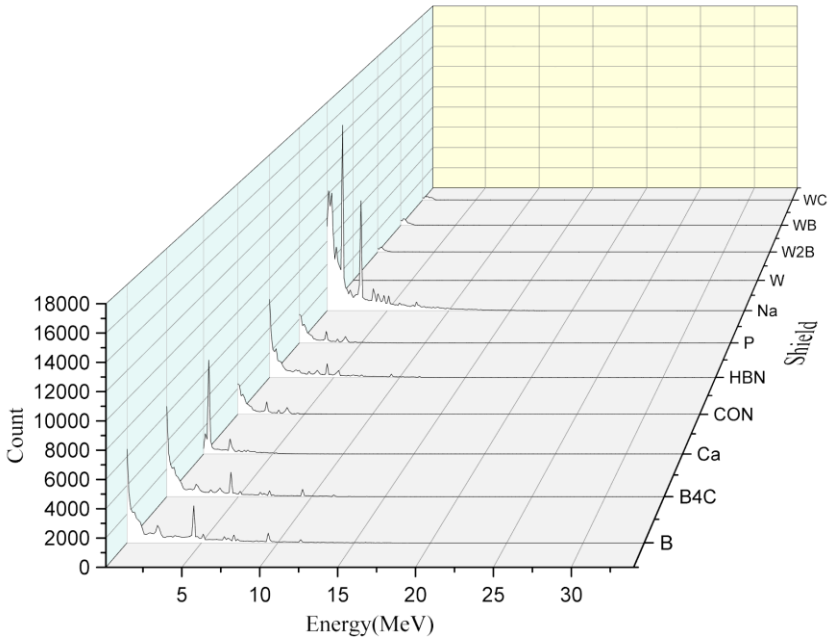

Figure 9: Transmission spectrum of gamma ray produced in 8 MeV D-D plasma collision with materials and metamaterial shield

Based on the studies in Fig 8 and 9, the Tungsten and Calcium, phosphorus and Tungsten between material and the Graphene/WC and Graphene/W_2B metamaterials, have the lower power shielding

compared to another materials and metamaterials. It's essential to note that Tungsten has the lowest performance and limited shielding tools compared to other materials. In case B, the Gamma ray spectrum was extracted by interaction of the neutron spectrum created in the 2.45 and 16 MeV plasma energy with materials and metamaterials shielding that result show in Figure 10 and 11.

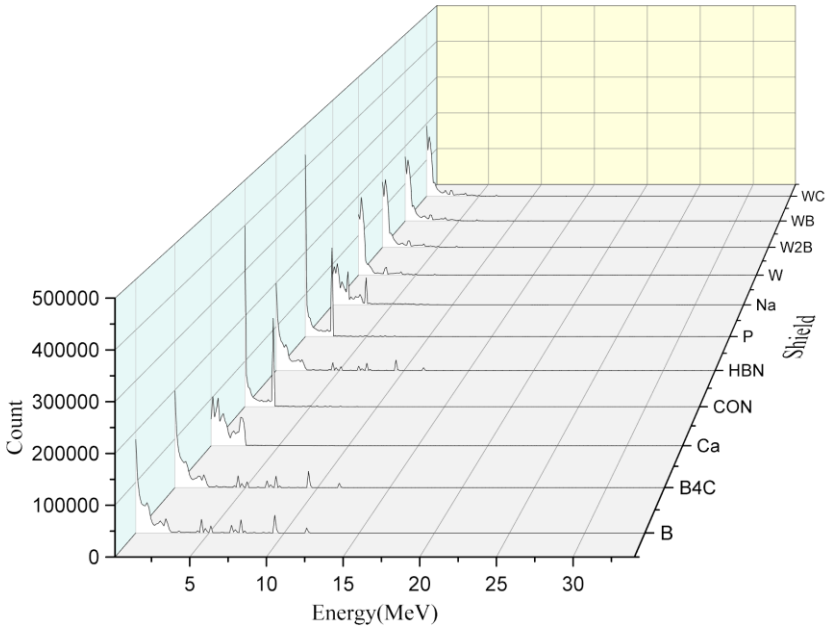

Figure 10: Transmission spectrum of gamma ray produced by collision of produced neutron with materials and metamaterial shield in 2.45 MeV D-D plasma interaction

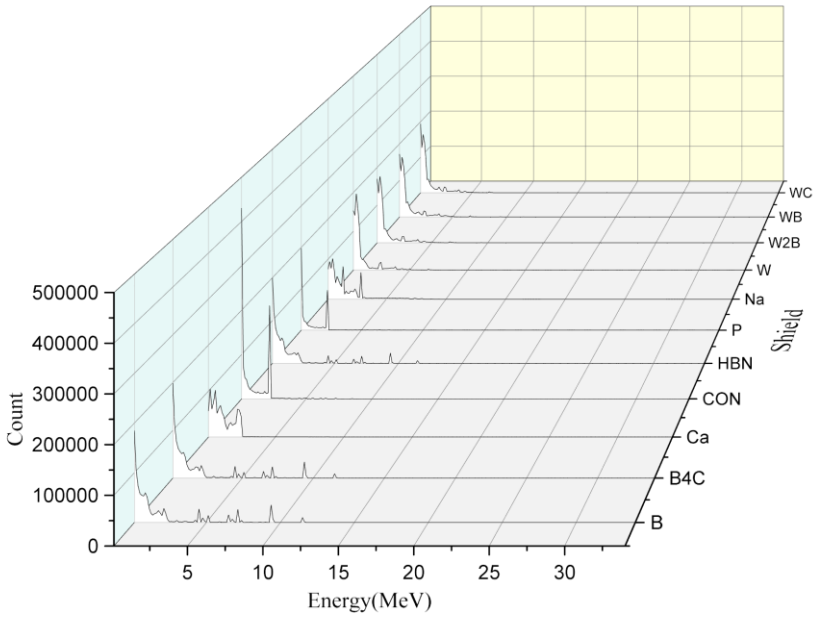

metamaterial shield

Figure 11: Transmission spectrum of gamma ray produced by collision of produced neutron with materials and metamaterial shield in 16 MeV D-D plasma interaction

Based on the info shown in Fig. 10 and 11, it can be shown that tungsten and tungsten-containing metamaterials like Graphene/WC, Graphene/W2B, and Graphene/WB, indicate impressive capacities in minimizing the intensity of gamma rays generated in the tokamak plasma. Thus, these materials have of importance potential as gamma absorbing materials for implementation in tokamak devices.

6. Conclusion

In this study, many materials and metamaterials were investigated as neutrons and gamma rays shielding in tokamak structure using Geant4 toolkit. In first case after 95% Geant4 validation, the neutrons spectrum production in D-D plasma interaction was extracted with different energy. In the second step, those of neutrons and gamma ray's spectrum was defined as source in Geant4 simulation and the neutrons and gamma ray's powers shielding of the Gr/B_4C, Gr/hBN, Gr/W_2B, Gr/WB and Gr/WC metamaterials and the B, Ca, Concrete, Na, P and W materials was calculated with Geant4 toolkit output orders. Previously Hassanpour et al investigated the neutron shielding power of graphene/h-BN metamaterial for Am-Be neutron source. In addition, an assessment was executed on the power shielding of graphene/h-BN and other metamaterials for fusion reactors. According to results of this research, it can be inferred that the graphene/WC and graphene/W_2B metamaterial showed the best shielding for Gamma ray and graphene/WC metamaterial showed the best shielding for neutrons The neutrons and gamma rays that inter to environment outside of tokamak can damage electromagnetic and electric device of machinery and produced radiation hazard for personal. the high thermal conductivity ratio of graphene/WC metamaterial provides an important advantage for heat transfer of tokamak shield. The hBN layer has 8.1 W/(m.K) thermal conductivity rate and graphene layer have a 4000 W/(m.K), thermal conductivity rate .Therfore graphene/hBN has an extremely high thermal conductivity. Because the WC layer's thermal conductivity rate is 110 W/(m.K) that is bigger than the h-BN layers, the thermal conductivity of graphene/WC is bigger than graphene/hBN. Graphene/WC, graphene/W_2B, and graphene/WC metamaterials have the lower gamma and neutron leakage than other material and metamaterial and can be introduced as proper shield with high degree of safety.

7. Reference

[1] E. R. Sadik-Zada, A. Gatto, and Y. Weißnicht, "Back to the future: Revisiting the perspectives on nuclear fusion and juxtaposition to existing energy sources," Energy, p. 129150, 2023.

[2] F. Cappelletti, "The Promise of Magnetic Fusion Technology for a Sustainable Future," *Antonios Nestoras*, p. 42.

[3] N. C. Reid, "Advanced thermo-mechanical and plasma-material interaction characterization and testing methodologies of tungsten-based materials for neutron-relevant environments," University of Illinois at Urbana-Champaign, 2023.

[4] M. J. Kim, S. J. Lee, and H. R. Kim, "Radiological safety evaluation of a recycling facility for dismantled concrete waste," *Progress in Nuclear Energy*, vol. 157, p. 104574, 2023.

[5] W. A. Metwally, O. A. Taqatqa, M. M. Ballaith, A. X. Chen, and M. A. Piestrup, "Neutron and photon dose mapping of a DD neutron generator," *Radiation Protection Dosimetry*, vol. 176, no. 3, pp. 258-263, 2017.

[6] G. Cambi, D. Cepraga, M. Frisoni, F. Carloni, and A. Chiasera, "Vacuum vessel contact dose build-up from start to end of ITER operations," in *20th IEEE/NPSS Symposium onFusion Engineering, 2003.*, 2003: IEEE, pp. 156-159.

[7] S. Fukada, Y. Oya, and Y. Hatano, "Review of recent Japanese activities on tritium accountability in fusion reactors," *Fusion Engineering and Design*, vol. 113, pp. 231-235, 2016.

[8] Q. Huang, Z. Chai, Y. Chen, Y. Wu, C. Chen, and M. Kong, "Design and analysis of the radiation shield and safety system for HT-7U tokamak," *Fusion engineering and design*, vol. 69, no. 1-4, pp. 749-756, 2003.

[9] A. Bell, P. Ballantyne, C. Gordont, and M. Wright, "The safety case for JET DT operation," *Fusion Engineering and Design*, vol. 47, no. 2-3, pp. 115-130, 1999.

[10] D. R. Fisher, "History of the 1 mSv Public Dose Limit," *Health Physics,* vol. 125, no. 6, pp. 448-449, 2023.

[11] M. A. Long and R. B. Hayes, "Evaluation of existing public dose limits applied to recreational spaceflight," *Radiation Protection Dosimetry,* vol. 199, no. 5, pp. 482-489, 2023.

[12] M. Edwards, "Development of radiation protection standards," *Radiographics,* vol. 11, no. 4, pp. 699-712, 1991.

[13] Li, Yinong, Jie Zhan, Changhui Song, Zhongwei Yan, Zhengtai Deng, Feng Liu, and Yongqiang Yang. "Design and performance of a novel neutron shielding composite materials based on AlSi10Mg porous structure fabricated by laser powder bed fusion." Journal of Alloys and Compounds 968 (2023): 172180.

[14] Q. Wang, J. A. Jackson, Q. Ge, J. B. Hopkins, C. M. Spadaccini, and N. X. Fang, "Lightweight mechanical metamaterials with tunable negative thermal expansion," *Physical review letters,* vol. 117, no. 17, p. 175901, 2016.

[15] X.-N. Liu, G.-K. Hu, G.-L. Huang, and C.-T. Sun, "An elastic metamaterial with simultaneously negative mass density and bulk modulus," *Applied physics letters,* vol. 98, no. 25, 2011.

[16] Chen WK, Hu LQ, Zhong GQ, Zhou RJ, Hong B, Li Q, Yang L. Study on the gamma rays and neutrons energy response optimization of a scintillating fiber detector for east with geant4. Nuclear Science and Techniques. 2023 Sep;34(9):134.

[17] W. Chen *et al.*, "Design of the radiation shield and collimator for neutron and gamma-ray diagnostics at EAST," *Fusion Engineering and Design,* vol. 172, p. 112775, 2021.

[18] Liu Y, Liu X, Lai C, Ma J, Meng X, Zhang L, Xu G, Lu Y, Li H, Wang J, Chen S. Boriding of tungsten by the powder-pack process: Phase formation, growth kinetics and enhanced neutron shielding. International Journal of Refractory Metals and Hard Materials. 2023 Jan 1;110:106049.

[19] Y. Chen, G. Hu, and G. Huang, "A hybrid elastic metamaterial with negative mass density and tunable bending stiffness," *Journal of the Mechanics and Physics of Solids,* vol. 105, pp. 179-198, 2017.

[20] E. D. Yalçin and A. Çanakçi, "RESEARCH PAPER CORROSION AND WEAR PERFORMANCE OF ZA27/GRAPHENE/B4C HYBRID NANOCOMPOSITES PRODUCED BY POWDER METALLURGY," *Acta Metallurgica Slovaca,* vol. 26, no. 3, pp. 126-131, 2020.

[21] A. De Sanctis, J. D. Mehew, S. Alkhalifa, F. Withers, M. F. Craciun, and S. Russo, "Strain-engineering of twist-angle in graphene/hBN superlattice devices," *Nano Letters,* vol. 18, no. 12, pp. 7919-7926, 2018.

[22] L. Zhang, Z. Bai, and Y. Chen, "Dual-functional hierarchical mechanical metamaterial for vibration insulation and energy absorption," *Engineering Structures,* vol. 271, p. 114916, 2022.

[23] A. Haque *et al.*, "Damage analysis of a perfect broadband absorber by a femtosecond laser," *Scientific Reports,* vol. 9, no. 1, p. 15880, 2019.

[24] D. Farnesi *et al.*, "Metamaterial engineered silicon photonic coupler for whispering gallery mode microsphere and disk resonators," *Optica,* vol. 8, no. 12, pp. 1511-1514, 2021.

[25] K. Mokhtari, M. K. Saadi, H. A. Panahi, and G. Jahanfarnia, "The shielding properties of the ordinary concrete reinforced with innovative nano polymer particles containing PbO–H3BO3 for dual protection against gamma and neutron radiations," *Radiation Physics and Chemistry,* vol. 189, p. 109711, 2021.

[26] S. W. Raja *et al.*, "Development of an innovative external (in air) Particle Induced Gamma-ray Emission method for rapid non-destructive determination of isotopic composition of boron in “As received” boron based ceramic neutron absorbers," *Analytica Chimica Acta,* vol. 1202, p. 339686, 2022.

[27] L. Seenappa, H. Manjunatha, K. Sridhar, and C. Hanumantharayappa, "Gamma, X-ray and neutron shielding properties of polymer concretes," 2018.

[28] N. A. Alsaif, I. Olarinoye, and Y. Rammah, "The role of titania on gamma and neutron attenuation competence of sodium lead borosilicate glasses," *Journal of the Australian Ceramic Society,* vol. 58, no. 3, pp. 939-947, 2022.

[29] K. Becker and J. Tuyn, "Thermal neutron response and intermediate and fast neutron personnel dosimetry with silver-activated phosphate glasses of different composition," *Health Physics,* vol. 11, no. 11, pp. 1225-1230, 1965.

[30] M. Salimi, N. Ghal-Eh, and E. A. Amirabadi, "Characterization of a new shielding rubber for use in neutron–gamma mixed fields," *Nuclear Science and Techniques,* vol. 29, pp. 1-8, 2018.

[31] S. Matsuo and M. Kiuchi, "Low temperature chemical vapor deposition method utilizing an electron cyclotron resonance plasma," *Japanese journal of applied physics,* vol. 22, no. 4A, p. L210, 1983.

[32] T. J. Dolan, R. W. Moir, W. Manheimer, L. C. Cadwallader, and M. J. Neumann, *Magnetic fusion technology*. Springer, 2013.

[33] J. Liu *et al.*, "Simultaneous measurement of energy spectrum and fluence of neutrons using a diamond detector," *Scientific Reports,* vol. 12, no. 1, p. 12022, 2022.

[34] Y. Lee, J.-G. Kwak, Y.-U. Nam, S.-W. Yoon, H.-S. Kim, and G. Park, "Diamond fast-neutron detector applied to the KSTAR tokamak," *Fusion Engineering and Design,* vol. 153, p. 111452, 2020.

[35] X. Peng *et al.*, "Measurement and simulation of the response function of time of flight enhanced diagnostics neutron spectrometer for beam ion studies at EAST tokamak," *Review of Scientific Instruments,* vol. 87, no. 11, 2016.

[36] K. Okada *et al.*, "Measurement of DT and DD neutrons with a TOF spectrometer for determination of fuel ion density ratio in ITER," 2009.

[37] A. Fubini and M. Haegi, "Diagnostics of fusion plasma with D (d, γ) 4He gamma-line broadening: a feasibility study," *Fusion technology,* vol. 25, no. 3, pp. 330-333, 1994.

[38] X. Yuan *et al.*, "First neutron spectrometry measurement at the HL-2A Tokamak," *Chinese Physics C*, vol. 37, no. 12, p. 126001, 2013.

[39] A. M. Sukegawaa and K. Okunob, "Estimation of neutron duct streaming with the feeder for the power supply system in the JT-60 tokamak fusion device facility," *Progress in Nuclear Science and Technology*, vol. 6, pp. 95-98, 2019.

[40] Y. A. Kaschuck, B. Esposito, L. Trykov, and V. Semenov, "Fast neutron spectrometry with organic scintillators applied to magnetic fusion experiments," *Nuclear Instruments and Methods in Physics Research Section A: Accelerators, Spectrometers, Detectors and Associated Equipment*, vol. 476, no. 1-2, pp. 511-515, 2002.

ICNST 2024
International Conference on Nuclear Science and Technology
6- 8 MAY 2024 | Isfahan, Iran

Analytical expression of the plasma particles distribution function effect on the electromagnetic instability growth rate in strongly coupled plasmas (Paper ID: 1283)

Nejadtaghi F[1], Mahdavi M [2*], Hassan pour S[1], khanzadeh H[2] and Tavassoli A[1]

[1]Department of Physics, Faculty of Basic Sciences, Nour Branch, Islamic Azad University, Nour 4817935861, Iran

[2]Department of Physics, Faculty of Basic Sciences, University of Mazandaran, P.O. Box 47415-416, Babolsar, Iran

[*2]Corresponding author's E-mail: m.mahdavi@umz.ac.ir

Abstract

The Weibel instability is one of the basic beam-plasma electromagnetic instabilities which dependents to the distribution function of plasma particles. The beam-plasma particle distribution function plays an important role in the energy traveling mechanism of relativistic electrons generated by the laser-plasma interaction in the Inertial Confinement Fusion Plasma. In this paper, an analytical expression of the beam-plasma particles distribution function effect such as; the Kappa, Semi-relativistic Maxwellian and Maxwell distributions on the Weibel electromagnetic instability growth rate is investigated in strongly coupled plasmas under the low- frequency wave condition. The obtained results show that instability growth rate of the plasma particles is depended on the temperature anisotropy, density gradient, quantum and relativistic parameters. It is shown that the plasma particles with the Kappa distribution function have the highest possible value of instability growth rate compared to the other two distribution function. Also, the plasma particles with Maxwellian distribution function have a more stable growth rate than the Kappa and the Semi-relativistic distribution functions.

Keywords: Weibel Instability, Coupled Plasmas, Temperature Anisotropy, Plasma Particles distribution Function, Low-Frequency Wave.

Introduction

A strongly coupled plasma (SCP) is defined as a system of charged particles in which the interactions are strong enough. So that the average value of the potential energy of the system is equal to or higher than the average value of kinetic energy. The strong coupled plasma with high energy density is appearing in many projects, such as; powerful magnetic generators, plasma generators, powerful sources of light radiation and the pulsed thermal reactors with inertial

confinement. The hot-dense plasmas are creating by interacting of the high-power lasers with the target fuels in the inertial confinement [1-3]. The appearance of various instabilities, including the Weibel electromagnetic instability, prevents the achievement of an ideal ignition. This instability is caused by temperature anisotropy in the plasma environment. In recent years, several investigations have been done on the effect of distribution functions such as Maxwellian, Kappa and generalized distribution on the growth rate of Weibel instability [4-5]. The comparison of growth rate of Weibel instability for two distribution functions, Maxwellian and delta-like, was studied in highly coupled plasma. The investigations showed that the impact effect reduces the growth rate in both distribution functions [6]. Also, the calculation of growth rate of Weibel instability for strongly coupled plasma with Kappa distribution function showed that growth rate of instability increases with increasing temperature anisotropy, relativistic parameter, and it is decreases with increasing spectral index and quantum parameter [7]. The plasma beam-particle distribution functions are an important parameter in the projectile beam energy transfer and the growth rate of electromagnetic instability in the fusion plasma environment. In this study, we have decided to analyze the effect of the plasma particles distribution functions on the Weibel instability growth rate. For this main, it is considered the electron beam with Semi-relativistic Maxwellian distribution function penetrates in the strongly coupled plasma with three different plasma distribution function such as the Kappa, Maxwellian and Maxwell-Boltzmann distribution functions.

Calculation of Theoretical Model

The general beam-plasma scattering equation is calculated using the Vlasov equation and its combination with the Wigner-Maxwell function for strongly coupled plasma as follows:

$$\omega^2 - c^2k^2 - \omega_{be}^2 + \pi\omega_{be}^2 \int_{-\infty}^{+\infty}\int_{0}^{+\infty} \frac{kp_\perp^3}{m\gamma(\omega - kv_\parallel)} \frac{\partial f_0^b}{\partial p_\parallel} dp_\perp dp_\parallel - \omega_{pe}^2 + \frac{m\omega_{pe}^2}{2n_p\hbar} \int_{-\infty}^{+\infty}\int_{0}^{+\infty} \frac{p_\perp^2}{(\omega - kv_\parallel)} \left[f_0^p\left(p_\perp, p_\parallel + \frac{\hbar k}{2}\right) - f_0^p\left(p_\perp, p_\parallel - \frac{\hbar k}{2}\right)\right] dp_\perp dp_\parallel = 0, \quad (1)$$

In this equation, ω and k are the frequency and wave number of wave instability respectively. ω_{be} and ω_{pe} are the beam frequency and the plasma frequency respectively. $H = \frac{\hbar k}{2}$ represents the quantum effect. In order to analyze the plasma distribution functions on the growth rate of the Weibel instability in the beam-plasma distribution, we consider a model in which the direction of electromagnetic wave propagation is $\vec{k} = k\hat{e}_z$. The beam with Semi-relativistic Maxwellian

distribution function, f_0^b , enters the strongly coupled plasma with different three distribution function such as Kappa, $f_0^{p,K}$, Maxwell, $f_0^{p,M}$, and Maxwell-Boltzmann, $f_0^{p,MB}$, distribution functions as follows.

For the beam distribution function [8];

$$f_0^b(p_\perp, p_\parallel) = \frac{1}{\pi^{\frac{3}{2}}}\left(\frac{1}{m^2\gamma^2\theta_{\perp b}^2}\right)\left(\frac{1}{m\gamma\theta_{\parallel b}}\right)\left(1+\frac{2c^2}{\theta_{\perp b}^2}\right)^{-1} exp\left(-\frac{(p_\parallel - p_d^b)^2}{m^2\gamma^2\theta_{\parallel b}^2} - \frac{2c^2}{\theta_{\perp b}^2}\sqrt{1+\frac{p_\perp^2}{m^2\gamma^2c^2}} - 1\right) \quad (2)$$

For the plasma distribution functions [9-11];

$$f_0^{p,K}(\mathrm{p}_\perp, \mathrm{p}_\parallel) = \frac{1}{\pi^{\frac{3}{2}}\theta_{\perp p}^2\theta_{\parallel p}}\frac{\Gamma(\kappa+1)}{\kappa^{\frac{3}{2}}\Gamma\left(\kappa-\frac{1}{2}\right)}\left[1+\frac{(p_\parallel+p_d^p)^2}{\kappa m^2\theta_{\parallel p}^2}+\frac{p_\perp^2}{\kappa m^2\theta_{\perp p}^2}\right]^{-\kappa-1} \quad (3)$$

$$f_0^{p,M}(\mathrm{p}_\perp, \mathrm{p}_\parallel) = \frac{\mathrm{n}_0}{\theta_{\perp p}^2\theta_{\parallel p}}\left(\frac{1}{\pi}\right)^{\frac{3}{2}}\exp\left(-\frac{p_\perp^2}{m^2\gamma^2\theta_{\perp p}^2} - \frac{(p_\parallel+p_d^b)^2}{m^2\gamma^2\theta_{\parallel p}^2}\right) \quad (4)$$

and

$$f_0^{p,MB}(\mathrm{p}_\perp, \mathrm{p}_\parallel) = \frac{\sqrt{\eta}\,\mathrm{n}_0}{\theta_{\perp p}^2\theta_{\parallel p}}\left(\frac{1}{\pi K_B}\right)^{\frac{3}{2}}\exp\left(-\frac{p_\perp^2}{K_B m^2\theta_{\perp p}^2} - \frac{\eta(p_\parallel+p_d^p)^2}{K_B m^2\theta_{\parallel p}^2}\right) \quad (5)$$

In Eqs. (2-5), κ represents the spectral index. p_d^b and p_d^prepresent the momentum of beam and plasma, respectively. Γ is the gamma function and θ is the thermal velocity of the particles, which is defined as follows.

$$\theta_{\perp,\parallel p}^2 = \left(\frac{2\kappa-3}{\kappa}\right)\left(v_{T_{\perp,\parallel}}^2\right) \quad ; \quad v_{T_{\perp,\parallel}}^2 = \left(\frac{T_{\perp,\parallel}}{m}\right) \quad ; \theta_{\perp b,\parallel b}^2 = \frac{2T}{m}$$

In order to calculate Eq. (1), it is necessary to calculate the necessary derivatives and integrals in Eq. (1) for the beam-plasma distribution functions. By introducing the following scattering functions

$$Z(\xi) = \frac{1}{\sqrt{\pi}}\int_{-\infty}^{+\infty}\frac{exp(-x^2)}{(x-\xi)}dx \quad , \quad \mathrm{Z}_\kappa^*(\eta) = \frac{1}{\sqrt{\pi}}\left[\frac{\Gamma(\kappa)}{\kappa^{\frac{1}{2}}\Gamma\left(\kappa-\frac{1}{2}\right)}\int_{-\infty}^{+\infty}\frac{\left(1+\frac{y^2}{\kappa}\right)^{-\kappa}}{(y-\eta)}dy\right] \quad (6)$$

Where;

$$\xi = \frac{1}{m\gamma\theta_{\parallel_b}}\left[\frac{\omega}{k} - p_d^b\right], \quad x = \frac{1}{m\gamma\theta_{\parallel b}}\left[\frac{p_\parallel}{m\gamma} - p_d^b\right] \text{ and } y = \frac{1}{m\theta_{\parallel p}}\left[p_\parallel + p_d^p \pm \frac{\hbar k}{2m}\right] , \eta = \frac{1}{m\theta_{\parallel_p}}\left[\frac{\omega}{k} + p_d^p \pm \frac{\hbar k}{2m}\right]$$

For ($\xi, \eta \ll 1$) the dispersion function Z(ξ), ($Z_{\kappa}^{*}(\eta)$ (For $\kappa = 3$)) becomes as follows.

$$Z(\xi) = -2\xi + \cdots + i\sqrt{\pi}\, exp(-\xi^2)$$
$$Z_3^*(\eta) = \eta(-1.66 - 0.370\eta^2 - \cdots) + i(1.539 - 1.539\eta^2 + \cdots) \qquad (7)$$

In the range of small quantum effects, ($H = \frac{\hbar k}{2}$)$\ll 1$, and small wavelengths $\xi, \eta \ll 1$, the dispersion relation of Eq. (1) becomes as follows.

$$\omega^2 - c^2k^2 - \omega_{be}^2 + i\frac{\omega_{be}^2}{\theta_{\|b} m\gamma}\frac{\theta_{\perp b}^2}{\theta_{\|b}^2}\frac{\omega}{k}\chi\sqrt{\pi} + \omega_{be}^2\frac{\theta_{\perp b}^2}{\theta_{\|b}^2}\chi - i\frac{\omega_{be}^2}{\theta_{\|b}}\frac{\theta_{\perp b}^2}{\theta_{\|b}^2}\frac{p_d^b}{m^2\gamma^2}\chi\sqrt{\pi} - \omega_{pe}^2 + \omega_{pe}^2\frac{\theta_{\perp p}}{\theta_{\|p}} +$$
$$\omega_{pe}^2\frac{\theta_{\perp p}}{\theta_{\|p}}(i\,1.539)\frac{1}{m\theta_{\|p}}\left[\left(\frac{\omega}{k} + p_d^p \pm H\right)\right] - \omega_{pe}^2\frac{\theta_{\perp p}}{\theta_{\|p}}\frac{H^2}{6} = 0 \qquad (8)$$

For ($\omega^2 \ll c^2k^2$)by substituting $\omega = \omega_r + i\,\delta$, the growth rate (for Kappa distribution function) is calculated as follows;

$$\delta_{\kappa} = \frac{k}{(1.539)\sqrt{\pi}}\left[u_{\kappa} - \frac{\left(1 + \frac{c^2k^2}{\omega_{pe}^2} + \beta\frac{H^2}{6}\right)}{n_{\kappa}}\right] \qquad (9)$$

Where $\alpha = \frac{\theta_{\perp b}^2}{\theta_{\|b}^2}$, $\beta = \frac{\theta_{\perp p}}{\theta_{\|p}}$ and

$$u_{\kappa} = \frac{\frac{\omega_{be}^2}{\omega_{pe}^2}[-1 + \alpha\chi] + \beta}{\left(\frac{\omega_{be}^2\alpha\sqrt{\pi}}{\omega_{pe}^2 m\gamma(1.539)\theta_{\|b}} + \frac{\beta}{\chi m\theta_{\|p}}\right)}, \quad n_{\kappa} = \frac{\omega_{be}^2\alpha\sqrt{\pi}}{\omega_{pe}^2 m\gamma(1.539)\theta_{\|b}} + \frac{\beta}{\chi m\theta_{\|p}} \qquad (10)$$

Where $\chi = \left(\frac{\theta_{\perp b}^2}{4c^2} + \frac{c^2}{3\theta_{\perp b}^2} + \frac{1}{2}\right)\Big/\left(1 + \frac{2c^2}{\theta_{\perp b}^2}\right)\left(\frac{c^2}{3\theta_{\perp b}^2}\right)$.

The growth rate (for Maxwell distribution function) is calculated as follows.

$$\delta^M = \frac{k}{\sqrt{\pi}}\left[u^* - \frac{\left(1 + \frac{c^2k^2}{\omega_{pe}^2} + \beta\frac{H^2}{6}\right)}{n^*}\right] \qquad (11)$$

Where $u^* = \frac{\frac{\omega_{be}^2}{\omega_{pe}^2}[-1 + \alpha\,\chi] + \beta}{\left(\frac{\omega_{be}^2\alpha}{\omega_{pe}^2 m\gamma\theta_{\|b}} + \frac{\beta}{\chi}\right)}$ *and* $n^* = \frac{\omega_{be}^2\alpha}{\omega_{pe}^2 m\gamma\theta_{\|b}} + \frac{\beta}{\chi}$ (12)

Also, the growth rate (for Maxwell Boltzmann distribution function) is calculated as follows

$$\delta^{MB} = \frac{\mathrm{k}}{\chi\sqrt{\pi}}\left[u^{\circ} - \frac{\left(1+\frac{c^2k^2}{\omega_{pe}^2}-\beta\sqrt{\eta}\frac{\mathrm{H}^2}{6}\right)}{n^{\circ}}\right] \qquad (13)$$

Where $\mathrm{u}^{\circ} = \frac{\frac{\omega_{be}^2}{\omega_{pe}^2}[-1+\alpha\,\chi]+\beta}{\left(\frac{\omega_{be}^2\alpha}{\omega_{pe}^2 \mathrm{m}\gamma\theta_{\|b}}+\frac{\beta}{\chi}\right)}$ *and* $\mathrm{n}^{\circ} = \frac{\omega_{be}^2\alpha}{\omega_{pe}^2 \mathrm{m}\gamma\theta_{\|b}} + \frac{\beta}{\chi}$ (14)

Results and Discussion

The general dispersion relation is derived by combining the relativistic Vlasov equation with the Wigner-Maxwell equation for the coupled beam-plasma. In this research, the electron beam that penetrates into the strongly coupled plasma is considered Semi-relativistic Maxwellian and the plasma distribution function is considered in three mode of Kappa, Maxwellian and Maxwell-Boltzmann distribution functions separately. The growth rate of Weibel electromagnetic instability have been calculated as function of different parameters as temperature anisotropy, density gradient, quantum parameter and relativistic parameter. In Fig. (1) is shown that, the plasma particles with the Kappa distribution function have its highest the growth rate of instability compared with three different plasma distribution function for temperature anisotropy, $\frac{\theta_{\perp \mathrm{p}}}{\theta_{\|\mathrm{p}}} = 2.2$. The effect of the quantum parameter on the growth rate of instability is shown in Fig. (2). It is shown that, the lowest growth rate is related to plasma with the Maxwell distribution function and the highest value is related to the Kappa distribution function for quantum parameter, $\mathrm{H} = 0.5$. In Fig. (3), the Weibel electromagnetic instability for three distribution functions are plotted for the relativistic parameter value ($\gamma = 1.4$). It is observed that the highest value of the growth rate is related to the Kappa distribution function. Finally, the obtained results show that the maximum growth rate of the plasma with Kappa distribution function is depended on the temperature anisotropy, quantum parameter and relativistic parameter and it has the highest possible value compared to the other two plasma distribution functions.

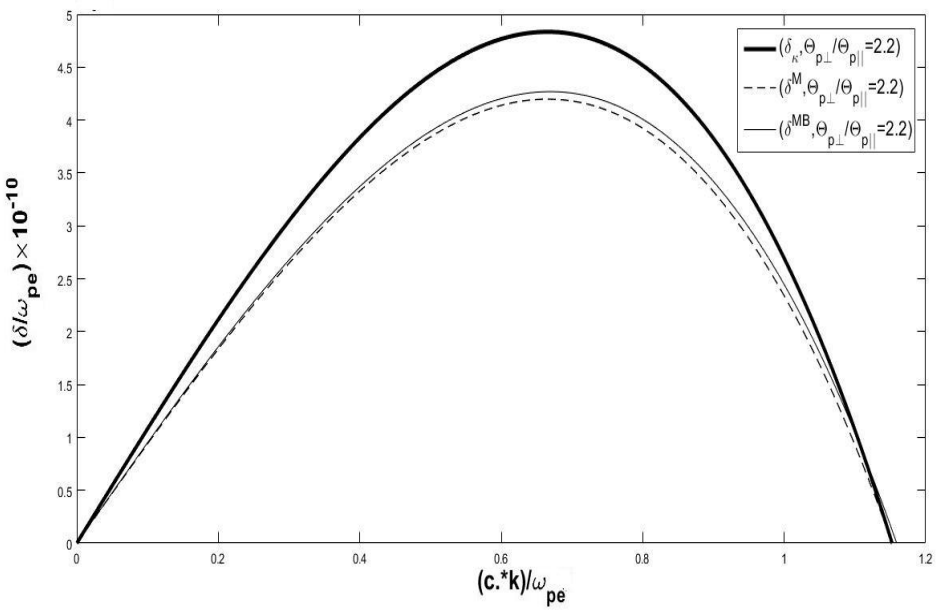

Fig .1: The instability growth rate of three distribution functions normalized ($\delta_\kappa, \delta^M, \delta^{MB}$), according to $\frac{ck}{\omega_{pe}}$ for temperature anisotropy parameter, $\frac{\theta_{\perp p}}{\theta_{\parallel p}} = 2.2$.

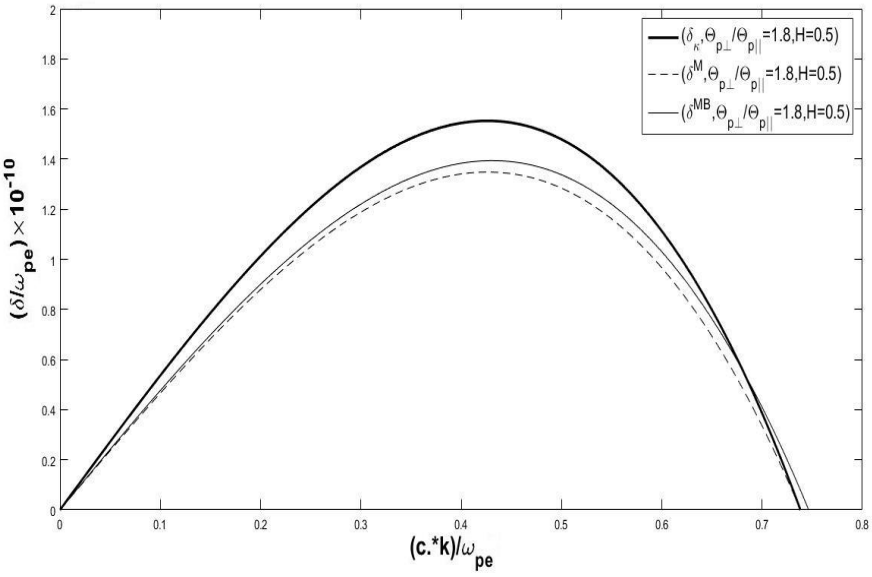

Fig. 2: The instability growth rate of three distribution functions normalized ($\delta_\kappa, \delta^M, \delta^{MB}$), according to $\frac{ck}{\omega_{pe}}$ for quantum parameter, $H = 0.5$.

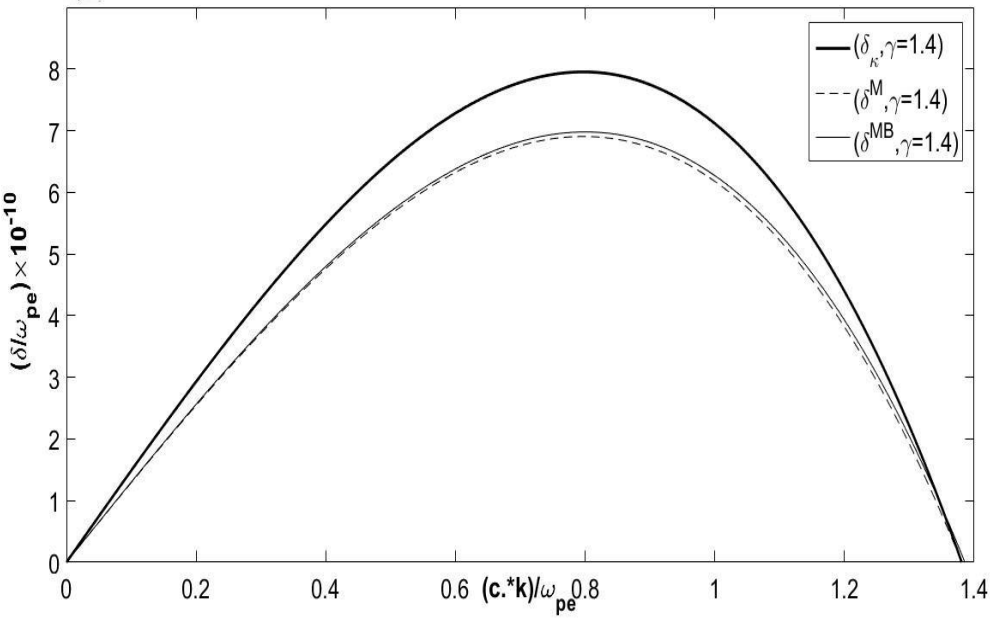

Fig. 3: The instability growth rate of three distribution functions normalized ($\delta_\kappa, \delta^M, \delta^{MB}$), according to $\frac{ck}{\omega_{pe}}$ for the relativistic parameter, $\gamma = 1.4$.

Conclusions

In this research, the plasma distribution function is considered in three models of Kappa, Maxwell, and Maxwell-Boltzmannian distribution functions and the electron beam that penetrates into the strongly coupled plasma is considered in the Semi-relativistic Maxwellian distribution functions separately. For this aim, an analytical expression is derived for imaginary parts of the dielectric constant as the instability Weibel growth rate for the plasma particle with three different distribution function under the low-frequency wave condition. The growth rate of instability depends on the temperature anisotropy parameter, density gradient, quantum parameter and relativistic parameter. The obtained results show that the maximum growth rate of the plasma with the Kappa distribution function is depended on the temperature anisotropy, density gradient, quantum parameter and relativistic parameter and it hase the highest possible value compared to the other two plasma distribution functions. The Maxwellian distribution function also has a more stable growth rate than the Kappa and the Maxwell-Boltzmannian distribution functions.

References

[1] Fortov, V. E. and Iakubov, I. T. and Khrapak, A. G. (2006). Physics of Strongly Coupled Plasma, Oxford University.

[2] Amininasab, S. and Sadighi-Bonabi, R and Khodadadi Azadboni, F. (2018). The effect of shear flow and the density gradient on the Weibel instability growth rate in the dense plasma, Physics of Plasmas, 25: 022122.

[3] Hosseini, S. A. and Mahdavi, M (2016). Weibel Instability Growth Rate in Magnetized Plasmas with Quasi-Relativistic Distribution Function, Communications in Theoretical Physics, 66: 709–712.

[4] Weibel, E. S. (1959). Spontaneously growing transverse waves in plasma due to ani–sotropic velocity distribution, Phys. Rev. Lett. 2:83.

[5] Zaheer, S. and Murtaza, G. (2007). Weibel instability with non-Maxwellian distribution functions, Physics of Plasmas, 14(2):022108.

[6] Mahdavi, M and Khanzadeh, H. (2014). The Weibel instability in a strongly coupled plasma Physics of Plasmas, Physics of Plasmas,21(6),062708.

[7] Nejadtaghi, F. and Mahdavi, M and Hassanpour, S and khanzadeh, H and Tavassoli, A(2024).Analytical expression of Weibel electromagnetic instability growth rate in strongly coupled quantum plasma, Accepted in Chinese Journal of Physics. https://doi.org/10.1016/j.cjph.2023.10.028.

[8] Zaheer, S and Murtaza, G. (2007). Weibel instability with semi-relativistic Maxwellian distribution function, Physics of Plasmas, 14(7): 072106.

[9] Kuri, D. K. and Das, N. (2014). Electron-ion collisional effect on Weibel instability in a Kappa distributed unmagnetized, Plasma. Physics of Plasmas, 21:042106.

[10] Mahdavi, M and Khanzadeh, H. (2013). Collisional effect on the Weibel instability with the bi-Maxwellian distribution function, Physics of Plasmas, 20(5):052114.

[11] Mahdavi, M and Khodadadi Azadboni, F. (2015). The quantum effect's role on weibel instability growth rate in dense plasma, Advances in High Energy Physics, 746212,1-6.

Energy Deposition of Proton Beams Toward Dense Fuel in Inertial Confinement Fusion (Paper ID: 1321)

Seyed Abolfazl Ghasemi[1,*], Amir Moslehi[2], Samira Faghih[3]

[1] *Plasma and Nuclear Fusion Research School, Nuclear Science and Technology Research Institute, PO Box 14399-51113, Tehran, Iran*
[2] *Radiation Applications Research School, Nuclear Science and Technology Research Institute, PO Box 11363-34861, Tehran, Iran*
[3] *Faculty of Engineering, Shahid Beheshti University, Tehran, Iran*
E-mail: abo.ghasemi@gmail.com

Abstract

In this research, the impact of external magnetic field with amplitudes $B_{ext} = (0-10)$ kT, on the proton beams energy deposition into the dense fuel with the density range $\rho_c \square (300 - 1000)$ g.cm^{-3}, were considered in fast ignition concept using Geant-4 simulation toolkit. Meanwhile, the simulation has been performed in the presence and absence of an external magnetic field with considering two types of Maxwellian and Gaussian energy distributions function for proton beams. Our simulations present that addition to the strength of the external magnetic field as well as the fuel density, the types of proton beam energy distribution function could incredibly affect the optimal energy deposition through the pre-compressed fuel. The results showed that under the external magnetic field amplitude $B_{ext} = (0-5)$ kT, the protons beams energy deposition gradually increased toward over-dense plasma, so that the peak values mostly obtained for $B_{ext} = 5$ kT. Meanwhile, the maximum deposited energy is obtained by considering Gaussian energy distribution function for the proton beams and for the fuel density $\rho_c = 300$ g.cm^{-3}.

Keywords: External Magnetic Field, Maxwellian Energy Distributions, Gaussian Energy Distributions, Fast Ignition, Geant4 Simulation.

Introduction

The interaction between charged particles and dense fuels, influenced by external magnetic fields, is a significant focus in plasma physics, particularly in Inertial Confinement Fusion (ICF). This area of research not only enhances our understanding of plasma physics and nuclear physics but also provides insights into fusion phenomena. External magnetic fields play a crucial role, enhancing confinement and heating while controlling particle trajectories. However, they also introduce considerations for instability suppression and energy loss mechanisms. Understanding and optimizing these effects is vital for applications in fusion research.

In ICF, the strong external magnetic fields are utilized to optimize energy deposition in dense fuel pellets. This approach capitalizes on the attractive effect of these fields on charged particles, ensuring maximum energy transfer to the fuel. Additionally, in these investigations into energy deposition is considered different energy distributions of proton beams, such as Maxwell and Gaussian distributions.

The concept of fast ignition (FI) in the decade 90s [1] and its evolution into fast ignition (FI), have prompted extensive efforts to optimize the ICF process, particularly for Deuterium -Tritium (DT) reactions in ICF. Simulations conducted in the presence of strong external magnetic fields [2-8] have been instrumental in these endeavors.

In Ref. [9], M. Roth et al, present a new concept for FI, which is based on an intense, short-pulse, laser-accelerated proton beam generated close to the compressed fuel pellet to provide the ignition spark, by providing an understanding of the advantages of ion-driven FI circumvents the issues related to the ion acceleration, pulse compression, focusing and transport [9].

M. Temporal et al, in Ref. [10], studies some aspects of the scheme of ICF fast ignition by laser-accelerated proton beams and capsule implosion by the 1D multi-group radiation-hydrodynamic code SARA up to a time close to maximum fuel compression is attained. The simulations performed in this reference, considering two types of exponential and Maxwellian energy distribution for the proton beam, show the same trends. Due to the shorter effective pulse duration for the Maxwellian distribution, the ignition energy for the exponential distribution is somewhat higher than the second distribution.

By continuing to study the fast ignition scheme of ICF by laser-accelerated proton beams considering a different energy distribution (Gaussian energy distribution) in reference [11], they show that by considering a distance d=500 m between the proton source and the capsule, the ignition energy threshold is 10 kJ. However, using the new scheme reduces the ignition energy threshold to a total of 7 kJ.

M. Temporal and et al, in Ref. [12], in the following of the study Ref. [11], Fast Ignition of a DT spherical fuel compressed to the uniform density =500 g/cm3 were investigated. They concluded by considering the Maxwellian energy distribution with a temperature Tp=4 MeV for the proton beam, the ignition energy when only one proton beam is used is 10 kJ, and if a sequence of two proton beams is considered, this energy is reduced to 8 kJ.

S. Atzeni et al, in Ref. [13], presented the first study of the ignition of DT fuel by fast protons and analysed the effects due to proton–fuel interaction, proton energy distribution, as well as to plasma hydrodynamics. They have performed 2D simulations, aimed at computing the minimum total proton energy E_{ig} required to ignite a precompressed homogeneous DT sphere by a cylindrical beam of protons with kinetic energy εp by assuming the instantaneous proton generation at distance d from the compressed fuel and exponential proton energy spectrum.

In the present work, the effect of the external magnetic field of $B_{ext} = (0-10)\ \mathrm{kT}$ on the energy deposition of the proton beam with two types of Maxwellian and Gaussian energy distributions into high density fuel of $\rho_c = (200\ -1000)\ \mathrm{g.cm^{-3}}$ in fast ignition concept has been investigated by using the Geant4 simulation toolkit.

Simulation Setup

Utilizing the advanced capabilities of version 10.5 of the Geant4 simulation toolkit, this study delves into the complexities of fuel dynamics within a fusion context. The geometric arrangement of the fuel, depicted in Figure 1 as a spherical shell enveloping a central hot spot. This configuration sets the stage for a detailed exploration of plasma interactions crucial to the understanding of fusion processes.

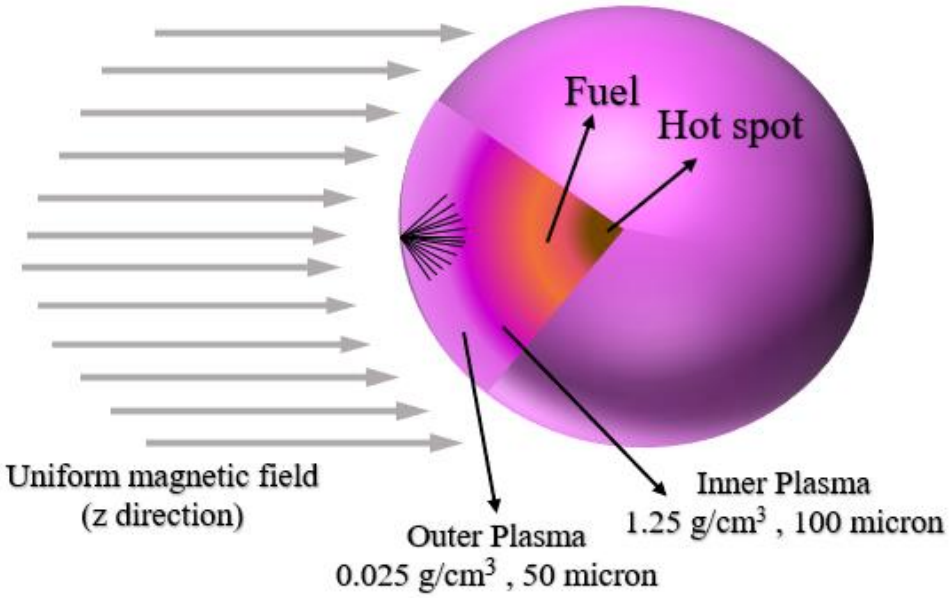

Fig. 1. Spherical layers of fuel in the simulation model [8].

Of particular interest are the two plasma shells surrounding the dense fuel: an inner layer characterized by low-density pre-plasma shell with a thickness of 100 μm and a density of 1.25 gcm^{-3} and, an outer layer forming another spherical plasma shell with a thickness of 50 μm and a density of 0.025 gcm^{-3}. The density of these two plasma shells is determined by the number of ions in them. These layers, defined by specific thicknesses and densities as outlined in Table 1, play a pivotal role in shaping the behavior of the fuel under simulation.

Table 1. Values of mass, density and fuel radius [8].

$M_C\,(mg)$	$\rho_C\ (g.cm^{-3})$	$R_C\ (\mu m)$
0.261	828	43
0.524	658	58.1
1.314	490	86.6
2.094	406	108
4.190	292	152

The simulated fuel sphere is placed in a vacuum. The proton beams, produced from the fast ignitor laser applied on low density pre-plasma, are emitted isotropically from a thin circular plate source

with a radius of 15 μm, between 0◦ and 180◦. The LowE_Livemore electromagnetic physics model is called for protons transport. By applying a strong external magnetic field with a magnitude of 10 times the reference [7], i.e. $B_{ext} = (0-10)$ kT , in the *z*-direction (laser radiation direction) to the whole simulation setup (total fuel sphere), the amount of energy absorbed into the fuel with density range $\rho_c \sim 300-1000$ g.cm^{-3} are estimated per proton. To reduce the relative statistical error in absorption energies (less than 5%), the number of protons is also considered as 10^6.

To achieve ignition with minimal energy in the inertial confinement fusion (ICF) utilizing the combined fast ignition (FI) model, a proton beam generated by a laser accelerator under the influence of a strong external magnetic field [7, 8] can be employed. This method entails the rapid production and acceleration of protons to tens of MeV within seconds and at a distance of less than 100 mm near the fuel pellet [9]. Consequently, the convergence of proton beam trajectories toward the fuel pellet under the influence of a strong external magnetic field facilitates the transfer of a significant portion of their energy into the pellet.

In the pursuit of comprehensively exploring the intricacies of energy deposition by proton beams and its interaction with an external magnetic field, we considered two distinct types of energy distribution functions for the proton beams: Maxwellian and Gaussian.

According to the reference [12], the considered Maxwellian distribution function for the proton beams is given as follows:

$$N(\varepsilon) = \frac{2N_0}{\sqrt{\pi}(T_p)^{3/2}} \sqrt{\varepsilon} e^{-\left[\frac{\varepsilon}{T_p}\right]}$$

where N_0 is the total number of ions, T_p is the ion temperature, and, ε is the kinetic energy of the protons.

While according to reference [11], the Gaussian distribution function with energy spread Δ (full width at half maximum) and average energy ε_0 , is defined as follows:

$$N(\varepsilon) = N_0 \frac{\sqrt{\alpha}}{\Delta} \sqrt{\pi} e^{-\alpha\left[\frac{(\varepsilon-\varepsilon_0)}{\Delta}\right]^2}$$

where $\alpha = -4\ln(1/2)$ is a constant coefficient.

Results and Discussion

The approach to achieving ignition with minimal energy in Inertial Confinement Fusion (ICF) through the Fast Ignition (FI) model revolves around swiftly generating and propelling protons to high energies close to the fuel pellet, thereby aiding in the efficient transfer of energy into the pellet.

Hence, this investigation aims to a parametric study on the energy deposition of heavy proton beams considering and examining two types of energy distribution—Maxwellian and Gaussian, dense fuel density and also external magnetic field strength.

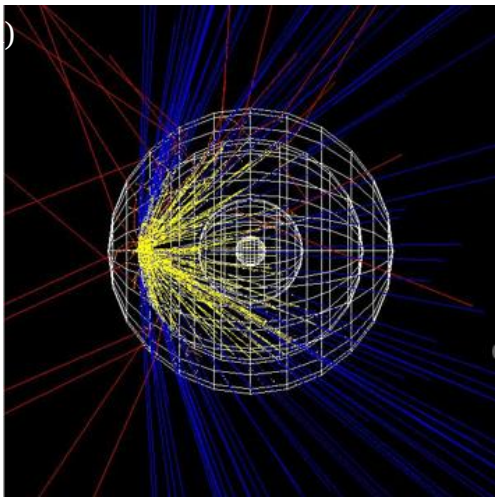

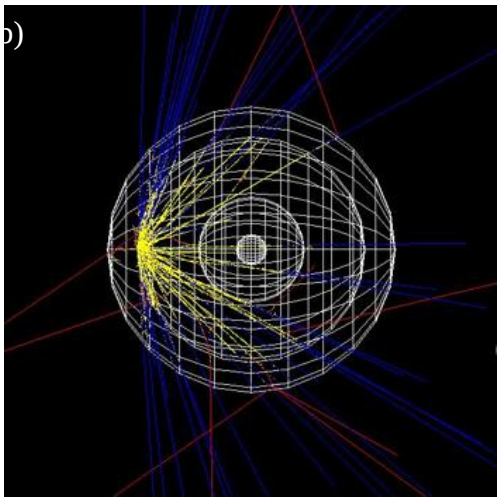

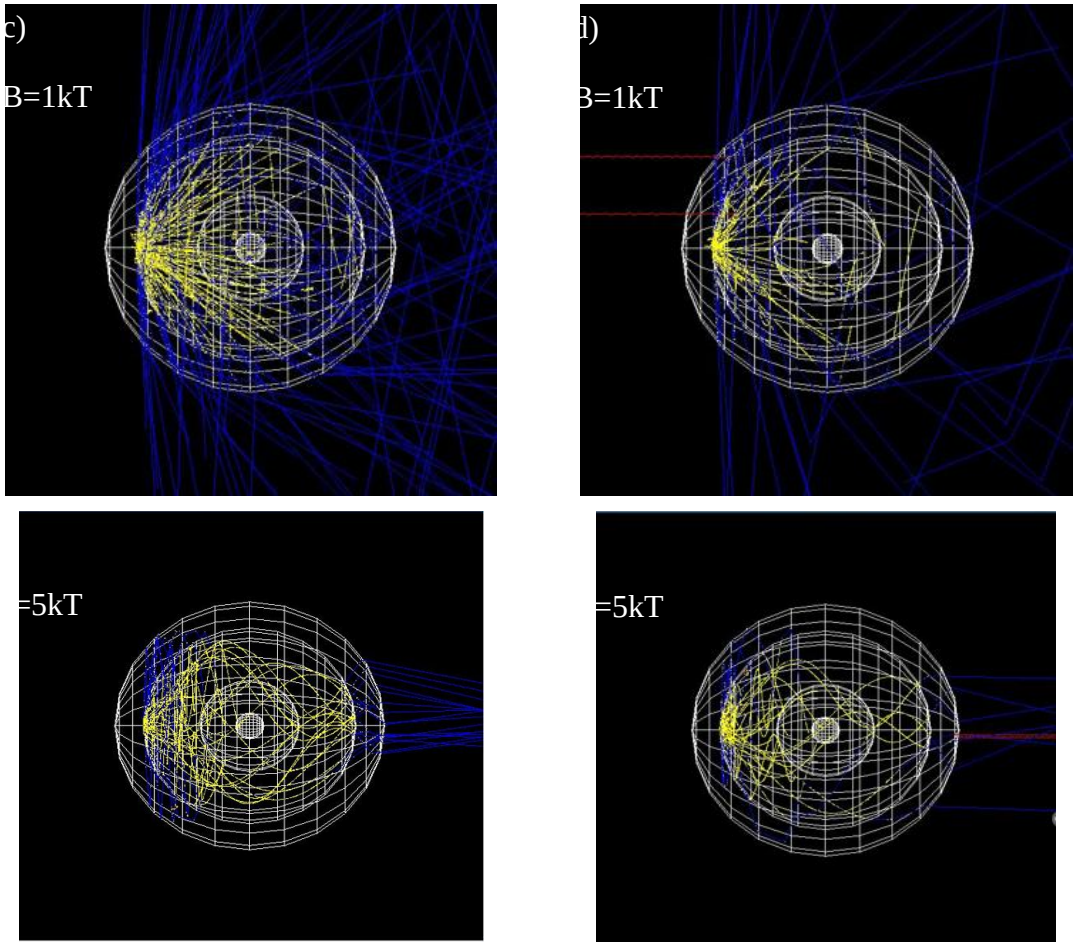

Fig. 2. Energy deposition per protons in fuel for $\rho = 490$ g.cm^{-3}; Panels (a-b) without external magnetic feild and panels (c-f) with external magnetic feild. By considerting panels (a, c, e) with Gaussian distribution function ,and (b, d, f) with Maxwellian distribution function for poroton beams. Blue lines indicate proton beams, red lines high energy electrons and yellow lines low energy electrons confined in the proton beams track direction.

The track of proton beams is shown typically in Fig.2, with or without the influence of a magnetic field for a fuel density of 490. As panels (a, b) show, when there is no magnetic field, most of the proton beams energy scatter to the sides. On the other hand, increasing the magnetic field, will converge the proton beams toward fuel spatially for the value B= 5 kT and for Gaussian distribution function, Panels (c, e). Further, it is observed that, by increasing the magnetic field, the fast electrons tracks vanish completely (high energy electrons diverge to the sides) for Gaussian distribution and the protons beams as well as low energy electrons collimate toward the dense fuel.

Considering the significant role of linear energy transfer (LET) of heavy particles in ICF it is shown in Graphs (a-f) that the heavy proton beams, with higher LET in comparison to the lighter

electrons deposit most of their energy in a short distance to some extent nearing to dense fuel pellet. While, the role of light low energy electrons produced during the fusion process around the track of proton beams, also contributes to the overall energy deposition and heating of the target material.

Electromagnetic interactions (due to charged particle current) as well as coulomb collision between charged particles (protons and electrons) during the interaction of produced MeV electrons and protons with background pre-plasma, lead to frequent changes in their direction and energy loss, and then by decreasing their kinetic energy, they deposit energy more efficiently toward the fuel sphere. Whereas electrons continuously and relatively uniformly lose energy as they move through matter through processes such as Coulomb scattering and Bremsstrahlung radiation. Also, Fig 2(a, f) reveals that the heavy protons deposit their energy far from the main fuel pellet in comparison to the electrons (yellow lines). As if the yellow lines form a spiral path around the protons.

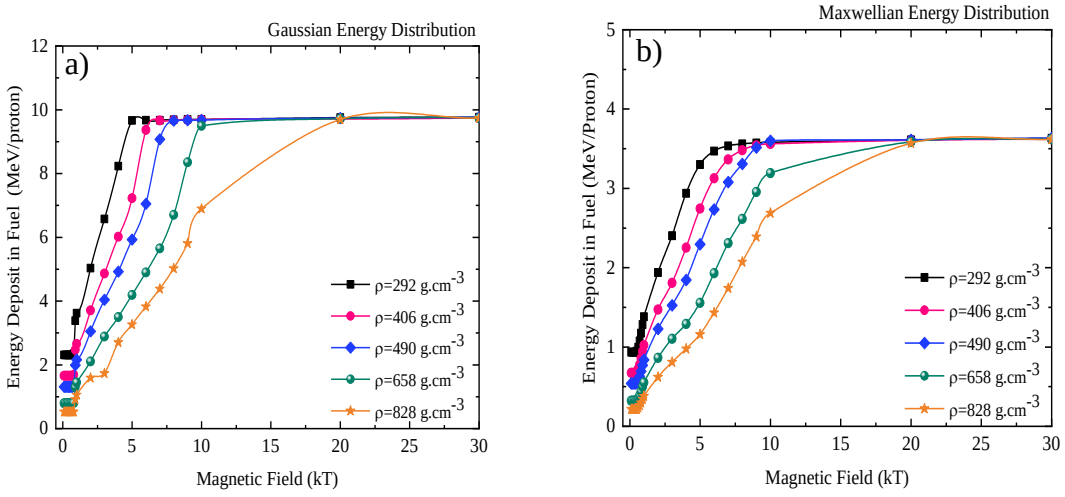

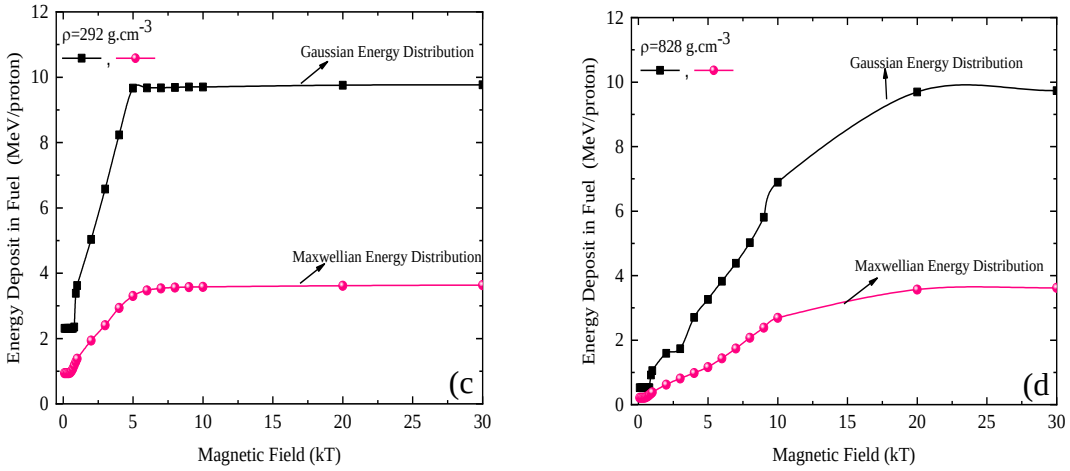

Fig. 3. Energy deposition in fuel by consideration, a) Gaussian distribution function and b) Maxwellian distribution function, for all densities: $\rho_c \square 300-1000\ \text{g.cm}^{-3}$, and for c) $\rho_c = 292\ \text{g.cm}^{-3}$, d) $\rho_c = 828\ \text{g.cm}^{-3}$.

The simulation results of energy deposition into the fuel considering two types of energy distribution functions for the proton beam and for the density range $\rho_c \square 300-1000\ \text{g.cm}^{-3}$ are shown in Figure 3.

Figure 3(a, b) clearly presents that without applying an external magnetic field, there is no collimation of the proton beams toward the fuel and a small amount of energy is also deposited about 1.5 MeV per proton. By applying an external magnetic field and increasing its strength, the energy deposition increases with a steep slope. So, for all the fuel densities the maximum value of energy deposition obtained is 10 MeV/protons. Meanwhile, it is observed that after the value of 10 kT, there is no increase in proton energy deposition and it became saturated. Comparing the figs. (a, b) reveal that the optimal energy deposition gained for the protons with Gaussian distribution function. It means that if we consider the Gaussian distribution for protons, the energy deposition efficiency will be 3 times more than the protons with Maxwellian function approximately for all the fuel range $\rho_c \square 300-1000\ \text{g.cm}^{-3}$ and this is amazing. Moreover, comparing the panels (a,b), one can conclude that the optimal values of protons energy deposition obtained from the critical range for magnetic field $B_{ext} \square (5-10)\ \text{kT}$ for both distribution functions. So for the smallest fuel density $\rho_c = 292\ \text{g.cm}^{-3}$, the optimal energy deposition is gained at $B_{ext} \square 5\ \text{kT}$

and for the highest fuel density $\rho_c = 828\ \text{g.cm}^{-3}$, it occurs at $B_{ext} \sim 10\ \text{kT}$. The difference between the two distribution functions is also depicted in panels (c, d). The benefit of Gaussian distribution is obviously presented. In addition, fuel density also plays an important role in proton beam energy deposition, so that, with increasing the fuel density, more amplitude of the external magnetic field is required for efficient energy deposition.

Conclusions

The simulation study highlights the impacts of energy distribution functions of proton beams as well as external magnetic fields and dense fuel density on the energy deposition toward dense fuel in the context of Inertial Confinement Fusion (ICF).

Our simulation results reveal that the external magnetic field significantly affects the energy deposition into the dense fuel, especially when comparing the simulation results with and without the magnetic field. So that for an intensity of the results showed that under the external magnetic field amplitude $B_{ext} = (0-5)\ \text{kT}$, the protons beam energy deposition gradually increased toward over-dense plasma, so the peak values were mostly obtained for $B_{ext} = 5\ \text{kT}$. Meanwhile, the optimal deposited energy is obtained by considering the Gaussian energy distribution function for the proton beams and for the fuel density $\rho_c \sim 300\ \text{g.cm}^{-3}$.

In addition, fuel density also plays an important role in proton beam energy deposition, so that, with increasing the fuel density, more amplitude of the external magnetic field is required for efficient energy deposition. In other words, for the biggest fuel density $\rho_c = 828\ \text{g.cm}^{-3}$, we need about 20 kT (two times more than one required for the densities $\rho_c \sim 292-658\ \text{g.cm}^{-3}$) magnetic field intensity to reach the energy deposition of about10 MeV/proton.

References

[1] Tabak, M., et al. (1994). Ignition and high gain with ultrapowerful lasers. Phys. Plasmas 1, 1626. https://doi.org/10.1063/1.870664

[2] Hong-bo Cai and Shao-ping Zhu and X. T. He. (2013). Effects of the imposed magnetic field on the production and transport of relativistic electron beams. Phys. plasmas 20, 072701

[3] Hohenberger, M. , et al. (2012). Inertial confinement fusion implosions with imposed magnetic field compression using the OMEGA Laser. Phys. plasmas 19, 056306

[4] D. J. Strozzi, et al. (2015). Imposed magnetic field and hot electron propagation in inertial fusion hohlraums. J. Plasma Phys, vol. 81, 475810603.

[5] X. H. Yang, et al. (2011). Effects of external axial magnetic field on fast electron propagation. Phys. plasmas 18, 093102.

[6] T. Johzaki, et al. (2016). Electron beam guiding by strong longitudinal magnetic fields, Journal of Physics: Conference Series 688 012041.

[7] Ghasemi, S. A., Moslehi, A., & Faghih, S. (2020). The effect of external magnetic field on the electron energy deposition in dense fuel for fast-shock ignition concept by using Geant4 simulation toolkit. Journal of Nuclear Science and Technology (JONSAT), 41(4), 84-91. https://doi.org/10.24200/nst.2021.1173

[8] Ghasemi, S. A. and et al (2022). Collimation of fast electron beams by strong external magnetic field in laser–solid interaction using Monte Carlo simulation. Laser Phys. Lett. 19 066001. https://doi.org/10.1088/1612-202X/ac642b

[9] Roth, M., and et al (2001). Fast Ignition by Intense Laser-Accelerated Proton Beams. Physical Review Letters, 86(3), 436–439. doi: https://doi.org/10.1103/physrevlett.86.436

[10] Temporal, M., Honrubia, J. J., Atzeni, S. (2002). Numerical study of fast ignition of ablatively imploded deuterium–tritium fusion capsules by ultra-intense proton beams. Phys. Plasmas; 9 (7): 3098–3107. https://doi.org/10.1063/1.1482375

[11] Temporal, M. (2006). Fast ignition of a compressed inertial confinement fusion hemispherical capsule by two proton beams. Physics of Plasmas, 13(12), 122704. https://doi.org/10.1063/1.2400592

[12] Temporal, M., Honrubia, J. J., Atzeni, S., (2008). Proton-beam driven fast ignition of inertially confined fuels: Reduction of the ignition energy by the use of two proton beams with radially shaped profiles. Phys. Plasmas; 15 (5): 052702. https://doi.org/10.1063/1.2918316

[13] Atzeni, S. et al (2002). A first analysis of fast ignition of precompressed ICF fuel by laser-accelerated protons. Nucl. Fusion 42 L1. https://doi.org/10.1088/0029-5515/42/3/101

ICNST 2024
International Conference on Nuclear Science and Technology
6- 8 MAY 2024 | Isfahan, Iran

Role of Temperature Anisotropy in the Inertial Fusion Process (Paper ID: 1322)

M. Mahdavi[1], F. Khodadadi Azadboni[2*] and E. Khademloo[1]

[1] *Department of Nuclear Physics, Faculty of Basic Sciences, University of Mazandaran, P.O. Box 47415-416, Babolsar, Iran*

[2,*] *Department of Physics Education, Farhangian University, P.O. Box 14665-889, Tehran, Iran*

F.khodadadi@cfu.ac.ir

Abstract

This paper investigates the influence of temperature anisotropy on the ignition criteria of deuterium-tritium (DT) and Proton-Boron-11 (PB) fuels in fast ignition fusion schemes using short-pulse laser-generated shock waves. The study demonstrates that higher temperature anisotropy leads to an increase in the required confinement parameter for both DT and PB fuels. Additionally, the fusion energy fraction (f_α) decreases as the temperature anisotropy parameter increases. The maximum fraction of absorbed α-particles in the hot spot is approximately 0.86 for DT fuel, whereas it is 0.32 for PB fuel. At a time scale of 5×10^{-13}s, a tenfold increase in temperature anisotropy results in a 4% increase in the maximum confinement parameter for DT fuel, while PB fuel experiences a 23% increase. Furthermore, the fusion energy fraction of DT fuel decreases to 40%, and PB fuel experiences a decrease of approximately 65%. The presence of temperature anisotropy can alter the critical values of temperature, density, and confinement time required for sustained fusion reactions. Anisotropic conditions can impact the energy deposition of beams in the fuel plasma, leading to variations in energy transfer efficiency and, consequently, overall ignition efficiency. These findings underscore the importance of considering temperature anisotropy in the ignition criteria of fast ignition fusion schemes. Managing temperature anisotropy is crucial for achieving the required confinement parameters and optimizing the fusion energy fraction for both DT and PB fuels.

Keywords: Fusion energy, Deuterium-Tritium fuel, Proton-Boron-11 fuel, Ignition criteria, Temperature anisotropy.

Introduction

Inertial confinement fusion (ICF) is a fusion energy method that involves compressing and heating a small amount of fusion material using external forces[1]. Fast ignition has emerged as a promising alternative approach to traditional inertial confinement fusion over the past few decades[2]. In the fast ignition scenario, temperature anisotropy, or uneven distribution of temperature, plays a crucial role in energy transport. High-power laser pulses interacting with the fuel create shock waves and generate electron beams, which heat the fuel in the direction of wave propagation, leading to a temperature anisotropy in the electron distribution. The anisotropic distribution functions in the velocity space may drive unstable electromagnetic modes, including the Weibel, fire hose, and mirror instabilities[3-5]. The Weibel electromagnetic instability takes place when the electron perpendicular temperature exceeds the parallel one, which creates electromagnetic waves propagating along the magnetic field and restoring isotropy in phase space [6]. Weibel instability is ubiquitous in many environments in space and astrophysical plasmas and shows a wide variety of conditions [7]. The fire hose instability occurs when the parallel temperature is larger than the perpendicular temperature and when the parallel thermal pressure exceeds the magnetic pressure and produces waves propagating along the magnetic field, relaxing the distribution to a more isotropic temperature[8]. Mirror instability happens when the perpendicular temperature is higher than the parallel temperature, producing electromagnetic waves propagating across the magnetic field lines and also relaxing the plasma to an isotropic distribution [9].

Numerous studies have examined various instabilities and their impact on fuel ignition[10-12]. Recent research has focused on investigating the effects of temperature anisotropy resulting from shock waves on electron beam propagation and energy deposition in the fuel plasma[13-15]. These studies have also explored the behavior of instabilities induced by temperature anisotropy in plasma different environments and its significance for achieving successful fusion reactions. However, there is currently a lack of research specifically addressing the influence of temperature anisotropy on the ignition conditions for DT and PB fuels in the context of fast ignition. The objective of this paper is to address this research gap by investigating the influence of temperature anisotropy, induced by shock waves, on the ignition conditions for DT and PB fuels in fast ignition fusion. By analyzing the ignition conditions and studying the effects of temperature anisotropy,

this study aims to provide insights that can optimize the ignition process and enhance the feasibility of inertial confinement fusion as a viable fusion energy source.

Energy balance Equation of DT fuel

The deuterium-tritium fuel is an important fuel in ICF because DT fuel has the largest cross-section at a relatively low temperature**.** The nuclear reaction $D+T \rightarrow \alpha(3.5\,MeV)+n(14.1\,MeV)$ results in the immediate decomposition of the nucleus into a neutron with an energy of 14.1 MeV and an alpha particle with an energy of 3.5 MeV. Linear transverse waves are considered in dense plasma composed of electrons and immobile ions.The plasma will be heated only in the velocity dimension along the wave propagation direction, leading to a temperature anisotropy of the electron distribution that varies with the wave motion. Because ions are heavier than electrons, in the initial stage after the interaction of the beam with the plasma, the electrons will experience temperature anisotropy. Temperature anisotropy is denoted $\beta = T_{\perp} / T_{\parallel}$, the temperature of electron T_e is defined as $Te = (T_{\perp})^{2/3}.(T_{\parallel})^{1/3}$. In that case, T_e can be written as β of follows $T_e = \beta^{2/3} T_{\parallel}$. The effective temperatures in the perpendicular and parallel direction with respect to the wave propagation are given by[13]

$$T_{\parallel} = \int m_e v_x^{\,2} f_0(v) / (2n_0) d^3v \quad (1) \quad T_{\perp} = \int m_e v_z^{\,2} f_0(v) / n_0 d^3v \quad (1)\,,$$

where the distribution function, f_0 is defined as

$$f_0 = \frac{n_0}{T_{\parallel}^{1/2} T_{\perp}} \left(\frac{m_e}{2\pi k_B}\right) exp\left(-\frac{m_e}{2}\left[\frac{(v_x^2+v_y^2)}{k_B T_{\perp}} + \frac{(v_z^2-v_{ez}^2)}{k_B T_{\parallel}}\right]\right). \qquad (2)$$

The hot-spot ignition condition for the fuel pellet can be determined by considering the power balance between fusion energy deposition and energy loss terms. The equation describing the ignition requirement is defined by

$$f_{\alpha} W_f - W_B - W_{he} - W_m \geq 0 \quad . \qquad (3)$$

The ignition fusion power W_f [erg/s.cm^3] is given by [3]

$$W_f\left[erg/cm^3.s\right] \approx 8.07\times10^{40} < \sigma v >_{DT} \rho^2{}_{DT} \quad , \tag{4}$$

where $<\sigma v>_{DT}$ is the reactivity of the DT reaction fitted in the domain of ion temperatures 1 keV $< T_i <$ 100 keV[16]

$$\prec \sigma v \succ_{DT} (\frac{cm^3}{s}) = 6.4341\times10^{-14}\varsigma^{-5/6}\left(\frac{6.661}{T_i}\right)^2 \exp(-19.983(\frac{\varsigma}{T_i(KeV)})) \tag{5}$$

where ζ is

$$\varsigma = 1+\frac{0.10675T_i{}^3 - 4.6064T_i{}^2 - 15.136T_i}{0.01366T_i{}^3 + 13.5T_i{}^2 + 75.189T_i + 1000}$$

The fraction of alpha particle that deposited energy inside the igniter domain can be estimated as follows [16]

$$f_\alpha = \begin{cases} \frac{3}{2}x_\alpha - \frac{4}{5}x_\alpha^2 & x_\alpha < \frac{1}{2} \\ 1-\frac{1}{4x_\alpha}+\frac{1}{160x_\alpha^3} & x_\alpha \geq \frac{1}{2} \end{cases}, \qquad x_\alpha(\tau) = \frac{R}{R_\alpha} \tag{6}$$

The igniter dimension R in our model is taken to be, $R = \left(u_s - u_p\right)\tau_L$, where u_s and u_p are the shock wave velocity and the particle velocity accordingly, τ_L is the laser pulse duration that causes ignition and c is the speed of light. Therefore R_α for the DT fuel is approximated by [2]

$$R_\alpha[cm] = 1.5\times10^{-2}\left(\beta^{\frac{2}{3}}T_{\square}(KeV)\right)^{\frac{5}{4}} / [1+8.2\times10^{-3}\left(\beta^{\frac{2}{3}}T_{\square}(KeV)\right)^{\frac{5}{4}}]\kappa\rho_0 \quad . \tag{7}$$

The initial density of the pre-compressed fuel is ρ_0 and κ is the shock wave compression during the fast ignition process. The losses due to electron conduction from the igniter domain for DT plasma are approximated by

$$W_{he}[erg/cm^3.s] = K_e\beta^{\frac{2}{3}}T_{\square}/R^2 = 3.11\times10^9\left(\beta^{\frac{2}{3}}T_{\square}(eV)\right)^{\frac{7}{2}}/R^2\ln\Lambda \quad . \tag{8}$$

The bremsstrahlung power density losses W_B with the relativistic corrections and the temperature anisotropy is given by

$$W_B\left[erg/cm^3.s\right]=1.5\times10^{-25}n_e\sum_{k=1,2}n_kZ_k{}^2\left(B^{\frac{2}{3}}\,T_{\square}(eV)\right)^{\frac{1}{2}}\left(1+2\beta^{\frac{2}{3}}\,T_{\square}(eV)/500{,}000\right)\ , \qquad (9)$$

where Z_k is the charge number of particle k, n_e, and n_k are the electron density and the ion densities of particle k, respectively. The mechanical expansion power loss is estimated by

$$W_m[erg/cm^3.s]=1.02\times10^{18}[\beta^{\frac{2}{3}}T_{\square}(eV)+T_i(eV)]^{1.5}\left(\rho/R\right)\ . \qquad (10)$$

By placing the above relationships in equations 2, we can get the value of ρR .

Energy balance Equation of PB fuel

The proton-boron 11 fusion reaction is indeed an interesting alternative because it does not produce any neutrons as byproducts. The reaction can be expressed as follows $p + {}^{11}B \rightarrow 3\alpha + 8.7MeV$. The number density raito of boron to proton is $\varepsilon = n_B / n_P$. The raito is usually less 0.4. The equation describing for the ignation of PB fuel is defined by

$$f_\alpha W_f - W_B - W_{he} - W_m \geq 0\ . \qquad (11)$$

The fusion power density of PB reaction is

$$W_f\left[erg/cm^3.s\right]=4.99\times10^{42}\varepsilon\rho^2\left\langle\sigma v\right\rangle_{p^{11}B}/(1+11\varepsilon)^2\ . \qquad (12)$$

Here, $<\sigma v>_{p\text{-}11B}$ is the reactivity of the p-11B reaction fitted in the domain of ion temperatures 50 keV < Ti < 500 keV which is obtained from the following relationship [16]

$$<\sigma v>_{p11B}\left(\frac{cm^3}{s}\right)=6382\times10^{-16}\xi^{-5/6}\left(\frac{17.708}{T_i{}^{1/3}}\right)^2\exp\left(-3\xi^{1/3}\frac{17.708}{T_i{}^{1/3}}\right)+5.41\times10^{-15}T_i{}^{-3/2}\exp\left(\frac{-148}{T_i}\right), \qquad (13)$$

where,

$$\xi=-\frac{-59.357\times10^{-3}T_i+1.0404\times10^{-3}T_i{}^2-.0091653\times10^{-3}T_i{}^3}{1+210.65\times10^{-3}T_i+2.7621\times10^{-3}T_i{}^2+.00098305\times10^{-3}T_i{}^3}.$$

The fraction of alpha particle is obtained from equation 3. R_α for the PB fuel is approximated by

$$R_\alpha(cm)=\left(\beta^{2/3}T_{11}/c\right)^b a/\rho \begin{cases} T_e\langle 50\,keV : a=0.25, b=0.79, c=10\,KeV \\ T_e \geq 50\,keV : a=1.1, b=0.31, c=100\,KeV \end{cases} . \quad (14)$$

Bremsstrahlung power density is

$$W_B\left[erg/cm^3.s\right]=4.74\times10^{-24}n_e\left(n_p+25n_B\right)\left(\beta^{\frac{2}{3}}T_{11}(eV)\right)^{1/2}\left(1+2\beta^{\frac{2}{3}}T_{11}(eV)/0.511\times10^6\right) \quad (15)$$

The mechanical expansion power loss is estimated for $p^{11}B$ by

$$W_m\left[erg/cm^3.s\right]=1.86\times10^{18}\left(\rho/R\right)\left[(1+5\varepsilon)(\beta^{\frac{2}{3}}T_{\square}(eV))+(1+\varepsilon)T_i(eV)\right]/(1+11\varepsilon)\Big]^{3/2} \quad (16)$$

The thermal conduction loss for $p^{11}B$ plasma is

$$W_{he}\left[erg/cm^3.s\right]=3.11\times10^9(\beta^{\frac{2}{3}}T_{11}(eV))^{7/2}/R^2\ln\Lambda \quad (17)$$

By placing the above relationships in equations 9, it can get the value of ρR .

The ignition criterion of DT and PB fuel

The igniter performance can be analyzed by an energy balance which depends on the ion and electron temperature:

$$\left(\frac{3}{2}\right)\frac{d}{dt}\left(n_e k_B\beta^{\frac{2}{3}}T_{\square}\right)=\eta_d W_d+W_{ie}-W_B+f_a\eta_f W_f$$
$$\left(\frac{3}{2}\right)\frac{d}{dt}\left(n_i k_B T_i\right)=\left(1-\eta_d\right)W_d-W_{ie}+f_a\left(1-\eta_f\right)W_f \quad (18)$$

where k_B is the Boltzmann's constant, W_d is the power density deposited by the driver, η_d is the fraction of the driver energy deposited in the electrons η_f is the energy fraction that is deposited in the electrons by the α-particles created in the fusion under consideration. W_{ie} is the ion- electron exchange power density is given by [3]

$$W_{ie}\left[\frac{erg}{cm^3.s}\right]=2.70\times10^{-22}n_e\left(T_i(KeV)-\beta^{\frac{2}{3}}T_{\square}(KeV)/\left(\beta^{\frac{2}{3}}T_{\square}(KeV)\right)^{1/5}\right)\sum_k\frac{Z_k{}^2n_k}{m_k}\ln\Lambda_{ek} \quad (19)$$

where $\ln\Lambda_{ek}$ is the electron coulomb logarithm term. The deposition power density W_d is dependent on the laser intensity I_L, pulse time duration τ_L and the shock compression $\kappa=\rho/\rho_0$,

$$W_d\left[\frac{erg}{cm^3.s}\right]=\frac{1}{4\times10^3}\frac{I_L\left(\frac{\omega}{cm^2}\right)\kappa}{\tau_L(s)} \quad (20)$$

The relation between the deposition power density and the laser parameters, as well as the particle u_p and shock u_s velocities, is obtained from the Hugoniot-Rankine equations.

Results and discussion

Contours of the confinement parameter, ρR, as a function of ions and electrons temperatures are shown in Fig. 1. It is observed that temperature ranges where the confinement parameter for PB fuel is less than 20 are 100-700 keV for the ions and 10-90 keV for the electrons. In the absence of temperature anisotropy (β= 1), for temperatures 1 keV < T_i < 360 keV, T_e < 10 keV, the confinement parameter is less than 1.5. For β= 10, the values of ρR are larger by about two orders of magnitude than for β = 1, requiring larger pre-compression and igniter size, and a larger energy laser. For different values of T_i, the ρR parameter of the PB fuel increases as the temperature anisotropy, β, increases. The suitable T_i is typically above 150 keV. This value, by increasing the temperature anisotropy, will increase, making ignition more difficult.

For DT fuel in the absence of temperature anisotropy (β= 1), for temperatures T_i, T_e in the range 10-50 keV, ρR < 1. For the temperature anisotropy β= 0.5, the confinement parameter ρR < 1 is obtained for T_i, T_e in the range 10-50 keV. But for the temperature anisotropy β= 10, the confinement parameter ρR<1 is obtained for T_e < 15 keV and T_i > 12 keV.

The confinement parameter first increases with increasing ion temperature and reaches its maximum value, then decreases. As the temperature anisotropy increases, the maximum value of the confinement parameter increases. The confinement parameter significantly depends on the

temperature anisotropy. As the temperature anisotropy increases, the value of the confinement parameter increases.

For PB fuel, by increasing the temperature anisotropy, the confinement parameter of less than 20 occurs in a lower range of the electron temperature and a higher range of the ion temperature. As the temperature anisotropy increases, a large gap will be observed between the temperature of the electron and the temperature of the ion. It is evident that as β approaches infinity, the small ρR required for ignition tends to quench.

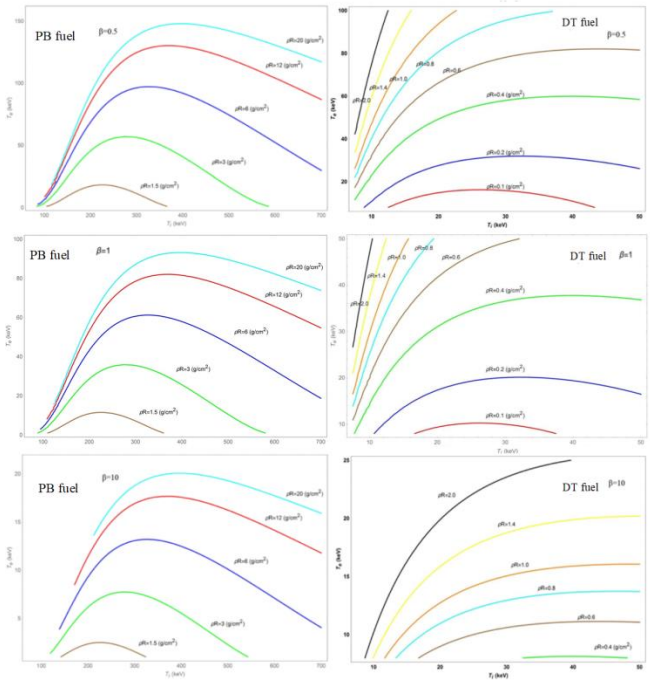

Fig. 1. The curve of the confinement parameter in the T_e and T_i plane for varying values of the temperature anisotropy β= 0.5, 1, 5, 100.

Figures 2(a) and 2(b) illustrate the confinement parameter ρR of DT and PB fuels as a function of time and temperature anisotropy β. In Figure 2(a), it can be observed that the confinement parameter increases with time. At a time of 5×10^{-13}s, when the temperature anisotropy is increased by a factor of 10, the maximum confinement parameter for DT fuel increases by 4%, while for PB fuel, it increases by 23%. In the time interval of 10^{-13}-1.5×10^{-13}, the confinement parameter of PB fuel initially decreases, but after that time, it gradually increases. On the other hand, the confinement parameter of DT fuel shows an upward trend from the beginning. In Figure 2(b), it is

evident that when $0 \leq \beta \leq 1$, the confinement parameter increases more steeply, whereas for $\beta > 1$, it increases uniformly with a smaller slope. Furthermore, Figures 2(a) and 2(b) indicate that the confinement parameter of DT fuel is greater than that of PB fuel. When the ions and electrons temperatures are slightly higher than 10 keV and ignition is initiated, the confinement parameter of DT fuel decreases to ρR=0.2 g/cm^2 at around 0.3 ps. Subsequently, the fusion energy deposition rises and surpasses the energy deposition from the shock wave. Furthermore, the confinement parameter exhibits rapid growth with increasing temperature anisotropy. At the end of the laser pulse, at 1 ps, the confinement parameter of DT fuel reaches 4 g/cm^2, and this value continues to increase with further increases in temperature anisotropy. In the absence of temperature anisotropy (β=1), for temperatures in the range of 1 keV < T_i < 360 keV and Te < 10 keV, the confinement parameter of PB fuel remains below 1.5. However, by increasing the temperature anisotropy, the confinement parameter reaches values lower than 20 within a lower range of electron temperature and a higher range of ion temperature.

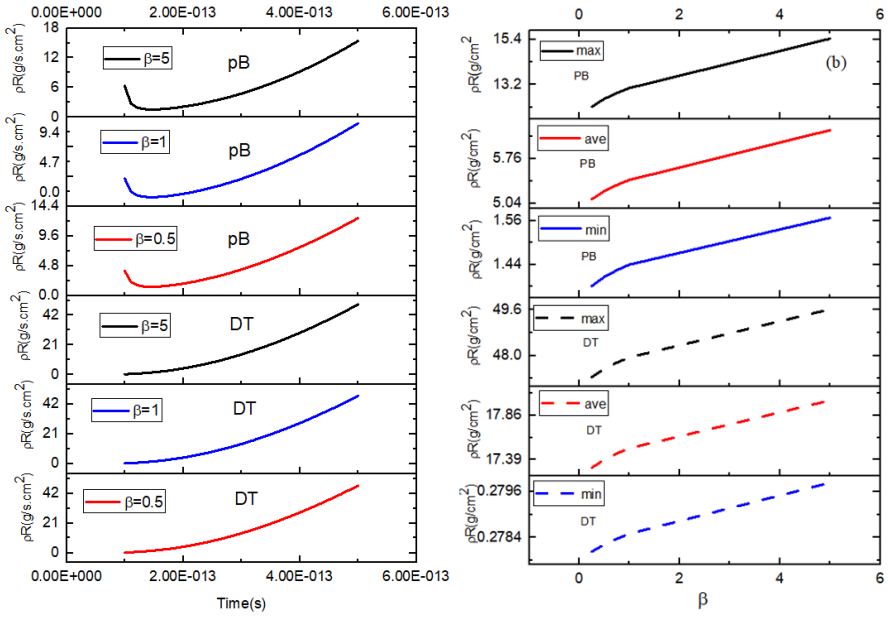

Fig. 2. (a)The confinement parameter, ρR , as function of time for DT and P11B fuels and fixed the temperature anisotropy, (b)The confinement parameter, ρR , changes in terms of the temperature anisotropy

As the temperature anisotropy increases, a significant gap emerges between the electron and ion temperatures. Notably, as β approaches infinity, the small ρR required for ignition tends to diminish, making ignition more challenging. For β = 5, the values of ρR are approximately two

orders of magnitude larger than those for β = 0.5, necessitating greater pre-compression, igniter size, and laser energy. The ρR parameter of PB fuel increases with increasing temperature anisotropy (β) for different values of T_i. An optimal T_i value is typically above 150 keV, which, when combined with an increased temperature anisotropy, raises the difficulty of achieving ignition. For example, the temperature anisotropy parameter of PB fuel is 5.3 g/cm^2 for β = 0.5, while it increases to 13 g/cm^2 for β = 5.

Figure 3(a) displays the fraction of absorbed α-particles in the hot spot as a function of time for varying values of the temperature anisotropy. It can be observed that as time progresses and temperatures increase, a larger fraction of α-particles leave the igniter region, thereby heating up the surrounding area. According to Figure 2(a), at 10^{-13} s, the fraction of absorbed α-particles (f_α) reaches its highest value. Between 10^{-13} -1.5×10^{-13} s, f_α decreases rapidly, but after that time, it gradually decreases and eventually stabilizes at 5×10^{-13} s. For DT fuel, f_α decreases with time and reaches its minimum value of approximately 0.05 at the end of the laser pulse. By increasing the anisotropy parameter β, this minimum value can be reduced to less than 0.0046. Similarly, for PB fuel, f_α decreases with time and reaches its minimum value of about 0.028 at the end of the laser pulse. By increasing the anisotropy parameter β, this minimum value can be reduced to less than 0.0079.

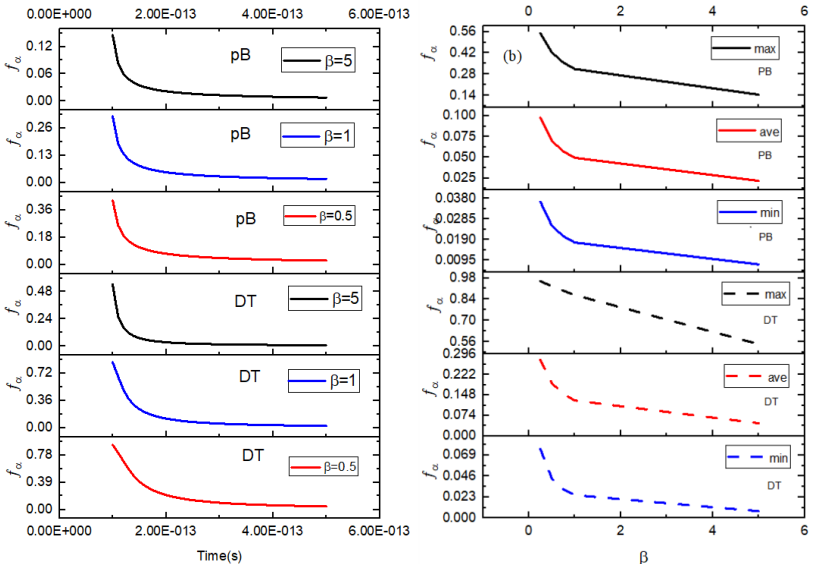

Fig. 3. (a)The fusion energy fraction deposited in the igniter domain for the DT and PB fuel, f_α, as a function of the time for variation value of the temperature anisotropic β = 0.5 and β = 5, (b) The fusion energy fraction changes as a function of temperature anisotropy β = 0.5 and β = 5.

In Figure 3(b), it can be observed that the fusion energy fraction (f_α) decreases with an increase in temperature anisotropy. Additionally, the figure shows that the fusion energy fraction of DT fuel is greater than that of PB fuel. The maximum fraction of absorbed α-particles in the hot spot is approximately 0.86 for DT fuel, whereas it is 0.32 for PB fuel. The fusion energy fraction (f_α) decreases as the temperature anisotropy parameter increases. With a 10-fold increase in temperature anisotropy at 10^{-13}s, the fusion energy fraction of DT fuel decreases by approximately 40%, while the fusion energy fraction of PB fuel decreases by approximately 65%.

Conclusions

This paper is investigated the impact of temperature anisotropy on the fuel ignition criterion for DT and PB fusion fuels. Anisotropic conditions were found to impact the critical values of temperature, density, and confinement time required for sustained fusion reactions. The presence of temperature anisotropy affected the energy deposition and transfer efficiency of beams in the fuel plasma, which in turn influenced the overall ignition efficiency. Instabilities and fluctuations induced by temperature anisotropy could hinder the sustained ignition of fusion reactions. Increasing the temperature anisotropy led to higher values of the confinement parameter. Also, the fusion energy fraction is decreased with increasing temperature anisotropy. It is worth noting that during the interaction of picosecond laser pulses with the fuel pellet, an increase in temperature anisotropy due to the coupling of shock waves and sidebands with the electron oscillatory velocity resulted in an increased fusion energy fraction. The study further revealed that for β = 5, the ρR values were significantly larger compared to β = 0.5, necessitating greater pre-compression, larger igniter size, and increased laser energy. Moreover, the confinement parameter and fusion energy fraction were generally higher for DT fuel compared to PB fuel.

These findings emphasize the importance of carefully considering and managing temperature anisotropy in the design and implementation of fusion reactors. Higher values of β necessitate additional measures and resources to achieve successful ignition and sustainable fusion reactions. Future research could explore innovative approaches and technologies to address the challenges associated with increased temperature anisotropy and optimize the ignition process for practical fusion energy applications.

References

[1] Martinez-Val, J. M., Velarde, G., and Ronen, Y. (2020). An introduction to nuclear fusion by inertial confinement. In *Nuclear Fusion by Inertial Confinement* (pp. 1-42). CRC Press.

[2] Atzeni, S. (2013). Inertial confinement fusion with advanced ignition schemes: Fast ignition and shock ignition. In Laser-Plasma Interactions and Applications (pp. 243-277). Heidelberg: Springer International Publishing.

[3] Zhang, C., Huang, C. K., Marsh, K. A., Clayton, C. E., Mori, W. B., and Joshi, C. (2019). Ultrafast optical field–ionized gases—A laboratory platform for studying kinetic plasma instabilities. *Science Advances*, *5*(9), eaax4545.

[4] Deutsch, C. (2003). Fast ignition schemes for inertial confinement fusion. *The European Physical Journal-Applied Physics*, *24*(2), 95-113.

[5] Bret, A. "Weibel, two-stream, filamentation, oblique, bell, buneman... which one grows faster?." The Astrophysical Journal 699, no. 2 (2009): 990.

[6] Weibel, E. S. (1959). Spontaneously growing transverse waves in a plasma due to an anisotropic velocity distribution. Physical Review Letters, 2(3), 83.

[7] Koepke, M. E. (2019). Interrelationship between lab, space, astrophysical, magnetic fusion, and inertial fusion plasma experiments. *Atoms*, *7*(1), 35.

[8] Lazar, M., and Poedts, S. (2009). Limits for the firehose instability in space plasmas. *Solar physics*, *258*, 119-128.

[9] Rose, D. J. (1965). General criterion for mirror instability of a plasma. *The Physics of Fluids*, *8*(5), 951-955.

[10] Xu, R. H., Wen, W., and Zhao, Y. K. (2022). Critical temperature for volume ignition of deuterium–tritium fuel in inertial confinement fusion: Effects of hydrodynamic instabilities. *Physics of Plasmas*, *29*(4).

[11] Khodadadi Azadboni, F. (2023). Effect of nonlinear saturation of electromagnetic instability on the viscosity of the inertial fusion fuel. *International Journal of Modern Physics B*, 2450047.

[12] Qiao, X., and Lan, K. (2021). Novel target designs to mitigate hydrodynamic instabilities growth in inertial confinement fusion. *Physical Review Letters*, *126*(18), 185001.

[13] F. Khdadadi Azadboni, (2021). Quantum effects role on the electromagnetic instability growth rate in turbulent state of the fuel fusion. *Chinese Journal of Physics*, *71*, 375-384.

[14] Kumar, A., Dhawan, R., Gupta, R., Sabharwal, N., and Sharma, J. (2023). Theoretical Study on Weibel instability in the existence of large amplitude Langmuir wave inside a Plasma. In *E3S Web of Conferences* (Vol. 430, p. 01272). EDP Sciences.

[15] Takabe, H. (2023). Theory of magnetic turbulence and shock formation induced by a collisionless plasma instability. *Physics of Plasmas*, *30*(3).

[16]Eliezer, S., Henis, Z., Nissim, N., Pinhasi, S. V., & Val, J. M. M. (2015). Introducing a two temperature plasma ignition in inertial confined targets under the effect of relativistic shock waves: the case of DT and pB11. *Laser and Particle Beams*, 33(3), 577-589.

ICNST 2024
International Conference on Nuclear Science and Technology
6- 8 MAY 2024 | Isfahan, Iran

Investigation of the poloidal flux for changes in the toroidal magnetic field in stable equilibrium for a spherical tokamak configuration (Paper ID: 1324)

Jafarzadeh M A[1*], Pirizad Hejrandoost S[2], Arjhangmehr A[3], Moradi Zamenjani F[4], Moazzemi Ghamsari M[2]

[1]Physics Department, Guilan University, Guilan, Iran

[2]Physics Department, Kashan University, Isfahan, Iran

[3]Nuclear engineering Department, Shahid Beheshti University G.C, Tehran, Iran

[4]Physics Department, University of Isfahan, Isfahan, Iran

Abstract

Spherical tokamaks are low-aspect-ratio tokamaks that exhibit steady-state and stable operating regimes. The advantages of these tokamaks include the possibility of using smaller devices and having smaller fusion power plants with lower costs. Large plasma elongation without the need for feedback control, better plasma stability compared to ideal and resistive modes, and higher beta values and the creation of a strong bootstrap current are among the features of these tokamaks. In order to develop the way, under the title of a selection, the characteristics of the main parameters of the MAST spherical tokamaks were examined. In this article, in order to increase the poloidal magnetic flux and the convergence error of the poloidal flux for changes in toroidal magnetic field of MAST tokamak to the extent of $B_t = 0.6 - 1.5\mathrm{T}$ and plasma Current $\mathrm{I} = 1 - 2\mathrm{MA}$ in the equilibrium of the fixed boundary, was analyzed. It can be seen that, with changes in the toroidal field, the values of poloidal flux and convergence error change strongly. In such a way that with the increase of the field, the poloidal magnetic flux, and also the convergence error. For example, in a toroidal field $B_t = 0.6\mathrm{T}$, the maximum value of poloidal flux will be $PSI_{max} = -5.471 \times 10^{-4}$ and the minimum value will be $PSI_{max} = -1.102 \times 10^{-1}$.

Keywords: Tokamak Equilibrium, MAST Tokamak, Fixed Boundary, MHD Equations of Magnetic Flux

Introduction

The tokamak is a toroidal fusion device that confines hot plasma using a strong toroidal magnetic field. Achieving and maintaining a stable plasma configuration is crucial for successful fusion reactions. In this context, the poloidal magnetic flux, denoted by ($\boldsymbol{\psi}$), plays a vital role in defining the equilibrium state of the plasma within the tokamak. This introduction explores the significance of changes in the poloidal magnetic flux within the steady-state boundary equilibrium of the tokamak. The poloidal magnetic flux represents the total toroidal current enclosed by a poloidal cross-section of the plasma [1]. It is essentially the integral of the toroidal magnetic field component ($\boldsymbol{B_t}$) along a poloidal path. Changes in the poloidal flux profile directly influence the plasma current profile, which in turn governs the stability of the confined plasma. Maintaining a steady-state equilibrium, where the poloidal flux remains constant over time, is essential for achieving a sustained fusion reaction. Several factors can influence the changes in the poloidal flux within a tokamak. These include: Plasma current diffusion: As the plasma current flows through the resistive tokamak vessel, it diffuses inward over time. This diffusion process leads to a gradual decrease in the poloidal flux at the plasma edge [2]. External current drive: To counteract the current diffusion and maintain a desired current profile, external current drive mechanisms like neutral beam injection or Radiofrequency heating can be employed. These techniques modify the poloidal flux by injecting current into specific plasma regions [3]. Vertical displacement of the plasma: Maintaining the plasma position within the vacuum vessel is crucial. Any deviation from the equilibrium position can lead to changes in the poloidal flux distribution across the plasma cross-section [4]. Understanding and controlling these changes in the poloidal flux is essential for achieving and maintaining a stable and controllable plasma configuration within the tokamak. Through active control techniques and careful design of the tokamak geometry, researchers strive to achieve a steady-state equilibrium with a desired poloidal flux profile, paving the way for a successful and sustained fusion reaction.

Research Theories

Assuming an axisymmetric system, the equilibrium structure of the plasma is completely defined by a nonlinear elliptic partial differential equation called the Grad-Shafranov equation [5, 6]. This equation in cylindrical coordinates is given by [5 and 6].

$$\frac{\partial}{\partial R}\frac{1}{R}\frac{\partial \psi}{\partial R}+\frac{\partial}{\partial Z}\left(\frac{1}{R}\frac{\partial}{\partial Z}\right)=-\mu_0 J_\phi=-\mu_0 R\frac{dp(\psi)}{d\psi}-\frac{1}{R}f(\psi)\frac{df(\psi)}{d\psi} \quad (1)$$

Where $J_\phi(\psi)$ is the total axial current density in the plasma region. $f(\psi)$ and $p(\psi)$ are the poloidal flux function and plasma pressure as a function of the poloidal magnetic flux, respectively. Since in fixed-boundary equilibrium, the plasma boundary is considered fixed in the calculations; it is necessary to define the shape of the plasma surface in advance. The boundary shape is defined using the parameters of the major radius R_0 ,the minor radius a, and also the plasma shaping parameters, including the elongation parameter κ and the triangularity parameter δ: As shown in Figure 1.

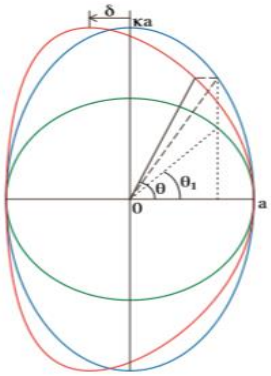

Fig. 27: Parameters defining the shape and boundary of the plasma.

In Figure 1, the shape of the plasma surface is given as follows:

$$R(\theta_1)=R_0+\alpha\cos(\theta_1+\delta\sin\theta_1),\ Z(\theta_1)=\kappa\alpha\sin\theta_1 \quad (2)$$

The shape of the plasma boundary can also be expressed as a function of the poloidal angle (θ) as follows:

$$\rho a(\theta)=a\sqrt{\cos^2(\theta_1+\delta\sin\theta_1)+\kappa^2\sin^2\theta_1},\ \tan\theta=\frac{\kappa\sin\theta_1}{\cos(\theta_1+\delta\sin\theta_1)} \quad (3)$$

To solve the Grad-Shafranov equation in fixed-boundary conditions, it is first necessary to define the poloidal variables (σ,θ) as shown in Figure 2.

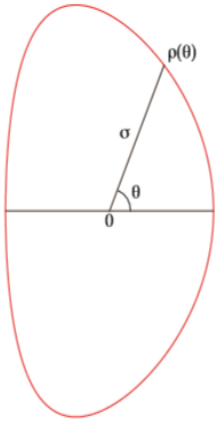

Fig. 28: Poloidal variables (σ,θ).

In the above equation, the range of variations of the normalized radial variable $\boldsymbol{\sigma}$ and the poloidal variable $\boldsymbol{\theta}$ is $\mathbf{0} \leq \boldsymbol{\sigma} \leq \mathbf{1}$ and $\mathbf{0} \leq \boldsymbol{\theta} \leq \mathbf{2\pi}$. The Grad-Shafranov equation in terms of poloidal variables are expressed as follows:

$$\frac{\partial}{\partial R}\frac{1}{R}\frac{\partial \psi}{\partial} + \frac{\partial}{\partial Z}\frac{1}{R}\frac{\partial \psi}{\partial Z} = \frac{1}{\rho_a^2 \sigma}\left[\frac{\partial}{\partial \sigma}\left(\frac{\sigma}{R} + \frac{\rho_a'^2 \sigma}{R\rho_a^2}\right)\frac{\partial \psi}{\partial \sigma} - \frac{\partial}{\partial \sigma}\frac{\rho_a'}{R\rho_a}\frac{\partial \psi}{\partial \theta} - \frac{\partial}{\partial \theta}\frac{\rho_a'}{R\rho_a}\frac{\partial \psi}{\partial \sigma} + \frac{\partial}{\partial \theta}\frac{1}{R\sigma}\frac{\partial \psi}{\partial \theta}\right] = -\mu_0 R\frac{dp(\psi)}{d\psi} - \frac{1}{R}f(\psi)\frac{df(\psi)}{d\psi} \quad (4)$$

According to the above equation, for a given pressure profile, the poloidal flux function and the application of appropriate boundary conditions, the function $\boldsymbol{\psi}(\boldsymbol{R}, \boldsymbol{Z})$ is obtained. The boundary conditions considered for solving the fixed-boundary problem are as follows: The value of the flux at the plasma boundary is zero: $\boldsymbol{\psi} = \mathbf{0}$. The value of the flux at the magnetic axis is equal to $\boldsymbol{\psi} = \boldsymbol{\psi_0}$. The normalized poloidal flux is defined as:

$$\psi_N = 1 - \psi/\psi_0 \quad (5)$$

According to the above equation, the normalized poloidal flux at the magnetic axis is $\boldsymbol{\psi_N} = \mathbf{0}$ and at the plasma boundary is $\boldsymbol{\psi_N} = \mathbf{1}$. To solve Equation 4, we need to have a relationship for the functions $\boldsymbol{p}(\boldsymbol{\psi})$ and $\boldsymbol{J}(\boldsymbol{\psi})$ with respect to the poloidal flux. In general, the relationship of these functions is not completely known. However, the physics of the problem, experiments, and measurements provide useful information about how these functions are related to the poloidal flux. The pressure and current density profiles considered for the right-hand side of the Grad-

Shafranov equations are given by Equations 6 and 7, respectively. The default values for the initial pressure and current density, along with the profile parameters, are given in Table 1. The graphs for these profiles as a function of the major radius are shown below:

$$P(\psi) = \mathbf{P_0}(1-\psi_N^{PROFR0})^{PROFP0} + \boldsymbol{P_1}\left(1-\psi_N^{PROFR1}\right)^{PROFP1} + \boldsymbol{P_2}\left(1-\psi_N^{PROFR2}\right)^{PROFP2} \quad (6)$$

$$f(\psi) = \mathbf{B}.\mathbf{R_0} + \boldsymbol{F_0}\left(1-\psi_N^{PROFR0}\right)^{PROFF0} - \mathbf{F_1}\left(1-\psi_N^{PROFR1}\right)^{PROFF1} - \boldsymbol{F_2}\left(1-\psi_N^{PROFR2}\right)^{PROFF2} \quad (7)$$

Table 1. Parameters related to pressure and flow density functions

Parameter	Initial value	Parameter	Initial value
P_0	0.64	PROFP0	1.5
P_1	0	PROFP1	1.5
P_2	0	PROFP2	2
F_0	1	PROFF0	1.5
F_1	0	PROFF1	1.5
F_2	0	PROFF2	1.5
PROFR0	1	PROFR1	2
PROFR2	2		

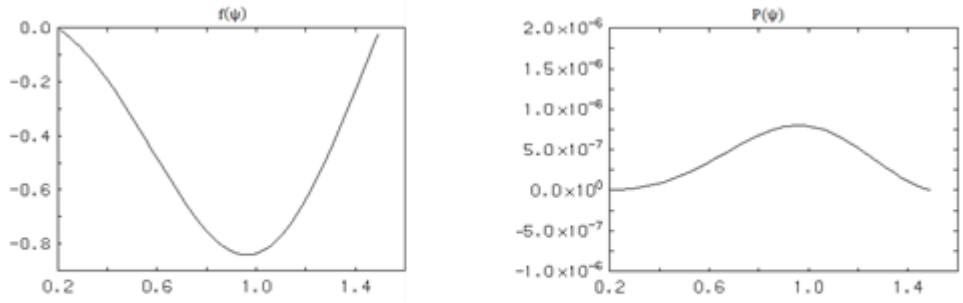

Fig. 1: Profiles of pressure and flow density function.

Results and Discussion

In this report, we first investigate the fixed-boundary equilibrium module for a limiter configuration for a tokamak similar to MAST [7]. In order to validate the results, the flux surfaces obtained from the TASK code [10, 11] was compared with the data obtained from solving the direct equilibrium in the fixed-boundary equilibrium solver of the TOPEOL code [8, 9] for a

similar configuration. The resulting equilibrium flux surfaces are shown in Figure 4. The calculation of the relative error for several selected flux surfaces shows very good agreement between the flux values in the two codes, which indicates the correct calculation process in the code used in this research.

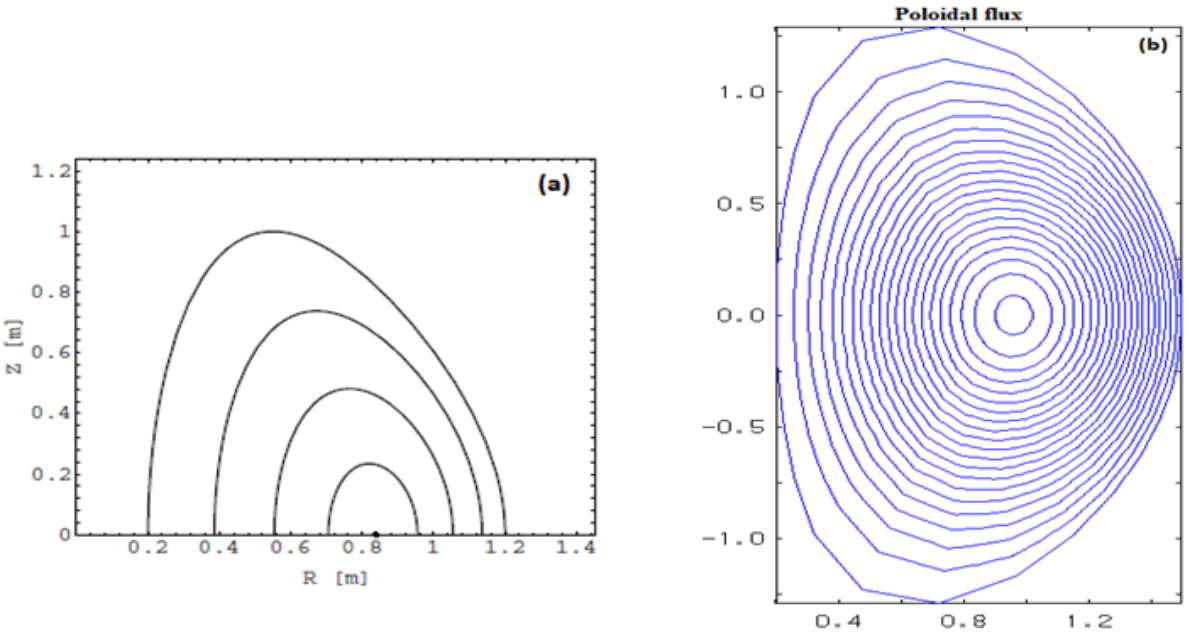

Fig. 1: Equilibrium flux surfaces obtained from (a) the TASK code and (b) the TOPEOL fixed-boundary equilibrium solver for a limiter configuration in a tokamak similar to MAST.

In the next step, in order to investigate the equilibrium properties of a spherical tokamak, the target plasma parameters were considered according to Table 2. The numerical solution method used in this code is the Newton iteration method, and 32 radial and 32 poloidal meshes are used to solve the Grad-Shafranov equation. Figure 5 shows the profiles of the poloidal flux surfaces, and Figure 6 shows the profiles of the convergence error of the poloidal flux. The maximum and minimum values of these profiles, along with the distance between the lines, are shown in Table 3.

Table 2. Main parameters of the target spherical tokamak [12]

Parameter	Symbol	Value
Aspect ratio	ϵ	1.3
Plasma major radius	R_0	0.85m
Plasma minor radius	a	0.65m
Magnetic field	B_t	0.6-1.5T
Plasma current	I_P	1-2MA
Elongation	κ	2
Triangularity	δ	0.3

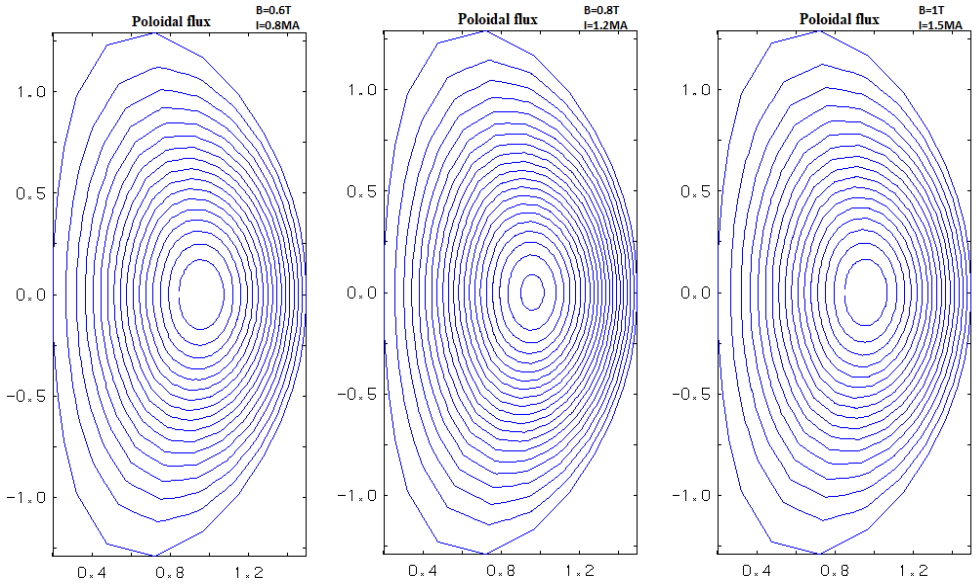

Fig. 29: Fixed-boundary equilibrium solution for a spherical tokamak in terms of poloidal flux surfaces.

The above graph shows the magnetic poloidal flux in a spherical tokamak with a fixed boundary state. The vertical axis of the graph shows (Z), and the horizontal axis shows the radius (R).

The graph includes several curves, each of which shows the poloidal flux at a constant radial surface.The maximum poloidal flux (max) occurs at the center of the tokamak $(R = 0)$. The minimum poloidal flux (min) occurs at the normalized plasma edge $(R = 1)$.

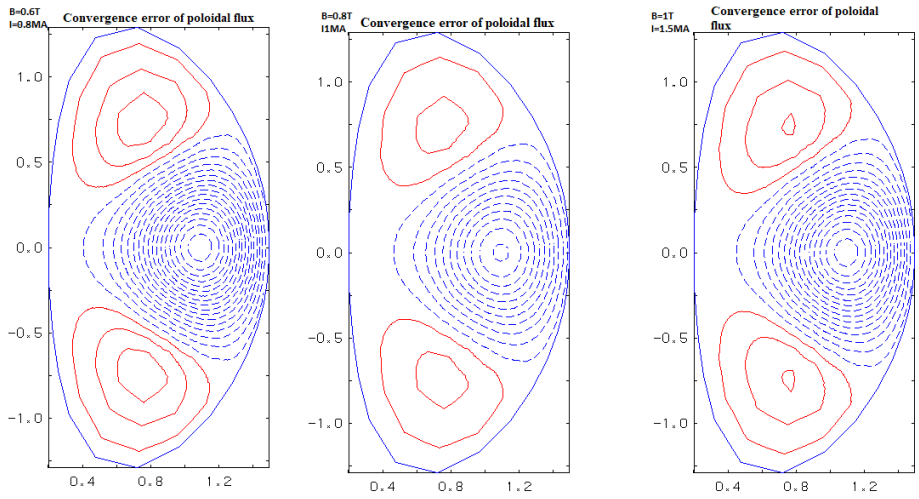

Fig. 6. Fixed-boundary equilibrium solution for a spherical tokamak in terms of convergence error of the poloidal flux.

These diagrams are convergence errors of the poloidal flux in the fixed-boundary equilibrium of the spherical tokamak. the convergence error of poloidal flux, the red solid line and blue dashed line represent different simulations.

Magnetic field strength (B): The red line could represent a higher B value compared to the blue line. A stronger magnetic field might lead to a different convergence behavior. Plasma current (I): The red line could indicate a higher plasma current than the blue line. Varying current can affect the convergence properties of the solution. Regarding the negative sign in convergence error: the convergence error is a relative error. Here's why: Convergence error refers to the difference between the approximate solution (obtained after a certain number of calculations) and the exact solution (which might be computationally expensive or even impossible to find directly). Relative error is typically expressed as a percentage of the desired quantity (in this case, the exact poloidal flux value). A negative sign doesn't necessarily imply a "bad" solution. It could simply indicate the direction of the error. A positive error means the approximate solution overestimates the true value. A negative error means the approximate solution underestimates the true value.

Table 3. Values of the fixed-boundary equilibrium module outputs

Parameter	max	min	Distance between lines
poloidal flux	-6.857×10^{-3}	-8.482×10^{-1}	1×10^{-1}
convergence error poloidal flux	3.262×10^{-7}	-8.540×10^{-7}	1.25×10^{-7}

In such a way that with the increase of the field, the polar magnetic flux and also the convergence error increase.

Conclusions

In this report, the fixed-boundary equilibrium in a spherical tokamak was investigated by solving the Grad-Shafranov equation. In this way, the equilibrium data was extracted using the TASK code. In the first step, the code was validated using the equilibrium data obtained from the fixed-boundary equilibrium solver of the TOPEOL code. Then, the pressure profiles and the current density functions were adjusted according to the initial profile parameters. Finally, the profiles of the poloidal flux surfaces and the plasma current density were obtained for the main parameters of the target spherical tokamak. With an increasing toroidal magnetic field and plasma current, the poloidal flux and convergence error change significantly and have an increasing trend. The poloidal flux and convergence error change significantly with an increasing toroidal magnetic field and plasma current. These factors need to be taken into account when solving the Grad-shafranov equation for a fixed-boundary equilibrium in a spherical tokamak.

References

[1] Wesson, John. "Tokamaks." Oxford University Press, 2004.

[2] Kruskal, Martin D. "Equilibrium of an idealized toroidal plasma." Physics of Fluids (1958-1988) 7.1 (1964): 343.

[3] Pochelon, A., et al. "Non-inductive current drive and plasma confinement in Tore Supra." Nuclear Fusion 36.7 (1996): 881.

[4] Shafranov, V. D. "Plasma equilibrium in magnetic systems." Reviews of Plasma Physics 2 (1966): 103.

[5] Li H, Zhu P. Solving the Grad-Shafranov equation using spectral elements for tokamak equilibrium with toroidal rotation. Computer Physics Communications. 2021 Mar 1; 260:107264.

[6] Jeon YM. Development of a free-boundary tokamak equilibrium solver for advanced study of tokamak equilibria. Journal of the Korean Physical Society. 2015 Sep; 67(5):843-53.

[7] G O Ludwig, "Direct variational solutions of the tokamak equilibrium problem.", Plasma Phys, Control. Fusion 39, 1997.

[8] Haynes P and Buttery R 1995 *TOPEOL, A User's Guide* edition 2.0, UKAEA Fusion, Culham, UK.

[9] Sykes A 1996 Private communication.

[10] http://bpsi.nucleng.kyoto-u.ac.jp/ . User Manual of the TASK Code. (2021).

[11] http://bpsi.nucleng.kyoto-u.ac.jp/ . User Manual of the TASK/EQ Code. (2021).

[12] Stork D, Meyer H, Akers R. "the upgrade to the Mega Amp Spherical Tokamak.", Fusion Energy, 2010; ICC/P5-06

ICNST 2024
International Conference on Nuclear Science and Technology
6- 8 MAY 2024 | Isfahan, Iran

Review of Stellarator researches (Paper ID: 1329)

Goudarzi Sh.[1*], Mazandarani A.[1], Esmaeli A.[1], Rostamifard D.[1], Noori E.[1], Sohrabi D.[1]

[1]Plasma and Nuclear Fusion Research School, Nuclear Science and Technology Research Institute, Tehran, Iran

Abstract

Stellarator is one of most important devices in nuclear fusion researches. Stellarator and tokamak are two main candidates for nuclear fusion power plants. The structure and theoretical problems of stellarator are very complicated in comparison to tokamak. In this article the history of stellarator, its models and the important projects carried out on it and long-term research programs in the field of stellarator which are planned to build nuclear fusion power plants of this model have been explained in detail. Then, the project of design and construction of an Iranian stellarator which started at beginning of 2023 in Plasma and Nuclear Fusion Research School of Iran have been described briefly and scientific, technological and economic capabilities of Iran for such projects have been explained. The fundamental studies phase of this project is finished, due to results of this phase, we decided to construct a small stellarator that its structure is similar to UST-1 (Spain) and SCR-1 (Costa Rica) devices.

Keywords: Stellarator, Nuclear Fusion, power plant, magnetic coils, confinement

Introduction

Stellarator is a magnetic confinement device with a non-axisymmetric toroidal vacuum chamber. In stellarator non-axisymmetric magnetic coils are used to generation of twisting magnetic fields inside the chamber (Fig. 1) [1]. The charged particles move around these fields for a long time without collision to inner wall of device [2]. In a tokamak, the poloidal magnetic fields for plasma confinement are produced by the plasma current but in stellarators, poloidal fields are produced by current passing through the external coils. Therefore, these devices do not need to plasma current for confinement and heating the plasma, and instabilities that are related to plasma current do not happen in stellarators. This is the most important advantage of stellarator than tokamak [1-3].

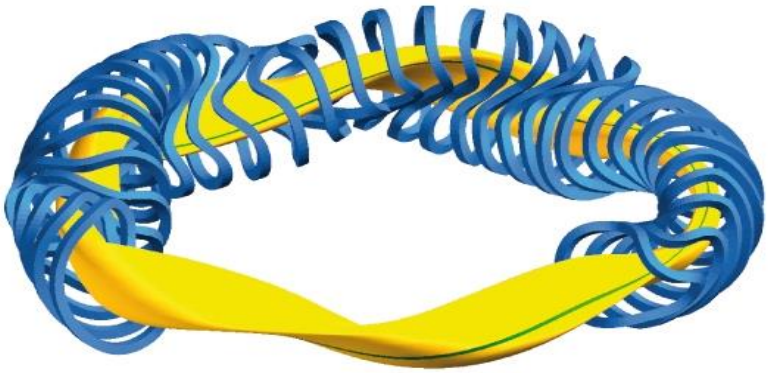

Fig. 1. A sample of structure of Stellarator

The brief description

Stellarator has been invented by Lyman Spitzer at Princeton Plasma Physics Laboratory in 1951 (Fig. 2) [3]. This device was an 8-shaped chamber with twisted coils and constructed by financial support of Department of Energy of United States. The plasma was generated by a radio frequency electric field inside the chamber. It showed poor performance and the plasma in it was quickly destroyed [3]. The purpose of its construction was to show that plasma is confined in a torus chamber better than other devices (open-ended devices) existed at that time, and plasma heating and nuclear fusion reactions were not considered [3].

Fig. 2. Lyman Spitzer with first stellarator device in the world

Princeton university's research in the field of stellarator developed with the construction of a more advanced device called Model C stellarator. This device started to work in 1961 and research activities on it continued until 1969 when it was changed to a tokamak geometry. Stellarator C

was the first stellarator that constructed in the form of a torus with twisted coils [3,4,5]. West Germany (Max-Planck Institute) [6] and Japan [7] also started extensive activity on the stellarator from the early 1960s.

In 1950 and 1960 decades, high research activities have been done in the field of stellarator. But the complexity of the mathematical equations of stellarator plasma physics, and excellent results in experiments with Soviet tokamaks, caused the activities on these devices to decrease since the late 1960s. The research in this field was not completely stopped, and extensive research activities on the stellarator continued in West Germany and Japan. In 1990 decade, the construction projects of two large stellarators were started. Now, more than seven decades after the construction of the first stellarator, the new stellarators are about to enter the operational stage [3].

There are several models of stellarators: Special or 8-shaped stellarators, Modular stellarators, Classic stellarators, Torsatron, Heliotron, and Helias [2,8,9].

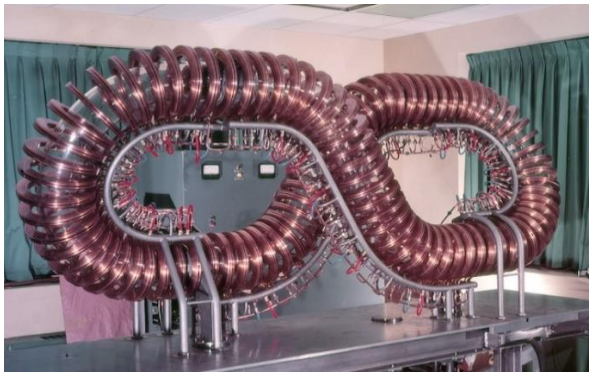

Special or 8-shaped stellarator

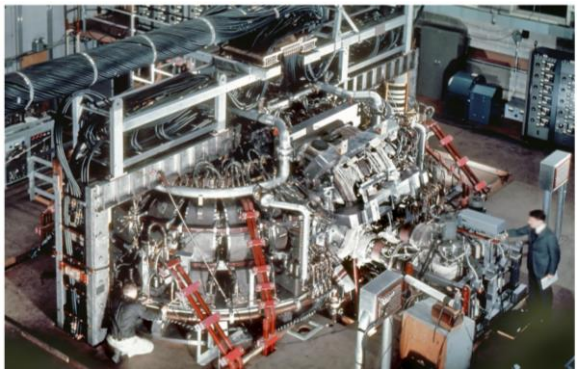

Classic stellarator

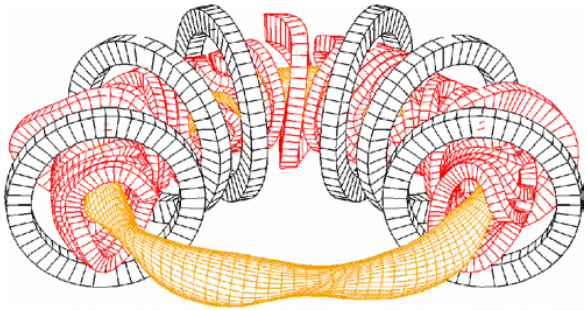

Modular stellarator

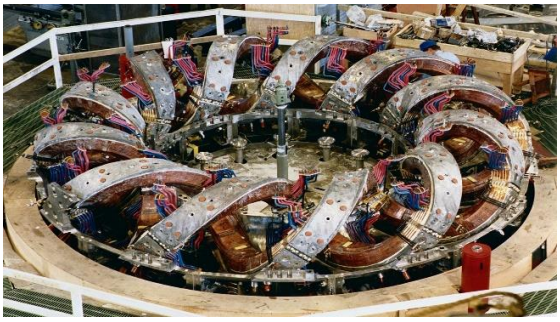

Torsatron

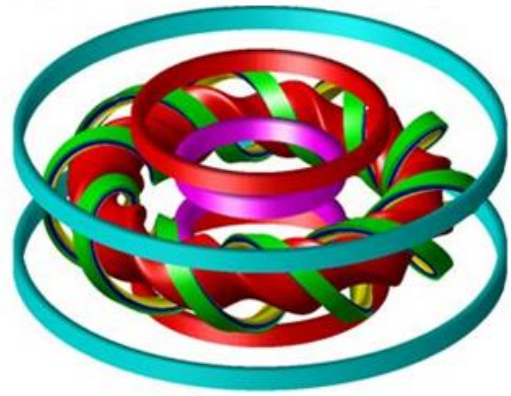

Heliotron

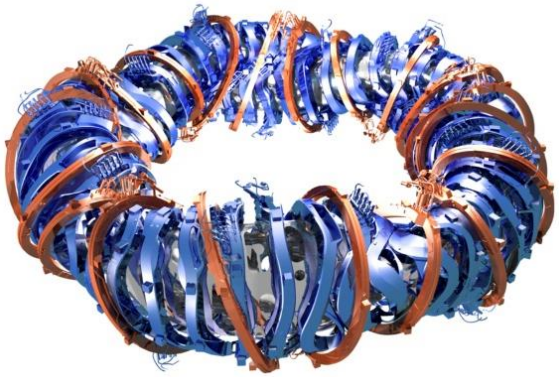

Helias

Fig. 3. Models of stellarators

In stellarators, ohmic heating does not occur due to the absence of plasma current. Neutral particle beam injection, ion cyclotron resonance heating and electron cyclotron resonance heating methods are used for plasma heating [8,9].

Since the invention of stellarator, many devices of this type have been built in 10 countries of the world. These countries are: United States, Germany, Japan, Russia, Ukraine, Spain, England, Australia, Costa Rica and China [10-12].

Some of famous stellarators are: Helical Symmetric Stellarator (HSX) in Wisconcin University (USA) [13], CNT in Colombia University (USA) [14], W7-AS in Max-Planck Institute of Physics in Germany [15], W7-X in Max-Planck Institute of Physics in Germany [16], L-2M (RUSSIA) [17], Heliotron J in Kyoto University (Japan) [18], Large Helical Device (LHD) (Japan) [19], U-2M (Ukraine) [20], and TJ-II (Spain) [21].

Large stellarators

The largest stellarators in the world are Wendelstein 7-X (W7-X) in Germany [16] and Large Helical Device (LHD) in Japan [19], the material of their coils are superconductor (NbTi). The cost of construction of these devices is more than one billion dollars [16,19]. The results of experiments which have been done with these devices are comparable with the best results of tokamaks, and stellarator is considered an important candidate for the future commercial Fusion power plants [22,23].

The LHD machine was designed and constructed in Japan and has been operating since 1998 [24]. This device is the second large Stellarator in the world [24,25]. In the experiments which have been done with this device until the end of 2021, depending on the conditions separately, the maximum plasma confinement time, the maximum electron temperature, the maximum ion temperature and the maximum electron density were 1.5 second, 6.6 keV, 10 keV and 1.2×10^{21} m^{-3}, respectively [25]. In figure 4 inside view of the vacuum chamber of LHD device is shown [26].

Fig. 4. Inside view of the vacuum chamber of LHD device

W7-X is the largest stellarator in the world that designed and constructed in Max-Planck Institute in Germany. This project started in 1997 and its construction was finished in 2014 and the experiments on it started from 2015. About 80% of the cost of this project was financed by Germany and about 20% by the European Union, the total cost for the construction and operation of this device between 1997 and 2014 was about 1.06 billion euros [22].

The goal of this device is to reach a plasma density of 3×10^{20} m^{-3} and a temperature of 60 to 130 million Kelvin [27]. The magnetic coils of this stellarator are fabricated using niobium-titanium superconducting wires and are cooled with liquid helium to superconductivity temperature [28].

In the experiments which have been done in June 2018 with W7-X device, the ion temperature, density and confinement time were about 40 million Kelvin, 8×10^{19} m^{-3} and 200 ms, respectively. A world record for the triple product of fusion (ion temperature× plasma density× confinement time) equal to 6×10^{26} (degree×s×m^{-3}) has been achieved [29]. The heads of this project claimed that based on these results and their plans, they expect that device reach to steady state performance in 2019 [29].

But in the end of October 2018 the experiments with W7-X have stopped for upgrading it up to August of 2022 [30,31]. During these years, the heating system of the W7-X device was upgraded and a new water cooling system, whose pipes are 6.8 km long, was added to the device for cooling the divertor and components of internal wall [30,31].

Next phase of experiments started in autumn 2022 and in them significant results were obtained, the goal for 2023 was to deliver one gigajoule of energy, but in the experiments in February 15, 2023, the researchers were able to deliver 1.3 gigajoules of energy with an average heating power of 2.7 megawatts, which is much more than the best results before upgrading the device (75 megajoules). Also, a new record of 8 minutes was obtained for the discharge time (before upgrading, the maximum plasma discharge time was 100 seconds) [22,23,32]. The aim is to increase the energy delivery to 18 GJ and the plasma discharge time to 30 minutes in the next few years [22,23,32]. German scientists say that their goal is to achieve the first stellarator fusion power plant in the 2030s [33].

Small stellarators

In recent years, three very small stellarators have been constructed (two in Spain and one in Costa Rica). The small Spanish devices named UST-1 and UST-2 have been designed and constructed in personal laboratory of Dr. Vicente Queral near Valencia. UST-1 is the smallest stellarator in the world that designed and constructed in 2005 and the experiments on it started in 2006, only about 2700 euros have been spent for all the materials and tools used in the construction of this device [34,35]. The major radius of this device is 119.2 mm and its medium minor radius (<a>) is about 21 mm and the volume of its plasma is 1.1 Liter. The heating in this device is done by ECRH (using a microwave magnetron with 100 W power), the power source of this device consists of five 12 V batteries connected in series and maximum value of generated pulsed current is 1200 A. A picture of this device is shown in figure 5 [34,35].

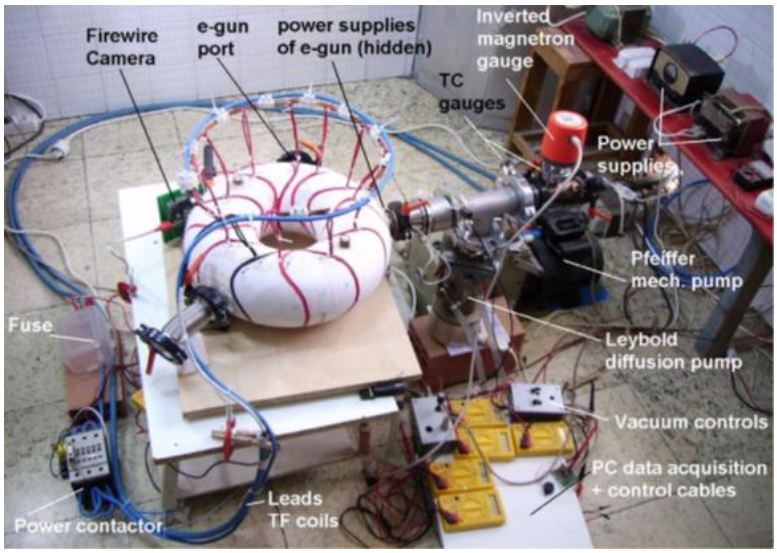

Fig. 5. A picture of UST-1

UST-2 is a small stellarator with major radius=0.29 m, minor radius=40.6 mm and plasma volume=9.5 Liter. This device is also constructed in the personal laboratory of Dr. Vicente Queral. The main purpose of construction of these two small stellarators was to investigate cheap manufacturing methods and develop small stellarator devices [36].

Costa Rica started research in the field of stellarators from the second decade of the 21st century. In 2016, a small modular stellarator called SCR-1 was constructed by the Plasma Laboratory for Fusion Energy and Applications in the Plasma Physics Department of the Costa Rica Institute of

Technology based on the model of the Spanish small stellarator UST-1 at a cost of about 500000 dollars [37]. All components of this device are made in Costa Rica, the goal of this small device is to reach a plasma temperature of 300000 K [38,39].

Iran's research program in the field of stellarators:

Plasma and Nuclear Fusion Research School of Iran in cooperation with Advanced Technologies Corporation of Iran have started the design and construction project of a stellarator from the beginning of 2023.The initial study phase of this project has been completed and based on the results of studies conducted and with respect to the budget of this project and experimental and theoretical capabilities of Iran resulting from more than 5 decades of research in the field of plasma physics and nuclear fusion, and due to relative simple structures and much lower costs of construction the SCR-1 and UST-1 devices in comparison to other stellarators in the world, we have concluded that the best options for our project are construction of a stellarator similar to UST-1 or SCR-1 devices.

Table. 1. Comparison of UST-1 and SCR-1 stellarators

Number	Parameters	UST-1	SCR-1
1	Place	Spain	Costa Rica
2	Model	Modular	Modular
3	Major radius	119.2 mm	247.7 mm
4	Minor radius	21 mm	40 mm
5	Heating system	ECRH, 1600 W	ECRH, 5 kW
6	Plasma volume	1.1 Liter	7.8 Liter
7	Discharge duration	2 ms	3 ms
8	Maximum current	1200 A	40 kA
9	Construction expenses	about 2700 euros	500000 dollars

As can be seen from table. 1, the construction expenses of UST-1 are very low in comparison to SCR-1. But the main purpose of construction of the UST-1 was to investigate cheap manufacturing methods and developing small stellarator devices, and study of nuclear fusion and plasma physics is not its main goal. Therefore, UST-1 is not suitable for a long-term research project in the field of nuclear fusion and plasma physics. Due to this disadvantage of UST-1, SCR-1 chose as the model of Iranian stellarator.

Conclusions

In this paper, stellarator, its history and different projects of this device have been explained. The stellarator research program of Iran described briefly and it was concluded that small Costa Rican device SCR-1 is the best option for design and construction a stellarator in Iran.

References

[1] Xu, Y. (2016). A general comparison between tokamak and stellarator plasmas. *Matter and Radiation at Extremes*, *1*(4), 192-200.

[2] Boozer, A. H. (1998). What is a stellarator?. *Physics of Plasmas*, *5*(5), 1647-1655.

[3] Stix, T. H. (1998). Highlights in early stellarator research at Princeton. *Journal of Plasma and Fusion Research SERIES*, *1*, 3-8.

[4] Spitzers (2013). 100th: Founding PPPL & Pioneering Work in Fusion Energy, Greg Hammett, Princeton Plasma Physics Laboratory Colloquium Dec. 4.

[5] Kulsrud, R. (2013 Dec). Some Stories From Working with Spitzer In the Early Years, Princeton Plasma Physics Laboratory Colloquium.

[6] Grieger, G., Renner, H., & Wobig, H. (1985). Wendelstein stellarators. *Nuclear fusion*, *25*(9), 1231.

[7] Wakatani, M. (1998). *Stellarator and heliotron devices* (Vol. 95). Oxford University Press, USA.

[8] Beidler, C. D., Harmeyer, E., Herrnegger, F., Kisslinger, J., Igitkhanov, Y., & Wobig, H. (2001, December). Stellarator fusion reactors-An overview. In *Proceedings of Toki Conference ITC12*.

[9] Ghafoori Fard, H., Goudarzi, Sh., Mazandarani, A. (2021). Stellarators, book, Amirkabir University of Technology Press.

[10] Braams, C. M., & Stott, P. E. (2002). *Nuclear fusion: half a century of magnetic confinement fusion research*. CRC Press.

[11] Mora, J., Vargas, V. I., Asenjo, J., Barillas, L., Coto-Vílchez, F., Esquivel-S, R., ... & Fernández-Vega, J. (2016, October). First results of the stellarator of Costa Rica 1 (SCR-1). In *26th IAEA Fusion Energy Conference (FEC IAEA)* (pp. 17-22).

[12] Xiong, G., Xu, Y., Shimizu, A., Kinoshita, S., Liu, H., Isobe, M., ... & Tang, C. (2020). Preliminary design and analysis of the CFQS supporting structure. *Fusion Engineering and Design*, *160*, 112021.

[13] ALMAGRI Abdnlgader F, et al, (1998). "Design and Gonstruction of HSX: a Helically Symmetric Stellarator", J. Plasma Fusion Res. SERIES, Vol.1 422-425

[14] Francesco A. Volpe. (2016 Sept). Experimental Stellarator Research at Columbia University, Dept. Applied Physics & Applied Mathematics, Columbia University, New York, Plasma Seminar at University of Maryland.

[15] Hirsch, M., Baldzuhn, J., Beidler, C., Brakel, R., Burhenn, R., Dinklage, A., ... & W7-AS Team. (2008). Major results from the stellarator Wendelstein 7-AS. *Plasma Physics and Controlled Fusion*, *50*(5), 053001.

[16] Wolf, R. C., Beidler, C. D., Burhenn, R., Geiger, J., Hirsch, M., Kisslinger, J., ... & Werner, A. (2010). From Wendelstein 7-X to a stellarator reactor. *Plasma and Fusion Research*, *5*, S1011-S1011.

[17] Ilgisonis, V. I., Ilyin, K. I., Novikov, S. G., & Olenin, Y. A. (2021). On the Program of Russian Research in the Field of Controlled Thermonuclear Fusion and Plasma Technologies. *Plasma Physics Reports*, *47*, 1085-1091.

[18] Wakatani, M., & Sudo, S. (1996). Overview of Heliotron E results. *Plasma physics and controlled fusion*, *38*(7), 937.

[19] Warmer, F., Takahashi, H., Tanaka, K., Yoshimura, Y., Beidler, C. D., Peterson, B., ... & LHD Experiment Group. (2018). Energy confinement of hydrogen and deuterium electron-root plasmas in the Large Helical Device. *Nuclear Fusion*, *58*(10), 106025.

[20] Georgiyevskiy, A. V., Rudakov, V. A., & Tolok, V. T. (2003). Development of a conception of the stellarator based on torsatron and modular systems. *Вопросы атомной науки и техники*.

[21] Garland, S., Manz, P., & Ramisch, M. (2020). The influence of magnetic field curvature on intermittency in drift-wave turbulence in the stellarator TJ-K. *Physics of Plasmas*, *27*(5).

[22] https://www.innovations-report.com/physics-astronomy/wendelstein-7-x-reaches-milestone/

[23] DOE/Princeton Plasma Physics Laboratory. "Common household cleaner can boost effort to harvest fusion energy on Earth", ScienceDaily, 11 January 2022.

[24] Takeiri, Y. (2018). The Large Helical Device: Entering deuterium experiment phase toward steady-state helical fusion reactor based on achievements in hydrogen experiment phase. *IEEE Transactions on Plasma Science*, *46*(7), 2348-2353.

[25] Osakabe, M., Takahashi, H., Yamada, H., Tanaka, K., Kobayashi, T., Ida, K., ... & LHD Experiment Group. (2022). Recent results from deuterium experiments on the large helical device and their contribution to fusion reactor development. *Nuclear Fusion*, *62*(4), 042019.

[26] https://www.iter.org/newsline/273/16386

[27] "Introduction the Wendelstein 7-X stellarator" Max-Planck-Institut für Plasmaphysik, Teilinstitut Greifswald, Retrieved 5 Nov.2014.

[28] Wolf, R. C., Ali, A., Alonso, A., Baldzuhn, J., Beidler, C., Beurskens, M., ... & Regaña, J. G. (2017). Major results from the first plasma campaign of the Wendelstein 7-X stellarator. *Nuclear Fusion*, *57*(10), 102020.

[29] Dinklage, A., Beidler, C. D., Helander, P., Fuchert, G., Maaßberg, H., Rahbarnia, K., ... & Zhang, D. (2018). Magnetic configuration effects on the Wendelstein 7-X stellarator. *Nature Physics*, *14*(8), 855-860.

[30] "The second experimentation phase". Max Planck Institute for Plasma Physics. Retrieved 26 September 2022.

[31] Milch, Isabella. "Wendelstein 7-X fusion device at Greifswald to be upgraded". Max Planck Institute for Plasma Physics. Retrieved 26 September 2022

[32] https://phys.org/news/2023-02-power-plasma-gigajoule-energy-turnover.html

[33] http://www.theengineer.co.uk/content/news/proxima-fusion-looks-to-take-stellarators-commercial/

[34] Queral, V. (2006 Dec). Design, construction and results in UST-1, a small low-cost educational stellarator, Seminar in National Fusion Laboratory , LNF , CIEMAT, Spain , EU.

[35] Queral, V. (2016). Design, construction and validation of the UST-1 modular stellarator. *Fusion Engineering and Design*, *112*, 410-417.

[36] Queral Mas, V. M. (2015). Rapid manufacturing methods for geometrically complex nuclear fusion devices: The UST-2 stellarator.

[37] Barillas, L., Vargas, V. I., Alpizar, A., Asenjo, J., Carranza, J. M., Cerdas, F., ... & Villegas, L. F. (2014, May). SCR-1: Design and construction of a small modular stellarator for magnetic confinement of plasma. In *Journal of Physics: Conference Series* (Vol. 511, No. 1, p. 012037). IOP Publishing.

[38] Coto-Vílchez, F., Vargas, V. I., Solano-Piedra, R., Rojas-Quesada, M. A., Araya-Solano, L. A., Ramírez, A. A., ... & Arias, S. (2020). Progress on the small modular stellarator SCR-1: new diagnostics and heating scenarios. *Journal of Plasma Physics*, *86*(4), 815860401.

[39] Sanchez Castro, J., & Vargas, I. (2020). Design of a Heterodyne Microwave Interferometer for the Measurement of the Electronic Density of Plasma in the SCR-1.

ICNST 2024
International Conference on Nuclear Science and Technology
6- 8 MAY 2024 | Isfahan, Iran

Investigating thermodynamic parameters of silicon carbide-nickel chromium nanocomposite film prepared using plasma focus device at high temperature (Paper ID: 1350)

H. Anousha[1*], Sh. Goudarzi[2], M. Esmailpour[1], and D. Rostamifard[2]
[1]*Department of Physics, Faculty of Basic Sciences, Shahid Madani University of Azerbaijan, Tabriz, Iran*
[2] *Plasma and Fusion Research Institute, Nuclear Science and Technology Research Institute, Tehran, Iran*
[*]h.anoosha@azaruniv.ac.ir

Abstract

In this study, SiC-NiCr nanocomposite was deposited on Zr substrate using Mather type plasma focus device in the presence of H_2 gas. In Plasma Focus (PF) devices, it is possible to test the coating sample in the presence of hydrogen gas, which can not be done by other methods. Target sample was prepared using silicon carbide, chromium, and nickel powders using a spark plasma sintering (SPS) procedure. Zr samples were 46.5 mm above the anode and the deposition process was carried out in 20 shots **.**The Zr substrate and coated with SiC-NiCr were subjected to thermal gravimetric analysis (TGA) at a rate of 20^0 C/min to a temperature of 1000^0 C for 1 hour. According to TGA results, activation energy (E_a) and activation entropy (ΔS_0) have decreased in the presence of the studied coating at high temperature. Also, the activation enthalpy value (ΔH_o) increases compared to the substrate, which indicates a higher protection efficiency.

Keywords: Plasma Focus, Zirconium, Silicon Carbide-Nickel Chrome, TGA

Introduction

Zirconium alloys are commonly utilized as nuclear fuel claddings due to their exceptional strength and corrosion resistance [1]. High temperature reactions of zirconium (Zr) and water result in large quantities of hydrogen gas being released [2, 3]. By releasing additional heat due to the exothermic reaction, Zr based claddings interact with steam at high temperatures (above 800^o C) and cause oxidation and embrittlement:

$$Zr\ (s) + 2H_2O\ (1) \rightarrow ZrO_2\ (s) + 2H_2\ (g) + 584.5\ kJ/mol$$

A practical solution to this problem is the development of protective coatings on the surfaces of Zr fuel sheaths. The protective coating should reduce the hydrogen absorption of Zr based alloys in reactors, improve corrosion resistance, and protect against high-temperature oxidation [4, 5].

The electron deposition method was used to prepare nanocomposite coatings from nickel on pure copper samples by Mansour Hashem et al. who realized that nickel-chromium, nickel-silicon and carbide chromium coatings with chromium and silicon carbide particles increases the microhardness and wear resistance [6]. Deposition of metal matrix composites (MMCs) consisting of carbides, metals and, some other materials is a flexible and low-cost method for composite coating. New composite SiC-NiCr films have shown better mechanical, tribological, anti-corrosion and anti-oxidation properties compared to the pure metal coatings.

In this article, the corrosion behavior of SiC-NiCr nanocomposite coating on Zr substrate at high temperature has been studied using thermal gravimetric analysis (TGA).

Experimental

A 2 kJ Mather type plasma focus device was used in this experimental study to deposit SiC-NiCr coatings. The schematic of the plasma focus device and the image of the PF device used in the research are shown in figure 1. Anode was prepared using silicon carbide, chromium, and nickel powders (99.9% purity) at weight ratios of 100, 80, and 20 gr, respectively, using a spark plasma sintering (SPS) procedure. During this process, powder materials are heated within a furnace at a temperature below their melting point. Thus, the atoms move within the powder particle (infiltrate), and the bond between them is formed. Figure 2 shows the SiC-NiCr target material made by the SPS method inside Cu anode that is installed in the plasma focus device.

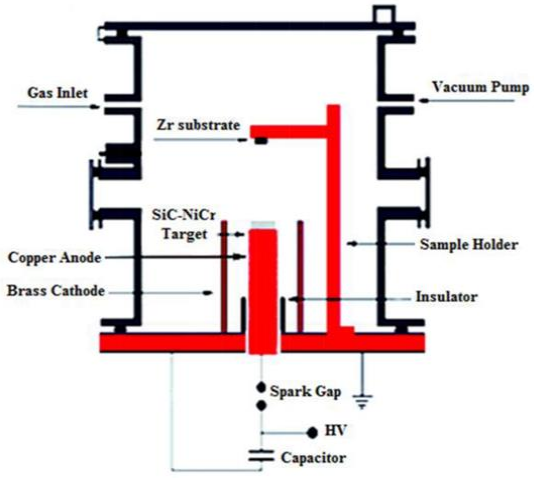

Fig. 1. Schematic of Mather plasma focus device

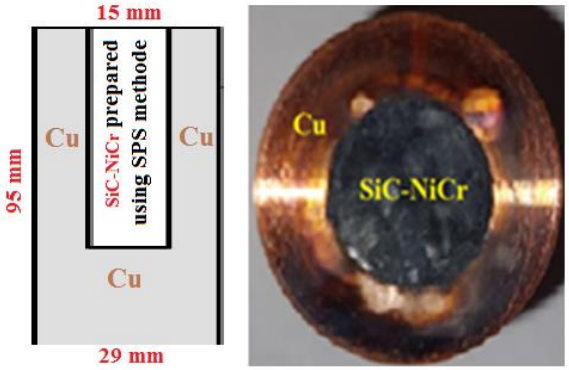

Fig. 2. SiC-NiCr target material inside Cu anode

A rotary compressor lowered the pressure of the entire electrode set to 0.2 torr within a vacuum container. Afterward, H_2 gas was injected into the vacuum container. An optimal pressure of 0.2 torr at a voltage of 12 kV was found to be optimal for an excellent pinch in the experiment. An oscilloscope was used to record the voltage in terms of the current waveform at pinch time received from the Rogowski coil (Fig. 3).

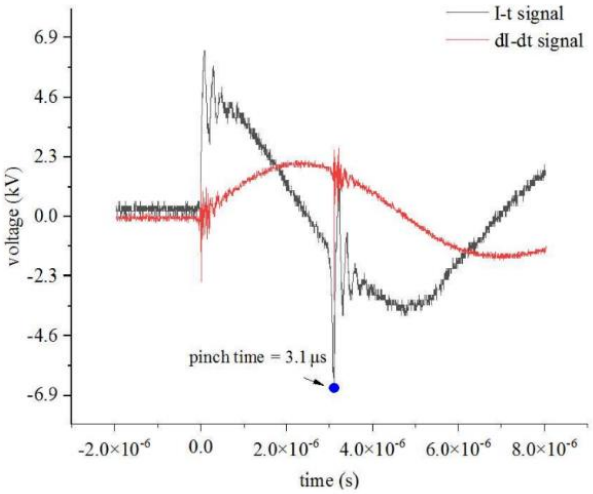

Fig. 3. Rogowski coil current derivative signal at pinch time

An electrostatic field was applied between the anode and cathode by means of a 39 μF capacitor recharged by a high voltage in order to operate the PF device. The surface of the insulator was then affected by an electrical discharge, resulting in layer of current on it. Lorentz force is created when

a self−consistent magnetic field is created to accelerate the current layer toward the anode's open end. This resulted in compression of the anode's current layer, creating heated dense plasma. The elimination of the plasma column generated a strong magnetic field, which must be noted. A collision between high−energy electrons and the anode occurred when the electrons and ions were accelerated in opposite directions. Samples were placed 46.5 mm above the anode. Table 1 shows the characteristics of the Plasma Focus device used in our experiments.

Table 1. Characteristics of the Plasma Focus device

effective length of the anode (mm)	95
anode diameter (mm)	29
effective insulation height (mm)	50
cathode rod height (mm)	145
cathode rod diameter (mm)	10
number of cathode rods	12
anode to substrate distance (mm)	46.5
number of shots	20
optimal voltage (kV)	12

Results and Discussion

A thermogravimetric analysis (TGA) is a technique used to measure the change in mass of a sample over time and temperature in a controlled environment. The oxidation rate can be determined by calculating the normalized mass gained during the oxidation process using the following equation: [7]:

$$W = K\, t^{n} \qquad (1)$$

where ***W*** is the normalized mass gain, ***K*** is the oxidation rate constant, ***t*** is oxidation time, and ***n*** is the rate law identifier (i.e. $n = 1$ for linear $n = 2$ for parabolic oxidation behaviour).

The activation energy of each alloy is determined via an Arrhenius equation according to

$$\ln(K) = \ln(A) + \left(\frac{1}{T}\right)\left(-\frac{E_a}{R}\right)\ \left[\frac{J}{mol}\right] \qquad (2)$$

where A is a constant, E_a is the activation energy, R is the ideal gas constant, and T is the isothermal oxidation temperature. The obtained ln(**K**) values from Equation (2) are plotted against the reciprocal of temperature (1/T) and fitted with a linear trend line. R-squared coefficient (**R^2** value**)** of lnK-1/T and lnK/T-1/T graphs is 0.98 and 0.94, respectively. The higher the **R^2** value of the graph, the better the fit.

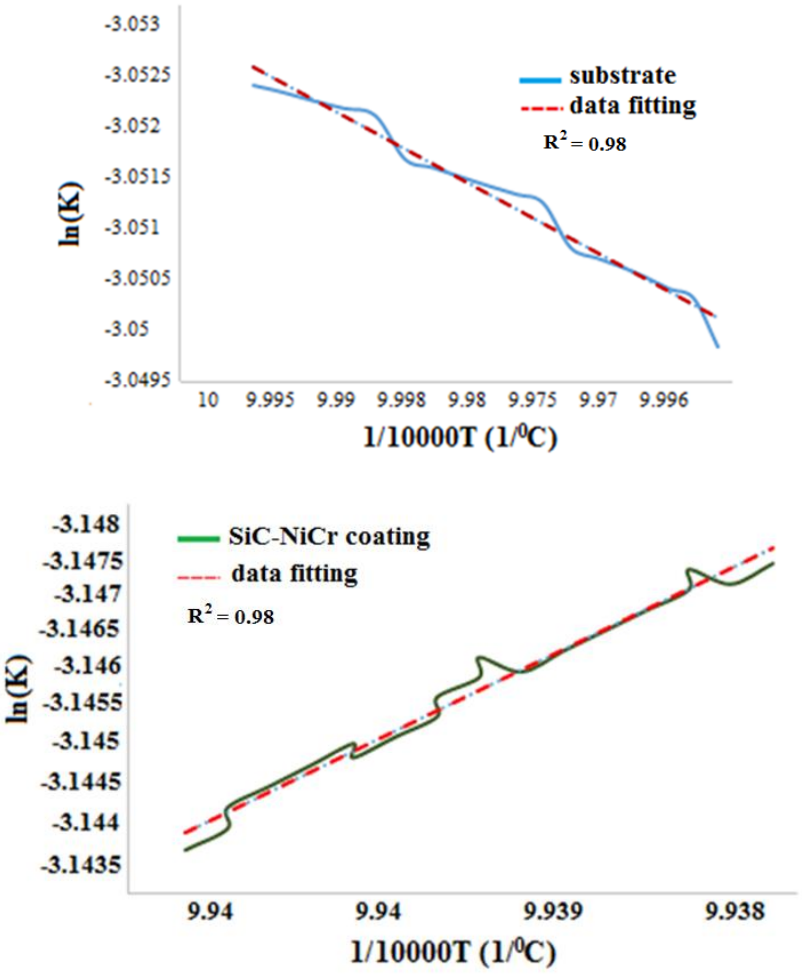

Fig. 4. Diagram **lnK** in terms of **1/T** at isothermal oxidation temperature (1000^0C) for substrate sample and SiC-NiCr coating

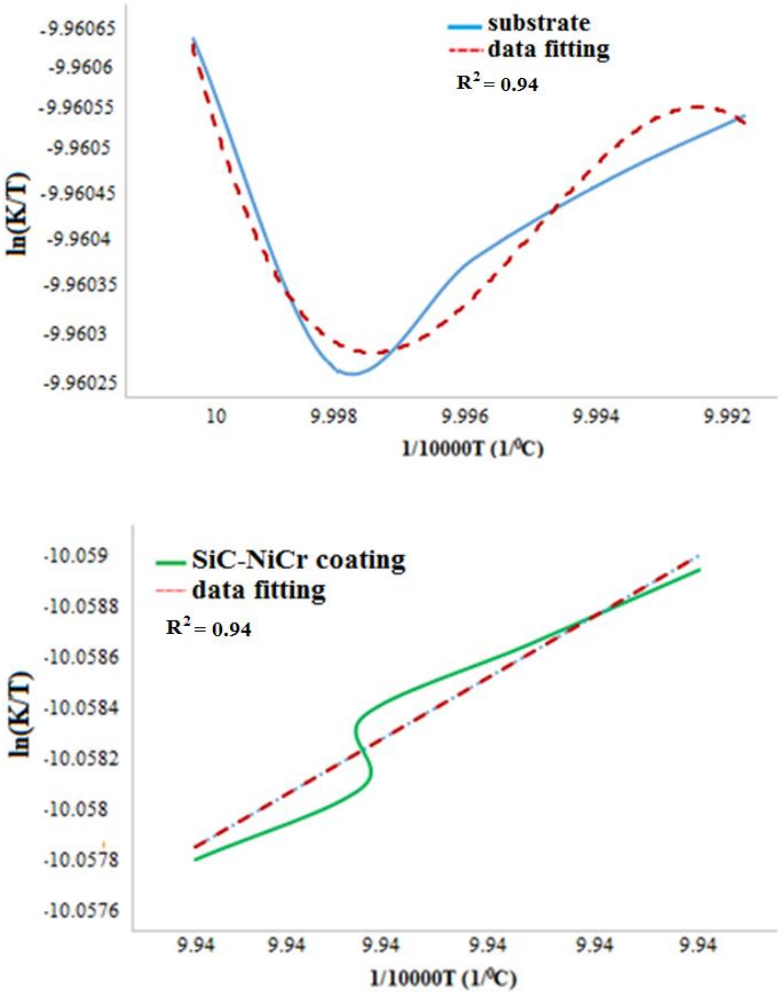

Fig. 5. Diagram **ln(K/T)** in terms of **1/T** at isothermal oxidation temperature (1000^0C) for substrate sample and SiC-NiCr coating

With the application of the SiC-NiCr coating, the activation energy (E_a) decreases significantly of 9.55 kJ.mol^{-1} to -195.69 kJ.mol^{-1}, indicating a higher corrosion rate, as depicted in Figure 4. By comparing the values of ΔS_0, it becomes evident that the activation entropy of the coating decreases relative with substrate. A lower ΔS_0 value suggests a slower dissolution of the metal in the presence of the coating. Table 2 illustrates the thermodynamic parameters of substrate and SiC-NiCr coating.

Table 2. Thermodynamic parameters of substrate and SiC-NiCr coating

ΔG_0 (kJ/mol)	$-\Delta S_0$ ($J.K^{-1}.mol^{-1}$)	$-\Delta H_0$ (J/mol)	E_a (kJ/mol)	ln(A)	
177.3	178.1	794.56	9.55	-1.9	Zr
64.94	642.94	-651.76	-195.69	-26.55	Zr-coated SiC-NiCr

Conclusion

In this experimental study, the SiC-NiCr coating was applied to the Zr substrate using a Mather type plasma focus device with an energy of 2 kJ, and then the samples were subjected to heat treatment at a temperature of 1000^0 C for 1 hour.

According to the TGA results and the slope of the graphs of ln(K) in terms of 1/T and ln(K/T) in terms of 1/T, the values of activation energy (E_a), activation entropy (ΔS_0) and activation enthalpy (ΔH_o) can be investigated the substrate and coating at high temperature.

The results show that E_a and ΔS_0 decrease and ΔH_0 increases in the presence of the studied coating, which indicates the slower dissolution of Zr metal with SiC-NiCr coating apply.

References

[1] Duan, Z. Yang, H. Satoh, Y. Murakami, K. and et al. (2017). Nucl. Eng, 316:131–150

[2] Kurata, M. (2016). Nucl. Eng. Technol, 48:26-32.

[3] Nishimura, T. Hoshi, H. Hotta, A. (2015). Nucl. Eng. Technol, 470:1-10.

[4] Tang, C. Stueber, M. Seifert, H. J, and Steinbrueck, M. (2017). Corrosion reviews, 35(3): 141-165.

[5] Maier, B. Yeom, H. Johnson, G. Dabney, T. and et al. (2018). JOM, 70:198–202.

[6] Hashim, M. Masoudi, M. Kamari, H. M. and Salit, M. S. (2013). Appl Nanosci, 3: 357–362.

[7] Vandegrift, L. J. Price, M. P. Stroud, J. P. Parga, J. C. and et al. (2019). Nuclear Materials and Energy, 20: 100692.

ICNST 2024
International Conference on Nuclear Science and Technology
6- 8 MAY 2024 | Isfahan, Iran

Effects of DBD cold plasma treatment on pinto bean seed germination and seedling growth (Paper ID: 1431)

Mazandarani A.[1*], Goudarzi Sh.[1], Bakhtiari H.[2], Esmaeili A.[1], Okhovat M.[3]

[1]Plasma and Nuclear Fusion Research School, Nuclear Science and Technology Research Institute, Tehran, Iran
[2] Department of Water, and Energy, Faculty of Civil Engineering, Imam Hossein University, Tehran, Iran
[3] Faculty of Mechanical Conversion Engineering, Tarbiat Modares University, Tehran, Iran

Abstract

The study investigated the impact of cold plasma generated by a dielectric barrier discharge (DBD) at atmospheric pressure and room temperature on the germination and seedling growth of pinto beans (Phaseolus vulgaris L.). Different power levels of cold plasma (30, 60, 90, and 120 W for 20 seconds) were applied to the seeds to assess their effects on germination. All plasma treatments demonstrated notable positive effects on germination-related traits, such as germination percentage, seedling growth, and vigor index. The experiments revealed a decrease in water contact angle and the development of a hydrophilic seed surface due to plasma treatment. The germination percentages for 30, 60, 90, and 120 W were 88.89%, 97.78%, 100%, and 100%, respectively, representing improvements of 5.3%, 15.8%, 18.43%, and 18.43% over the control. Notably, the 120 W treatment significantly enhanced seed germination potential and vigor index compared to the control. In conclusion, the use of cold plasma was found to significantly enhance the germination and seedling growth of pinto bean seeds.

Keywords: cold plasma, pinto bean, seed germination, DBD plasma

Introduction

It is anticipated that the global population will reach 9.7 billion individuals by 2050 [1]. This rise in population could lead to a 35 to 56 percent surge in food demand [2]. Grains and legumes are noteworthy for being abundant in protein and carbohydrates [3], and they hold a crucial position in human health by managing glucose metabolism, lowering blood cholesterol levels, and mitigating heart ailments [4]. Beans, a type of legume, are predominantly grown in temperate and tropical zones and enjoy popularity among various populations [5]. The global dry bean production reached 27.5 million tons in 2020, cultivated across 34.8 million hectares [6]. Pinto beans, renowned in America for their protein content of 21.4% to 23.6%, are a favored variety [7]. This

type of bean was introduced in 2021 due to its ability to grow vertically, high yield, and resistance to abiotic stresses [8].

Given the challenge of water scarcity, there is a growing recognition of the importance of adopting innovative technologies to enhance agricultural output and efficiency to ensure an adequate food supply [9]. Boosting seed germination stands out as a key approach to enhancing agricultural productivity [10]. One of the fundamental stages in a plant's life is seed germination [11], which enhances germination speed, establishment, and growth [12], and improves sunlight absorption by the plant, ultimately boosting the plant's yield [13]. Various techniques have been developed to enhance germination. Cold plasma, considered the fourth state of matter, is a novel and efficient technology in plant growth and increasing crop yield, without causing harmful biological pollution or requiring the use of chemicals on seeds [14- 16]. Dielectric barrier discharge (DBD) is the most common method for producing cold plasma (CP). This technique involves a high-voltage electrode and a ground electrode, with one or both electrodes being covered by insulating materials or floating between them to prevent the generation of thermal plasma [17]. DBD typically operates at frequencies ranging from 50 Hz to 10 MHz and pressures between 10^4-10^6 Pascal [18]. The benefits of this approach include a large discharge area, operation at room temperature, low maintenance costs, and a notable sterilization effect [19]. Cold plasma, a novel non-thermal technology, finds extensive applications in medicine, electronics, material science, and agricultural science [20]. Research has demonstrated that CP holds significant potential for enhancing seed germination rates and seedling survival [21]. Recently, there have been notable advancements in treating wheat and barley seeds [14], peas [22], millet [23], oats [24], and beans with cold plasma. This method has been shown to enhance germination speed by increasing the hydrophilic nature of the bean seed coat [15, 25].

No articles have yet reported on the treatment of pinto beans with plasma. This study introduces, for the first time, the impact of DBD atmospheric cold plasma on germination, seedling length, water absorption, surface morphology, and germination index of pinto beans. Cold plasma, as a cost-effective and innovative method, has the potential to enhance seed germination, appealing to farmers and researchers. This article aims to explore the influence of plasma power consumption

on pinto bean germination characteristics and to offer an experimental model illustrating the impact of these power levels on seed treatment.

Research Theories

The experiments were conducted using a completely random design for pinto bean seeds (Phaseolus vulgaris L.) with three replications. All experiments were performed on healthy specimens. Initially, all seeds were disinfected with a 2% sodium hypochlorite solution for 60 seconds, followed by three rinses with distilled water. Subsequently, they were treated with a 2% benomyl fungicide solution for 30 seconds and rinsed three times with distilled water. Each glass petri dish utilized in the study held 15 seeds. To mitigate water evaporation effects, caps were employed to cover the Petri dishes [26].

After 48 hours, the seeds were transferred to a germinator set at a constant temperature of 21 degrees Celsius and a relative humidity of 43% for a 10-day germination assessment period [15]. Daily checks and recordings were made on the seeds and their germination rate. Upon completion of the experiment, the lengths of the roots and shoots were measured.

Experimental

The experimental setup comprises 4 high voltage power supplies and a dielectric barrier discharge (DBD) reactor housed in a Plexiglas enclosure. The custom-built DBD device (see Fig. 1) utilized in the trials had specific technical parameters. The power units employed could generate voltages ranging from 0 to 15 kV at a consistent frequency of 25 kHz and fixed wattages of 30, 60, 90, and 120 watts. Throughout the experiment, the frequency, thickness, electrode-dielectric gap, electrode material (aluminum), and dielectric material (Pyrex) remained constant at 25 kHz, 2 mm, 4 mm, aluminum, and Pyrex, respectively. Seed samples were exposed to power levels of 30, 60, 90, and 120 watts for 20 seconds.

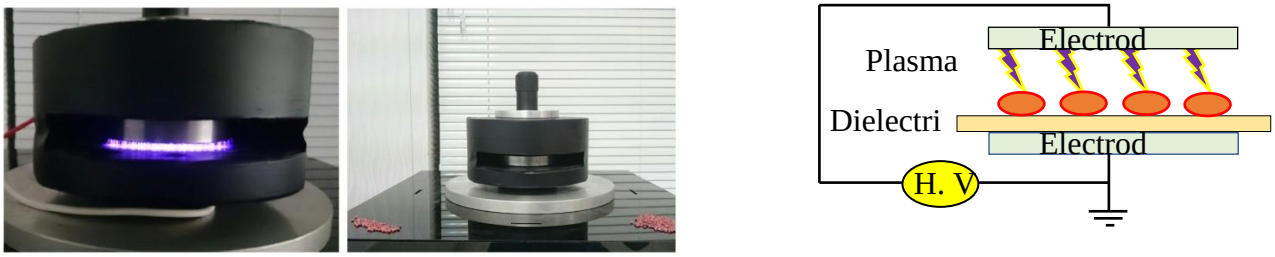

(a) (b)

Fig. 1. (a) The DBD reactor and the plasma generated within it and (b) the schematic showing seed placement within the plasma

Seed Germination and Seedling Growth

The final germination percentage is a crucial parameter in seed germination assessment, directly linked to seed quality and vitality. Higher seed quality leads to increased germination percentage and number of germinated seeds, resulting in a higher germination index. This attribute is calculated using the following equation:

Final Germination Percentage after 10 days = [Number of germinated seeds / Total number of seeds] ×100

The length of the shoot and root after 10 days was measured using a ruler and plotted on a graph. Measurements are reported in millimeters. The product of the length of the plant at the final germination represents the vigor index. The vigor index represents the germination percentage and potential, the lower the seed quality, the lower the germination percentage, and the vigor index decreases [14].

Scanning Electron Microscope (SEM)

Irradiated and non-irradiated pinto bean seeds (seed coat) were examined using high-resolution SEM (ZEISS-EVO 18).

Water Contact Angle (WCA)

The main way to quantitatively assess wettability in plasma seed treatment is by measuring the WCA, or apparent contact angle. WCA measurements were conducted on untreated and plasma-treated pinto bean seeds to evaluate surface wettability. After plasma treatment, 3 seeds from each group were randomly chosen, and a droplet of water was applied to the seeds using a dropper to

measure the water contact angle for all these seeds. The results are presented in a table as an average.

Results and discussion

Seed Germination and Seedling Growth

The final germination percentage of pinto bean seeds increased significantly with higher plasma power compared to the control group. All plasma treatments boosted germination, seedling length, and vigor index by creating electron pores on the seed surface. The plasma weakened the shell, aiding sprout emergence with less energy. The germination percentages for 30, 60, 90, and 120 W were 88.89%, 97.78%, 100%, and 100%, respectively, representing improvements of 5.3%, 15.8%, 18.43%, and 18.43% over the control (refer to Fig. 2).

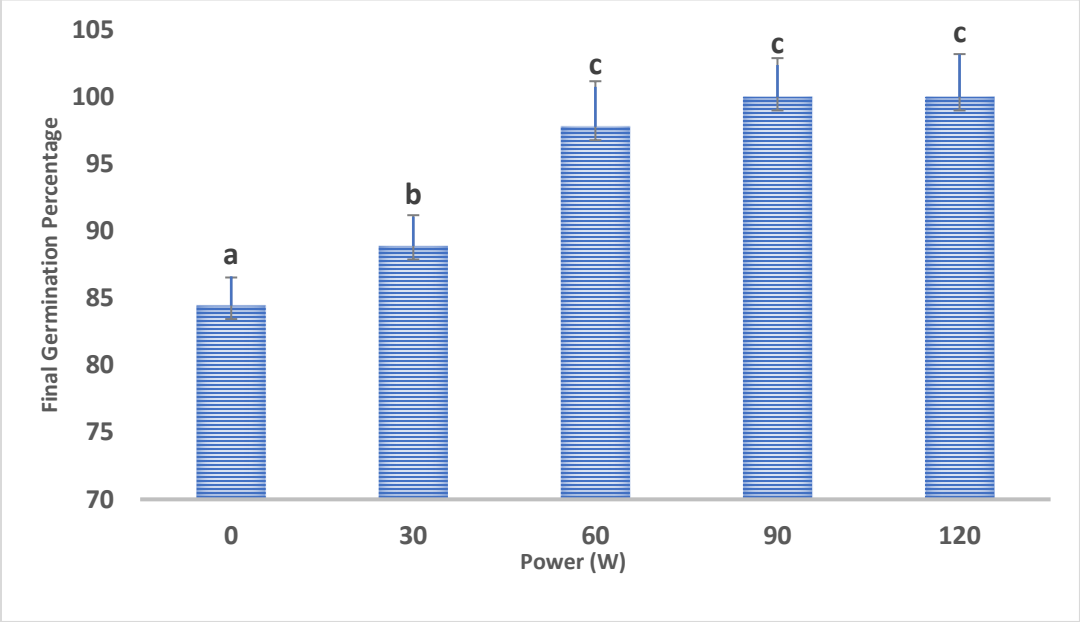

Fig. 2. Effect of DBD plasma treatments on final germination percentage

According to Figure 3, in the treatment with powers of 30, 60, 90, and 120 W compared to the control, there was a 28%, 40%, 44.1%, and 47.2% increase in root length and a 47.9%, 60.8%, 64.4%, and 69.4% increase in shoot length, respectively. These findings indicate that bean seed seedlings subjected to the 120 W treatment are likely to exhibit superior establishment and resilience compared to the other groups.

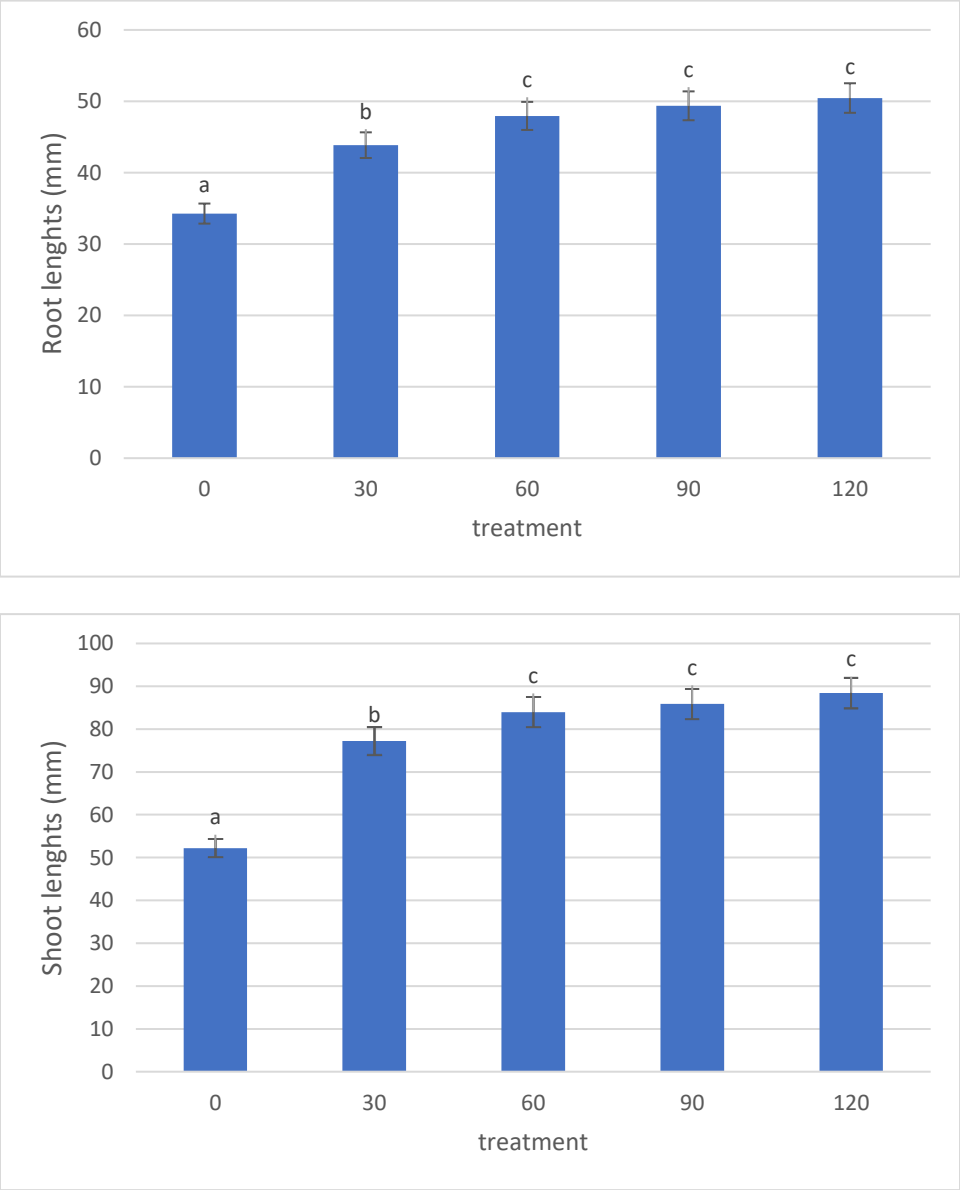

Fig. 3. Effect of DBD plasma treatments on root length and shoot length

Success or failure in production relies on factors like germination percentage, speed, and plant strength. Maximum plant establishment occurs when seeds overcome unfavorable conditions and react appropriately. Any factor hindering establishment and reducing germination speed and uniformity also impacts performance. Therefore, proper germination is crucial for plant establishment and desired yield production across various conditions. The 30, 60, 90, and 120 W vigor index shows enhancements of 47.4%, 76.6%, 85.1%, and 90.2% compared to the control,

respectively (see Fig. 4). The study of bean seed vigor index under cold plasma treatment revealed a significant increase in germination power, attributed to enhanced water absorption potential leading to improved germination uniformity [11, 14- 16].

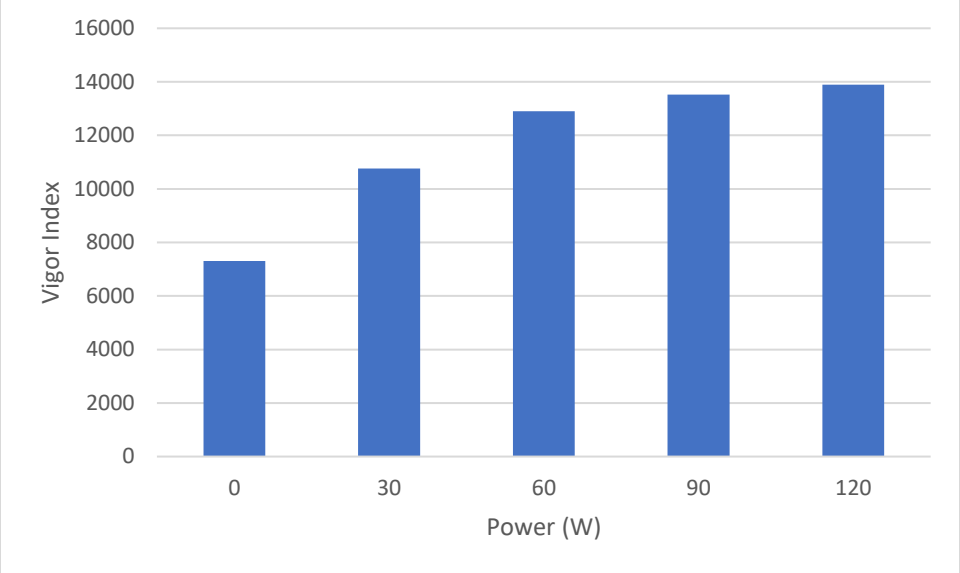

Fig. 4. Effect of DBD plasma treatments on vigor index

Scanning Electron Microscope (SEM)

SEM was utilized to assess the modifications in the surface morphology of the seed coating. The SEM images of the seed coating (refer to Fig. 5) indicate that the surface of the treated seeds has changed, showing small cracks on the seed surface caused by the plasma treatment. The changes on the surface of the plasma-treated seeds may potentially improve and accelerate water absorption. The surface erosion level of pinto bean seeds under 120 W plasma treatment was notable, leading to the creation of numerous cracks that promoted water infiltration into the seed, fortifying the shell for better embryo growth and ultimately boosting the germination of bean seeds [14, 15].

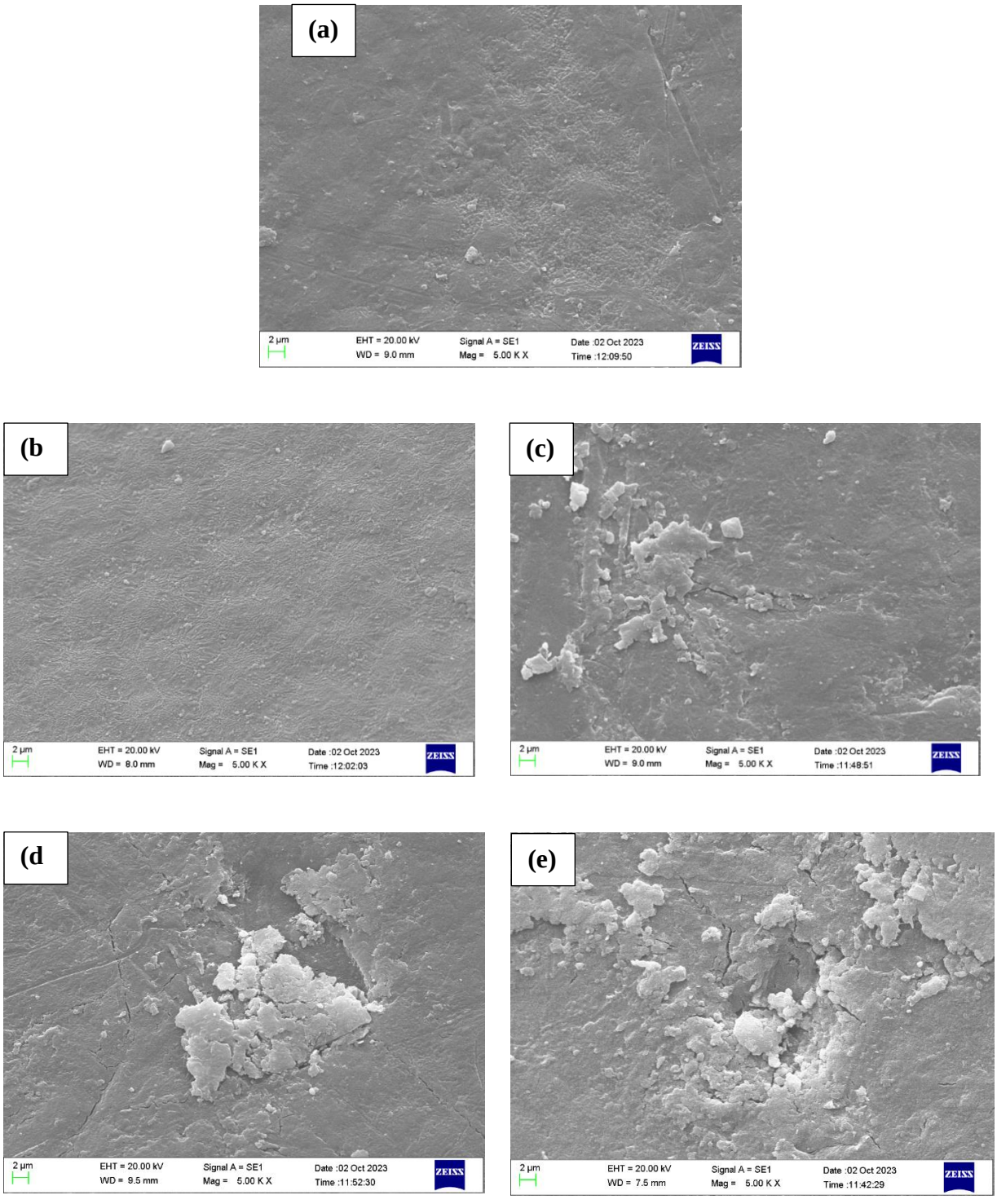

Fig. 5. Coat images of pinto bean seeds: (a) untreated seeds, (b) seeds treated with 30 W, (c) 60 W, (d) 90 W, and (e) 120 W powers; the scale bars = 2 µm

Water Contact Angle (WCA)

The results reveal that treating seeds with plasma induces chemical and morphological alterations on their surface, resulting in a decline in the water contact angle. In the table below, it is evident that the contact angle reduction is directly influenced by the plasma power. As plasma power increases, the contact angle decreases, indicating a rise in water absorption. Essentially, longer plasma treatment durations and higher plasma powers correlate with reduced contact angles and heightened wetting rates [27]. All values in Table 1 are presented in degrees.

Table 1. Water Contact Angle

control	30 W	60 W	90 W	120 W
73.3	53.9	47.1	44.8	38.5

Conclusions

Researchers reported that plasma treatment can modify the surfaces of different seed varieties, potentially enhancing germination based on the seed type [14, 15]. This research aimed to evaluate the effects of DBD plasma treatment on seed germination, seedling growth, vigor index, and surface morphology of pinto bean seeds. SEM images were used to analyze structural changes in bean seeds after plasma treatment, showing cracks on the seed surface due to plasma interaction. Increasing plasma power from 30 to 120 W resulted in more extensive and larger cracks. Improved germination and seedling growth were observed with higher plasma power, associated with better water and nutrient absorption, as well as enhanced oxygen diffusion through established pathways. Noticeable changes in the wettability of pinto bean seeds post-DBD plasma treatment were also observed. The findings indicated that optimal treatment with 120 W DBD plasma significantly boosted germination, leading to a higher final germination rate and vigor index compared to untreated seeds [14- 20].

References

[1] Manida, M. (2022). The future of food and agriculture trends and challenges. Agriculture & Food E-Newsletter.

[2] Van Dijk, M., Morley, T., Rau, M. L., & Saghai, Y. (2021). A meta-analysis of projected global food demand and population at risk of hunger for the period 2010–2050. Nature Food, 2(7), 494-501.

[3] Fabbri, A. D., Schacht, R. W., & Crosby, G. A. (2016). Evaluation of resistant starch content of cooked black beans, pinto beans, and chickpeas. NFS journal, 3, 8-12.

[4] Zhu, Y., Li, J., Feng, X., Shi, Z., Yao, Y., & Shen, R. (2022). Structural characterisation of two polysaccharides from white common bean (Phaseolus vulgaris L.) and the application in microencapsulation of probiotics. International Journal of Food Science & Technology, 57(11), 7184-7193.

[5] Bai, Q., Li, M., Zhou, J., Imran, A., de Souza, T. S., Barrow, C., ... & Suleria, H. A. (2023). Influence of processing methods on phytochemical composition of different varieties of beans (Phaseolus vulgaris). Food Reviews International, 1-39.

[6] Losa, A., Vorster, J., Cominelli, E., Sparvoli, F., Paolo, D., Sala, T., ... & Kunert, K. (2022). Drought and heat affect common bean minerals and human diet—What we know and where to go. Food and Energy Security, 11(1), e351.

[7] Aliabbasi, N., Emam-Djomeh, Z., Askari, G., & Salami, M. (2023). Pinto bean protein ultrasonicated cold-set emulsion gels catalyzed by transglutaminase/glucono-δ-lactone: Development, characterization and in vitro release characteristics. Journal of Drug Delivery Science and Technology, 81, 104239.

[8] Miklas, P. N., Soler-Garzón, A., Valentini, G., & Pastor-Corrales, M. (2023). Registration of ‘USDA Rattler’pinto bean. Journal of Plant Registrations.

[9] Dubey, P. K., Singh, A., Chaurasia, R., Pandey, K. K., Bundela, A. K., Dubey, R. K., & Abhilash, P. C. (2021). Planet friendly agriculture: Farming for people and the planet. Current Research in Environmental Sustainability, 3, 100041.

[10] Elnahal, A. S., El-Saadony, M. T., Saad, A. M., Desoky, E. S. M., El-Tahan, A. M., Rady, M. M., ... & El-Tarabily, K. A. (2022). The use of microbial inoculants for biological control, plant growth promotion, and sustainable agriculture: A review. European Journal of Plant Pathology, 162(4), 759-792.

[11] Ling, L., Jiafeng, J., Jiangang, L., Minchong, S., Xin, H., Hanliang, S., & Yuanhua, D. (2014). Effects of cold plasma treatment on seed germination and seedling growth of soybean. Scientific reports, 4(1), 5859.

[12] Zhang, M., Gao, B., Chen, J., & Li, Y. (2015). Effects of graphene on seed germination and seedling growth. Journal of Nanoparticle Research, 17, 1-8.

[13] Parveen, A., & Rao, S. (2015). Effect of nanosilver on seed germination and seedling growth in Pennisetum glaucum. Journal of Cluster Science, 26, 693-701.

[14] Mazandarani, A., Goudarzi, S., Ghafoorifard, H., & Eskandari, A. (2020). Evaluation of DBD plasma effects on barley seed germination and seedling growth. IEEE Transactions on Plasma Science, 48(9), 3115-3121.

[15] Volkov, A. G., Hairston, J. S., Marshall, J., Bookal, A., Dholichand, A., & Patel, D. (2020). Plasma seeds: Cold plasma accelerates Phaseolus vulgaris seed imbibition, germination, and speed of seedling growth. Plasma Medicine, 10(3).

[16] Starič, P., Vogel-Mikuš, K., Mozetič, M., & Junkar, I. (2020). Effects of nonthermal plasma on morphology, genetics and physiology of seeds: A review. Plants, 9(12), 1736.

[17] Feizollahi, E., Misra, N. N., & Roopesh, M. S. (2021). Factors influencing the antimicrobial efficacy of dielectric barrier discharge (DBD) atmospheric cold plasma (ACP) in food processing applications. Critical Reviews in Food Science and Nutrition, 61(4), 666-689.

[18] Zhang, H., Ma, D., Qiu, R., Tang, Y., & Du, C. (2017). Non-thermal plasma technology for organic contaminated soil remediation: A review. Chemical Engineering Journal, 313, 157-170.

[19] Nasiru, M. M., Frimpong, E. B., Muhammad, U., Qian, J., Mustapha, A. T., Yan, W., ... & Zhang, J. (2021). Dielectric barrier discharge cold atmospheric plasma: Influence of processing parameters on microbial inactivation in meat and meat products. Comprehensive Reviews in Food Science and Food Safety, 20(3), 2626-2659.

[20] Okyere, A. Y., Rajendran, S., & Annor, G. A. (2022). Cold plasma technologies: Their effect on starch properties and industrial scale-up for starch modification. Current Research in Food Science, 5, 451-463.

[21] Shelar, A., Singh, A. V., Dietrich, P., Maharjan, R. S., Thissen, A., Didwal, P. N., ... & Patil, R. (2022). Emerging cold plasma treatment and machine learning prospects for seed priming: a step towards sustainable food production. RSC advances, 12(17), 10467-10488.

[22] Li, R., Li, X., Tu, A., Jing, C., Dong, S., Chen, S., & Guo, P. (2023). Effects of dielectric barrier discharge plasma treatment on the structural orders and functional properties of chickpea starch. International Journal of Food Science & Technology, 58(7), 4009-4021.

[23] Sonkar, S., Jaddu, S., Pradhan, R. C., Dwivedi, M., Seth, D., Goksen, G., ... & Lorenzo, J. M. (2023). Effect of atmospheric cold plasma (pin type) on hydration and structure properties of kodo-millet starch. LWT, 182, 114889.

[24] Lee, M. J., Lee, H. J., Lee, Y., Yang, J. Y., Song, J. S., Woo, S. Y., ... & Park, S. I. (2023). Cold Plasma Treatment Increases Bioactive Metabolites in Oat (Avena sativa L.) Sprouts and Enhances In Vitro Osteogenic Activity of their Extracts. Plant Foods for Human Nutrition, 78(1), 146-153.

[25] Bormashenko, E., Shapira, Y., Grynyov, R., Whyman, G., Bormashenko, Y., & Drori, E. (2015). Interaction of cold radiofrequency plasma with seeds of beans (Phaseolus vulgaris). Journal of experimental botany, 66(13), 4013-4021.

[26] Gholami, A. A., & Kaviani, B. (2018). Somatic embryogenesis, encapsulation, cold storage, and growth of hybrid Citrus [C. paradisi Macf.(‘Duncan’)× C. reticulata Blanco.(‘Dancy’)] shoot tip segments.

[27] Ling, L. I., Jiangang, L. I., Hanliang, S. H. A. O., & Yuanhua, D. O. N. G. (2018). Effects of low-vacuum helium cold plasma treatment on seed germination, plant growth and yield of oilseed rape. Plasma Science and Technology, 20(9), 095502.

Numerical simulation of foam layer type and its physical characteristics on target energy gain of double-shell targets (Paper ID: 1445)

Rezaie-Chamani, A; Khoshbinfar, S. [Correspondent][i]

Department of Physics, University of Guilan, Rasht, Iran

Abstract

Non-cryogenic double-shell targets can be imploded and ignited as an alternative to traditional single-shell targets. In this paper, the implosion and ignition of non-cryogenic double-shell targets driven by heavy ions have been studied numerically. We have employed 1-D, 3T computer code, Deira-4, developed for heavy ion-driven inertial confinement fusion. Here, we have assessed the impact of fuel density gradient on the whole performance of implosion, ignition, and burn stages. The target energy gain has significantly improved by an increase in fuel mass of 0.7 mg due to the density gradient in the middle gas. The inner fuel compression process is also improved and shells have sufficient time to collide with each other. One of the concerns in double-shell targets is the growth of the Rayleigh-Taylor instability at the fuel-pusher interface. We have managed a density gradient profile in both the inner and outer shells to address this issue. We have observed that the ion temperature of the inner fuel layer will be below 10 keV at maximum compression, and the implosion velocity will arrive at 212 km/s.

Keywords: Numerical simulation, double-shell target, high energy gain, gradient density layer

Introduction

Inertial confinement fusion is a method to obtain clean, safe, and economical nuclear energy, and it is being experimented and researched using various approaches. Numerous efforts have been made in target construction, beam energy, and methods to attain this approach. The low convergence ratio, ignition temperature, and implosion velocity make double-shell targets a preferred approach in recent decades. At the US National Ignition Facility (NIF), the targets driven with lasers have an inner shell, an in-between foam layer, and an outer shell. The inner shell encloses the fuel. Interest in these targets has been enhanced by the use of low-density DT gas or liquid DT with a density of 0.1-0.2 g/cm^3 instead of cryogenic DT [1]. Because one of the disadvantages of common single-shell targets is the construction and maintenance of cryogenic DT.

To overcome these problems, a low-Z tamper layer surrounds the inner pusher, and an inner shell is equipped with a gradient density layer. This density gradient of W-Be for the inner shell has been successfully fabricated [2]. To simulate this fabrication, a double-shell target is used [1]. By using the gradient density layer as a multiple tamper layer, Rayleigh-Taylor instability in the deceleration and acceleration stage can be reduced [1]. Another simulation included the addition of a density gradient of about 5-20 μm between the inner pusher and tamper layers [3]. The capsule performance in these targets is the best due to its thin outer gold coating. The ratio of measured neutrons to released neutrons in one-dimensional simulation for a gold coating is higher than 1 and close to 10% [4]

The inner shell only receives high-wavelength perturbations from the outer shell because of the foam layer between them. Pressure can be increased within a range of 2 Gbar by the middle layer of foam when the inner and outer shells collide [1]. Laser beams are employed to design the research described above. Heavy ions have higher efficiency compared to lasers, and the accelerator has a high repetition rate (10-30 Hz) [5]. Heavy ions have higher stopping power than light ions, but with a low current (10-15 kA), they can provide the necessary power (~ 200 TW) for inertial fusion [6]. The high efficiency of heavy ion targets (ranging from 20-30 %) indicates that high target energy gain can be achieved with lower driver requirements [5]. In double-shell targets, due to the collision between the two outer heavy shells and the inner light shell, it is possible to produce a high areal density. In double-shell targets driven by heavy ions, an outer fuel is used to increase the target energy gain. The structure and function of laser and ion double-shell targets are almost close to each other. In laser-driven double-shell targets, when the high-intensity laser focuses on the Hohlraum gold wall, it creates asymmetric preheating. The implosion of double-shell targets in previous decades was challenging due to the M-band radiation of gold causing this pre-heating. Research has been conducted to reduce this radiation and it has been mostly successful [4]. However, such a challenge is eliminated in double-shell targets driven by heavy ions The layers of a double-shell target designed by ion drivers will be distinct from those of laser drivers. Our aim in this research is to examine the density gradient of the middle foam layer and compare it with the target without gradient density. Liquid or DT gas fuel-based heavy-ion targets have not been investigated yet, as we mentioned earlier in this paper. The following section will introduce a double shell target that uses non-cryogenic fuel and compare it to a target

with a gradient density layer between the two shells. A target with an inner and outer shell that has a density gradient has also been proposed in this paper. Our demonstration shows that optimizing the target can enhance the stability of the double-shell target. We also show that a target with gradient density layers can produce more energy gain compared to a target without gradient density layers.

Research Theories

Simulations and experiments have been carried out in NIF and also by OMEGA laser on double-shell targets as direct and indirect drives [7]. These targets generally consist of a high-Z inner shell, an outer shell, and foam in between. The inner shell contains high-density DT gas or liquid DT fuel, which decreases radiation loss [7]. Cryogenic double-shell targets with heavy ion drive have received little research, but they have demonstrated greater compression and efficiency than single-shell targets[5]. In this approach, low-density DT gas is used instead of foam in the between shells. One of the most obvious advantages of the double-shell targets driven by laser is the use of non-cryogenic fuel, which causes problems in its construction. Cryogenic fuel should be kept at the triple point of deuterium (18.3 K) and maintained in a low-enough adiabatic state.

In this paper, we study the double-shell target driven by heavy ions, which includes inner and outer non-cryogenic fuels. The design of the target is similar to that of the heavy ion cryogenic target as mentioned above. Figure 1-a) and Figure 1-b) show the non-cryogenic target without a gradient density layer and the non-cryogenic target with gradient density in the middle DT gas, respectively. A non-cryogenic target with gradient density in three layers can also be seen in Figure 1-c). The density gradient is linear and all targets have been optimized. As illustrated in Figure 1, for example, the initial density of inner Pb in target c, which is in the range of 0.2-11.3 g/cm^3, increases linearly with an increase in radius. The targets were driven by Bi-209 ion beams with 5 MJ energy and 250 TW power for a duration of 20 ns. The one-dimensional three-temperature Deira-4 code is used to simulate the hydrodynamic behavior [8].

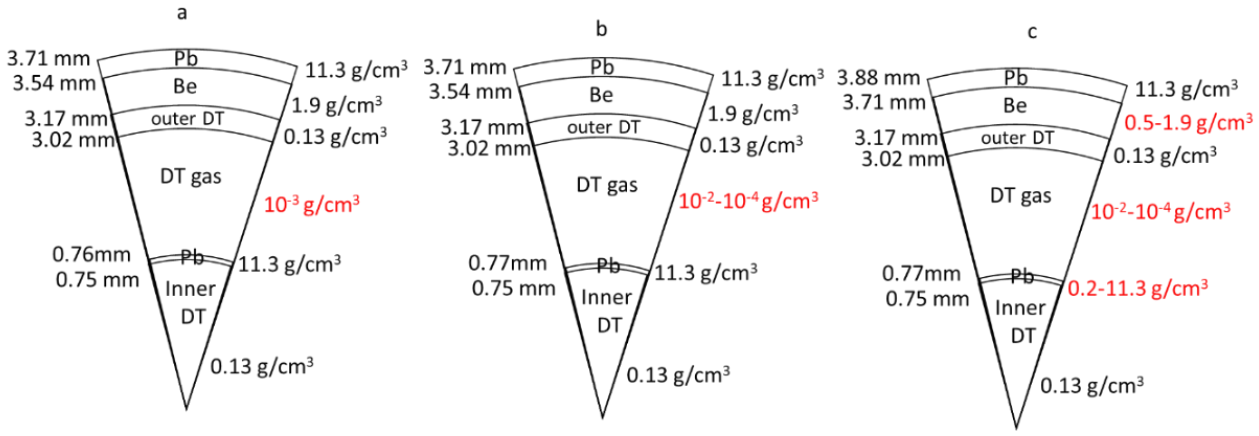

Figure 30: Configuration of target a) without gradient density layers, b) with DT gas gradient density layer, and c) with gradient density layers.

Results and Discussion

a) Density gradient in foam layer

In this section, we want to investigate a non-cryogenic double-shell target driven with heavy ion beams compared to a target with a density gradient in the gas between the shells. In double-shell targets, the outer shell launches a shock wave towards the middle gas, and then the space between the two shells causes the outer shell to accelerate inwards. In these targets due to the gas in the middle, the shells have enough time to collide with each other. Thermonuclear gain is lower in non-cryogenic double-shell target ignitions than in cryogenic single-shell targets [9]. Our simulations on target a in Figure 30 showed that the thermonuclear gain is significantly less than that of the cryogenic fuel case. The cryogenic fuel is solid DT fuel with a density of 0.224 g/cm^3. The energy gain in double-shell cryogenic is 70, while non-cryogenic is 26. It is possible to design double-shell targets that ignite at a lower temperature than the central ignition approach [7]. Target 1-a) was not successful in achieving this condition. The ion temperature of the center cell in the inner fuel at maximum compression was approximately 131 keV, while the average temperature of the cells was approximately 65 keV. The implosion velocity estimate was around 340 km/s, which is not a satisfactory value for double-shell targets. We analyzed the target following Figure 30-b), which has a density gradient in the middle gas layer. The density gradient in the middle gas causes the stored pressure, and with the same input energy, it creates more compression in the inner fuel. Figure 31 shows that a target with a density gradient and a solid line shows more compression than target 1- a).

The thermonuclear energy produced by target 1- b) is higher than target 1- a), as shown in Figure 32. The energy gain for target 1- b) will be around 57 as a result. The increase in target energy gain is a consequence of the mass increase in the middle gas caused by the density gradient. Target 1-a) had a 0.1 middle gas mass while Target 1-b) had a 0.8 middle one. Despite this, the implosion velocity at the pusher-fuel interface remains high at 314 km/s, which we will discuss in the following section.

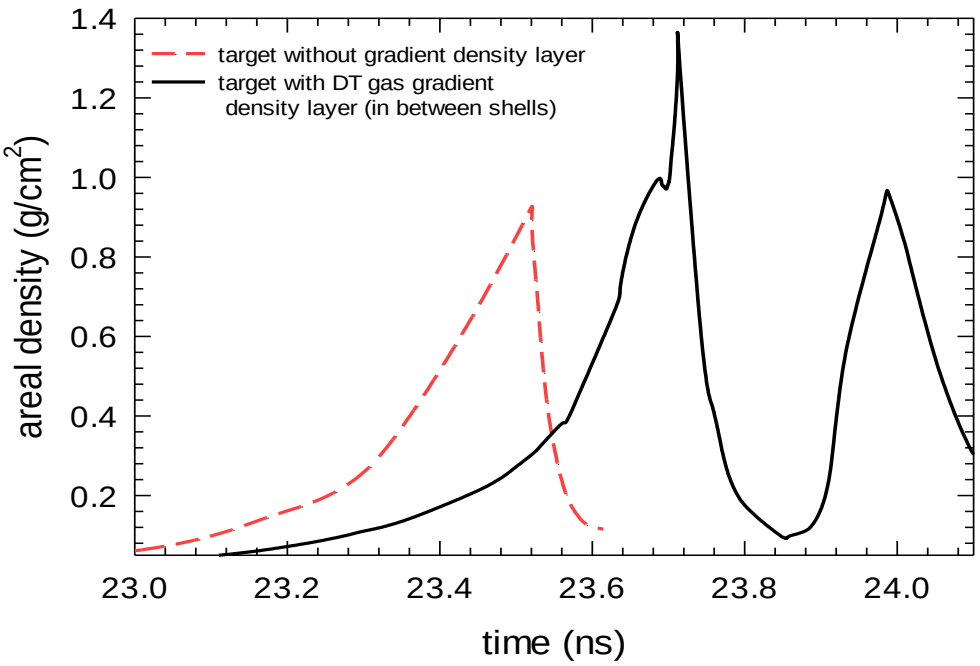

Figure 31: Examining the evolution of the inner fuel areal density over time in target 1-a (dashed line) and target 1-b (solid line).

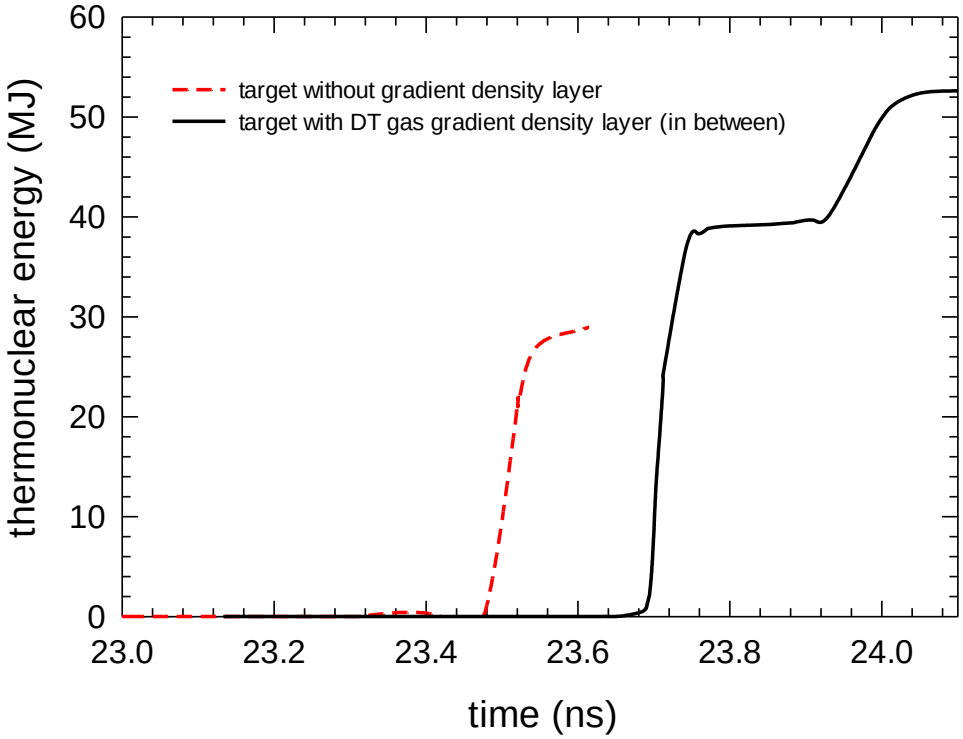

Figure 32: Examining the evolution of the inner fuel thermonuclear energy over time in target 1-a (dashed line) and target 1-b (solid line).

b) Density gradient in inner pusher

Our focus in this section will be on a target that has a density gradient in its layers, which is causing Rayleigh-Taylor instability and decreasing the implosion velocity. Consequently, we ignite the targets in Figure 1. The implosion velocity in target 1-c) is equivalent to 212 km/s. Double-shell laser-driven targets were also estimated to have such a velocity [10]. By using heavy ion beams, we were able to achieve a velocity with a gradient non-cryogenic target for the first time. In addition, the ion temperature for the fuel inner cell is 10 keV, while the other cells are only 3 keV. These results show that we were able to control the temperature and implosion velocity by adjusting the density gradient of the inner shell. The implosion velocity of targets 1-a) and 1-c) is compared in Figure 33, and target 1-c) was found to have better results when there was a density gradient present.

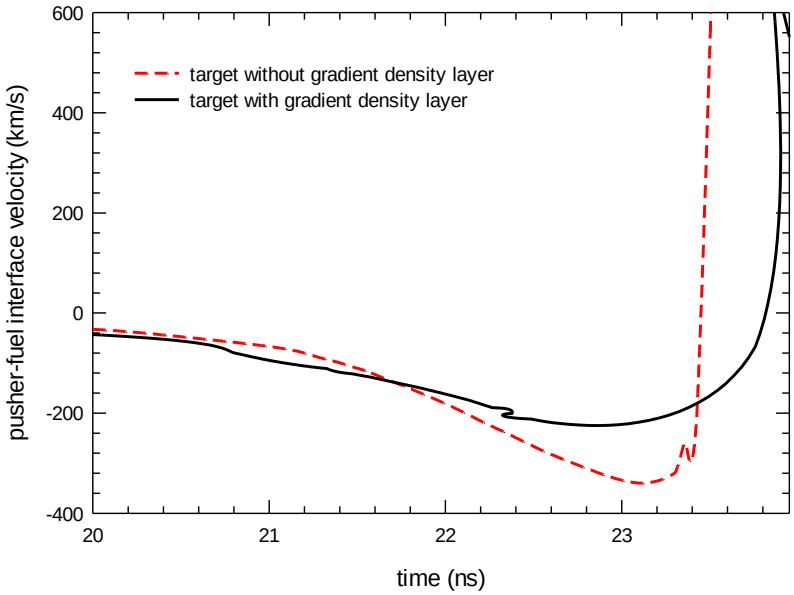

Figure 33: Temporal evolution of the pusher-fuel interface velocity for targets 1-a (dashed line) and 1-c (solid line).

Recently, there has been a study on the hydrodynamic instabilities in multi-shell targets [11]. Rayleigh-Taylor and Richtmyer-Meshkov are two important challenges. The Rayleigh-Taylor instability occurs when a light fluid accelerates into a heavy fluid. On the other hand, the Richtmyer-Meshkov instability is a result of disturbances, like a strong shock, happening at the interface between two fluids. The Richtmyer-Meshkov instability is responsible for the perturbation, while Rayleigh-Taylor sustains it [11].

As previously stated, the density gradient of the inner shell was utilized to minimize the growth of the Rayleigh-Taylor instability. The expression for Rayleigh-Taylor growth is $\sim e^{\gamma}$. According to the growth rate of Rayleigh-Taylor $\gamma = \int A(t) \frac{a(t)}{D(t)} dt$ relationship, the growth of Rayleigh-Taylor instability decreases with increasing thickness D and decreasing the implosion velocity (which is also proportional to the acceleration, a(t)) [6, 11]. Here, A(t) is the Atwood number, $A(t) = \frac{|\rho_1 - \rho_2|}{\rho_1 + \rho_2}$. The thickness of the inner shell of the targets1- a) and target1-c) is shown in Figure 34. According to this Figure, the thickness of the inner pusher in the target with gradient density is higher than in the target without gradient density. The velocity profile in target 1-c) is lower than target 1- a) so the A(t) in the target with gradient density is lower than the other in Figure 33 . By this result, the

instability in target 1- c) during the implosion phase (up to 23 ns), will have a lower value than target 1-a). Therefore, we achieved the control of Rayleigh-Taylor instability in the implosion stage (up to 23 ns) by creating a density gradient in the inner and outer shells.

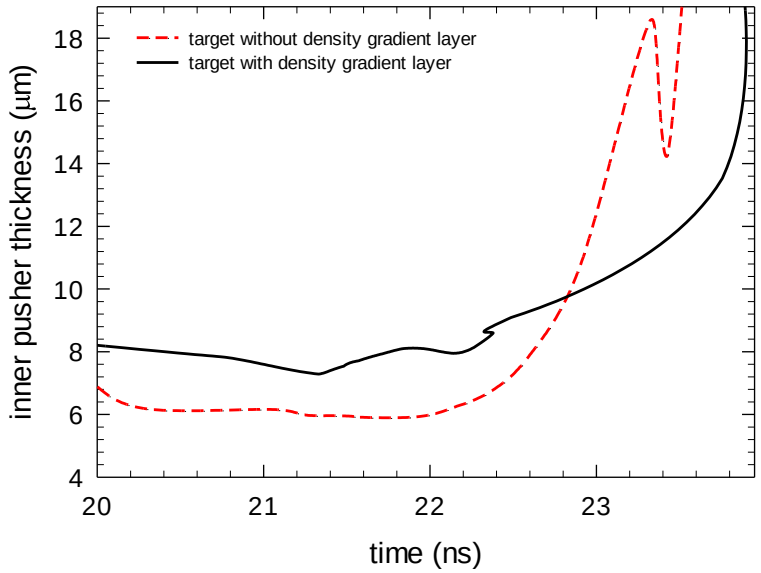

Figure 34: Temporal evolution of the inner pusher thickness for targets 1-a (dashed line) and 1-c (solid line).

Conclusion

Simulations and experiments on double-shell targets driven with laser beams have been carried out in recent years. Heavy ion beams are a drive option for these targets that have not received much attention. Heavy ions were utilized to drive non-cryogenic double-shell targets in this paper. The presence of density gradient in the layers of these targets was investigated. We observed that we can achieve optimal energy gain with less concern for Rayleigh-Taylor instability. The density gradient prevents the preheating of the inner fuel, and by compressing it more at a lower temperature, it causes a higher energy gain than without the density gradient.

References

S. Hu, R. Epstein, W. Theobald, H. Xu, H. Huang, V. Goncharov, S. Regan, P. McKenty, R. Betti, E.M. Campbell, "Direct-drive double-shell implosion: A platform for burning-plasma physics studies", *Physical Review E*, **100** (2019) 063204; DOI: 10.1103/PhysRevE.100.063204.

H. Xu, H. Huang, J. Walker, M. Schoff, F. Elsner, M. Farrell, "Gradient coating for NIF double-shell targets", *Surface and Coatings Technology*, **349** (2018) 838-845; DOI: 10.1016/j.surfcoat.2018.05.080.

N.N. Vazirani, M.J. Grosskopf, D.J. Stark, P.A. Bradley, B.M. Haines, E. Loomis, S.L. England, W.A. Scales, "Coupling 1D xRAGE simulations with machine learning for graded inner shell design optimization in double-shell capsules", *Physics of Plasmas*, **28** (2021) 122709; DOI: 10.1063/5.0063745.

G.A. Kyrala, N. Delamater, D. Wilson, J. Guzik, D. Haynes, M. Gunderson, K. Klare, R.W. Watt, W.M. Wood, W. Varnum, "Direct drive double shell target implosion hydrodynamics on OMEGA", *Laser and Particle Beams*, **23** (2005) 187-192; DOI: 10.1017/S0263034605050330.

M.S. Moreno, N. Tahir, J.L. Cela, A. Piriz, D. Hoffmann, "Heavy ion driven reactor-size double shell inertial fusion targets", *High Energy Density Physics with Intense Ion and Laser Beams*, (2008) 69.

N. Metzler, J. Meyer-Ter-Vehn, "Target study for heavy ion beam fusion", *Laser and Particle Beams*, **2** (1984) 27-48; DOI: 10.1017/S0263034600000604.

P.A. Amendt, H.F. Robey, H.-S. Park, R. Tipton, R. Turner, J. Milovich, M. Bono, R. Hibbard, H. Louis, R. Wallace, "Hohlraum-driven ignitionlike double-shell implosions on the omega laser facility", *Physical review letters*, **94** (2005) 065004; DOI: 10.1103/PhysRevLett.94.065004.

M. Basko, "High gain DT targets for heavy ion beam fusion", *Nuclear fusion*, **32** (1992) 1515; DOI: 10.1088/0029-5515/32/9/I02.

J.D. Lindl, P. Amendt, R.L. Berger, S.G. Glendinning, S.H. Glenzer, S.W. Haan, R.L. Kauffman, O.L. Landen, L.J. Suter, "The physics basis for ignition using indirect-drive targets on the National Ignition Facility", *Physics of plasmas*, **11** (2004) 339-491; DOI: 10.1063/1.1578638.

D. Montgomery, W. Daughton, B. Albright, A. Simakov, D. Wilson, E. Dodd, R. Kirkpatrick, R. Watt, M. Gunderson, E. Loomis, "Design considerations for indirectly driven double shell capsules", *Physics of Plasmas*, **25** (2018) 092706; DOI: 10.1063/1.5042478.

R. Roycroft, J.P. Sauppe, P.A. Bradley, "Double cylinder target design for the study of hydrodynamic instabilities in multi-shell ICF", *Physics of Plasmas*, **29** (2022) 032704; DOI: 10.1063/5.0083190.

ICNST 2024
International Conference on Nuclear Science and Technology
6- 8 MAY 2024 | Isfahan, Iran

Design and Construction of Retarding Field Energy Analyzers for Ion Temperature Measurements in Alborz Tokamak (Paper ID: 1552)

Maryam Askari Shayegan[1], Zahra Khoshniatbayati[1], Samaneh Fazelpour[2*], Reza Amrollahi[1], Hossein Sadeghi[1]

[1] Energy Engineering and Physics Department, Amirkabir University of Technology, P.O. Box 1591634311 Tehran, Iran

[2] Plasma Physics and Nuclear Fusion Research School, Nuclear Science and Technology Research Institute, P.O. Box 14155-1339, Tehran, Iran

Abstract:

The ion temperature or ion energy distribution is a very important parameter of the plasma boundary in nuclear fusion devices which can have great impacts on physical processes such as ablation of surfaces exposed to plasma and the deposition processes transferred by plasma. Measurement of ion temperature in the SOL (Scrape Off Layer) region typically uses a Retarding Field Analyzer (RFA) that is variable according to the selective tract or retard of plasma ions by an electric field. In order to measure the ion temperature of plasma in Alborz tokamak, a retarding field analyzer (RFA) has been used. This analyzer consists of four grids were made of stainless steel-316, insulating pieces between them and a copper collector. To investigation of the probe correct operation in Alborz tokamak chamber. The tests were performed by a glow discharge plasma based on define applied pressure and voltage on anode and cathode, and thus the ion energy distribution function in plasma has been investigated.

Keywords: ion temperature, ion energy distribution, retarding field analyzer, tokamak, SOL plasma, diagnostic.

1. Introduction

Currently, in fusion reactors, plasma is being investigated as a suitable approach to produce large amounts of energy without pollution. Achieving a high quality plasma in which ion particles have appropriate energy distribution is one of the most important issues in tokamaks. Ion energy research is optimally used to identify and understand plasma properly, especially in the scrape of layer (SOL) and plasma edges. e. i, High Field Side (HFS) and Low Field Side (LFS) [1].

The ion energy distribution function in the edge of plasma shows that the sputtering efficiency of the materials on the first wall of the tokamak is depending to 1) the amount of energy of the ion

particles, 2) ion bombardment and unusual interactions in ELMs (edge localized mode) that transfer ions to SOL region [2].

In addition, many industrial applications of plasma require to getting know extensively with the ion energy distribution function (IEDF). Many plasma applications, especially in the field of industrial plasma, for example; Surface modification in semiconductors, deposition of atomic layers and reactive ion etching are dependent on ion flux density and ion energy distribution function.

Retarding potential analyzers (RPA), also called retarding field energy analyzers (RFEA), are commonly used to measure the ion energy and ion temperature.

To date, RFEAs have been used on JET[3,4] , ISTTOK [5], EAST [6], STOR-M [7], ASDEX [1] tokamaks and other plasma device . These types of analyzers do not have very large dimensions; they are very affordable in the field of plasma industrial too [8]. On the other hand, plasma thrusters equipped with RFA are being used to measure ion beam intensity in space missions [9].

Alborz tokamak as a fusion machine with a plasma which its lifetime is about one millisecond needs a set of diagnostics related to measurement of ion characteristics in order to provide the necessary measurements for control, evaluate, optimize the plasma performance and further understand the physics of the plasma in tokamak. In this article, the design and construction of an RFA diagnostic tool to measure the ion energy in Alborz tokamak has been discussed. In theory part, the general process of the operation of this type of diagnostic tool is explained. In the design and construction section, the dimensions of the probe that built are mentioned, and in the experimental setup section, the measurement of ion energy in glow discharge system of Alborz tokamak is discussed.

2. Theory

In tokamaks there is an unconfined region of plasma known as SOL**.** Plasma particles are transferred from plasma core to the inner solid surfaces area of the tokamak, in fact, this layer determines the degree of plasma with surface interaction [10].

RFA is one of the diagnostic device used in plasma production systems to calculate the energy distribution function of plasma ions. Typically, an RFA consists of two or three grids to detect ion energy and suppress secondary electron emission. RFA as a meshed energy analyzer is a diagnostic with biased electrode at different voltages in certain ranges. The voltages are chosen according to density and temperature of the plasma to filter the charged species of plasma in order to determine the characteristics of plasma such as ion density, ion temperature, ion energy distribution and plasma particle velocities**.**

In addition to the ion energy distribution function, the electron energy distribution function (EEDF) can be measured by the analyzer with inverting the grid potential in RFEA [9]. One of the main parameters of plasma that determines the discriminating in design and configuration of components in RFA is the distance that a particle is significantly affected by the electrostatic charge, which is called the Debye length [11]. This distance varies according to the temperature and density of electrons in plasma. Debye length is determined by the temperature T_e and density n_e of electrons in plasma

$$\lambda_d \approx \sqrt{\frac{\varepsilon_0 k_B T_e}{n_e q_e^2}} \qquad (1)$$

Where, k_B is Boltzmann's constant, n_e is electron density, and T_e is the electron temperature. The main issue in designing RFA is the distance between the electrodes and determining the size of the meshes on grid. when the plasma enters to RFA and the ions pass through the grids that are in contact with them [12]. finally, the plasma beam with a high percentage of high-energy ions collide to the detector surface in a range proportional to the voltage applied to third grid. When ions have collision with collector, a series of secondary electrons are created. The current caused by the impact of the ions on the collector is a function of the energy intensity of the ions passing through the third grid, which have been able to overcome the electric field caused by the grids and reach to the surface of collector consequently.

$$I_c(V_d) = -\frac{{Z_i}^2 e^2 n_i A}{m_i} \int_{eV_d}^{\infty} f(E) dE \qquad (2)$$

$$\frac{dI_c}{dV} = -\frac{{Z_i}^2 e^2 n_i A}{m_i} f(E) \qquad (3)$$

$$\frac{dI_c}{dV} \propto -f(E) \qquad (4)$$

The changes of the collector current in terms of the third grid voltage are proportional to factors such as: the surface of the collector that is in contact with the ion beam in plasma(A), the ion density of the plasma(n_i), and the mass of the ion particles(m_i). The most effective factor in changing the current of collector in terms of ion voltage is related to the ion charge ($z_i^2 e^2$) [13]. The flow of incident and secondary electrons caused by the collision of high-energy ions to the collector are measured as collector current, and the graph of changing in collector current according to the changes of the third grid voltage [10].

3. Design and Construction

In this study, a four-grid RFA designed and constructed. This diagnostic has been used to measure the ions energy of glow discharge plasma in Alborz tokamak. Alborz tokamak is a D-shaped cross-section machine with major radius of 0.45 m, minor radius of 0.15 m and toroidal magnetic field of 0.85 T by 16 magnetic coils to achieve a 20 kA plasma current. It is one of the small tokamaks and the first tokamak that was built by Iranian researchers which is located in Amirkabir University now. Figure (1) shows a view of Alborz tokamak.

Figure 1: View of Alborz Tokamak

In order to achieve the energy distribution function of plasma ions has been implemented a four-electrode RFA arrangement, the potential applied to the grids from the outermost to the innermost electrode successively is floating potential, negative voltage, positive voltage and negative voltage. In addition, the collector is connected to a current measurement circuit outside the vacuum chamber.

The first electrode is connected in such a way that the first grid is connected to a floating potential with the aim of reducing plasma disturbances. A constant negative voltage is applied to the second grid, which is a defensive of electrons from the plasma. In order to filter the ions of plasma based on their energy, a positive voltage is applied to the third grid so that the ions with high energy that are able to pass through the electric field caused by the applied voltage to this grid will pass through it. Finally, a negative voltage is applied to the innermost grid, which is on the path after the third grid, it causes the electrons to be repelled from the plasma.

So that the percentage of ions with high energy in the plasma that reaches the collector after passing through four grids be higher than the percentage of electron [5]. In figure (2), the schematic of the four-grids RFA probe is shown.

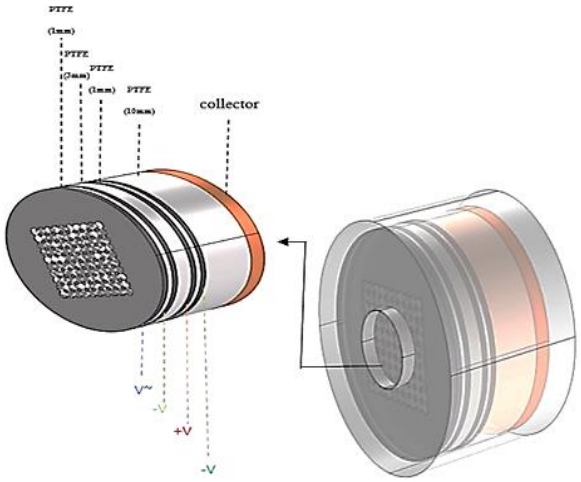

Figure 2: Schematic of four-grids RFA probe.

the designs reported in this study implement the standard RFA arrangement of four parallel electrodes based on retarding field are placed in such a way that charged particles enter the chamber through a hole. they are analyzed pursuant to retard has been created by electric field

through the bias potentials applied to the grids. the RFA designs described in this study that the inlet hole must be wide enough to allow transfer sufficient flux from the plasma of tokamak. Besides, the hole should be small enough so that the electrostatic sheath created around the edges of the gap is large enough to fill the width of the aperture and protect the diaphragm from huge volume of plasma.

A cylindrical stainless steel -316 housing with a diameter of 13.5 mm. there is a hole at the end of the cup that the length of its edge is about 80 mm. Inside this cup, a cylindrical insulation made of polytetrafluoroethylene (PTFE) with dimensions of 50 ×65 mm is used. Inside the housing, four circular mesh plates with a diameter of 40 mm. The electrodes are insulated from each other by PTFE plates with different thicknesses. The copper collector with diameter of 40 mm and thickness of 3 mm is placed. In figure (3), a view of constructed RFA probe is shown**.**

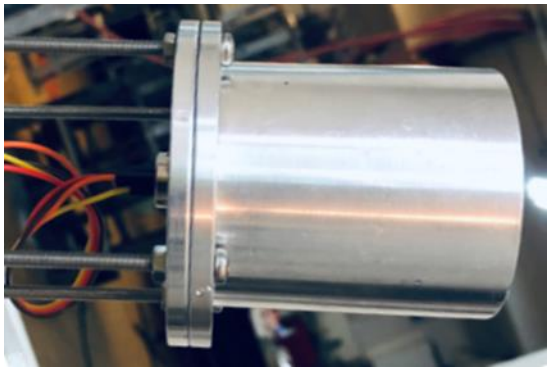

Figure 3: a view of constructed RFA probe

4. Experimental Setup

To create a glow discharge inside Alborz tokamak, a steel electrode with a radius of 1 cm and a height of 5.5 cm is embedded on one of Alborz tokamak `s valves. By connecting this electrode to the body of the plasma vacuum chamber, the electrode will act as the anode and the vacuum chamber will play the role of cathode. An electric discharge will be formed between these two electrodes by connecting the power supply. Experiments have been performed with glow discharge plasma at pressure of 2.1 x 10^{-1} Torr. Argon is working gas, in which the discharge is produced at voltage of 500 volts at the stated pressure. In Figure 4, a view of the glow discharge plasma formed in Alborz tokamak is shown. In Figure 5, the measured current from the collector is shown in terms of voltage applied to the positive grid.

Figure 4: a view of glow discharge plasma formed in the Alborz tokamak

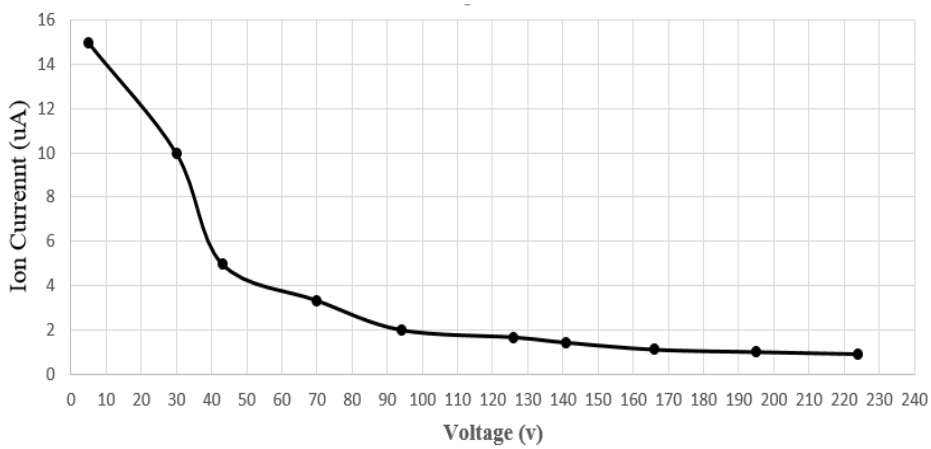

Figure 5: the measured current from the collector in terms of voltage applied to the positive grid

The diagram above is based on the measured current from the collector and the voltage applied to the positive grid. According to the diagram, the temperature of the ion in the voltage range of 0 to 30 Volt is equal to 8-10 electron volts. as reported by experiments, as much as the applied potential on the electrodes to ionize the gas in the chamber increases, the maximum measured current increases and the temperature of the ion also increases.

In the case of RFA sweeping, we can calculate the ion temperature for every half-period of the RFA grid voltage sweep. The ion temperature now can be described by I–V characteristics. The results obtained by the probe were compared with the results of the Langmuir probe and the correctness of these results was confirmed.

5. Conclusion

The ion temperature in the edge of a tokamak is a very important parameter to analyze the plasma interaction with the first wall materials. RFA is designed and constructed as a diagnostic tool for measuring ion energy. This probe was installed in Alborz tokamak and it was used to estimate the ion energy of the glow discharge plasma in tokamak. The ion energy of glow discharge plasma in Alborz tokamak was evaluated at certain pressure and voltage.

References

[1] Ochoukov, R., Dreval, M., Bobkov, V., Faugel, H., Herrmann, A., Kammerloher, L., Leitenstern, P., Team, A. U., & Team, E. M. (2020). Ion temperature measurement techniques using fast sweeping retarding field analyzer (RFA) in strongly intermittent ASDEX Upgrade tokamak plasmas. Review of Scientific Instruments, 9.(6)

[2] Takahashi, H., Seino, T., Nishimura, R., Yoshimura, K., Kanno, A., Hara, T., Takahashi, Y., Kagaya, S., Matsuyama, A., & Hayashi, Y. (2023). Impact of selective ion transmission on measurement by retarding field analyzer. Physics of Plasmas, 30. (5)

[3] Guo, H., Matthews, G., Davies, S., Erents, S., Horton, L., Monk, R., & Stangeby, P. (1996). Ion temperature measurements in JET boundary plasmas using a retarding field analyser. Contributions to Plasma Physics, 36(S1), 81-86.

[4] Pitts, R., Chavan, R., Davies, S., Erents, S., Kaveney, G., Matthews, G., Neill, G., Vince, J., contributors, J.-E. w., & Duran, I. (2003). Retarding field energy analyzer for the JET plasma boundary. Review of scientific instruments, 74(11), 4644-4657.

[5] Nedzelskiy, I., Silva, C., Figueiredo, H., Fernandes, H., & Varandas, C. (2006). Compact retarding field energy analyzer for the tokamak ISTTOK boundary plasma. Review of scientific instruments, 77(10).

[6] Li, Y., Xu, G., Xiao, C., Wang, H., Yan, N., Wan, B., Chen, L., Liu, Y., Zhang, H., & Zhang, W. (2016). Retarding field analyzer for the EAST plasma boundary. Review of scientific instruments, 87(12).

[7] Dreval, M., Rohraff, D., Xiao, C., & Hirose, A. (2009). Retarding field energy analyzer for the Saskatchewan Torus–Modified plasma boundary. Review of scientific instruments, 80(10).

[8] Henkel, M., Li, Y., Liang, Y., Drews, P., Knieps, A., Killer, C., Nicolai, D., Hoeschen, D., Geiger, J., & Xiao, C. (2020). Retarding field analyzer for the wendelstein 7-X boundary plasma. Fusion engineering and design, 157, 111623.

[9] Izquierdo-Reyes, J., Bigelow, Z., Lubinsky, N. K., & Velásquez-García, L. F. (2022). Compact retarding potential analyzers enabled by glass-ceramic vat polymerization for CubeSat and laboratory plasma diagnostics. Additive Manufacturing, 58, 103034.

[10] Batishchev, O., Krasheninnikov, S., Catto, P. J., Batishcheva, A., Sigmar, D., Xu, X., Byers, J., Rognlien, T., Cohen, R., & Shoucri, M. (1997). Kinetic effects in tokamak scrape-off layer plasmas. Physics of Plasmas, 4(5), 1672-1680.

[11] Chen, F. F. (1984). Introduction to plasma physics and controlled fusion (Vol. 1). Springer.

[12] Ferda, B. (2015). Retarding potential analyzer theory and design. Princeton University, 18.

[13] Heubel, E., & Velásquez-García, L. (2013). Batch-fabricated MEMS retarding potential analyzer for high-accuracy ion energy measurements. 2013 IEEE 26th International Conference on Micro Electro Mechanical Systems (MEMS),

2D PIC simulation of electron acceleration in interaction of a proton beam with a plasma containing a small step density (Paper ID: 1575)

[1]*Plasma and Fusion Research School, Nuclear and Science Technology Research Institute, Tehran, Iran*
[2]*Department of Physics, Faculty of Sciences, Gonbad Kavous University, Gonbad Kavous, Iran*

Abstract

In this paper, using two-dimensional PIC simulation, the acceleration of the injected electron beam and the evolution of the excited plasma wave in the interaction of a high-energy proton beam with an underdense plasma having a small step density along its uniform density have been investigated. The simulation results indicate that in the proton beam-plasma interaction system with considered optimum parameters, in the presence of a small step density along the uniform plasma, the excited electric field corresponding to the plasma wave remains stable for longer distances and its amplitude increases up to 280 MeV/m in a short time and distance. Moreover, it turns out that the electron beam that enters the plasma containing a step small density, at a distance about one plasma wavelength behind the proton beam, can gain energy from the generated stable plasma wave field for longer times and reach high acceleration gradients while maintaining its emittance appreciably.

Keywords: 2D PIC Simulation, Small step density, Intense proton beam, Beam emittance, Acceleration gradient.

Introduction

In plasma accelerators, the main factor for particle acceleration is a large-amplitude plasma wave excited in the plasma. Large-amplitude plasma waves are usually excited by injecting a short and intense laser pulse or a high-energy particle beam into the plasma. Recent research shows that the proton beams are the most promising driver for exciting the plasma fields for one-step acceleration of electrons [1-2]. In this method, the high-energy proton beam is propagated in the plasma and creates a strong plasma wave, and in this process, the energy of the particle beam is transferred to the plasma through the excited plasma wave. A part of this energy can be used to accelerate an electron beam known as a witness beam which has much lower energy than the proton beam, and thus the high-energy electron beams are produced [3].

The mechanism of the particle acceleration in plasma is known as LWFA [4] for laser drivers and PWFA [5] for particle beam drivers. For both techniques, the amount of effective energy for the

acceleration is determined by the energy of the driving beam and the gain of energy transfer from the beam to the electron beam. To effectively create a plasma wave by a particle beam, the length of the driving particle beam, ∂_z, must be such that $k_p \partial_z \cong \sqrt{2}$ where k_p is the electron plasma wave number [6]. The size of the transverse spot of the particle beam, ∂_r, should also be such as $k_p \partial_r \leq 1$ to prevent filamentation instability [7].

In recent years, the interaction of the proton beam with plasma has been widely studied. The results of the research in this field show that in the electron acceleration system by plasma wave, the appropriate choice of the plasma parameters and accelerator proton beam is important. In reference [8], plasma parameters have been investigated to achieve energies in the order of Giga-electron volts. Also, it has been shown in various research experimentally and theoretically [9-11] that it is important to select a suitable profile for the plasma density to achieve a stable plasma wave field.

In this paper, the spatiotemporal propagation of the plasma wave and its corresponding electric field due to the high-energy proton beam propagation in an underdense plasma with a uniform density, with a small step density along it, is studied by two-dimensional PIC (Particle-In-Cell) simulation method. The results illustrate that in the proton-plasma beam interaction system, considering the appropriate parameters for the plasma and also for the driver and witness beams, an electron beam of several Mega-electron volts can be accelerated up to the order of several hundred Mega-electron volts by the excited strong plasma fields. Meanwhile, the emittance of the electron beam which is one of the most important criteria for measuring the accelerated beam quality is considerably maintained during the propagation. The paper is organized as follows: in section 2, we introduce the simulation method and considered simulation parameters. In section 3, the simulation results are presented and discussed. Finally, section 4 is devoted to the summary and conclusion

Two-Dimensional Pic Simulation

In this article, the FBPIC simulation code [12] is used. This code is a precise two-dimensional PIC simulation code in cylindrical coordinates, which is very suitable for simulating systems with symmetry, including the particle-plasma beam interaction systems. To simulate the considered

system using a two-dimensional FBPIC simulation code, the plasma with density $2.6 \times 10^{20}\ m^{-3}$ is assumed to have a uniform density profile with length $20mm$ that has a small density gradient as $\delta n / n = 0.03$ along its profile. Also, 12 proton micro bunches with the shape of Gaussian profile with characteristics as $\partial_z = 0.4/k_p$, $\partial_r = 0.4/k_p$ and $N_P = 2.5 \times 10^8$ are considered as the driver beam. The witness electron beam is also considered with Gaussian profile with characteristics $\partial_z = 60\mu m$ and $\partial_r = 10\mu m$. Moreover, the dimensions of the simulation box in the direction of z and r are $60mm$ and $1mm$, respectively. Also, the time and distance steps are respectively considered as $0.05\mu m$ and $0.2fs$.

In general, in the PIC simulation technique, the density of particles on the grid is calculated by the weighting method. Then, the electric field is obtained by solving the Poisson equation on the grid points. The electric field of the network is calculated by interpolation at the location of the particles. After that, the new position and velocity of the particles are calculated using the relativistic Newton-Lorentz equations. In this procedure, each particle moves according to the Lorentz force applied by the electromagnetic fields in the position of the particle,

$$\vec{F} = q(\vec{E} + \frac{\vec{v}}{c} \times \vec{B}) \qquad (1)$$

The evolution of the electromagnetic fields is done according to Maxwell's equations [13],

$$\vec{\nabla}.\vec{E} = 4\pi\rho \qquad (2)$$

$$\vec{\nabla} \times \vec{B} = \frac{1}{c}\frac{\partial \vec{E}}{\partial t} + \frac{4\pi}{c}\vec{j} \qquad (3)$$

$$-\vec{\nabla} \times \vec{E} = \frac{1}{c}\frac{\partial \vec{B}}{\partial t} \qquad (4)$$

$$\vec{\nabla}.\vec{B} = 0 \qquad (5)$$

$$\vec{j}(\vec{x}) = \sum_{i=1}^{N} q_i v_i \delta(\vec{x} - \vec{x}_i) \qquad (6)$$

$$\rho(\vec{x}) = \sum_{i=1}^{N} q_i \delta(\vec{x} - \vec{x}_i) \qquad (7)$$

Result and Discussion

Considering the specifications mentioned in the previous section, the high-energy proton beam is sent into the uniform plasma. A plasma wave is formed by the repulsion of plasma electrons and disturbance in the plasma background. The witness electron beam also enters the plasma at a distance of one plasma wavelength behind the driver proton beam. Figures 1(a) and 1(b) show the electric field of the plasma wave in a plasma with a small step density $\delta n / n = 0.03$ at times $t = 26\text{ps}$ and $t = 67\text{ps}$, respectively. As can be seen, the amplitude of the excited plasma wave field increases with time and in longer time ($t = 67\text{ps}$) its amplitude is approximately about $280Mev / m$. The small step density in the uniform plasma profile causes the generated plasma wakefield remain stable for longer distances.

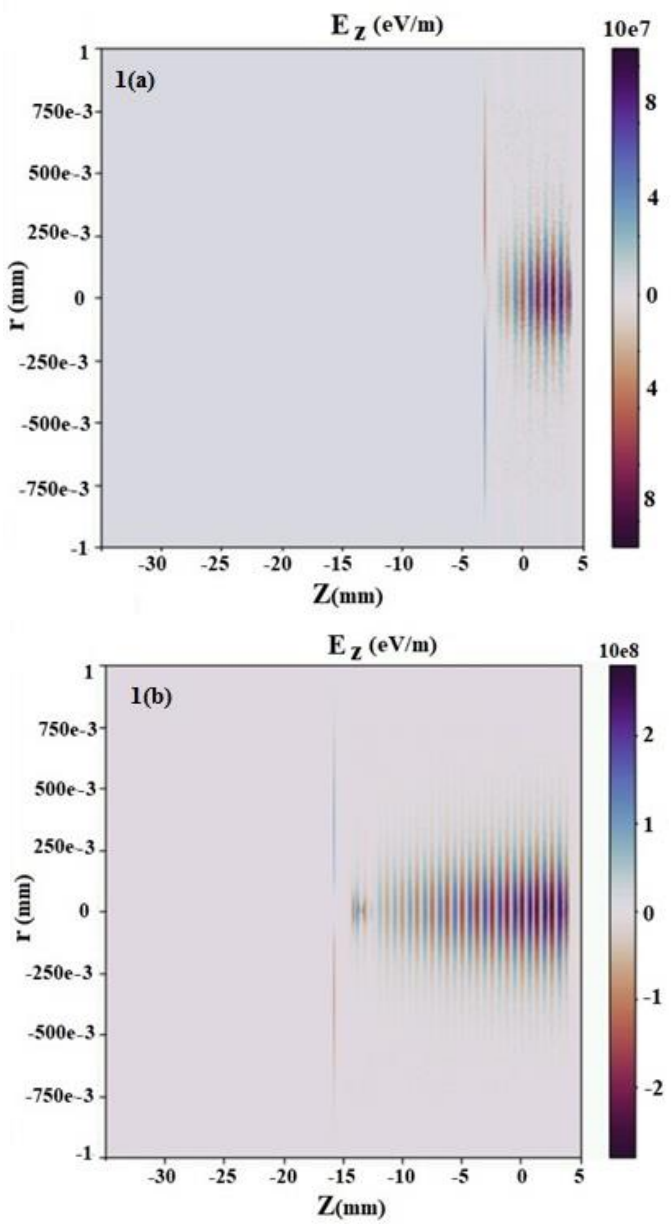

Figure1. Evolution of the plasma wave field in a plasma with $\delta n / n = 0.03$ at time (a) t=26ps and (b) t=67ps.

Figures 2(a) and 2(b) also show the electric field corresponding to the plasma wave in a plasma without taking into account the small step density ($\delta n / n = 0$) at times $t = 26\text{ps}$ and $t = 67\text{ps}$, respectively. By comparison of the plasma wave amplitudes in Fig. 1 and Fig.2, one can see that in the short time ($t = 26\text{ps}$) the plasma field amplitude in both plasmas is almost the same, but by increasing the time, the field amplitude in the plasma with a small step density has increased more

than the plasma with a completely uniform density. Moreover, in absence of a small step density in the plasma profile, the field stability starts to be reduced with time during the propagation in the plasma.

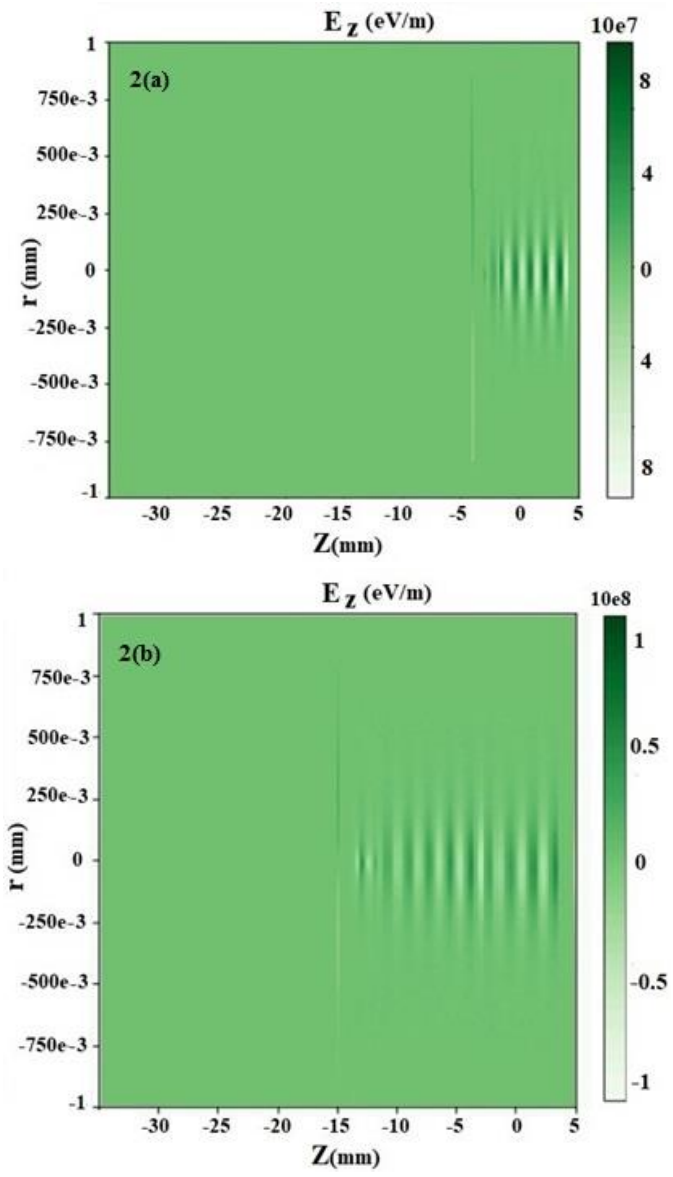

Figure2. Evolution of the plasma wave field in a plasma with $\delta n / n = 0$ at time (a) t=26ps and (b) t=67ps.

The reason for this behavior is that in the interaction of the beam of energetic particles with the plasma, by increasing the time, due to the beam energy reduction as well as the appearance of the nonlinear and relativistic phenomena in the system which causes the increment of the wavelength and reduction of the phase velocity of the excited plasma wave, the electric field corresponding to

the excited plasma wave becomes unstable and its amplitude starts to decrease. By creating a small change in the plasma density, the phase velocity of the plasma wave and its wavelength change, and therefore this leads to the stability of the field and the increase of its amplitude. In such a system, the witness electron beam that enters the plasma behind the driving ion beam can be trapped in the plasma wave field for longer distances and get energy from the stable plasma wave field for more times.

In the system of plasma wave excitation by the particle beams unlike the laser-driven plasma wave generation system, the phase velocity of the excited plasma wave is not equal to the driver group velocity. In beam-plasma interaction system, the wave phase velocity decreases over time and there is a considerable difference between the beam velocity and the wave phase velocity which increases by propagating through the plasma [10]. Here, the final excited plasma wave amplitude enhances by superposition of the waves excited by the proton micro bunches train propagating in the plasma. Therefore, with the decrease in the wave phase velocity, the constructive superposition does not happen, and the wave amplitude decreases over time, and the wave damping eventually occurs. On the other hand, in addition to decreasing the phase velocity, the plasma wavelength increases during propagation due to the nonlinear and relativistic effects, and the wavelength of the excited wave which is in the order of the plasma wavelength changes and finally it leads to a wave with a weak amplitude. In the presence of a small step density, in fact, an increase in density leads to a decrease in the plasma wavelength and an increase in the phase speed, and in longer times, the wave amplitude is amplified and remains stable.

One of the important criteria in measuring the quality of the accelerated electron beam is the emittance (ε) of the electron beam. The emittance of a beam is a criterion of the energy dispersion and spatial distribution of the particles in the beam. The smallness of the emittance value means that the dispersion is less. Also, the beam luminance ($B = I/\lambda\varepsilon$) increases by decreasing the emittance. The components of the transverse emittance ($\varepsilon_x, \varepsilon_y$) are given by

$$\varepsilon_x = \sqrt{\overline{(x-\overline{x})^2}\,\overline{(x'-\overline{x}')^2} - [\overline{(x-\overline{x})(x'-\overline{x}')}]^2} \qquad (8)$$

$$\varepsilon_y = \sqrt{\overline{(y-\overline{y})^2}\,\overline{(y'-\overline{y}')^2} - [\overline{(y-\overline{y})(y'-\overline{y}')}]^2} \qquad (9)$$

where x and x' are the position and angle of the particles [14]. In these furmulas $\bar{x}$ is the average of x-coordinate of all particles of the electron beam and $x' = dx/dz = \beta_x/\beta_z$. $\bar{x}'$ is also the average of x'-coordinate of all particles of the electron beam.

Here, in Figures 3(a) and 3(b), the temporal evolution of the transverse spatial distribution of the accelerated electron beam particles in the interaction of the high-energy proton beam with the plasma containing a small step density along its uniform profile has been indicated in times $t = 26\text{ps}$ and $t = 67\text{ps}$, respectively. The calculated emittance value is written on the figures. As it can be seen, with the increasing time, the electron beam emittance remains appreciably constant in the considered system.

Figures 3(c) and 3(d) illustrate the temporal evolution of the transverse spatial distribution of the accelerated electron beam particles in the plasma with uniform profile in times $t = 26\text{ps}$ and $t = 67\text{ps}$, respectively. As seen, in the presence of the small step density, the emittance of electron beam is more preserved in comparison with the uniform plasma.

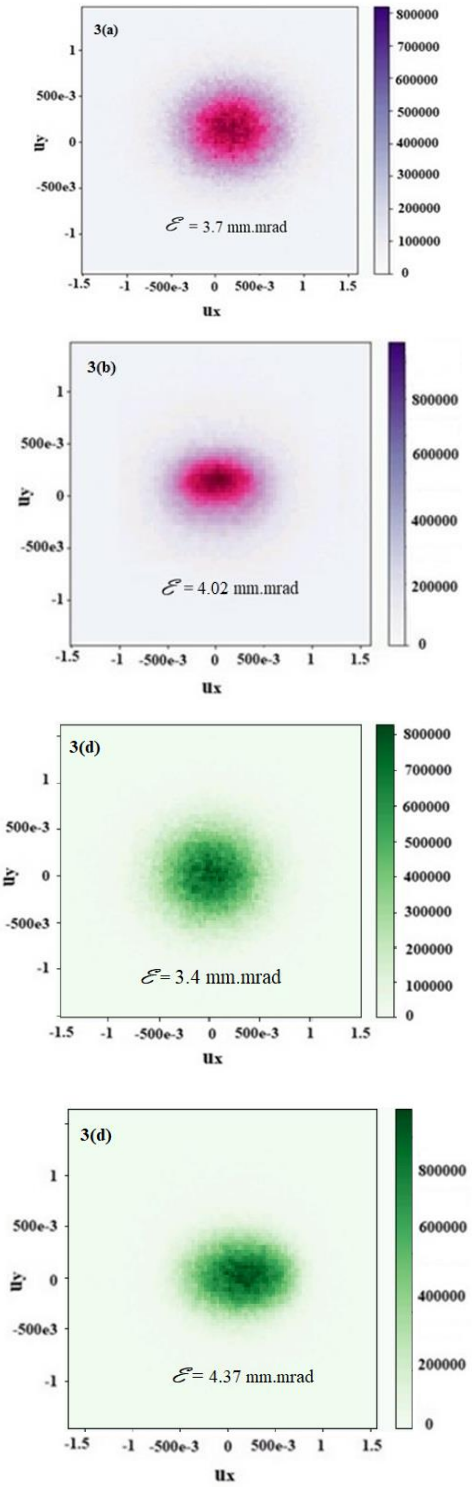

Figure 3. Evolution of the transverse emittance of the electron beam in a plasma with $\delta n / n = 0.03$ at time (a) t=26ps and (b) t=67ps and in a uniform plasma at time (c) t=26ps and (d) t=67ps.

In general, the accelerated electron beam tends to diverge and as a result, the emittance increases. One of the ways to preserve beam emittance is to control the forces acting on the beam. The focusing forces in the plasma can be changed by changing the plasma density. In the presence of a small step density, the plasma density is smoothly increased and the focusing forces on the accelerated beam increase slowly, and finally the emittance can be maintained to an acceptable level.

Conclusions

In summary, in this paper, the evolution of the plasma wave in the interaction of a high-intensity proton beam with a uniform underdense plasma that has a small step density along its profile density, using the two-dimensional PIC simulation method has been investigated. The simulation results show that when the energetic proton beam passes through the plasma, a plasma wave is created and the electric field corresponding to this wave increases with time. Furthermore, in the presence of a small step density along the plasma, the electric field corresponding to the plasma wave maintains its stability for longer times and the field amplitude increases more. In this system, the witness electron beam, which is sent into the plasma behind the proton beam, is trapped in the created plasma wave field and can accelerate to energies of several hundred Mega-electron volts while maintaining its emittance.

References

[1] A. Caldwell, K. Lotov, Alexander Pukhov, and F. Simon, Proton-driven plasma-wakefield acceleration; Nature Physics 5 (2009) 363-367.

[2] R. Assmann, R. Bingham, T. Bohl, C. Bracco, B. Buttenschön, A. Butterworth, A. Caldwell et al, Proton-driven plasma wakefield acceleration: a path to the future of high-energy particle physics; Plasma Physics and Controlled Fusion 56 (2014) 084013.

[3] K. V. Lotov, A. P. Sosedkin, A. V. Petrenko, Lígia Diana Amorim, Jorge Vieira, R. A. Fonseca, L. O. Silva, E. Gschwendtner, and P. Muggli, Electron trapping and acceleration by the plasma wakefield of a self-modulating proton beam; Physics of Plasmas 21 (2014) 123116.

[4] A. Pukhov, J. Meyer-ter-Vehn, Laser wake field acceleration: the highly non-linear broken-wave regime; Applied Physics B 74 (2002) 355-361.

[5] C. Joshi, E. Adli, W. An, C. E. Clayton, Sebastian Corde, S. Gessner, M. J. Hogan et al. Plasma wakefield acceleration experiments at FACET II; Plasma Physics and Controlled Fusion 60 (2018) 034001.

[6] W. Lu, C. Huang, M. M. Zhou, W. B. Mori, and T. Katsouleas, Limits of linear plasma wakefield theory for electron or positron beams; Physics of plasmas 12 (2005) 063101.

[7] B. Allen, V. Yakimenko, M. Babzien, M. Fedurin, Karl Kusche, and P. Muggli, Experimental study of current filamentation instability; Physical review letters 109 (2012) 185007.

[8] G. Plyushchev, R. Kersevan, A. Petrenko, and P. Muggli, A rubidium vapor source for a plasma source for AWAKE; Journal of Physics D: Applied Physics 51 (2017) 025203.

[9] F. Braunmüller, T. Nechaeva, E. Adli, R. Agnello, M. Aladi, Y. Andrebe, O. Apsimon, R. Apsimon, A.M. Bachmann, M.A. Baistrukov, F. Batsch, Proton bunch self-modulation in plasma with density gradient; Physical review letters, 125 (2020.) 264801.

[10] A. Pukhov, N. Kumar, T. Tückmantel, A. Upadhyay, K. Lotov, P. Muggli, V. Khudik, C. Siemon, and G. Shvets, Phase velocity and particle injection in a self-modulated proton-driven plasma wakefield accelerator; Physical review letters 107 (2011) 145003.

[11] A. Caldwell, E. Adli, L. Amorim, R. Apsimon, T. Argyropoulos, R. Assmann, A.M.Bachmann, F. Batsch, J. Bauche, V.B. Olsen, and M. Bernardini, Path to AWAKE: Evolution of the concept; Nuclear Instruments and Methods in Physics Research Section A: Accelerators, Spectrometers, Detectors and Associated Equipment 829 (2016) 3-16.

[12] R. Lehe, M. Kirchen, S. Jalas, K. Peters, and I. Dornmair. Fourier-Bessel Particle-In-Cell (FBPIC) v0. 1.0. No. FBPIC; Lawrence Berkeley National Lab. (LBNL), Berkeley, CA (United States) (2017).

[13] R. W. Hockney, J. W. Eastwood, Computer simulation using particles; crc Press (2021).

[14] S. Peggs; T. Satogata, Introduction to accelerator dynamics. Cambridge, United Kingdom. ISBN 978-1-316-45930-0. OCLC 1000434866.

ICNST 2024
International Conference on Nuclear Science and Technology
6- 8 MAY 2024 | Isfahan, Iran

Collisionnal Current Filamentation Instability of Diluted Electron Beam in Ionosphere Layers (Paper ID: 1576)

Tajiknezhad S.[1], Kargarian A.[2]

[1]*Department of Physics, Faculty of Sciences, Gonbad Kavous University, Gonbad Kavous, Iran*

[2]*Plasma and Fusion Research School, Nuclear and Science Technology Research Institute, Tehran, Iran*

Abstract

The ionosphere is a region of Earth's upper atmosphere, which is composed of a plasma consist of positively charged ions, negatively charged electrons, and neutral particles. Due to the complex interplay between various physical processes, such as solar winds, lightning discharges, radio waves, and high-energy particles, the ionosphere is susceptible to a wide range of plasma instabilities that can cause fluctuations in density, temperature, and electric field. Therefore, to understand the behavior of the ionosphere and improve the performance of radio communication and navigation systems, it is essential to investigate the various plasma instabilities that occur in this region.

The current filamentation instability is one of the important instabilities in the ionosphere which plays a significant role in the amplification of magnetic fields in the ionosphere, particularly when a solar wind electron beam encounters a weakly ionized plasma. In this paper, the current filamentation instability of the interaction of an electron beam with different layers of the ionosphere and the growth rate of instability has been investigated. By solving the fluid description in the presence of binary collision terms between charged and neutral particles and using the local approximation method, the dispersion relation of unstable mode has been obtained and the effect of magnetic field driven-destabilization and current-driven stabilization on the growth rate of instability has been studied. Results show the magnetic threshold for the current filamentation instability in the collisional magnetized ionosphere, in which the instability will disappear for a larger magnetic field than one. Studies show that the value of the magnetic threshold increases by increasing electron beam current density. These results could be important in the explanation of many phenomena that happened in the ionosphere.

Keywords: Current Filamentation Instability, Magnetic Field, Weakly Ionized Plasma

Introduction

The ionosphere is a region of Earth's upper atmosphere, which is composed of a plasma consisting of positively charged ions, negatively charged electrons, and neutral particles [1]. This region of the atmosphere which extends from about 60 kilometers to over 1,000 kilometers from the Earth's surface, plays a critical role in radio communications and navigation systems, and its conditions can have significant effects on satellite positioning systems, radio antennas, and radar systems. Due to the complex interplay between various physical processes, such as solar winds, lightning discharges, radio waves, and high-energy particles, the ionosphere is susceptible to a wide range of plasma instabilities that can cause fluctuations in its density, temperature, and electric field. Therefore, to understand the behavior of the ionosphere and improve the performance of radio communication and navigation systems, it is essential to investigate the various plasma instabilities that occur in this region [2-5].

One such important instability of the ionosphere is the current filamentation instability, which is a type of current-driven plasma instability that usually occurs in the F region of the ionosphere. When an electron beam penetrates a plasma, provided that the electron current is much higher than Alfven limiting current, a return current is produced to neutralize the beam current, leading to various current instabilities in the beam-plasma system [6-13]. Current filamentation instability (CFI), which is excited by transverse perturbations perpendicular to the electron beam, a magnetic repulsion between the two oppositely directed currents tends to reinforce the initial transverse perturbation and consequently, a magnetic field is produced and grows exponentially in time. The current filamentation instability plays a significant role in the amplification of magnetic fields in the ionosphere, particularly when a solar wind electron beam encounters a weakly ionized plasma. Therefore, the behavior of this instability under different conditions in the ionosphere has been considered in recent years [14-16].

In this paper, the current filamentation instability of the interaction of a diluted electron beam with the F region of the ionosphere and the growth rate of instability has been investigated. By solving the fluid description in the presence of binary collision terms between charged and neutral particles and using the local approximation method, the dispersion relation (DR) of unstable mode has been

obtained and the effect of magnetic field driven-destabilization and current-driven stabilization on the growth rate of instability has been studied.

Model Description

We consider a long and warm diluted electron beam with density n_{eb}^0 and non-relativistic velocity V_{eb}^0 in the *x* direction passing through weakly ionized plasma region of the ionosphere in the presence of an external magnetic field $\vec{B}_0 = B_0 x$ with cyclotron frequency $\omega_c = eB_0/cm_e$. Adopting the multi-fluid approach as well as considering the beam temperature and collisional effects, the time evolution of system can be investigated by the continuity, momentum, and Maxwell equations, (for simplicity, hereafter on, we used the subscripts *b*, *e*, *i*, and *n* for beam, electron plasma, ion plasma, and neutral background respectively.)

$$\frac{\partial}{\partial t} n_{j,n} + \nabla.\left(n_{j,n}\vec{V}_{j,n}\right) = 0, \qquad (j=b, e, i) \tag{1}$$

$$m_j n_j \left(\frac{\partial}{\partial t} + \vec{V}_j .\nabla\right)\vec{V}_j = q_j n_j \left[\vec{E} + \frac{\vec{V}_j \times (\vec{B}+\vec{B}_0)}{C}\right] - \nabla P_j - \nu_{jn}\, m_j n_j \left(\vec{V}_j - \vec{V}_n\right), \tag{2}$$

$$m_n n_n \left(\frac{\partial}{\partial t} + \vec{V}_n.\nabla\right)\vec{V}_n = -\nabla P_n - \sum_j \nu_{nj}\, m_n n_n \left(\vec{V}_n - \vec{V}_j\right), \tag{3}$$

$$\nabla \times \vec{E} = -\frac{\partial}{\partial t}\vec{B}, \tag{4}$$

$$\nabla \times \vec{B} = \frac{4\pi}{c}\vec{J} + \frac{1}{c}\frac{\partial}{\partial t}\vec{E}, \tag{5}$$

In Eqs. (1)-(5), q_j is the charge of species *j*, *c* is the speed of light in vacuum, and $m_{j,n}$, $n_{j,n}$, $P_{j,n}$, $\vec{V}_{j,n}$ are the mass, number density, pressure, and fluid velocity of charged species *j*, and neutral respectively. $\vec{E}$ and $\vec{B}$ are the electric and magnetic fields and ν_{jn} (ν_{nj}) is the elastic collision frequency of charged species *j* (neutrals) with neutrals (charged species *j*). As seen in these equations, the ionization and recombination terms have been ignored. In the momentum equation, the pressure gradient of cold background species and neutrals are negligible, $\nabla P_n \cong \nabla P_i \cong \nabla P_e \cong 0$, which the pressure gradient of beam electrons can be expressed as $\nabla P_b = \gamma_b T_b \nabla n_b$ where T_b is the temperature expressed in units of energy and γ_b is the heat capacity ratio.

The equilibrium state of the beam-return current system considering the collision of charged particles with neutral atoms has been investigated in detail in non-magnetized [15] and magnetized [16] cold plasma by the authors of this article.

Assuming quantities perturbed according to $\exp[ik_y y - i\omega t]$, with wave vector $\vec{k}$ perpendicular to the beam velocity, $\vec{k} = k_y \hat{y}$, and magnetic field parallel to the z-axis and electric field $\vec{E} = E_x\, \hat{x}$ and using local approximation method, we find the linearized equations,

$$-i\omega n_j^1 + ik_y\, n_j^0 V_{jy}^1 = 0, \quad (j=b, e, i, n) \tag{6}$$

$$\left(-i\omega + \nu_{bn\parallel,\perp}\right)\vec{V}_b^1 = -\frac{\nabla P_b^1}{m_e\, n_b^0} - \frac{e}{m_e}\left(\vec{E}_1 + \frac{\vec{V}_b^0 \times \vec{B}_1}{c} + \frac{\vec{V}_b^1 \times \vec{B}_0}{c}\right) + \nu_{bn\parallel,\perp}\, \vec{V}_n^1 - \nu_{bn\parallel}\, \vec{V}_b^0\, \frac{n_b^1}{n_b^0}, \tag{7}$$

$$\left(-i\omega + \nu_{en}\right)\vec{V}_e^1 = -\frac{e}{m_e}\left(\vec{E}_1 + \frac{\vec{V}_e^1 \times \vec{B}_0}{c}\right) + \nu_{en}\, \vec{V}_n^1\,, \tag{8}$$

$$\left(-i\omega + \nu_{in}\right)\vec{V}_i^1 = \frac{e}{m_i}\left(\vec{E}_1 + \frac{\vec{V}_i^1 \times \vec{B}_0}{c}\right) + \nu_{in}\, \vec{V}_n^1, \tag{9}$$

$$\left(-i\omega + \nu_n\right)\vec{V}_n^1 = \nu_{ni}\, \vec{V}_i^1 + \nu_{ne}\, \vec{V}_e^1, \tag{10}$$

where $\nu_{bn\parallel,\perp}$ is the effective collision frequency of beam to neutral particles in the parallel and perpendicular direction to the beam velocity [39], and $\nu_n = \nu_{ni} + \nu_{ne}$ is the effective frequency of the neutral collisions.

The following linearized Maxwell equations complete the description of the system:

$$\frac{i\omega}{c}\vec{B}_1 = i\vec{k} \times \vec{E}_1 \tag{11}$$

$$i\vec{k} \times \vec{B}_1 = \frac{4\pi}{c}\vec{J}_1 - \frac{i\omega}{c}\vec{E}_1 \tag{12}$$

where the perturbed current density is

$$\vec{J}_1 = \sum_j q_j n_j \vec{V}_j = e\left(n_i^0 \vec{V}_i^1 - n_e^0 \vec{V}_e^1 - n_b^0 \vec{V}_b^1 - \vec{V}_b^0 n_b^1\right). \tag{13}$$

The dispersion relation, *Dr*, describing the linear dynamics current filamentation instability of the electron beam- magnetized ionosphere can be obtained by solving the coupled Maxwell-fluid equations as follows:

$$Dr = \left\{K^4 \beta_{\mathrm{tb}}^2 \mathrm{B}_0 + i\mathrm{C}_0 \bar{\omega}^2 (\alpha \mathrm{B}_3 + \bar{\omega}\mathrm{B}_1 + \bar{\nu}_{\mathrm{bn}\parallel}\mathrm{B}_2) - K^2 \bar{\omega}\left[\beta_{\mathrm{tb}}^2 (\bar{\nu}_{\mathrm{bn}\perp} - i\bar{\omega})(\alpha \mathrm{B}_3 + \bar{\nu}_{\mathrm{bn}\parallel}\mathrm{B}_2) - (\bar{\nu}_{\mathrm{in}} - i\bar{\omega})(\bar{\nu}_{\mathrm{en}} - i\bar{\omega})\left(\alpha\beta^2 (i\bar{\nu}_{\mathrm{bn}\perp} + \bar{\omega}) - \mathrm{C}_0 (i\bar{\nu}_{\mathrm{bn}\parallel} + \bar{\omega})\right)\right]\right\}\left\{\bar{\nu}_{\mathrm{in}}{}^2 \mathrm{C}_1 + \mathrm{C}_2 + 2\bar{\nu}_{\mathrm{in}}\left[-i\bar{\omega}\mathrm{C}_1 + \bar{\nu}_{\mathrm{ni}}\left(\bar{\omega}^2 A + \bar{\nu}_{\mathrm{ne}}(\bar{\nu}_{\mathrm{en}}\bar{\omega}^2 - i\bar{\omega}u + \mu\nu_{\mathrm{en}}\Omega^2)\right)\right]\right\} \tag{14}$$

where the expressions of u, A, w, $B_{0,1,2,3}$, and $C_{0,1,2}$ are

u=$\bar{\omega}^2 - \Omega^2$

$A = (\nu_{en}{}^2 - 2i\nu_{en}\bar{\omega} - \bar{\omega}^2 + \Omega^2)$
$w = (1 - i\nu_{en}\bar{\omega} - \bar{\omega}^2)$
$B_0 = (\bar{\nu}_{bn\parallel} - i\bar{\omega})(\bar{\nu}_{bn\perp} - i\bar{\omega})(\bar{\nu}_{in} - i\bar{\omega})(\nu_{en} - i\bar{\omega})$
$B_1 = \bar{\nu}_{ne} + \mu(\bar{\nu}_{en} - i\bar{\omega}) - i\bar{\omega}w - i\bar{\nu}_{ni}\bar{\nu}_{en}\bar{\omega} + \bar{\nu}_{in}w$
$B_2 = i\bar{\nu}_{ne} + i\alpha\bar{\nu}_{ne} + \bar{\omega}w + \bar{\nu}_{ni}\bar{\nu}_{en}\bar{\omega} + \mu\big(i\bar{\nu}_{ni} + (1+\alpha)(i\bar{\nu}_{en} + \bar{\omega})\big) + i\bar{\nu}_{in}w$
$B_3 = (\bar{\nu}_{en} - i\bar{\omega})\big(i\bar{\nu}_{in} + (1+\mu)(i\bar{\nu}_{ni} + \bar{\omega})\big)$
$C_0 = \big(\bar{\nu}_{bn\perp}{}^2 - 2i\bar{\nu}_{bn\perp}\bar{\omega} - u\big)$
$C_1 = \bar{\nu}_{ne}{}^2 u + \bar{\omega}^2 A + 2\bar{\nu}_{ne}\bar{\omega}(\bar{\nu}_{en}\bar{\omega} - iu)$
$C_2 = (\bar{\omega}^2 - \mu^2\Omega^2)[2i\bar{\nu}_{ne}\bar{\omega}(i\bar{\nu}_{en}\bar{\omega} + u) + \bar{\nu}_{ni}{}^2 A + 2\bar{\nu}_{ne}\bar{\omega}(\bar{\nu}_{en}\bar{\omega} - iu) - 2i\bar{\nu}_{ni}(\bar{\nu}_{ne}(\nu_{en}\bar{\omega} - iu) + \bar{\omega}A) - C_1]$

In the above equation, $\mu = m_e/m_i$ is the ratio of the electron to ion mass and $\alpha = n_b^0/n_e^0$ is the ratio of the unperturbed beam to plasma electron number density. The obtained DR has been expressed in terms of the following dimensionless variables:

$K = ck_y/\omega_p,\ \beta = V_b^0/c,\ \beta_{Tb} = V_{Tb}/c,\ \bar{\omega} = \omega/\omega_p, \Omega = \frac{\omega_c}{\omega_p}$ ، $\bar{\nu} = \nu/\omega_p$,

where $\omega_p = (4\pi n_e^0 e^2/m_e)^{1/2}$ is the background plasma frequency.

Results and Discussion

In this section, the results of numerical analysis of the dispersion relation solutions *Dr=0* of the collisional current filamentation instability in the ionosphere are presented. In the F region of the ionosphere, at a distance of 150-1000 km from the earth's surface, the electron density is in the range of 10^5-10^6 cm^{-3} and the ionization degree is up to a maximum of 1%. Experimental observations indicate that the ratio of the density of penetrating electron beams to the plasma electron number density in different layers of the ionosphere can vary from 10^{-2} to 10^{-4} [1]. To analyze the current filamentation instability, by solving the dispersion equation *Dr=0*, the normalized growth rate of the most unstable normal mode (γ/ω_p) versus normalized wave number (ck_y/ω_p) has been depicted in Fig. 1 for magnetized ionosphere with a cyclotron frequency of $\Omega = \frac{\omega_c}{\omega_p} = 0.015$ and non-magnetized ionosphere with $\Omega = 0$. Appropriate physical parameters of the ionosphere are the ratio of unperturbed beam to plasma electron number density $\alpha = n_b^0/n_e^0 = 4 \times 10^{-3}$, electron beam temperature $T_b = 3\ eV$, initial electron beam velocity $V_b^0 = 0.4\ c$, $T_e = T_i = 0.02$ eV, neutral density $n_n = 10^{10} cm^{-3}$, and the ionization degree $i = n_e^0/n_n^0 = 10^{-3}$.

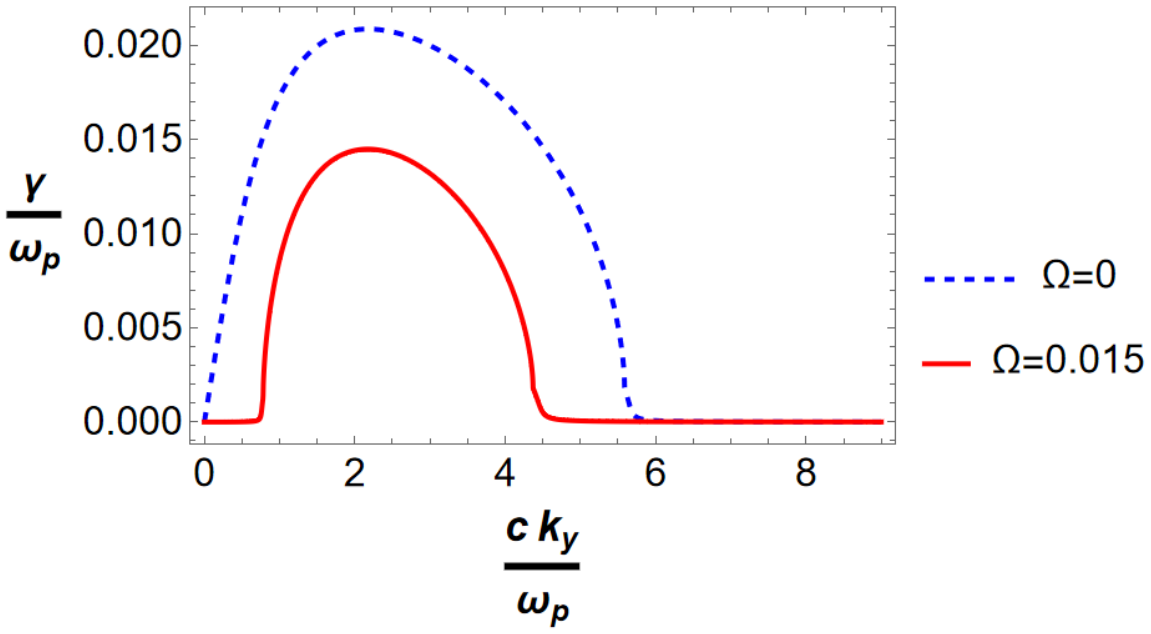

Fig. 1. The growth rate of the CFI in the magnetized ($\Omega = \frac{\omega_c}{\omega_p} = 0.015$) and unmagnetized ($\Omega = 0$) regime for $\alpha = 4 \times 10^{-3}$, $V_b^0 = 0.4\ c$, plasma density $n_e^0 = 10^6$ cm^{-3} and $i = 10^{-3}$

As seen from this figure, the magnetic field can reduce the instability growth rate, in agreement with our previous results reported by [16]. Physically, the growth rate of the instability is proportional to the deviation of the filament currents in the increase of the static magnetic field of the input disturbance. The presence of an external magnetic field in the direction of the beam prevents the deviation of electrons and thus prevents the increase of the filament current density, reducing the growth rate of the current filamentation instability. For further investigation, the numerical evaluation of the maximum growth rate in terms of the reduced vector is displayed in Fig. 2 for magnetic field intensity $\Omega = \frac{\omega_c}{\omega_p}$ from 0 to 0.03. The other parameters are the same as Fig.1.

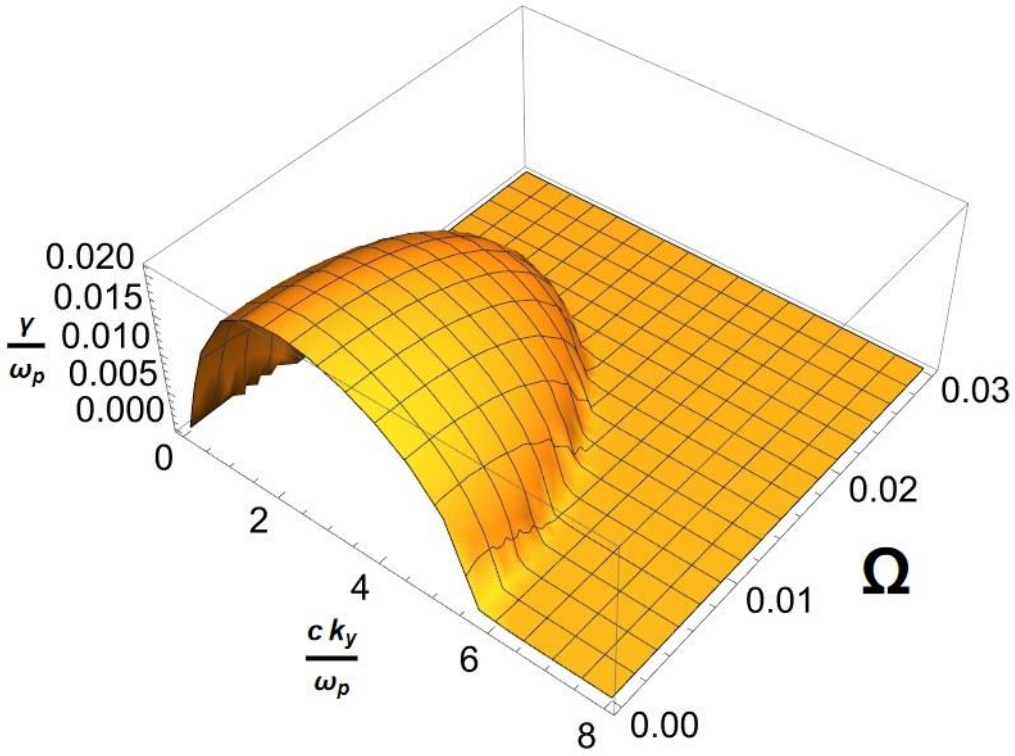

Fig. 2. Numerical evaluation of the normalized growth rate γ/ω_p in terms of normalized wave number ck_y/ω_p and cyclotron frequency Ω.

It is found from this figure that increasing the magnetic field intensity decreases the cut-off wave number, i.e., reduction of unstable wavelength region, to stabilize the system at large Ω. Also, Ω reduces the maximum growth rate of instability at any given wavelength. On the other hand, there exists a threshold cyclotron frequency where the instability disappears for $\Omega > \Omega_{th}$. This threshold value depends on various parameters of the beam, including the ratio of the number density of the beam to the plasma, α, and the beam velocity, β. Thus, to investigate their role the maximum growth rate of instability for various admissible α values and various β have been investigated in Fig. 3 and Fig. 4.

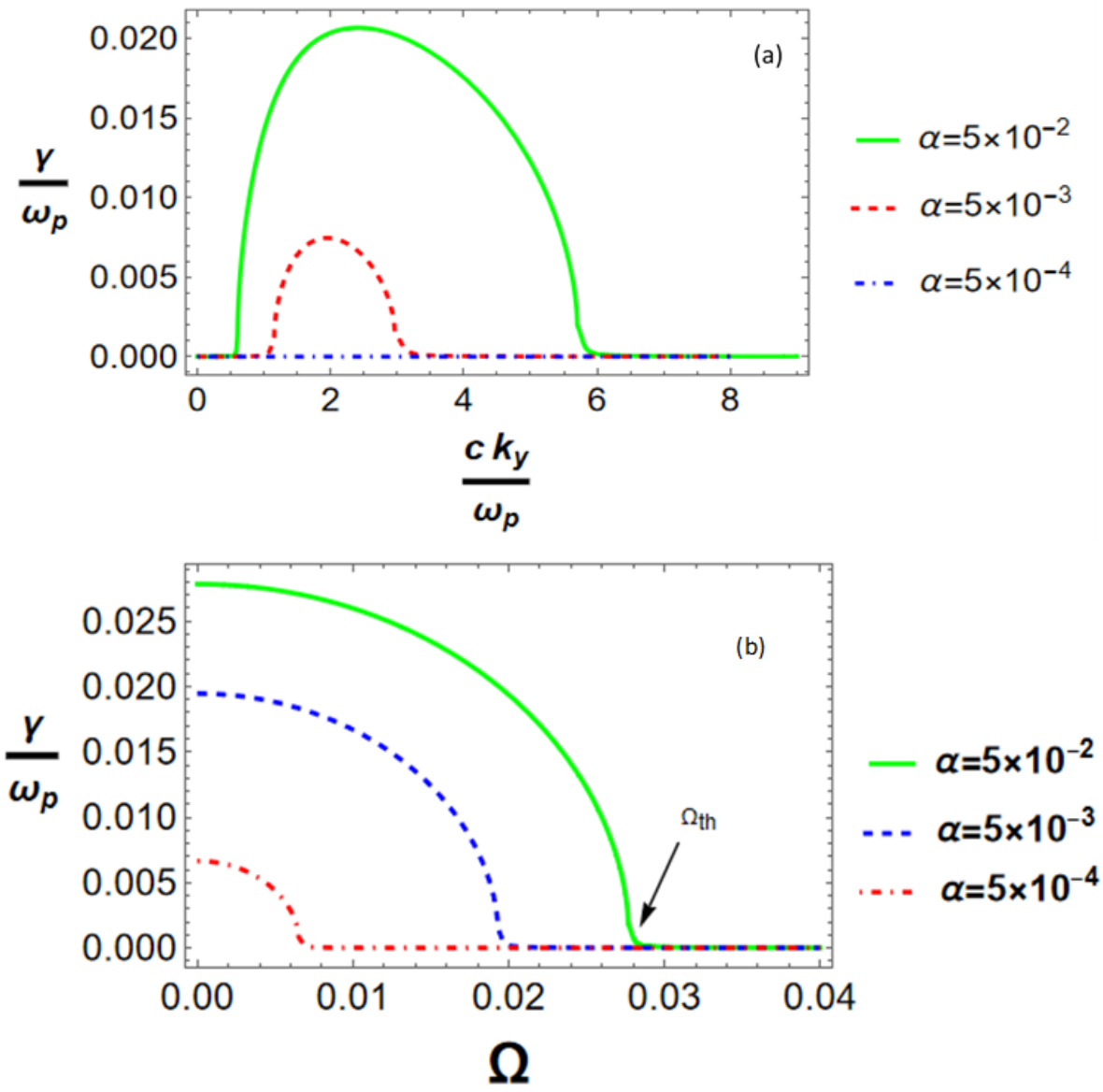

Fig. 3. Dimensionless growth rate γ/ω_p in terms of (a) dimensionless wave number ck_y/ω_p, (b) cyclotron frequency Ω for three values of $\alpha = 5 \times 10^{-2}, 5 \times 10^{-3}$, and 5×10^{-4}. The other parameters are the same as Fig. 1.

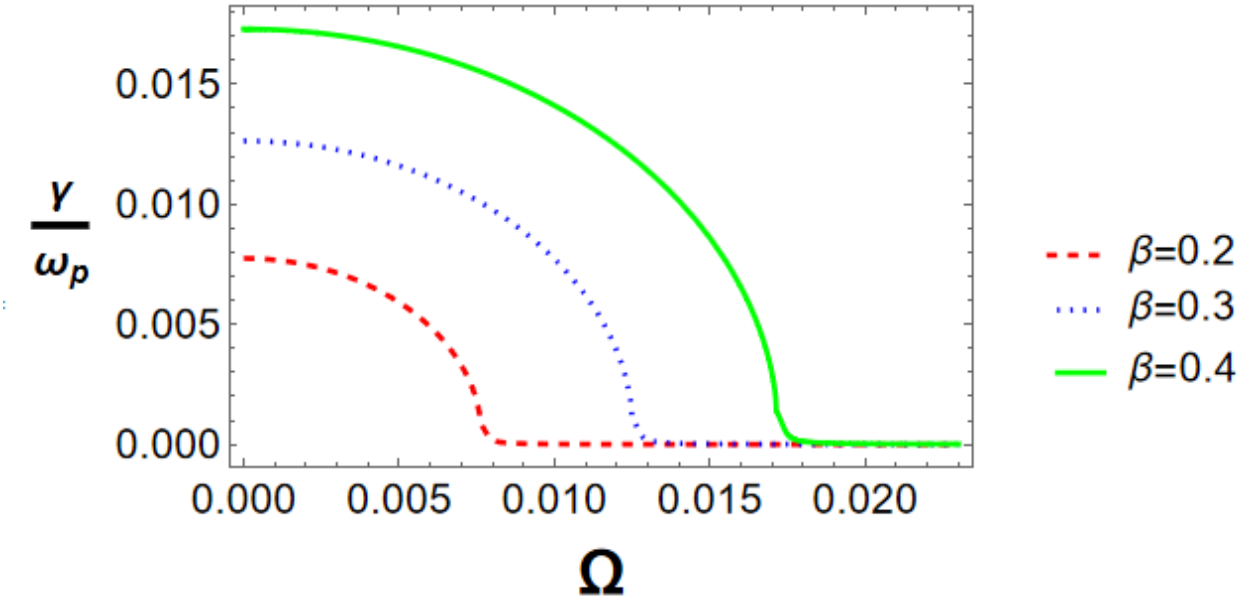

Fig. 4. The plot of CFI growth rate versus cyclotron frequency for $\beta = 0.2, 0.3,$ and 0.4 .

It is evident from Fig. 3(a), as the ratio of beam to plasma density increases, the electron beam becomes denser, and the instability growth rate increases. Therefore, for a fixed value of magnetic field, the system becomes more unstable. Fig. 3(b) shows that increasing α results in an increase the cut-off wave number, which causes a broadening of unstable wavelength region, as well as an increase the maximum growth rate of instability for any arbitrary unstable wavelength because of growing the magnetic field fluctuation with current density. On the other hand, it is found from Fig 4 that increasing the velocity of beam, β, enhances the maximum growth rate due to the increase in current density, the main factor of instability. So, as both α and β increase, the threshold value of magnetic field Ω_{th} also increases. Hence, larger magnetic fields are needed to prevent the excitation of current filamentation instability at high current densities and beam velocities.

Conclusion

In this paper, the current filamentation instability is studied in the ionosphere. The incoming solar wind electron beam interacts with different layers of the ionosphere and gives rise to several plasma unstable modes, especially the CFI. By analyzing the dispersion relation of unstable mode, the effect of magnetic field driven-destabilization and current-driven stabilization on the growth

rate of instability has been studied. Results show there is a magnetic field threshold for the current filamentation instability in the collisional magnetized ionosphere, in which the instability will disappear for a larger magnetic field than ones. One can deduce that the value of the magnetic threshold increases by increasing electron beam current density, indicating that the presence of magnetic field stabilizes the current filamentation instability. Furthermore, decreasing the magnetic field increases the unstable wavelength region as well as the maximum growth rate of the instability. On the other hand, in the magnetized ionosphere, with the increment of the velocity and density of electrons beam, the growth rate of instability becomes larger, and the system is more unstable for a fixed magnetic field. These results could be important for understanding the many phenomena that occur in the ionosphere.

References

[1] D. Le Queau, R. Pellat, and A. Saint Marc, Phys. Rev. A 24, 448 (1981).

[2] X. Xing, R. A. Wolf, JGR: *Space* Physics 112, A12209 (2007).

[3] D. L. Hysell, E. Kudeki, JGR: *Space* Physics 109, A11301 (2004).

[4] H. Mirzaei, M. Kazemi, G. Etaati, M. Abbasi, M. Karimi Kafshgari, H. Rajabalinia Jelodar, JTAP 16, 3, (2022).

[5] M. Chakraborty, V. K. Yadav, R. Kumar, Advances in Space Research 71, 6 (2023)

[6] A. Bret, L. Gremillet, and M. E. Dieckmann, Phys. Plasmas 17, 120501 (2010).

[7] B. D. Fried, Phys. Fluids 2, 337 (1959).

[8] B. Hao, Z.M. Sheng, J. Zhang, and Y.T. Li, Laser Part. Beams 32, 79 (2014).

[9] H. Mehdian, K. Hajisharifi, and A. Hasanbeigi, ApJ. **801**, 89 (2015).

[10] F. Califano, R. Prandi, F. Pegoraro, and S. V. Bulanov, Phys. Rev. E 58, 7837 (1998).

[11] M. Honda, Phys. Rev. E 69, 016401 (2004).

[12] A. Bret, M. C. Firpo, and C. Deutsch, Phys. Rev. E 72, 016403 (2005)

[13] B. Hao, Z. M. Sheng, and J. Zhang, Phys. Plasmas 15, 082112 (2008).

[14] H. Mehdian, K. Hajisharifi, and A. Hasanbeigi, ApJ. 801, 89 (2015).

[15] K. Hajisharifi, S. Tajik-nezhad, H. Mehdian, Phys. Plasmas 24, 032120 (2017).

[16] K. Hajisharifi, S. Tajik-nezhad, H. Mehdian, IJPR19, 1.17 (2019).

ICNST 2024
International Conference on Nuclear Science and Technology
6- 8 MAY 2024 | Isfahan, Iran

Particle-in-Cell Simulation of the Existence and Excitation of Ion and Electron Bernstein Waves by RF Heating in NSTX Spherical Tokamak Plasma (Paper ID: 1577)

Ghassami S. Correspondent[1*], Eydan A. Co-Author[1], Ali Asgarian M. Co-Author[2]
[1]Department of Physics and Energy Engineering, Amirkabir University of Technology, Tehran, Iran
[2]Department of Physics, University of Isfahan, Isfahan, Iran

Abstract

The particle-in-cell (PIC) method, based on plasma kinetic theory without further approximation is employed to demonstrate the existence and excitation of the ion and electron Bernstein waves. These electrostatic modes have the capability to penetrate high-density regions in tokamaks, making them suitable candidates for radiofrequency (RF) heating schemes aimed at reaching and heating the core regions of tokamaks. The presence of Bernstein waves involved in the RF heating is illustrated through the reconstruction and simulation of the NSTX spherical tokamak plasma, located at the upper hybrid resonance point-a site of wave generation due to mode conversion. Utilizing the XOOPIC code, an approximated uniform plasma slab is simulated with parameters corresponding to the NSTX plasma at this point. Theoretical and computational analyses of these waves are conducted by by comparing the power diagrams obtained from the PIC method and dispersion curves derived from theory. The strong alignments between the computational power diagrams and theoretical dispersion curves confirms the efficacy and robustness of the PIC method within this context.

Keywords: Electron Bernstein Waves; Ion Bernstein Waves; Particle-in-Cell Method; Plasma Heating; Radio Frequency Waves.

Introduction

Electrostatic Bernstein waves, with frequencies falling within the electron or ion cyclotron range, offer a unique advantage by being able to propagate within the high-β devices operating in over-dense regimes, such as the spherical tokamaks that routinely operate at relatively high densities.

This characteristic makes them promising candidates for heating and current drive in over-dense fusion plasmas [1-3].

Radiofrequency (RF) heating, applied within both the ion and electron gyrofrequency regimes, serves as a method to excite Bernstein waves through mode conversion, with the ultimate goal of achieving burning plasmas [4, 5]. These waves travel across the magnetic field, making them particularly effective for heating the plasma core, as they can penetrate beyond the cutoffs of other magnetized waves. They are strongly absorbed at cyclotron resonances, offering potential for localized heating and serving as options for ion and electron cyclotron resonance heating.

Electron Bernstein waves (EBWs) can only propagate within the upper hybrid resonance (UHR) region surrounding over-dense plasma. Consequently, plasma heating involves exciting plasma waves by launching electromagnetic waves from the edge plasma into the core. Microwave launchers located outside the plasma [1] couple microwave power to EBWs through the mode conversion process near the UHR region [6-8]. The launched electromagnetic wave propagates into the plasma until it reaches a point where the resonance cyclotron harmonics match the wave frequency [9].

Ion Bernstein waves (IBWs) are utilized in fusion devices to transfer RF energies to ion cyclotron harmonics. They are categorized into pure and neutralized IBWs based on their propagation angle relative to the magnetic field direction. Pure IBWs, in conditions where electrons are stationary, propagate almost perpendicular to the magnetic field with a narrow frequency range. In contrast, neutralized IBWs, occurring when electrons are in Boltzmann equilibrium with the wave potential, propagate at an angle close to perpendicular, but with a wider frequency range due to electron movements [10-15].

Spherical tokamaks, such as the National Spherical Torus Experiment (NSTX) at the Princeton Plasma Physics Laboratory (PPPL), routinely operate in high-β regimes, featuring over-dense plasmas with densities up to 10^{20} m^{-3}, resulting in the first four electron cyclotron harmonics being over-dense. This study focuses on Bernstein waves within a plasma sample using NSTX parameters. NSTX employs high-power RF waves ranging from 1-2 MW and beyond for subsequent programs. The ramping of power to these levels commenced approximately a decade

ago with the availability of powerful gyrotrons. These power levels induce challenging nonlinear effects, which are addressed numerically [16-18].

The particle-in-cell (PIC) method utilizes fundamental equations without approximations, enabling the retention of the plasma's nonlinear physics. This method captures most physics from first principles, including the kinetic description of the plasma and the complete set of Maxwell's equations for the waves, without further approximation [19, 20].

Similar studies using PIC codes have been conducted over the past two decades. For instance, J. S. Lönnroth et al. investigated Ion Bernstein wave excitation using the self-consistent two-dimensional particle-in-cell method [21], while Thomas G. Jenkins et al. numerically studied nonlinear effects associated with radiofrequency wave propagation through plasma in the time domain, employing both fluid and PIC methods [22]. Animesh Kuley et al. developed a particle simulation model to control instability for steady-state operations of fusion experiments, providing a first-principles tool for studying RF nonlinear interactions with plasmas [23], and A. Kuley et al. developed and verified a nonlinear simulation model for radiofrequency waves using fully kinetic ion and drift kinetic electron [24].

This study examines Bernstein waves theoretically and computationally in the context of resonant heating for fusion plasma generation. Initially, we analyze the dispersion relation of electron and ion Bernstein waves using parameters specific to the NSTX spherical tokamak. Subsequently, we simulate the plasma at the tokamak's resonant point using the PIC method. Our simulations employ a uniformity approximation for magnetic field and density, focusing on demonstrating the possibility of wave excitation within a confined plasma.

The essence of resonant RF heating methods lies in the excitation of plasma waves within their resonant regions through mode conversion. In these processes, incident wave energy is channeled into resonant pathways via wave-wave interactions, subsequently transferring energy to particles through wave-particle interactions. Notably, the excitation of electron and ion Bernstein waves plays a pivotal role in these methodologies applied in Tokamaks. We proceed by discussing the theory and obtaining dispersion curves specific to the NSTX parameters.

Dispersion Relation In a Magnetized Plasma

The dispersion relation in a magnetized plasma is given by [25-27]:

$$1 = 2\sum_{\sigma=\mathrm{i,e}} \frac{\mathrm{e}^{-k_\perp^2 r_{\mathrm{L}\sigma}^2}}{k_\perp^2 r_{\mathrm{L}\sigma}^2} \sum_{n_\sigma=1}^{\infty} \frac{n_\sigma^2 \omega_{\mathrm{p}\sigma}^2}{\omega^2 - n_\sigma^2 \omega_{\mathrm{c}\sigma}^2} I_{n_\sigma}(k_\perp^2 r_{\mathrm{L}\sigma}^2), \tag{1}$$

Here, the first summation represents ion (i) and electron (e) species, and the second is for $n_\sigma = 1,2,\cdots$, denoting the order of generalized Bessel function, I_{n_σ}. In this equation, ω and $k_\perp$ stand for the frequency and perpendicular wave-number of the wave, respectively. ω_c and ω_p represent the cyclotron and plasma frequencies, while r_L is the Larmor radius.

Since $r_{\mathrm{Li}} \gg r_{\mathrm{Le}}$, solely electrons are focused, the electron Bernstein modes emerge within the range of electron cyclotron frequency and electron Larmor radius, including their resonances at electron cyclotron harmonics as illustrated in Figure 1.

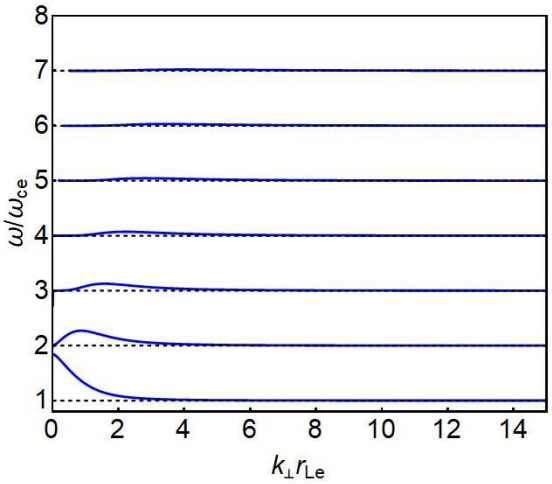

Figure 1. Dispersion curves of Electron Bernstein waves derived from Eq. (1) theoretically.

On the other hand, considering the ion component reveals the presence of ion Bernstein modes. Figure 2(a) displays upper branches related to electrons with resonances around the first and second electron cyclotron harmonics $\omega_{\mathrm{ce}} \approx 1836\omega_{\mathrm{ci}}$. Conversely, lower accumulated branches in Figure 2(b) correspond to ion cyclotron harmonics concentrated near zero, with resonances ($k_\perp \rightarrow \infty$) around the ion cyclotron harmonics.

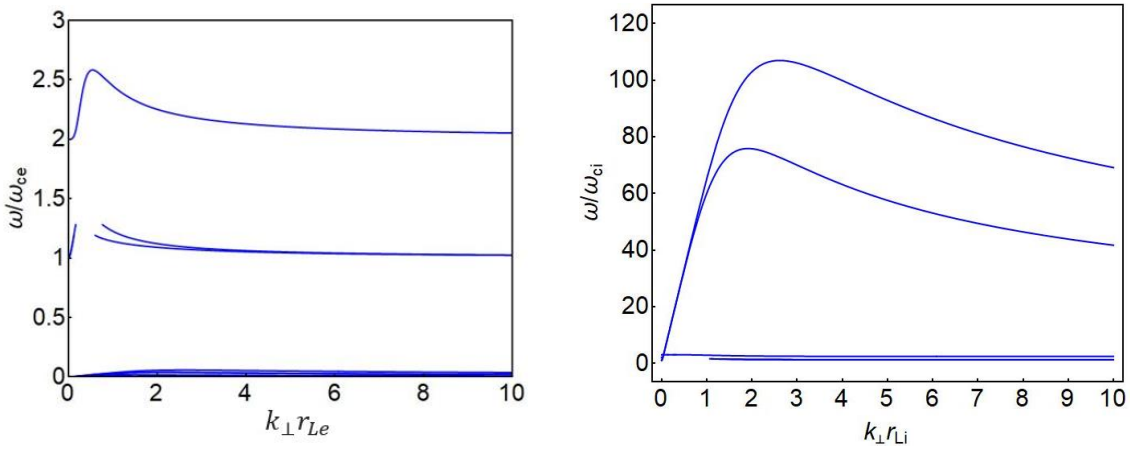

(a) (b)

Figure 2. Dispersion of (a) Electron Bernstein waves and (b) Ion Bernstein waves derived from Eq.(1) theoretically.

The dispersion relation, Eq. (1), highlights two critical features: (1) In non-magnetized plasmas (zero cyclotron frequency), Bernstein waves do not excite. (2) These waves are not constrained by plasma density (plasma frequency), making them ideal for heating the dense plasma core at the center of tokamaks. They propagate perpendicular to the external magnetic field and are characterized by their longitudinal (electrostatic) nature, with the electrical field component aligned with propagation.

Particle-in-Cell Simulation Method

The dispersion relations for electron and ion Bernstein waves are derived using plasma kinetic theory, necessitating consideration of kinetic effects in models aimed at simulating these waves. Subsequently, a plasma containing fusion characteristics is simulated using a PIC kinetic model to demonstrate the existence and excitation of these waves within the plasma.

All kinetic plasma models rely on Maxwell's equations to compute electromagnetic fields; their differences lie in how they calculate sources of charge and electric current densities. In the PIC method, the Lorentz equation is integrated into the system of Maxwell's equations when determining these sources based on the position and velocity of individual particles [28]. The advantage of PIC over other methods, such as ray-tracing [29, 30] and full-wave calculations used

for simulating wave-plasma interactions, lies in its ability to closely adhere to the fundamental physics governing plasma behavior [3]. Initially, periodic electrostatic simulations, encompassing basic effects, were conducted in one dimension with particle counts ranging from $10^2 \sim 10^3$ on computers with a memory capacity of 100 kB. Presently, fully relativistic electromagnetic simulations, incorporating wave and particle injectors at boundaries, as well as collision effects, are carried out in three dimensions with $10^6 \sim 10^{10}$ number of particles on highly parallelized computing systems.

A key characteristic of the PIC method is its utilization of super-particles to reduce computational volume, where a certain number of actual particles are represented by these super-particles. These super-particles are defined in continuous position and velocity spaces, while electromagnetic fields are defined in discrete position spaces, with their temporal changes considered in discrete time steps. By starting with an initial value, successive time points are calculated. The time difference between positions and velocities is $\Delta t\ /2$, allowing for integration of motion equations using the leapfrog method.

Following the computation of fields from initial values, motion equations for particle positions are solved using the finite difference time domain (FDTD) method. Subsequently, boundary conditions such as particle absorption and emission are applied. Collisions are investigated using the Monte Carlo method. The source sentences are obtained through adapting continuous particle positions to discrete grid positions for use in field equations, after which fields advance a time step, and this time cycle is repeated.

RF waves are utilized for heating in the NSTX Spherical tokamak, with a minor radius $a = 44$ cm and a major radius $R = 1.05$ m. In a heating experiment depicted in Figure. 3, a wave at a frequency of $f_0 = 15$ GHz is emitted by an RF antenna located near the tokamak's equator. Bernstein waves are excited in a region where the input wave frequency matches the upper hybrid frequency, spanning from 1 cm to the plasma edge. Once excited, these waves propagate towards the core of the plasma, heating the central regions of the tokamak.

Figure. 4 illustrates the simulation conducted on a slab with dimensions $\Delta x = 1$ cm and $\Delta y = 0.002$ cm, positioned on the equatorial plane ($\theta \approx 0$). Referring to Figure. 3 [17], in the radial

direction, x ranges from $x_s = 43$ cm to $x_f = 44$ cm, while in the poloidal direction, y ranges from $y_s = 0$ to $y_f = 0.002$ cm. The toroidal direction is denoted by z. The slab's parameters are based on those of the fusion plasma at the NSTX Spherical tokamak edge: electron and ion density of $n_e = n_i = 0.18 \times 10^{19}$ #/m^3, electron temperature $T_e = 63$ eV, and ion temperature $T_i = 0.0025$ eV. The magnetic field in this region comprises two components, $B_y = 0.21$ T and $B_z = 0.18$ T. Accordingly, the ratio ω_{pe}/ω_{ce}used for the simulations is 1.55.

The simulation employs 2048 cells along the x-direction, with periodic boundary conditions utilized in the y-direction due to the system's approximate symmetry in this dimension. The number of super-particles assigned is an average of approximately 2861 per cell.

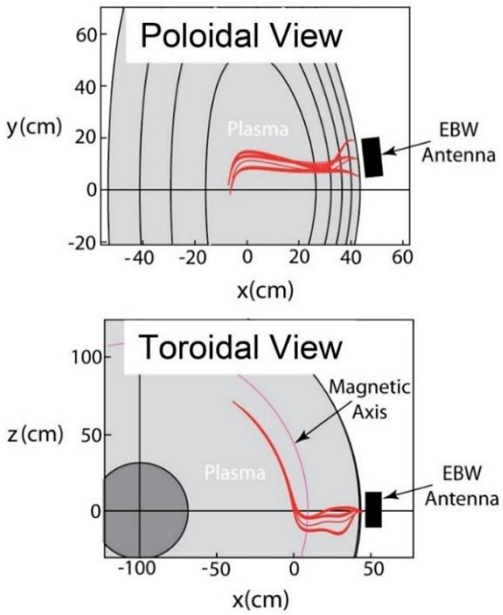

Figure 3. Outboard wave injection to excite EBW current drive, launched in the equatorial plane, from both poloidal and toroidal views for NSTX [17].

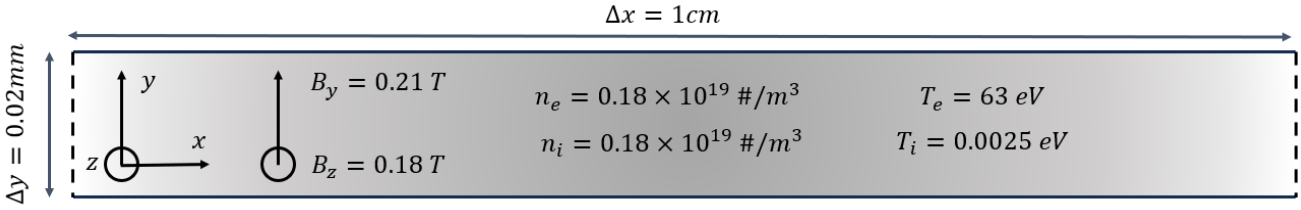

Figure 4. The plasma slab used in the simulation based on the parameters of NSTX.

Results and Discussion

Demonstrating the presence of the electron and ion Bernstein waves in the simulated region is crucial to illustrate the potential for RF heating and the excitation of Bernstein waves. After conducting the Particle-in-Cell (PIC) simulation on a slab depicted in Figure 4, the electric field E_x was examined over a two-dimensional plane, comprising position (x) and time (t) axes, by conducting a diagnosis along a horizontal line at y = 0.01 mm for a time period of Δt = 4 ns, as depicted in Figure 5, we explored the system without the incident RF wave. Here, the input wave amplitude was set to zero, signifying no wave entry. This analysis clearly shows the existence of the electron and ion Bernstein waves. Demonstrating the excitation of Bernstein waves and the effectiveness of RF heating requires showing the existence of Bernstein waves without the input RF wave. After parametric studies and running the simulation for t = 4 ns, we obtained the electric field E_x at y = 0.01 mm, confirming the presence of these waves within this specific region of space and time.

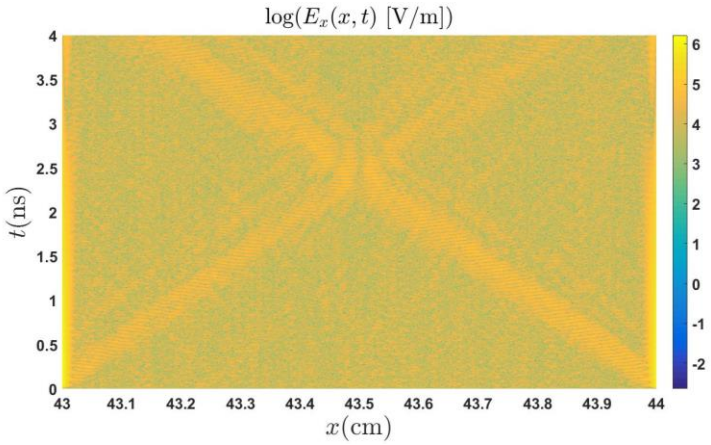

Figure 5. The electric field $\boldsymbol{E_x}$ on a horizontal line at the position $\boldsymbol{y = 0.01\ mm}$, for a timespan of $\boldsymbol{\Delta t = 4\ ns}$, obtained on a two-dimensional plane consists of two position ($\boldsymbol{x}$) and time ($\boldsymbol{t}$) axes.

To confirm the existence of Bernstein waves, a 2D Fourier transformation of this electric field was performed across both position and time domains, yielding the frequencies and wave-numbers of these excited waves, respectively. The resulting power spectrum, depicted in Figure 6, highlights regions of energy accumulation (the bright areas). The frequencies and wavelengths within these areas correspond to the excited waves carrying this energy. By correlating these regions with the dispersion curves shown in Figure 1 and Figures 2, we can classify the type of these excited waves. The color bar on the right side of Figure 6 indicates the magnitude of power $P_x(k_\perp, \omega)$ assumed to

propagate in the x-direction perpendicular to the external magnetic field. The yellow regions within the diagrams, representing the maximum values of the color bar, signify the highest power or energy accumulation resulting from the gyro motions of electrons and ions in the mechanisms of Bernstein waves.

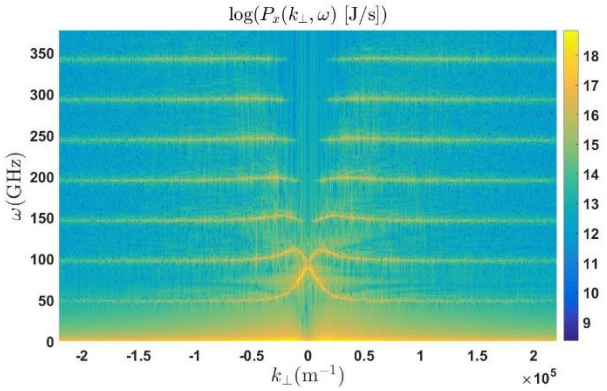

Figure 6. The power spectrum of $\boldsymbol{E_x(x,t)}$ derived from Figure 4 by a 2D Fourier transformation.

Figure 6, can be evaluated in two distinct regions representing low and high frequencies corresponding to ion and electron harmonics, respectively. Figure 7, specifically focuses on the high-frequency region of Figure 6, where the frequency and wave-number axes are logically normalized to the electron cyclotron frequency and the electron Larmor radius, respectively. In this power diagram, the highlighted yellow lines indicate the excited electron cyclotron harmonics, which precisely match the lines illustrated in Figure 1. Comparing Figures 7 and 1 clearly demonstrates the presence and driving of the electron Bernstein waves in the simulation region.

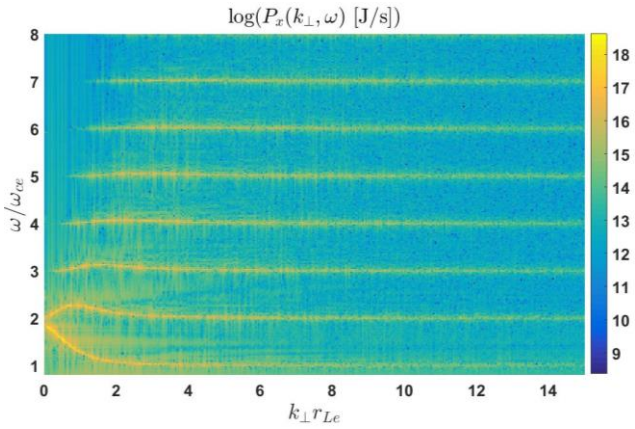

Figure 7. The power spectrum of $\boldsymbol{E_x(x,t)}$ derived from Figure 4 by a 2D Fourier transformation in the ranges of high electron frequencies.

Figure 8, zooms in on the low-frequency zone of Figure 6, with the frequency and wave-number axes normalized to the electron cyclotron frequency and the ion Larmor radius, respectively. Notably, the lower brightened areas near the horizontal axis signify a concentration of power and consequent energy accumulation due to the ion resonant modes within the range of ion cyclotron frequencies. The accumulation observed in the ion cyclotron frequency region is likely a result of the gyro motions of ions characteristic of the ion Bernstein waves. Comparing Figures 8 and 2(a), and noting the significant overlap of the resonant regions in these graphs, clearly demonstrates the presence and excitement of the ion Bernstein waves in the simulation region.

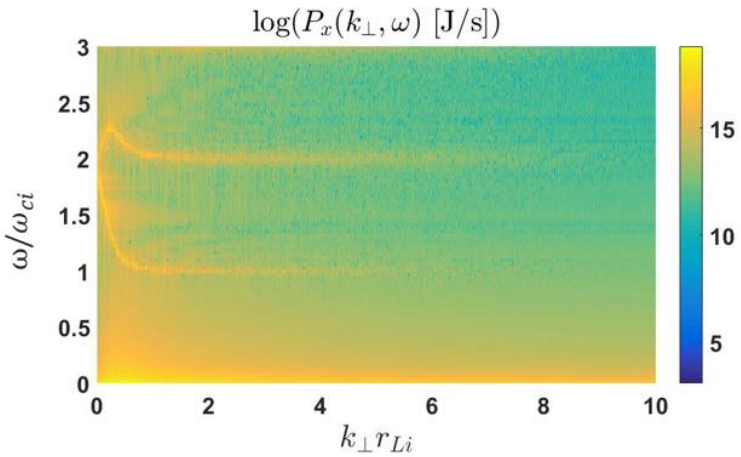

Figure 8. The power spectrum of $\boldsymbol{E_x(x,t)}$ derived from Figure 4 by a 2D Fourier transformation in the ranges of low ion frequencies.

Conclusion

The Particle-in-Cell (PIC) method was employed to simulate electron and ion Bernstein waves, essential for the RF heating scheme designed to reach and heat the core regions of tokamaks. These electrostatic waves represent two crucial modes in tokamaks, capable of penetrating high-density regions to heat the plasma core. The PIC method, rooted in plasma kinetic theory, offers the advantage of maintaining the fundamental physics governing plasmas. This method enables us to investigate the evolution of the particle velocity distribution function, which acts as the source for these waves.

As an experimental example of Bernstein wave excitation, the RF heating scheme in the NSTX spherical tokamak was reconstructed and simulated. A plasma with parameters matching those of

the NSTX spherical tokamak in the Upper Hybrid Resonance (UHR) layer with $n_e = n_i = 0.18 \times 10^{19}$ #/m^3, $T_e = 63$ eV and $T_i = 0.0025$ eV, $B_y = 0.21$ T and $B_z = 0.18$ T was simulated using the XOOPIC code on a slab characterized by the same density, temperature, and poloidal and toroidal magnetic fields.

The power diagrams derived from the PIC method within the designed slab effectively demonstrated the existence and excitation of Bernstein waves in both ion and electron modes. The strong alignment of the simulation diagrams with the dispersion curves of these waves obtained from theoretical relations affirms the efficacy of the PIC method.

Having explored the existence of Bernstein waves in the nonlinear regime, the subsequent step involves identifying and elucidating the potential nonlinear phenomena expected to arise with high levels of injected power. A comprehensive simulation of RF coupling must consider the nonlinearities arising from perturbations in particle orbits.

While full-wave theory cannot calculate nonlinear effects within this framework, this paper successfully demonstrated the presence and driving of Bernstein waves in both ion and electron forms within the NSTX tokamak plasma. We made the simplifying assumption that the plasma's characteristics—such as density, temperature, and external magnetic fields—remained uniform due to the confined area of their excitation in the UHR layer during the mode conversions associated with RF heating.

Acknowledfment

The authors gratefully appreciate the expert assistance of professor John P. Verboncoeur and the Plasma Theory and Simulation Group (PTSG: http://ptsg.egr.msu.edu/) in using the XOOPIC code.

References

[1] H P Laqua, *Plasma Phys.* Controlled Fusion., 49, 4 (2007)

[2] A Kohn, A Cappa, E Holzhauer, F Castej on, A Fern andez, and U Stroth, *Plasma Phys. Controlled Fusion*., 50, 085018 (2008)

[3] M Ali Asgarian, J P Verboncoeur, A Parvazian, and R Trines, Plasmas Phys., 20, 102516 (2014)

[4] Five Year Plan for 2009-2013 National Spherical Torus Experiment, NSTX Research Program (2009)

[5] NSTX Upgrade Five Year Plan for FY2014-2018, National Spherical Torus Experiment (2014)

[6] T Maekawa, T Kobayashi, S Yamaguchi, et al. (2001), Phys. Rev. Lett., 86, 3783

[7] V Shevchenko, Y Baranov, M O'Brien, and A Saveliev, Rev. Lett. (2002), 89, 265005

[8] Y Yoshimura, K Nagasaki, T Akiyama et al. (2006), Plasma and Fusion Res., 1053

[9] V Erckmann and U Gasparino, (1994) Plasma Phys. Control Fusion., 36, 1869

[10] W C Demarcus, and J Astron. (1958), 32

[11] W B Hubbard, and R Smoluchowski, to be published

[12] F V Grigor'ev and et al. (1972), Pis'ma Zh. Eksp. Teor. Fiz., 16, 286

[13] R E Kidder, (1968) Nucl. Fusion., 8, 3

[14] C A Nuckolls and et at. (1972), Nature., 39, 139

[15] J M Schmitt, (1973) Phys. Rev. Lett., 31, 982

[16] Five-year plan for 2009–2013, NSTX research program (2009)

[17] five-year plan for 2014–2018, NSTX upgrade (2014)

[18] N Xiang and J R Cary, Phys. Rev. Lett., 100, 085002 (2008)

[19] J P Verboncoeur, (2005). Plasma Phys. Controlled Fusion., 47, 231

[20] J P Verboncoeur, A B Langdon, and N T Gladd, Comput. (1995). Phys. Commun., 87

[21] J S Lonnroth, J A Heikkinen, K M Rantamäki, and S J Karttunen, (2002). Phys. Plasmas 9, 2926

[22] T G Jenkins, T M Austin, D N Smithe, J Loverich, and A H Hakim, (2013). Phys. Plasmas 20.

[23] Animesh Kuley, Z X Wang, Z Lin, and F Wessel, (2013). Phys. Plasmas 20, 102515

[24] A Kuley, Z Lin, J Bao, X S Wei, Y Xiao, W Zhang, G Y Sun, and N J Fisch, (2015). Phys.

[25] I B Bernstein, Phys. Rev., 10, 109 (1958)

[26] I B Bernstein, and F Engelmann, (1966). Phys. Fluids., 9, 937

[27] I B Bernstein, E A Frieman, M D Kruskal and R M Kulsrud, Proc. R. Soc. Lon. Ser. A, (1958).

[28] C K Birdsall, A B Langdon, McGraw-Hill, (1985).

[29] J Preinhaelter, V Kopecký, J. Plasma Phys (1973) ., 10.

[30] T Meakawa, S Tanaka, Y Terumichi, Y Hamada, (1978). *Phys. Rev. Lett*., 40, 1379

ICNST 2024
International Conference on Nuclear Science and Technology
6- 8 MAY 2024 | Isfahan, Iran

Plasma Optimization Using a Monte Carlo Simulation (Paper ID: 1610)

Hoseinzade M. Correspondent*

Physics and Fusion Energy Department, Atomic Energy Organization of Iran, Tehran, Iran

Abstract

A Monte Carlo simulation code has been developed to optimize the number of magnets confining the plasma in the H- multicusp ion source. This code improves the existing drawbacks in the particle studio CST program and predicts the lifetime of primary electrons and the effects of collisions of electrons and hydrogen gas atoms. In this work, the CYCLONE30 multicusp negative ion source is analyzed by using a 3D Monte Carlo simulation code to trace electron trajectories. A realistic geometry and multicusp magnetic field configuration are taken into account, and the electron trajectories are followed. Vibrationally excitation of hydrogen by fast electrons, dissociative attachment to highly vibrationally-excited molecules and ionization related to production of the H- ion are three reactions that are considered.

In this simulation 12 cusps are found to provide the highest plasma intensity in our configuration. Our simulation illustrates the existence of an optimum point in choosing the number of permanent magnets for confining the plasma.

Keywords: Multicusp ion source, Magnetic confinement, Electron trajectory

Introduction

Multicusp ion sources have been widely used in particle accelerators [1-3] and fusion reactors [4]. Permanent magnets can be utilized to improve the density and the uniformity of DC discharge plasma. The underlying idea of a set of permanent magnets is to force the electrons to spend a large portion of their flight path inside the plasma. In this way, the probability of a collision with a neutral gas molecule in the plasma is enhanced. This procedure increases the probability of an ionizing process, i.e., the current of a negative ion beam. Experimental results indicate that the large increase in density in this type of source is mainly due to the confinement of the primary ionizing electrons by the magnetic fields of the magnets. The confinement of ions, however, is

found to be significantly weaker. Plasma can be lost to the line cusps and to the regions between the cusps [5].

In this work, we analyze the CYCLONE30 multicusp negative ion source [6] by using a 3D Monte Carlo simulation code (C#) to trace electron trajectories. A realistic geometry and multicusp magnetic field configuration are taken into account, and the electron trajectories are followed. The neutral gas atom is hydrogen in the present study. In this article, we focus our attention mainly on processes the H- volume is produced. The types of collisions that we calculated are vibrational excitation of hydrogen by fast electrons, dissociative attachment to highly vibrationally-excited molecules and ionization related to production of the H- ion. Our simulation illustrates the existence of an optimum point in choosing the number of permanent magnets for confining the plasma.

Research Theories

The electron trajectories are calculated numerically by solving the 3D equation of motion

$$m d\mathbf{V}/dt = q(\mathbf{E} + \mathbf{V}\times\mathbf{B}), \quad (1)$$

where m, **V**, q, **E**, and **B** are the electron's mass, velocity, and charge, and the electric and magnetic fields, respectively**.** The electric field is neglected in the above equation because it is negligibly small over the entire plasma region. When **x** is the position vector, the definition of the velocity vector is given by

$$d\mathbf{x}/dt = \mathbf{V}. \quad (2)$$

We have used a Runge-Kutta integrator to solve the two equations of motion above.

Here we only consider production processes to follow electron orbits in the chamber. The following production processes and ionization are taken into account by the Monte Carlo method in each time step [7]:

Vibrational excitation of H_2 $$H_2 + e_{fast} \rightarrow H_2^* (\upsilon'' \geq 5) + e, \quad (3)$$

Dissociative attachment $$H_2^* (\upsilon'') + e_{slow} \rightarrow H^- + H. \quad (4)$$

The vibrational levels (υ'') are also taken into account because the reaction cross-sections are also υ'' dependent [8]. Dissociative electron attachment to vibrationally-cold H_2 ($\upsilon'' = 0$) molecules is known to have a very small cross section (10^{-21} cm^2).

The experiment of Allan and Wong [9] and the theoretical calculations of Wadehra and Bardsley [10] showed that the DA (dissociative attachment) cross section increases by five orders of magnitude when the hydrogen molecules are vibrationally excited from $\upsilon'' = 0$ to $\upsilon'' = 5$, and stay constant at higher υ''. The collisions between electrons and neutral atoms are calculated by the Monte Carlo method. The collision length is the distance between two successive collisions caused by a test particle and is defined as:

$$l = -\lambda \ln(r), \qquad (5)$$

where λ is the mean free path of the collision and r is a random number between 0 and 1. Because the cross sections are energy dependent, we consider three corresponding to different energies.

At the beginning or after a collision, the particle starts with a speed derived from Maxwell's speed distribution, and a random direction is chosen to continue the trajectory calculation.

The following scheme is used to generate the Maxwell speed distribution of the particles for the Monte-Carlo calculation:

$$v = \mathrm{abs}\left[\left\{v_m \times \sqrt{\ln\left(\frac{1}{r}\right)}\right\} + \left(\frac{v_m}{3}\right)\right], \qquad (6)$$

where r is a random number and $v_m = \sqrt{\frac{2k_BT}{m}}$ is the most probable speed of the particle having temperature T and mass m.

The mean free path λ for individual reaction is calculated from the reaction cross-section. Because the reaction rates and the cross sections are energy dependent, Maxwell's speed distribution of the electrons is considered. The flight length ζ is obtained by integrating the flight path in each time step as follows:

$$\zeta = \int_{t_0}^{t} |\boldsymbol{V}|\, dt \quad . \qquad (7)$$

If ζ becomes equal to l, the collision process is included in that time step. Here, we assume that the hydrogen atoms fill the chamber as a neutral gas and have no kinetic energy because their thermal energy is considerably less than that of electrons.

Physical Model of The Multicusp Ion Source

Fig 1 shows the simulated ion source configuration. This ion source consists of four major parts: the source body (walls of the plasma chamber), the lid which holds the filament, the magnetic filter and the puller assembly. The body of the original design of the source is a 150-mm-long, 100-mm-diameter copper cylinder around which ten columns of permanent magnets with magnetic field of 6.2 kG are mounted. In the center of the chamber we assume there is a filament made of tungsten that generates electrons after heating.

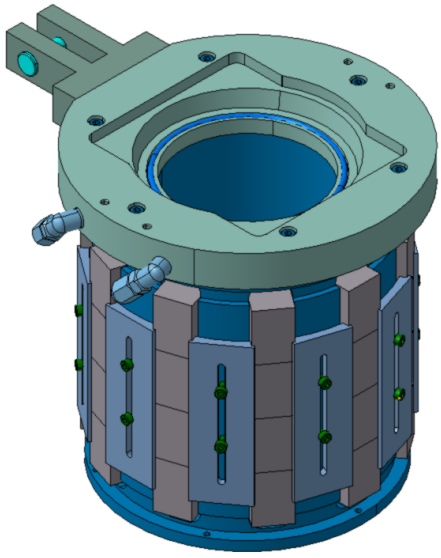

Fig. 1. Schematic layout of the CYCLONE30 chamber.

Magnetic Field Calculation

The complete topology of the magnetic field configuration of the ion source is calculated in a separate computer code, CST PARTICLE STUDIO [11]. Fig 2 shows a simulated magnetic field configuration.

The filament power supply has a current of 100 A and a voltage of 10 V. According to Bio-savart's law, the magnetic field of a wire with a current of 100 A in the 2 cm surrounding the wire is calculated as follows:

$$B = \mu_0 I/2\pi r = (4\pi \times 10^{-7} \times 100) / (2\pi \times 0.02) = 10^{-3}\ T = 10\ G. \quad (8)$$

As is clear from Fig 2, near the surfaces of the magnets the magnetic field is roughly 1800 G, and in the center of chamber, it is zero. Thus in comparison with such a high magnetic field (1800G), we ignored the field induced by the filament (10 G).

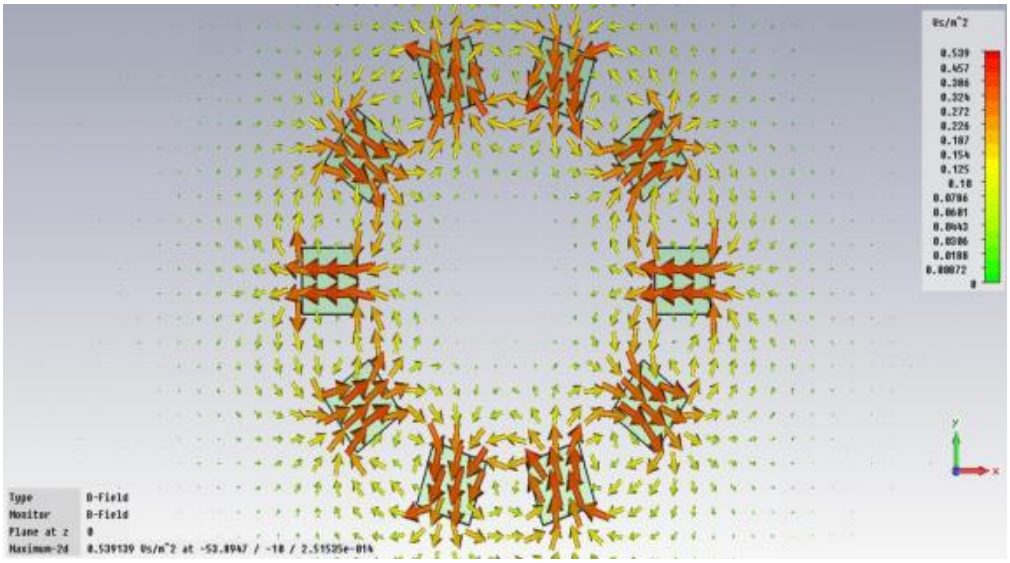

Fig. 2. Multicusp magnetic field configuration from a top view inside the ion source.

Simulation Method

To the best of our knowledge, no specific simulation method has been reported yet to explore the optimal number of cusps of the magnetic field; furthermore, are lacking proper theoretical methods to economize the time and the cost of the design and the fabrication. To evaluate the performance of different cusp spacing, we simulated the total distance that electrons travel.

CST is able to track particles in an electric and magnetic field but it does not simulate the interactions of particles. Also, it provides data concerning neither the particle trajectory, position and velocity at the desired time nor the total path traveled by a particle. In order to optimize the CYCLONE30 ion source, we developed a computer program. Our developed Monte Carlo code was used to find the total distance that electrons traveled.

The process of optimization is as follow: the number of permanent magnets used to create magnetic field lines is the optimization parameter, and the chamber's radius, height and filament position are constant. The number of magnets is varied from 4 to 14 with the geometrical specifications shown in Fig 1. The magnetic field is calculated by using CST software and exported to our Monte Carlo code. Because of having a magnetic flux density at every point of the chamber, 5000 electrons are emitted from the filament and are allowed to leave the filament cathode in different positions, and because they have random velocity direction, they move in the magnetic field created by the surrounding magnets.

The simulations are performed for 4 to 14 magnets with the geometrical specifications shown in Fig 1. The magnetic field is calculated by using CST software and exported to our Monte Carlo code. Electrons are emitted from the filament and are allowed to leave the filament cathode at different positions and different initial angles; they move in the magnetic field created by the surrounding magnets. The initial energy of the emitted electrons is assumed to be 200 eV in the present simulations-because the discharge voltage is 200 V. Electrons collide with neutral atoms elastically or inelastically and their movement is affected by the magnetic field. In the case of

inelastic collisions, electrons ionize or excite the atoms. When the electron's energy decreases to very low energies like 1 eV, according to dissociative attachment reaction it is attached to excited hydrogen molecules or it collides with the chamber wall and leaves the chamber. In this simulation, the total length that electrons have traveled, the total number of collisions and the percentage of electrons involved in gas ionization are calculated.

Results and Discussion

Table 1 shows the value of the total electron path and the number of collisions of electrons with neutral gas for different numbers of magnets. As can be seen, these values are the highest for 12 magnets, which shows a super performance in comparison to the other configurations for this specific dimension. When 12 columns are employed, electron trajectories and numbers of collisions are higher. This result shows that 12 is an optimum case because electrons take more trajectory which results in more collisions, ionization, and finally more plasma density, which is the goal of this research. Electrons are stopped either due to complete loss of their energy in the process of interactions or due to collision with the chamber of ion source.

Table 1. Calculation of the total electron trajectory and number of collisions for the CYCLONE30 multicusp in different numbers of magnets.

	4	6	8	10	12	14
Sum of electron trajectory(m)	11376	18568	21793	37062	43589	18758
Total number of collisions	3309	3068	3685	6864	7070	3990
Average confinement time of electrons in the chamber (s)	2.1E-06	7.3E-06	4.9E-06	6.9E-06	7.4E-06	3.6E-06

Fig 3 shows the percentage of electrons that lose their energy due to interactions in the chamber at a hydrogen pressure of 4 mTorr. The number of samples is 5000. As Fig 3 shows the maximum

percentage of electrons involved in ionization, excitation and dissociative attachment interactions occurs when the number of permanent magnets is 12**.**

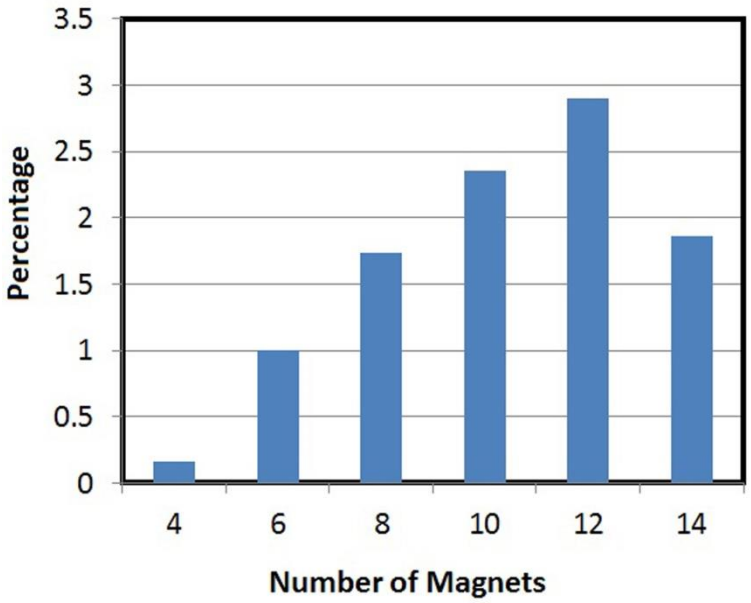

Fig. 3. Percentage of electrons that lost their energy completely due to interactions at a hydrogen pressure of 4 mTorr.

Fig 4 shows the flight time of electrons. The total number of electrons for each simulation is 5000, and almost 90 percent of them hit the wall and stop in our simulation, but a small fraction of them collide with hydrogen molecules. As is evident in Fig 4 when the number of magnets is 12, more electrons fly in the chamber, which entails more negative-ion current production.

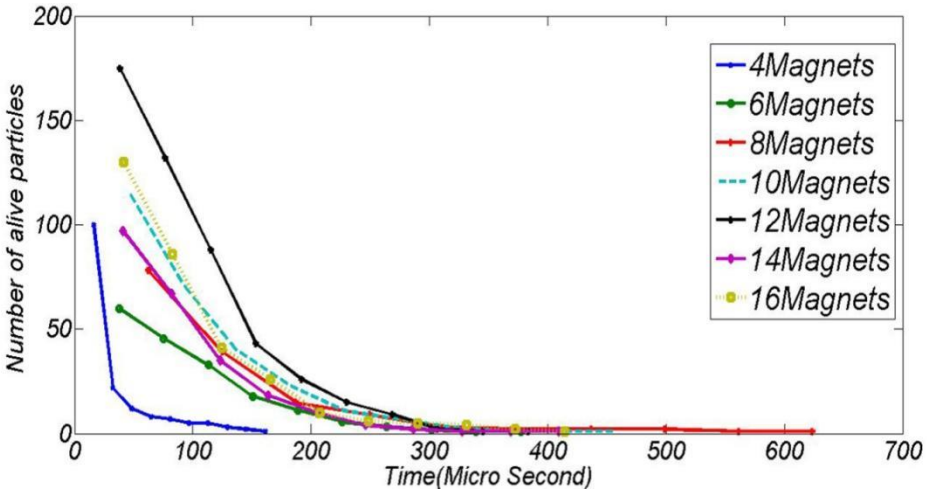

Fig. 4. Flight time of electrons.

References

XianLu Jia, TianJue Zhang, Xia Zheng, and JiuChang Qin, Rev. Sci. Instrum. **83**, 02A730 (2012)

[2] X. Jia, T. Zhang, X. Zheng, S. Zhang, J. Zou, and J. Lin, Rev. Sci. Instrum. **81**, 02A712 (2010).

[3] Kun Uk Kang, Dong Hyun An, Hong Suk Chang, and Jong Seo Chai, Rev. Sci. Instrum. **79**, 02A522 (2008).

Tae-Seong Kim, Seung Ho Jeong, and Sang-Ryul In, Rev. Sci. Instrum. **83**, 02B112 (2012).

[5] K. N. Leung, T. K. Samec and A. Lamm, Phys. Lett. **51** A 490 (1975).

[6] M. Dehnel, T. Stewart, M. Roeder, K. Le Du, **Nucl. Instrum. Methods Phys. Res. B** 241**, 896 (2005).**

M. Bacal, Chem Phys. **398** (2012).

[8] J. R. Hiskes, J. Appl. Phys. **70**, 3409 (1991)

[9] M. Alan and S. F. Wong, Phys. Rev. Lett. **41,** 1791 (1978).